THE OUTER ATMOSPHERES OF 'HYBRID' GIANTS

Graham M. Harper

Trinity College

This Thesis is submitted in partial fulfilment of the requirements for the degree of Doctor of Philosophy in the University of Oxford.

November, 1988

THE OUTER ATMOSPHERES OF 'HYBRID' GIANTS

Graham M. Harper, Trinity College, Oxford

A thesis submitted for the degree of Doctor of Philosophy,

November 1988.

ABSTRACT

This Thesis is concerned with the physical nature of the outer atmospheres of the 'hybrid' bright giants. These stars show C IV emission and evidence of cool, fast winds – unlike giants of similar effective temperature, which possess only cool chromospheres. The K3 II star ι Aur is studied in detail.

Chapter 1 discusses the importance of these stars in the context of the H-R diagram. Chapter 2 examines the evolutionary status of the 'hybrid' bright giants and sets out the physical parameters which are adopted in the atmospheric modelling.

In Chapter 3, the high and low resolution IUE data extracted for ι Aur are discussed. In Chapter 4, the emission line fluxes and profiles are analysed and an emission measure distribution is calculated. Simple hydrostatic models of the transition region and corona are constructed.

Chapter 5 describes the methodology employed to construct model chromospheres using non-LTE radiative transfer. In Chapter 6, computations of the chromospheric structure of a 'hybrid' star are presented for the first time. Calculations made for the first time show that the excitation of the Fe I $y^5G^o_3$ level by the Mg II k line can produce the observed emission in other transitions from the $J = 3$ level.

In Chapter 7, non-isothermal Alfvén wave driven wind models are calculated. It is shown that ι Aur proves to be a severe test of these models and that the transition region and the cool wind are physically separate.

A brief resumé, and possible future research topics are given Chapter 8.

ACKNOWLEDGEMENTS

I am extremely grateful to Dr. C. Jordan for her invaluable assistance and advice during the past three years, while I was a research student in the Department of Theoretical Physics.

I would also like to thank the following for providing an interesting and stimulating environment in which to learn and study: Drs. J. Binney, C. McGill, P. Judge, I. Pallister and D. ter Haar, also P. Tribble, M. Munday, S. Vassar and P. Saha. I would like to thank J. Drake for sharing ideas and resources, and all the departmental staff who help to make life run smoothly. I would also like to thank Drs J. Drew and P. B. Byrne for their helpful comments in the preparation of this work. I am indebted to Dr. B. Montesinos who let me share his office in the last six months.

I would like to thank the staff of the Vilspa Ground Station, Rutherford Appleton Laboratory and the Goddard Space Flight Center who have been very cooperative in supplying data taken with the IUE satellite.

This research has been funded by the SERC, with additional assistance from Trinity College, Oxford. I would also like to thank Mr. A. Davison, Mrs. S. Orian and my parents for warmth and material support during my research period.

Regan Whitelaw Harper was also of invaluable help and assistance.

To Regan, who agreed to share my life.

The time will come when diligent research over long periods will bring to light things which now lie hidden. A single lifetime, even though entirely devoted to the sky, would not be enough for the investigation of so vast a subject... And so this knowledge will be unfolded only through long successive ages. There will come a time when our descendants will be amazed that we did not know things that are so plain to them... Many discoveries are reserved for ages still to come, when memory of us will have been effaced. Our universe is a sorry little affair unless it has in it something for every age to investigate... Nature does reveal her mysteries once and for all.

Seneca, *Natural Questions,*
Book 7, first century

CONTENTS

CHAPTER 1. INTRODUCTION

The aim of this research is to investigate the outer atmospheres of the K 2-4 II, 'hybrid' bright giants by analysing high and low resolution spectra obtained with the International Ultraviolet Explorer Satellite (IUE), together with other available data, in order to construct models of their chromospheres, transition regions, coronae and winds. These models allow the physical processes and energy balance in the outer atmospheres of these stars to be investigated. Stars with 'hybrid' atmospheres show the presence of transition region material (*i.e.,* plasma at 10^5 K which is characterised by emission lines from species such as N V, C IV and Si IV) and also show the presence of a moderate stellar wind with a velocity $\sim 100\,\mathrm{km\,s^{-1}}$. This is in contrast with the properties of other cool stars which are believed to have *either* transition region plasma (and by inference coronal plasma) and a hot wind of negligible mass ('solar-type stars') *or* cool chromospheric material (at $\sim 10^4$ K) and a cool massive wind ('non-solar-type stars') (see Hartmann, Dupree and Raymond, 1980).

The study of the outer atmospheres of cool stars is relevant to many different fields of astrophysics. Stellar activity appears to depend on the presence of magnetic fields generated by dynamo action in the outer convection zone. Thus the interaction of stellar rotation and convective envelopes as stars evolve should be reflected in the magnetic fields generated by the stellar dynamos. Observations of stellar chromospheres and coronae, therefore, provide a way of testing dynamo theories as a function of stellar evolution. The range of conditions in stars with different properties may also allow a better understanding of mechanisms that heat coronae and drive stellar winds. The rate of mass loss and the interaction of stellar winds with the interstellar medium are also of interest in the context of stellar evolution. (See for example reviews by Belvedere, 1983; Dupree and Reimers, 1987.) As a result of early surveys with the IUE satellite (*e.g.,* Linsky and Haisch, 1979; Dupree *et* *al.*, 1979; Brown *et al.*, 1979; Carpenter and Wing, 1979) it became apparent that the spectra of late-type stars were of two basic types. Linsky and Haisch (1979) found that these could be classed as 'solar-type' and 'non-solar-type', separated by a 'Transition Region Dividing-Line' in the H-R diagram. The spectra of the 'solar-type' stars contain the chromospheric lines of H Ly-α, C I, O I and Si II and lines which are formed at higher temperatures, *e.g.*; C II λ1335 (20,000 K), C IV λ1549 (10^5 K), Si IV $\lambda\lambda$1394, 1403 (80,000 K) and N V λ1240 (2×10^5 K). The spectra of the 'non-solar-type' stars contain H Ly-α, C I, and O I and Si II but none of the lines which are formed at higher temperatures.

The aim of this Thesis is to investigate the physical conditions in the outer atmospheres of a group of stars occupying the region in the H-R diagram which, until the discovery of the 'hybrid' bright giants (Hartmann *et al.*, 1980), had been thought to include only 'non-solar-type' stars (*e.g.*, Linsky and Haisch, 1979). Figure 1 shows the location of some of the 'hybrid' bright giants in the H-R diagram. These stars are thought to have 'intermediate' masses ($2M_\odot < M_* < 8M_\odot$), in which case they have evolved from the main sequence where they would have been B stars with $T_{eff} \sim 2 \times 10^4$ K (see Figure 1) and would not have had an outer convection zone. As these stars evolve towards the red giant branch, their surfaces cool and outer convection zones develop and then deepen as the stars climb the giant branch (see review by Iben, 1967). The activity observed in the 'hybrid' bright giants is not typical of that seen in other 'non-solar-type' stars to the right of the dividing line, which share the same region of the H-R diagram. This region of the H-R diagram is populated with stars on their first and second crossing of the Hertzsprung gap and for this reason the 'hybrid' stars are of particular interest in the context of stellar evolution. The evolution of these stars is discussed in Section 2-1.

In this work attention is given to the analysis of ι Aur which seems to be a typical 'hybrid' bright giant. Comparisons are made with another 'hybrid' star,

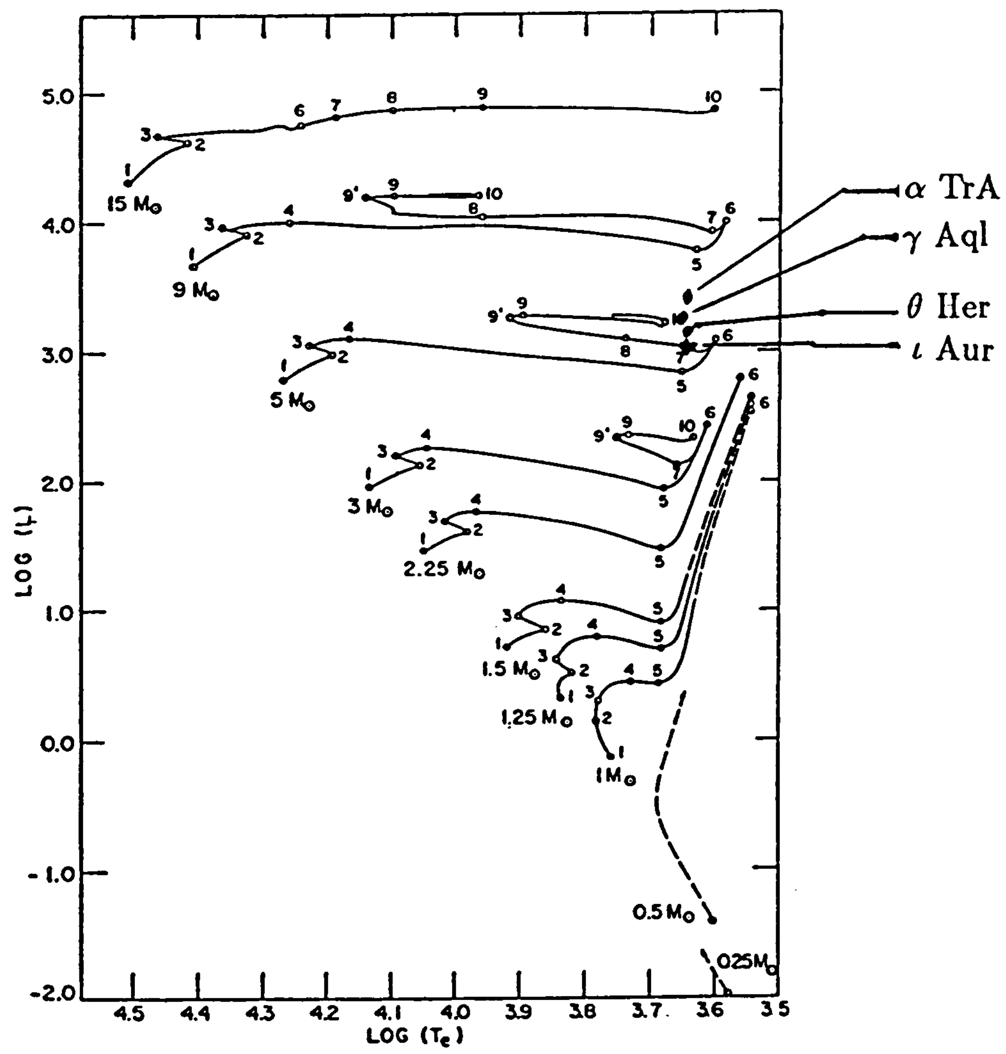

Figure 1. The approximate location of the stars ι Aur, θ Her, γ Aql and α TrA in the Hertzsprung-Russell diagram. Luminosity is in solar units, $L_{\odot} = 3.86 \times 10^{33}$ erg s^{-1} and the temperature T_e is in Kelvin. The diagram also shows representative evolutionary tracks for low-mass, intermediate-mass and high-mass stars. From Iben (1967).

α TrA (K4 II), which together with θ Her (K1 II) and γ Aql (K3 II) have been studied in detail by Hartmann, Jordan, Brown and Dupree (1985) (hereafter called HJBD).

1-1 Historical Context

This section will briefly cover the development of ideas about chromospheres, coronae and winds in the context of the H-R diagram. (For good reviews on stellar chromospheres, transition regions and winds see Jordan and Linsky, 1987; Dupree and Reimers, 1987; Linsky, 1980.) Prior to the IUE, the existence of stellar chromospheres was recognised through the chromospheric emission lines of Ca II H & K (Schwarzschild and Eberhard, 1913; Wilson and Bappu, 1957). Rockets had been used to observed the Mg II h & k lines (Weiler and Oegerle, 1979), while satellites (*e.g.*, Copernicus and TD-1) observed the hydrogen Ly-α line. The earliest spectral classes for which the Ca II H & K lines were observe in emission were F0 V–F0 I (Linsky, 1980). The early observations of the chromospheres of cool giants showed that the strength of the O I resonance lines was enhanced relative to that in the dwarf stars. This has been explained by fluorescent excitation of O I by hydrogen Ly-β (Haisch *et al.*, 1977). For good reviews of cool star spectra see Jordan and Judge (1984) and Jordan *et al.* (1985).

The first detection of a non-solar transition region came from observations of α CMi (F5 IV-V) (Evans, Jordan and Wilson, 1975), made with the Copernicus satellite and with the TD-1 satellite (Jamar, Macon-Hercot and Praderie, 1976). The former detected H Lyman-α, Si III λ1206 and O VI λ1032, O VI being formed at $\sim 2\times10^5$ K. The latter detected the C IV λ1550 doublet which is formed $\sim 10^5$ K. With the new IUE data, Linsky and Haisch (1979) found that the spectra of giant stars could be divided into 'solar-type' and 'non-solar-type'. The division occurs in the H-R diagram as a nearly vertical line at (V-R)$\sim$ 0.8 or K1 III across the giant branch and covering luminosity classes II - IV. The term 'solar-type' was adopted because the spectra showed close similarities to solar UV spectra. The presence of transition region material, together with the measured electron density implies the presence of steep temperature gradients at $\sim 10^5$ K and hence material at coronal temperatures. There are no coronal lines in the IUE wavelength coverage ($\sim 1200 - 2000$Å) of sufficient strength to observe in stellar spectra.

Ayres *et al.*, (1981b) used EINSTEIN Imaging Proportional Counter (IPC) data to find where soft X-ray emission (0.2-0.4 KeV) is observed in the cool half of the H-R diagram. The presence of soft X-rays indicates the presence of gas at coronal temperatures ($T > 10^6$ K). They detected X-rays from F-M dwarfs and in late F to early K giants, but not from cooler giants other than the spectroscopic binary ϵ Car (K0 II + B), or from any supergiants except α Car (F0 Ib-II). Haisch and Simon (1982) used new EINSTEIN IPC and High Resolution Imager (HRI) measurements to investigate the transition region dividing-line, and found that no single stars to the right of the dividing-line showed the presence of X-ray emission. Unfortunately, EXOSAT was not used to observe many late-type stars and added little to the information already collected.

The location of the dividing-line in the H-R diagram is also close to a region where the properties of stellar winds and chromospheric bulk mass motions appear to change. The presence of out-flowing circumstellar material in stars was detected from blue-shifted absorption features by Deutsch (1956), while circumstellar gas was detected from the scattering of the K I resonance line around Betelgeuse (Bernat *et al.*, 1978). Reimers (1977) undertook a systematic search for circumstellar (CS) absorption features in the Ca II resonance lines in red giants earlier than M0. He found CS features indicating mass loss in all K giants and G & K supergiants, which are cooler and more luminous than the region in the H-R diagram designated by spectral type K5 and absolute visual magnitude $M_V = 0.0$, (K4, -1), (K2, -1.8) and (G5, -4). (See Figure 1-2.)

Further observational evidence of mass outflows comes from the asymmetric line profiles in the Ca II H & K lines. Stencel (1978) studied the Ca II ratio K_{2V}/K_{2R} (denoted V/R by Wilson, 1976) for a sample of stars whose spectral type ranged from early F through to late M, with luminosity classes III, II, Ib and Ia. (See Figure 1-3 for a description of the terminology for the Ca II and Mg II self-reversed line profiles.) The ratio will be less than unity if there are bulk, outward accelerating or inward decelerating motions, and greater than unity if there are bulk, outward decelerating or downward accelerating motions. Stencel found that the ratio V/R

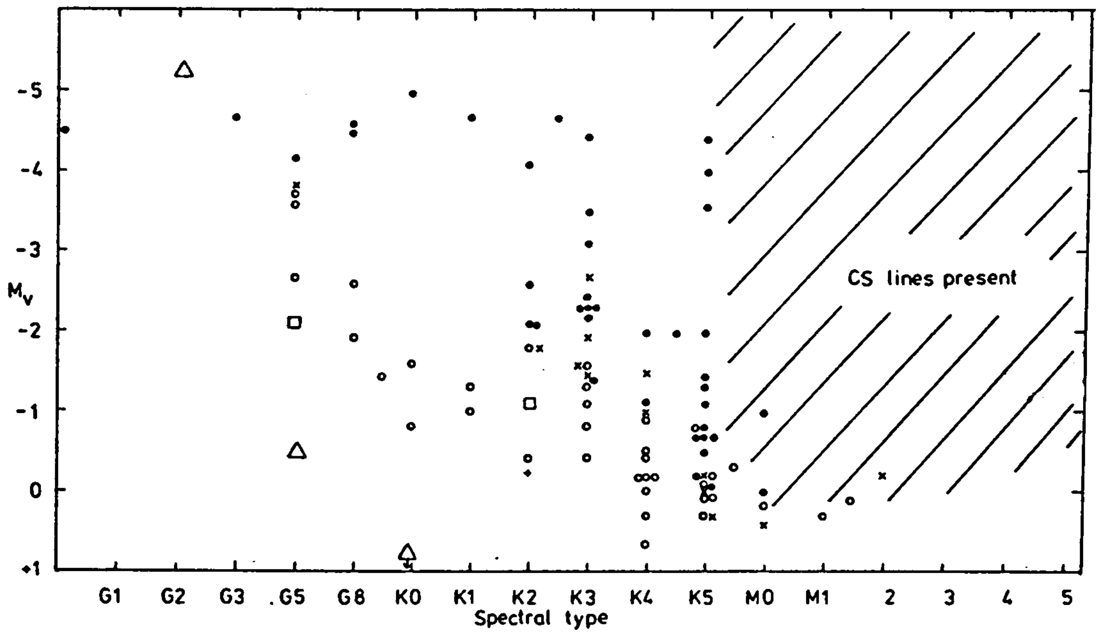

Figure 1-2 The occurrence of the circumstellar absorption features in the Ca II K line in red giants earlier than M0 in the H-R diagram. The spectral types and absolute magnitudes are from Wilson (1976) and Reimers (1977). Solid circles are stars which show permanent CS lines, x's are stars which sometimes show CS lines, empty circles are stars for which no CS lines have been detected, empty triangles are stars with stellar coronae (β Gem, α Aur and α Aqr), the cross is the star α Boo and the empty squares are HD 138481 and HD 13480. From Reimers (1977).

varies smoothly from less than unity in late K and M giants to greater than unity for G giants. This trend also appeared to hold for the bright giants as well. The study of profile asymmetries in the Mg II h & k lines by Stencel and Mullan (1980 a,b) also showed a similar transition to be present in the same region of the H-R diagram. These different delineations of the H-R diagram are shown in Figure 1-4.

The Hybrid Stars

Hartmann, Dupree and Raymond (1980) found that two stars, α Aqr (G2 Ib) and β Aqr (G0 Ib), had evidence of both outflowing material, from the strong blue-shifted absorption components in the Mg h & k line profiles, and material at transition region temperatures (*e.g.,* C IV). They called these stars 'hybrid' stars. Hartmann, Dupree and Raymond (1981) then identified α TrA (K4 II) as having 'hybrid' properties and Reimers (1982) added θ Her (K3 II), ι Aur(K3 II) and δ TrA (G2 II).

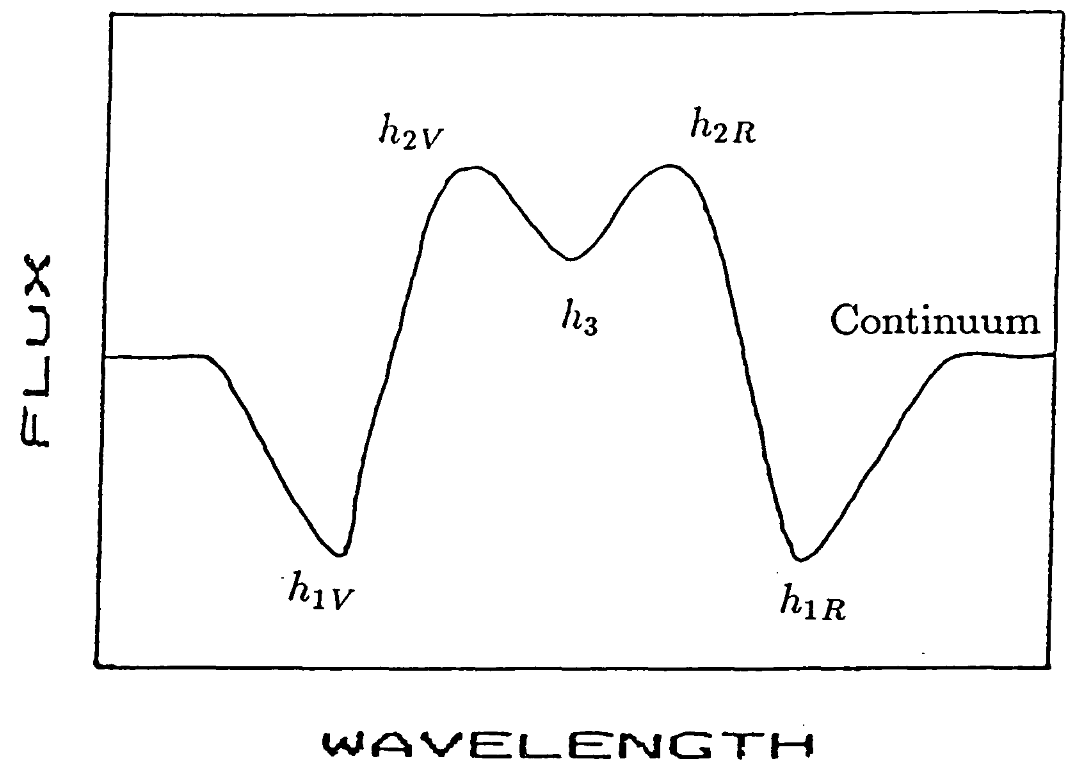

Figure 1-3 Schematic representation of a self-reversed chromospheric emission core. The terms used to describe the different profile features are shown.

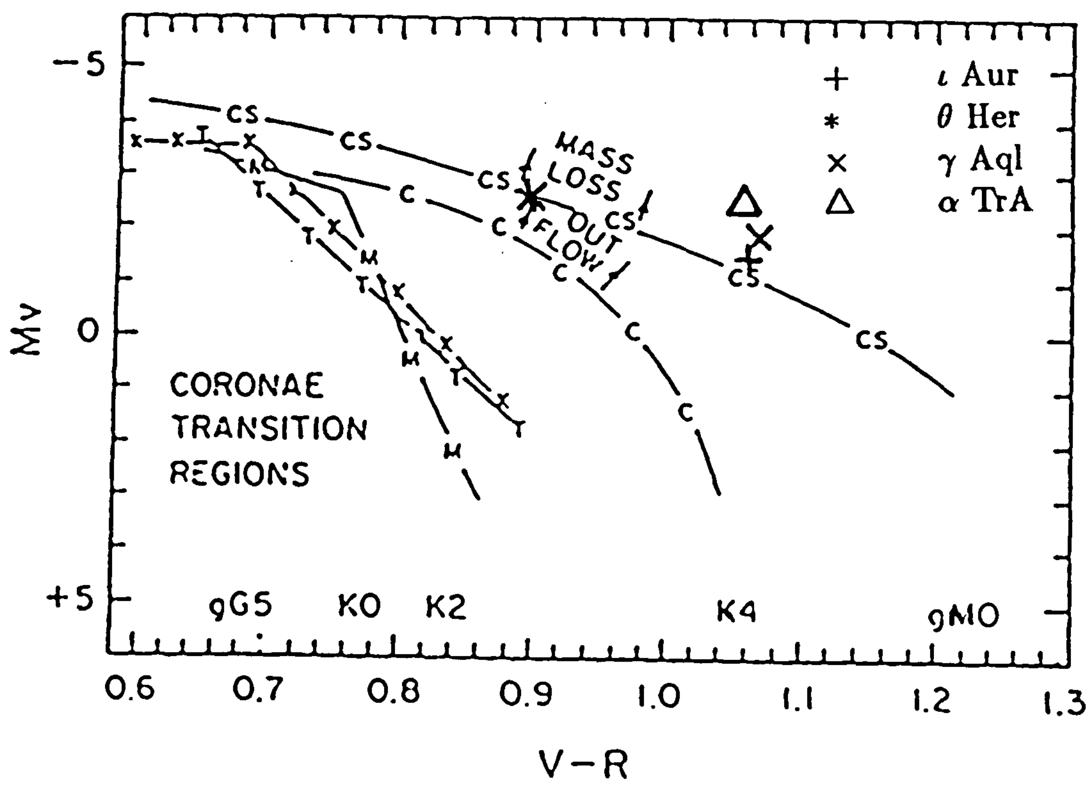

Figure 1-4 Dividing-Lines for different phenomena in the H-R diagram. x's separate regions where soft X-rays (left) are detected and X-rays are not detected (right) (Ayres *et al.,* 1981a). T's separate regions where C IV is present (left) and absent (right) (Linsky and Haisch, 1979). M and C's delimit the regions where massive winds are present (above) and absent (below) as inferred from the profile asymmetries in the Mg II and Ca II resonance lines, respectively. The CS line marks the onset of permanent CS absorption (above) (Reimers, 1977a). From Linsky (1980). The positions of the 'hybrid' bright giants are indicated.

In the paper by HJBD, γ Aql (K3 II) was added to the 'hybrid' stars. These stars showed double absorption features in both the Ca II and Mg II resonance lines: a low velocity component ($\sim$ 10 km s^{-1}) which is believed to be due to interstellar absorption, and a high velocity component ($\sim$ 100 km s^{-1}) caused by the scattering of the line by outflowing cool gas. The presence of high temperature material (C IV) is important because these stars are located in the H-R diagram on the 'non-solar' side of the dividing line.

Up to this time the stars identified as having 'hybrid' atmospheres had been bright giants or supergiants. Judge, Jordan and Rowan-Robinson (1987) found that the giant star δ And (K3 III) also has the characteristics of the 'hybrid' stars. δ And has anomalously strong C IV emission for a K3 III star and also evidence of a high velocity wind. There are now 10 stars that are 'confirmed' hybrids and they are listed in Table 1.

There appears to be fundamental changes in the atmospheric structure of stars near the dividing-line originally proposed for the giant stars, but the position of these changes depends on the stellar mass and is not a simple line in the H-R diagram. The transition from stars with 'solar' to 'non-solar' atmospherės, which show massive cool winds, suggests that important changes in structure do occur in this region. Several arguments have been put forward to explain the changes in atmospheric structure as a function of stellar evolution and these are described in Section 2-1.

1-2 Outer Atmospheres of Cool Stars

The Sun is the best studied star and it is useful to consider the structure of the Sun as a starting point for modelling cool star atmospheres. The cool main sequence stars all show strong emission lines formed between $\sim$ 6000 K and 2×10^5 K, and

Table 1. List of known stars with 'hybrid' properties. Compiled from Reimers (1982, 1987) and Brown (1986).

Star	HD	Visual Magnitude	Spectral Type
α Aqr	209750	2.96	G2 Ib
β Aqr	204867	2.91	G0 Ib
δ TrA	145544	3.85	G2 II
θ Her	163770	3.86	K1 II
ι Aur	31398	2.69	K3 II
α TrA	150798	1.92	K2 II
γ Aql	186791	2.72	K3 II
q Car	HR 4050	3.40	K3 II
δ And	3627	3.27	K3 III
....	81817	4.29	K3 III

which are characteristic of the solar spectrum. Where electron densities have been determined for these stars, it has been found that the pressures are similar to those in different regions of the solar atmosphere. The presence of C IV in the spectra shows that the stars possess transition regions and, by analogy with the Sun, coronae. The presence of coronae is confirmed by the X-ray observations. The giants and supergiants which show the presence of C IV and other high temperature lines have spectra which are broadly similar to those of main sequence stars. However, when comparing the atmospheres of low gravity stars to the solar atmosphere, it should be remembered that the giants and supergiants will have lower electron densities and larger scale heights, so that the relative importance of conduction and radiation from the corona may change.

A full account of the structure and morphology of the solar atmosphere is given in the text by Athay (1976). The observationally inferred run of temperature against height above the solar photosphere, as illustrated in Figure 1-5 from Avrett (1981), shows that an assumption of radiative equilibrium is not valid. The electron temperature T_e is much greater than the solar effective temperature T_{eff}.

Non-LTE processes such as the Cayrel mechanism, where the electron temperature is increased to the temperature of the photoionising radiation field of the photosphere, cannot produce values of $T_e \gg T_{eff}$ in the outer atmosphere of the Sun (Mihalas, 1978). Therefore some non-radiative (non-thermal) heating must be occurring. Globally, the observed cooling of the atmosphere must be matched by some combination of heating processes to maintain the temperature of the atmosphere. Understanding the heating mechanism is important as it determines the structure of the atmosphere. A summary of the energy losses observed in the Sun is given in Figure 1-6.

The solar chromosphere is the region between the temperature minimum, $T_{min} \sim 4 \times 10^3$ K ($\simeq$ 500 km above the level where the optical depth at λ5000 is unity) and $T \simeq 10^4$K (at $\sim$ 2000 km). In the lower chromosphere, hydrogen is mainly neutral and the electrons come from singly ionised metal atoms. The heating in this region comes partly from photospheric radiation and partly from the dissipation of mechanical energy since conduction is not significant here owing to the low temperature (Avrett, 1981). In the Sun, the middle of the chromosphere appears to be non-uniform, *e.g.,* the Ca II K emission line is stronger at the supergranulation network boundaries than in the cell interiors. It is thought that the convective motions below the photosphere sweep the magnetic field from the centre of the convection cell to the edge, where it is concentrated. The correlation of stellar activity with magnetic fields suggests that the supergranulation boundaries may be the site of locally enhanced non-thermal heating and thus, of enhanced chromospheric emission. The H Lyman continuum is optically thick in this region so the ionisation of hydrogen occurs from photoionisation by the Balmer continuum of the collisionally populated $n = 2$ level. The cooling in this region is mainly via the collisionally excited resonance lines of Ca II and Mg II, together with the subordinate lines of the calcium infrared triplet and the Balmer continua and lines.

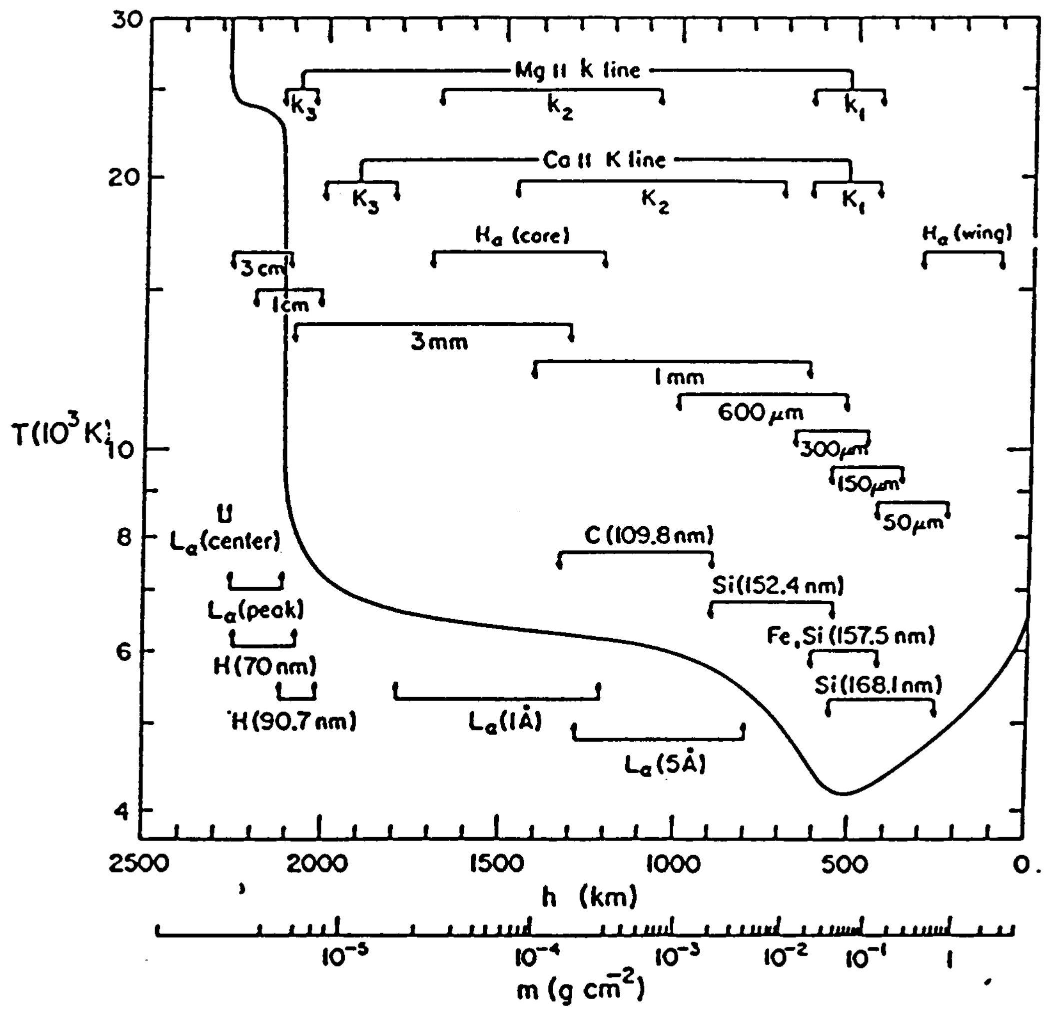

Figure 1-5 The average quiet-sun temperature distribution derived from the EUV continuum, Ly-α and other observations. The approximate depths where the various continua and line components originate are indicated. From Avrett (1981).

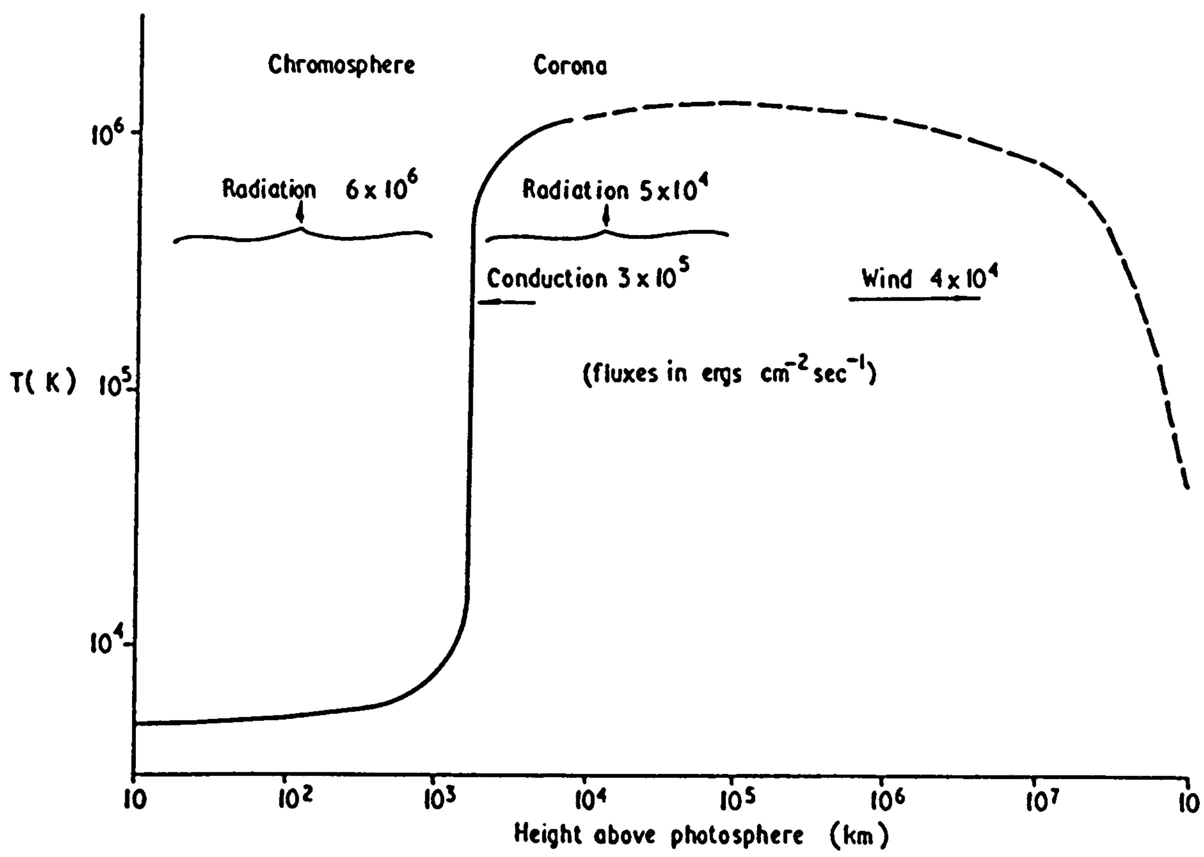

Figure 1-6 Dominant energy loss processes in the solar chromosphere and corona. From data presented in Kuperus (1969).

In the low transition region from 2000 km to $\simeq$ 2300 km ($10^4 < T_e < 3 \times 10^4$ K) the Lyman continuum becomes optically thin as the hydrogen becomes ionised. In Figure 1-5 there is a small temperature plateau in the region of the hydrogen Ly-α emission. The plateau is required to give sufficient optical depth in the Lyman lines to produce the observed central reversals. It is not known if the plateau is an essential feature of the temperature stratification or a result of line of sight observations through structures such as spicules projecting into the corona (Avrett, 1981).

Against the limb of the Sun, rapidly moving spicules can be seen in the strong chromospheric emission lines of H-alpha and Ca II H & K. These *jetlike* structures move upwards at $\sim$ 25 km s^{-1} and reach high ($>$ 11000 km) into the corona before fading (Beckers, 1972). They seem to originate from the upper chromospheric supergranulation boundaries.

The transition region has a thickness of only $\sim$ 30 km for the temperature rise from 3×10^4 K to 3×10^5 K and a thickness of 2500 km for the temperature rise from 3×10^5 K to 10^6 K (Burton *et al.*, 1971). Here the local isothermal pressure scale height is smaller than the characteristic temperature scale so that the pressure does not change significantly throughout the transition region. In the upper chromosphere, the local heating is balanced by radiation losses, while heat conduction from the corona becomes an important source of energy deposition in the energy balance around $1 - 2 \times 10^5$ K. Above $\sim 2 \times 10^5$ K the corona loses energy by conduction to the transition region and by the radiation from highly ionised species at extreme ultraviolet (EUV) and X-ray wavelengths. The outer corona also loses energy in the solar wind. A detailed review of the energy balance and momentum transport in the solar atmosphere has been given by Withbroe and Noyes (1977).

Methods of constructing chromospheric models will be described in Chapter 5 and the methods of making models of the transition regions and coronae are described in Chapter 4, Section 4-5. Some general conclusions from earlier work on model atmospheres are described below. The models of stars which possess solar-type spectra and are observed in the X-ray waveband, show that they also have steep transition regions with coronal gas at $\sim 10^6$ K (*e.g.*, Jordan *et al.*, 1987). In the simple models of main sequence and giant stars made so far, the atmosphere is usually treated in spherical symmetry. This does not allow for the different surface structures. Solar observations show the presence of different components in the atmosphere such as, the quiet-sun, plage, and bright network regions (Reeves *et al.*, 1976). There is also some evidence of non-uniform regions on other stars. For example, Jordan *et al.* (1986) find that in a one-component model of Procyon, the pressure estimated from the X-ray flux is higher than that estimated from the UV line fluxes and widths. These can be reconciled if the UV flux is formed from a limited area, perhaps in *supergranulation boundaries*. One of the problems of linking models of the corona to the transition region is that in the spectral range of the IUE satellite there are no emission lines of sufficient strength formed between 3×10^5 K and the corona. The temperature range $2 \times 10^5 \sim 10^6$ K has been observed only for the Sun.

The energy losses in stellar chromospheres are still expected to be dominated by radiative losses in H-α, Mg II h &k, Ca II H & K and the Ca II infrared triplet, while the importance of conduction is expected to be less in the low gravity stars since the larger scale heights will mean that the temperature gradients will be smaller. Linsky and Ayres (1978) found that the ratio of Mg II h & k radiative losses to the surface flux, $F_{MgII}/\sigma T_{eff}^4$, is independent of gravity. If the radiative losses in the other lines are also independent of gravity, this suggests that the heating mechanism cannot be purely acoustic because acoustic heating theories have a gravity dependence.

Most stellar model chromospheres have been constructed by calculating line profiles of the Ca II and Mg II resonance lines and then comparing the results with the observations. The model is then adjusted to bring them both into closer agreement. It is important to understand the formation of the Ca II H & K and Mg II h & k line profiles, because the approximation of complete redistribution (CRD) is not always valid in the damping wings, where scattering of the resonance lines is nearly coherent and the monochromatic source function decouples from the Planck black-body source function. (See for example Hummer, 1969.) There are some treatments of the effects of partial redistribution (PRD), but there are still uncertainties concerning the validity of the approximations. For a review of the effects of CRD and PRD on line formation see Linsky (1985). The Ca II and Mg II lines are formed below 8000 K, so additional information is needed to extend the models to higher temperatures. This is discussed in Chapter 5.

In this Thesis a model chromosphere/lower transition region for ι Aur is constructed which extends up to 25000 K and then joins onto a model transition region. To supplement the analysis of the Mg II h & k line profiles, transitions from the Fe I (uv44), Al II and Si II are also included. This ensures that the final model is well constrained over a range of temperature.

One important point should be made clear: the models produced suffer to some extent from *non*-uniqueness. It is possible to have more than one model which satisfies a given profile (*e.g.*, Hearn, 1967). However, the simultaneous use of several spectral diagnostics, such as lines formed in overlapping but not identical regions of the atmosphere, or the study of optically thin and thick emission lines formed in similar regions, help to alleviate this problem and this is the approach adopted here. However, the actual atmospheres may be inhomogeneous (in that different temperatures may exist at different heights in the atmosphere) and thus one component models may not describe accurately any of the components individually, but should be regarded as describing the mean atmosphere of the star.

Some of the general trends that have come from these chromospheric models are summarised as follows:

(1) In solar active region models, the photospheric temperatures inferred from the Mg II k line wings are hotter than expected from radiative equilibrium models (*e.g.*, Morrison and Linsky, 1978). This would imply that the photosphere itself is non-radiatively heated in active regions.

(2) Kelch *et al.* (1979) suggest that the temperature minimum in dwarf stars moves to lower mass column density with decreasing non-radiative heating. There is some evidence that the ratio $T_{\rm min}/T_{\rm eff}$ decreases with age for main-sequence stars (Linsky *et al.,* 1979). This would be expected if the non-radiative heating decreased with age.

(3) Active chromosphere dwarf stars have steeper chromospheric temperature rises and greater radiative losses than quiet chromosphere dwarf stars. This is in agreement with model chromospheres of different components of the solar atmosphere, the more active regions having the steeper temperature gradients (Avrett, 1981).

(4) The use of models with velocity fields has shown that caution should be used when analysing asymmetric line profiles (Basri *et al.*, 1981). It is found also in the present work that profiles can result from very different model chromospheres by choosing a suitable velocity field (see Section 6-2-2). It is desirable to have information on the velocity fields in the Ca II and Mg II line forming regions so that the choice of velocity field used in the model chromospheres can be constrained.

1-3 Sources of Heating and Wind Momentum

So far several references have been made to non-thermal heating mechanisms, the nature of which has not been discussed. There are a number of suggested non-thermal heating mechanisms including weak acoustic shocks and Alfvén wave damping. For recent reviews see Vilhu (1987), Cram (1987) and Schrijver (1987). The heating mechanisms that have been proposed must satisfy the energy balance in the outer atmospheres and also provide energy and momentum to drive the observed winds. It is possible that two or more processes may be occurring simultaneously. One process may, for example, be magneto-acoustic waves which damp in the chromosphere and account for the observed radiation losses, the other being fast or Alfvén wave modes which drive a massive wind further out from the star. The present interest in Alfvén wave driven winds originates from the 'hybrid' bright giants and T Tauri stars, which have mass-loss rates in the range of $5 \times 10^{-8} \sim 10^{-10} M_{\odot} \mathrm{yr}^{-1}$ (Hartmann *et al.*, 1985; Jordan, 1986).

Building on the earlier work of Belcher (1971), Hollweg (1973) and Jacques (1977) in the context of the solar atmosphere, Hartmann and MacGregor (1980) made theoretical studies of the effects of Alfvén wave energy and momentum deposition in the atmospheres in late-type stars. They found that massive cool stellar winds can be driven by this process. This theory was applied to the T Tauri stars by Hartmann, Edwards and Avrett (1982) and to the 'hybrid' bright giant α TrA by Hartmann, Dupree and Raymond (1981). These models predict line fluxes, turbulent broadening and wind velocities which can be compared with observations. These models are schematic and produce only qualitative agreement with observations. Hartmann and Avrett (1984) also modelled the chromosphere of α Orionis and found that the wave-driven models did not reproduce the observed line profile parameters.

The energy losses in coronae and in the solar Parker-type winds are small compared to the radiative losses in chromospheres. The 'hybrid' stars have evidence for both high temperature material (and coronae by inference) and a cool massive wind. However, this is not likely to affect the global energy balance because the energy in the cool massive wind is still small compared to the radiative losses. The massive winds in the cool stars are not likely to be driven by thermal pressure (Parker-type winds) because the gas densities where the wind becomes supersonic are too low (see Chapter 7).

In Chapter 7, the non-isothermal Alfvén driven wind formulation of Hartmann and Avrett (1982) is applied to ι Aur. The base of the wind is specified by the chromospheric models described in Chapter 6 and the results are compared to observations.

1-4 Summary

The 'hybrid' bright giants have been discussed in the context of the observed UV and X-ray properties of stars in different parts of the H-R diagram. These stars are important as they are intermediate mass stars where activity cannot have developed on the main sequence but at a later stage of evolution. Their defining properties are the presence of both transition region material ($\sim 10^5$ K) *and* Mg II absorption formed by scattering of photons in an outflowing moderately fast wind ($v \sim 100\,\mathrm{km\,s^{-1}}$).

In this Thesis, models of the chromosphere, transition region, corona and wind of the 'hybrid' bright giant ι Aur are constructed. The physical processes involved in the energy balance in these regions are investigated. These models may allow a better understanding of mechanisms that heat coronae and drive stellar winds by establishing conditions in stars which are substantially different from main-sequence dwarfs or cool giant stars.

CHAPTER 2. EVOLUTION AND STELLAR PARAMETERS

This chapter examines the evolutionary state and the essential physical parameters of the 'hybrid' bright giants, which are required to construct model atmospheres of these stars. There are uncertainties in the parameters of these field stars and the assumptions made are stated below. Most of these stars are believed to be single but Reimers (1982) suggested that the then known 'hybrid' stars (α TrA, α Aqr and β Aqr) might be undetected binary systems with enhanced activity due to larger than average rotation rates. Ayres (1985) proposed that α TrA has an early F dwarf companion which may be the source of the transition region material, but HJBD have rejected this solution. It is assumed that if the stars are in binary systems then the companions are not directly responsible for any of the observed features. A compilation of the physical parameters is given at the end of the chapter.

2-1 Evolution

The general evolution of main-sequence and red giant stars is believed to be reasonably well understood, although in detail the models are far from complete for the more massive stars. There are still uncertainties in the physics which goes into evolutionary models, for example in the nuclear reaction rates and opacities. A more complete treatment of mass loss during evolution is also desirable. When studying the evolution of stars it is convenient to separate them into three categories, for which typical evolutionary tracks are shown in Figure 2-1. *i.e.,*

(i) Low–Mass stars: $\sim 0.8\,\mathrm{M}_{\odot} < \mathrm{M} < 2 \sim 3\,\mathrm{M}_{\odot}$.

(ii) Intermediate–Mass stars: $2 \sim 3\,\mathrm{M}_{\odot} < \mathrm{M} <\sim 10\,\mathrm{M}_{\odot}$.

(iii) High-Mass stars: $\mathrm{M} >\sim 10\,\mathrm{M}_{\odot}$.

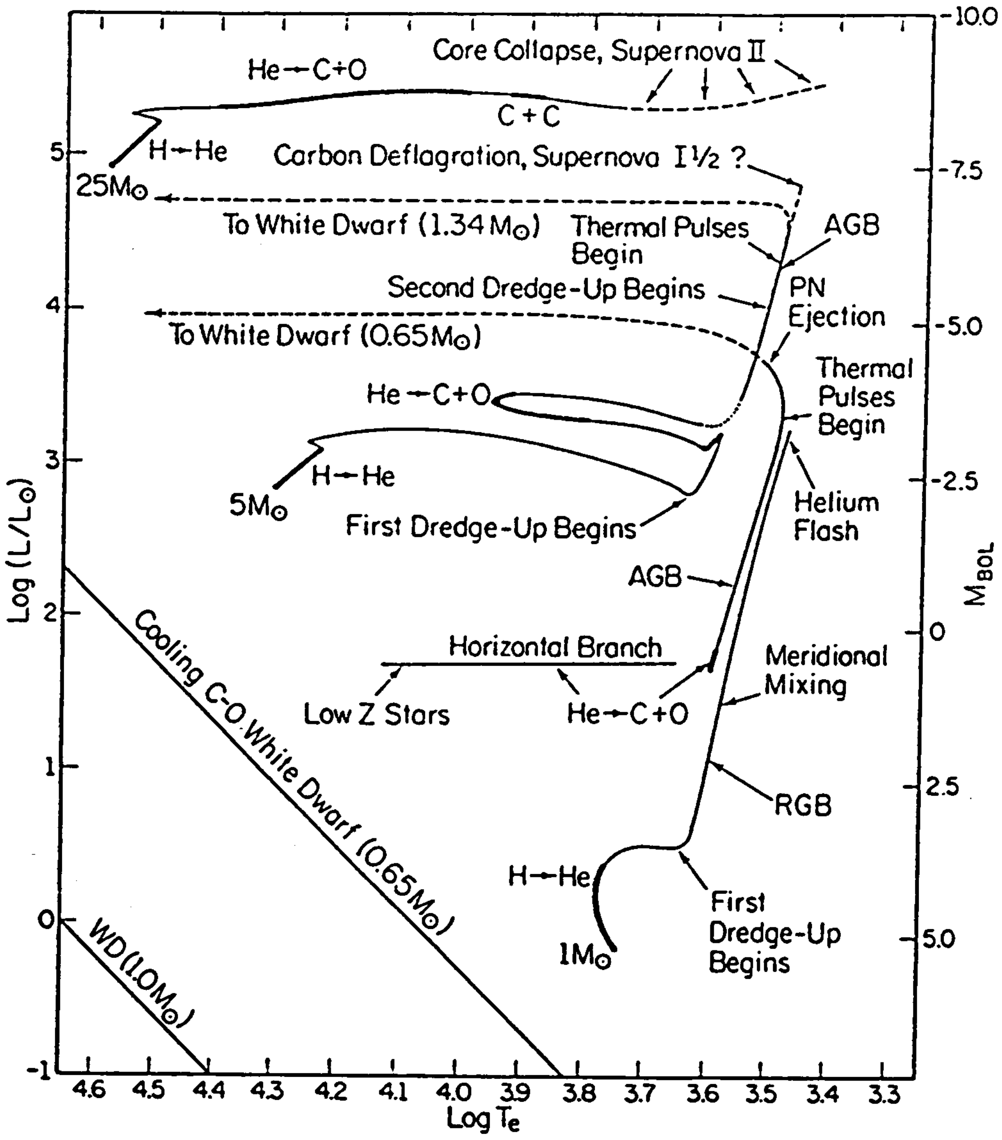

Figure 2-1 Representative evolutionary tracks for stars of class (i), (ii) and (iii). The thick line indicates where nuclear burning in the stellar core takes place on long time scales. The $5\,M_\odot$ star exhibits considerable looping following core helium burning, this has been suppressed and marked by dots. From Iben, (1981).

The 'hybrid' bright giants are considered to be intermediate mass stars, on the basis of their position in the H-R diagram and their photospheric abundances. The evolution of a 5 $M_\odot$ star will be used to illustrate the typical behaviour of an intermediate mass star, and this is shown in Figure 2-2.

For full reviews on stellar evolution see Iben (1967, 1981). An intermediate mass star starts its life on the main sequence as a B star. In particular, a star with mass $\sim 5\ M_\odot$ (such as the one described in Figure 2-2) has a spectral type on the main sequence around B6–B8. At this evolutionary stage, an intermediate mass star is too hot to have a convective zone. As the star evolves off the main-sequence, its surface temperature drops and an outer convective zone develops as the ionised hydrogen recombines. As the stars reach the base of the red giant branch

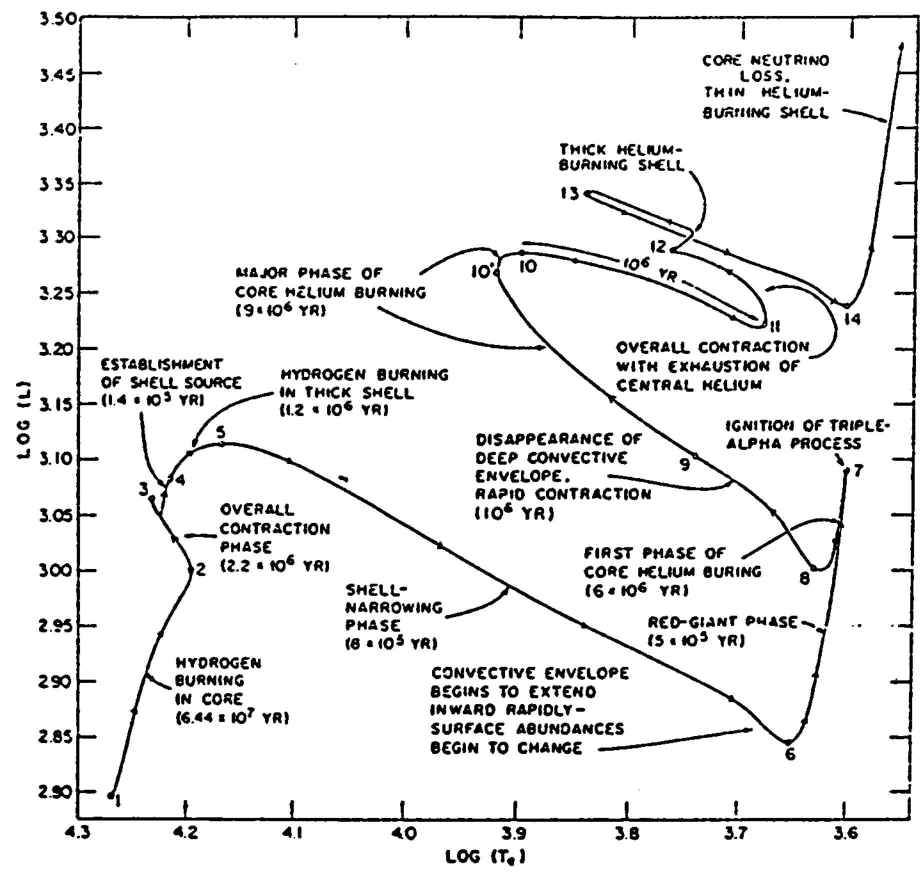

Figure 2-2 The path of metal rich $5M_\odot$ star in the H-R diagram. Luminosity is in solar units, $L_\odot = 3.86 \times 10^{33}$ erg sec^{-1}, and the surface temperature T_e in Kelvin. Traversal times between labelled points are given in years. From Iben (1967).

(RGB), the bottom of the convective envelope moves down towards the interior. The intermediate-mass stars do not have a degenerate electron core on the RGB and undergo helium burning without the helium flash. As can be seen in Figure 2-1, the track moves blueward and then loops before climbing the asymptotic giant branch (AGB).

It is not strictly known whether the 'hybrid' giants are on the first giant branch or on the asymptotic giant branch. Figure 1-1, shows the location of the 'hybrid' bright giants in the H-R diagram. The uncertainty arises from the difficulty in comparing the location of 'hybrid' stars in the observed H-R diagram with their location in theoretical H-R diagrams. The mass and the abundances need to be known in order to compare with calculated evolutionary tracks in the H-R diagram. This also requires that the absolute magnitude and the effective temperature be known. First, since the stars are not spectroscopic binaries their masses cannot be determined directly. Second, abundances as described in Section 2-3 have not been measured for all the 'hybrid' stars and the 'typical' values adopted may be different from the actual ones. These uncertainties make it difficult to determine which giant branch the 'hybrid' bright giants are on. A further problem is that the parallaxes of these stars are quite uncertain and the only other distance estimates are from the statistical properties of the stellar velocities (Egret *et al.*, 1982) or from the Wilson-Bappu effect (Wilson, 1976). The difference in absolute magnitude determined by these two methods can be of the order of ~ 1 magnitude. Here, the working values will be those derived from Wilson (1976). The reason for this choice is that Wilson derived values from *physical* properties of the individual stars, while Egret *et al.*, (1982) derived values from *statistical* properties of a group of stars.

The association between the level of stellar activity with the rotation rate and age in main sequence stars with a convective envelope is well known. Marilli and Catalano (1984) found that the emission in Ca II, C IV and X-rays decreases exponentially when the rotation period increases, independently of the spectral type of the star. While the stellar rotation period is a natural parameter to test rotation-activity correlations, some authors prefer to use the Rossby number, $R_o = V_m/(\Omega L_C)$, where V_m is the maximum convective velocity, Ω is the rotation rate and L_c is the depth of the convection zone. This relates the convective turnover time to the rotation rate, and this represents a measure of dynamo activity. Mangeney and Praderie (1984) found that the same relation between X-ray luminosity and the Rossby number exists for all main sequence stars from spectral type M to O. This suggests that the activity-rotation correlations might be due to the dependence of the dynamo action on rotation. Simon *et al.*, (1985) found that activity decreases exponentially with age for transition region lines, these having a shorter e-folding time than the chromospheric lines. Flux-rotation correlations have been made for giant stars by Simon (1984) and Oranje, Zwaan and Middlekoop (1982), the latter finding that the transition region and chromospheric fluxes both correlate with the rotation rate. Simon (1984) studied the C IV emission from F5 III – G8 III giants thought to be on their first crossing of the H-R diagram. The normalised C IV flux (*i.e.,* the ratio of the C IV flux to the bolometric luminosity) was found to increase until G0 and then decrease, with later spectral type. The normalised C IV fluxes for these stars were found to be, on average, 25 times greater than for other G0–K0 giants, which include the He-burning red giants. The first crossing yellow giants also have larger $v \; sin \; i$'s, so these observations are consistent with an activity-rotation correlation.

Ayres *et al.*, (1981b) proposed that as a result of stellar evolution, the region in the H-R diagram around the G-K giants is occupied by two different types of stars. The K giants are older ($t > 3 \times 10^9$ yr) and less massive ($M \sim 1 \; M_\odot$) than the G giants ($t \leq 3 \times 10^8$ yr and $M \geq 3 \; M_\odot$). The progenitors of the K giants are of a later spectral type and will thus be slower rotators than the progenitors of the G giants. So as a result of the K giants increased age and the slower rotation of its progenitor, the dynamo activity will be less than that of the G giants. To study this proposal further, detailed calculations must be made which include such factors as the depth of the convection zones. This is thought to be an important factor in determining the strength of dynamo activity.

There appears to be a discontinuity in the stellar rotational velocities of the giant stars near G5 III (Gray, 1982), the stars of earlier spectral type having velocities a factor of 5 greater than those of later spectral type. There is a similar change in rotational velocities of subgiants at G0 IV. However, Gray and Toner (1986) found no evidence for such a discontinuity for the bright giants. The 'hybrid' bright giants do not show anomalously high surface rotational velocities.

Endal and Sofia (1979) calculated the effects of evolution on the surface rotational velocities of Population I stars. They assumed conservation of angular momentum and that the star rotates as a rigid body. The radii of the stars increase as they evolve up the giant branch and hence the surface rotation rates decrease. They found that for stars with the mass of a typical 'hybrid' bright giant on the RGB, the surface velocities would be $\sim 3.5\,\mathrm{km\,s^{-1}}$. (The main-sequence progenitor, spectral type B would have a rotational velocity of $\sim 200\,\mathrm{km\,s^{-1}}$ and a radius of $\sim 2.5\,R_{\odot}$.) They found that the calculated surface rotation velocities compared well with the observations, suggesting that there is no evidence for substantial angular momentum loss on the RGB. Gray and Toner (1986) measured the values of $v\ sin\ i$'s for ι Aur, θ Her and γ Aql, and found that they have $v\ sin\ i \leq 4\,\mathrm{km\,s^{-1}}$. These results suggest that 'hybrid' stars have evolved onto the RGB. If the observed rotational velocities were larger it would suggest that the 'hybrids' were moving towards, or were at, the base of the RGB; conversely, smaller observed velocities (if detectable) would imply that the 'hybrids' had evolved to the helium shell burning phase on the AGB.

From Figure 2-2 it can be seen that when a $5\,M_{\odot}$ star moves onto the blue-loop the deep convective envelope disappears. This would mean that any dynamo activity would be diminished so one would not expect to see much stellar activity. When the star returns to the region of lower surface temperature it will be rotating more slowly than when it was on the RGB. The magnetic field will then disperse as the convection zone disappears and any dynamo action is expected to be greatly reduced. It is reasonable to assume that the 'hybrids' are between points 6 and 8 in Figure 2-2. If these assumptions are valid, then by inspection of Figure 1 (Chapter 1) the masses of these 'hybrid' bright giants are likely to be between $5-9\,M_{\odot}$.

2-2 Mass and Radius

To estimate the masses of the 'hybrids', the relationship,

$$(M/R)_{*}/(M/R)_{\odot} \sim 0.1 \tag{2.1}$$

was adopted (Hartmann, Dupree and Raymond, 1981). This relationship is derived from the average properties of K3 II and K4 II stars and is used because a more accurate method of determining masses is not available. From this relationship the mass and the radius can be calculated if the angular diameter and the distance are known. The angular diameters can be derived from the Barnes-Evans relationship (Barnes, Evans and Moffett, 1978). This is an empirical relationship between the visual surface brightness parameter F_V, defined as $F_V = 4.2207 - 0.1V_0 - 0.5Log(\phi')$, and the $(V-R)_0$ colour index. V_0 is the unreddened apparent magnitude in the Johnson UBVRI photometric system and ϕ' is the stellar angular diameter (10^{-3} arcsec). This relationship has been extended to other colour indices. Using the colours obtained from the 11 colour catalogue, it has been found that the best determination of the angular diameters comes from the $(V-R)$ relationship ($8.0(\pm1.2)\times10^{-3}$ arcsec) because this relationship has the smallest scatter (no interstellar extinction correction has been made). The given uncertainty is the standard deviation of the scatter of the data points about the mean relationship and is consistent with the observational uncertainties. The angular diameters derived from the relationship for the $(R-I)$ ($8.0(\pm2.3)\times10^{-3}$ arcsec) index agree well with the $(V-R)$ values but the uncertainty in the derived measurement is greater. The $(U-B)$ and $(B-V)$ indices do not provide unique solutions for the size of the angular diameters but the results are consistent with the $(V-R)$ value.

Using infrared stellar photometry, Blackwell and Shallis (1977) have measured the angular diameter of ι Aur and find $\phi = 8.03(\pm0.3)\times10^{-3}$ arcsec. This value is in good agreement with that derived from Barnes-Evans relationships and will be used in the present work.. Blackwell and Shallis adopt a value of $T_{eff} = 4340(\pm81)$ K for ι Aur and this will also be adopted in the present work.

The distance to ι Aur can be calculated from the difference in apparent and absolute magnitudes. The empirical relationship between the width of the Ca II H &

K lines and the absolute stellar luminosity (the Wilson-Bappu effect) has been used to calculate the absolute magnitude. Wilson (1976) found a value of $M_V = -1.5$ (with a mean deviation of the line width measurement giving ±0.1 magnitudes and an estimate of the mean error of the empirical relationship of ±0.5 magnitudes) for ι Aur, using this method. The distance to ι Aur, calculated from the Wilson-Bappu effect is 69 ± 22 pc. Using equation (2.1) and the measured value of ϕ, the radius is $59(\pm21)\,R_{\odot}$ and the mass of ι Aur is then $5.9(\pm2.1)\mathrm{M}_{\odot}$. (If the absolute magnitude had been calculated from the relationship based on the *statistical* properties of field stars (Egret *et al.*, 1982), the distance would be a factor of 1.6 greater, but as explained above this method is not expected to yield accurate values for individual stars.)

A further estimate for the uncertainty in the mass can be made by considering the evolutionary tracks shown in Figure 1 (page 3). Assuming an uncertainty of 81 K in the effective temperature from Blackwell and Shallis (1977), which corresponds to only $\pm < 0.01$ in the logarithm of temperature, then the position of the star on the temperature axis of Figure 1 will not be significantly affected. Then, neglecting abundance effects, the uncertainty in the logarithm of the luminosity (in solar units, see Figure 1) is ±0.25. If ι Aur is at 91 pc, this corresponds to a mass of $\sim 7M_{\odot}$, if the star is at 47 pc then the mass becomes $\sim 4\,M_{\odot}$. If equation (2.1) had been used instead to calculate the change in mass due to the change in distance then the mass estimate would be $3.8 - 8.0\,M_{\odot}$.

With the measured ϕ, the distance $d = 69(\pm22)$ pc and the masses discussed above, the surface gravity is $46(+29)(-16)$ cms^{-2}. Because the surface gravity is an important stellar parameter in constructing model atmospheres it would be of value to obtain a spectrographic gravity from high resolution optical spectra. These could also be used to measure abundances.

The value of the surface gravity adopted is typical of the gravities expected for stars in luminosity class II. The mass of 5.9 $M_\odot$ calculated from equation (2.1) is in good agreement with the mass of 6 $M_\odot$ derived on the basis of its location in the evolutionary tracks (see Figure 1).

2-3 Abundances

In a galactic context, the combination of mass loss, chemical evolution and the number of intermediate mass stars is important in changing the chemical abundance of the interstellar medium. In this section the effects of the evolution of intermediate mass stars on their surface abundances is briefly described. The abundances need to be known in order to interpret emission line fluxes. Measurements of the electron density often rely on the ratio of fluxes in two different element species, *e.g.,* the ratio of the Si III] λ1893 and C III] λ1909 lines can provide an electron density estimate in the range 10^8 cm^{-3} $< N_e <$ 10^{10} cm^{-3}. If the abundances are not well determined these density diagnostics are not reliable. Conversely, if the electron density is known from another method, then the ratio of the element abundances can be estimated.

As an intermediate mass star evolves off the main-sequence, the surface temperature falls and a convective envelope forms and extends rapidly inwards towards the core (see Figure 2-2). Near point 6, before the star ascends the RGB, the convection zone reaches down to regions of partially processed nuclear material. This material has had its original content of carbon, nitrogen and oxygen processed in the CN cycle. The processed material is then redistributed in this *first dredge-up phase*. The changes in the abundances of carbon and nitrogen are important as these elements produce some of the stronger ultraviolet lines. Lambert (1981) has discussed the chemical composition of Population I giants and supergiants with masses $> 1\ M_\odot$. The relevant results are summarised below. The changes refer to the abundances after the first dredge-up compared with the initial abundances. These are,

(1a) A reduced ^{12}C abundance.

(1b) A higher ^{14}N abundance.

(1c) A slight reduction in the ^{16}O abundance.

During the helium-core burning phase, which is initiated at the top of the RGB, the convection zone does not overlap with processed material, so no significant changes in surface abundances are expected. As the helium is exhausted, the star evolves up the AGB, where conditions may become suitable for further element mixing. For stars of a certain mass range (see below), material from a former hydrogen-burning shell is brought to the surface in the *second dredge-up phase.* The changes in abundances which occur at this stage are briefly (from Iben, 1972);

(2a) A higher He/H ratio.

(2b) A further reduction in the ^{12}C abundance.

(2c) An enhancement of the ^{14}N abundance

(2d) A further slight reduction in ^{16}O abundance.

The mass range in which the second dredge up phase can occur is $3 \sim 5\,M_\odot < M < 8 \sim 10\,M_\odot$ (Kahler *et al.,* 1978). This is relevant for the hybrid giants as they are thought to have masses in this range. There is a further *third dredge-up phase* which is thought to be responsible for high C abundances. This stage occurs beyond the second phase on the AGB.

Table 2-1 Abundance determinations for the 'hybrid' bright giants. The data have been compiled from Williams (1971, 1975) and Rego, Williams and Peat (1972). The abundances for α TrA are taken from Kovács (1983). The abundance values are given in the usual notation.

Table 2-1 'Hybrid'Bright Giant Abundances				
	ι Aurigae	θ Herculis	γ Aquilae	α Tr Australis
HD	31398	163770	186791	150789
T_{eff} (K)	4124	4349	4145	4140
Log(g)	1.5	1.5	1.3	1.45
[Fe/H]	-0.17	0.23	-0.01	-0.05
[Mn/H]	-0.03	0.14	0.01	0.4~0.04
[Na/H]	-0.01	0.05	-0.10	0.21
[Ca/H]	–	0.14	0.00	-0.14
[Ba/H]	0.17	0.71	0.04	0.52

Stellar abundances for the 'hybrids' have been determined from narrow-band photometry and synthetic spectra, the observations being converted into indices and then matched to theoretical indices computed from model atmospheres. These results suffer from uncertainties in the model atmospheres and from the blending of lines in the observed spectra (Williams, 1971). Abundances have also been obtained by Kovács (1983), for α TrA, from a comparison of high-resolution spectra with a model atmosphere. The abundance determinations from the narrow band photometry are shown in Table 2-1, together with the abundances for α TrA. Note that the physical parameters given in Table 2-1 are those of the authors referenced and in view of other work discussed above are not necessarily those adopted here. (The adopted parameters are given in Table 2-3.)

The abundance values in Table 2-1 are given in the usual notation,

$$[\mathrm{X/H}] \equiv \mathrm{Log}_{10}(\mathrm{X/H})_* - \mathrm{Log}_{10}(\mathrm{X/H})_\odot. \qquad (2.2)$$

The error bars given by the authors for the abundance values in Table 2-1 are derived from comparisons of their results with high resolution data and/or a comparison with previous abundance determinations. The error bars (standard errors) are as follows; Fe (0.2–0.3), Na (0.2), Ba (0.3), Mn (0.3) and Ca (0.2). In the case of α TrA the errors are standard deviations. The two values for Mn in α TrA are obtained from lines of high and low excitation. The differences may be due to non-LTE line formation in the photosphere.

From Table 2-1 it can be seen that, within the errors and except for Ba, the stellar abundances for these metals can be represented by solar values. The mild over-abundance of barium could suggest that the stars have evolved past the RGB and could be on the AGB where the third dredge-up phase is occurring. But Kovács (1983) points out that by comparing the effective temperature and bolometric magnitudes, these stars are too hot and too faint to be in the double shell phase (Scalo, 1976). The barium stars also show an enhancement of s-process elements which implies some unaccounted for source of these elements. One theory is that the barium stars are formed from binary systems where the companion has evolved to the third dredge-up phase. Then the s-process enriched atmosphere has transferred material to the observed barium star, leaving the other star as a white dwarf companion. Another theory suggests that the barium over-abundance involves mixing events inside the star itself and is not dependent on a companion star.

The true barium stars show an enhancement of s-process elements by factors of $5 \rightarrow 10$ and a carbon over-abundance by a factor of two. Sneden, Lambert and Pilachowski (1981) showed that for a sample of mild barium stars the C, N and O abundances were those of normal G and K giants and were not C enriched. This implies that the mild barium over-abundance may not be due to internal mixing of the s-process elements, but due to the stars forming out of gas with higher than average s-processed elements. There is no observational evidence that the 'hybrids' considered here have white dwarf companions, but other mild barium stars, *e.g.*, 56

Table 2-2 Adopted abundances for ι Aur. The values for C, N and O are based on the observed abundances of stars of luminosity class IV–I, from Luck (1978), Luck and Lambert (1981), Lambert and Ries (1981), Bonnel and Bell (1982) and Kjaergaad *et al.* (1983). The Al and Si abundances are taken from Kovács (1983). This summary is from HJBD.

Element	$(N_E/N_H)_\odot$	$(N_E/N_H)_*$ (evolved)
C	2.5(−4)	1.4(−4)
N	8.0(−5)	2.1(−4)
O	6.3(−4)	6.3(−4)
Al	2.5(−6)	2.1(−6)
Si	4.0(−5)	5.4(−5)

Peg (K0 II), have been found to have a white dwarf companion from observations of UV continua in the IUE spectrum.

From their position on evolutionary tracks the 'hybrid' stars are expected to have reached at least the first dredge up phase, so on this basis it is justifiable to use ***evolved*** abundances for carbon, nitrogen and oxygen. The analysis of α TrA by HJBD showed that the use of ***evolved*** abundances resulted in less scatter in the derived emission measure distribution (see Chapter 4). The present analysis of ι Aur leads to the same conclusion. The values adopted in the present work are described in the paper by HJBD (except for magnesium, which is assumed to have the solar abundance) and are shown in Table 2-2.

The 'evolved' abundances are also adopted in the calculations of the model chromospheres in Chapter 6. The abundances of other elements are assumed to be solar.

2-4 Compilation of Physical Parameters

The data for ι Aur discussed in the previous sections are summarised below in Table 2-3. The physical parameters of three other 'hybrids', α TrA, θ Her and γ Aql, are given in Table 2-3 for comparison. The parameters of the other stars are not used further.

The effective temperature of γ Aql was obtained from the temperature scale of Ridgeway *et al.,* (1980) using V-K colours from the 11 colour catalogue. The value used for ι Aur was taken from Blackwell and Shallis (1977) (see Section 2-3). For α TrA the effective temperature was taken from Kovács (1983) and the value for θ Her was adopted from Williams (1975) (see Section 2-3). Uncertainties are not quoted for stars other than ι Aur - but the parameters for these stars are not so well determined.

Data not described in the text were obtained from the Centre de Données Stellaires Observatoire Astronomique de Strasbourg.

2-5 Summary

The evolution of a 5 $M_{\odot}$ star and the relationship between stellar activity (as a function of physical structure and evolution) and the H-R diagram have been discussed. On the basis of theoretical evolutionary tracks ι Aur is probably between the base of the RGB and the point on the evolutionary track where the helium core has recently ignited, but before the deep convective envelope disappears (see Figure 2-2). This would be consistent with its level of activity, using simple arguments regarding dynamo action. ι Aur would then be expected to have undergone the first dredge-up phase, with the result that with respect to the initial surface abundances, ^{12} C has been reduced, ^{14} N has been increased and ^{16} O is approximately the same. Typical *evolved* abundances, shown in Table 2-2, are therefore adopted in the following work. There is evidence that ι Aur has a mild over-abundance of bar-

Table 2-3 Physical parameters of ι Aur, θ Her, γ Aql and α TrA.

Parameter	ι Aur	θ Her	γ Aql	α TrA
MK Spectral Type	K3 IIvar	K1 IIvar	K3 II	K4 II
V	2.70	3.82	2.72	1.92
M_V	−1.5	−2.7	−1.9	−2.4
U–B	1.78	1.46	1.68	1.56
B–V	1.53	1.35	1.52	1.44
V–R	1.06	0.90	1.07	1.06
R–I	0.82	0.63	0.75	–
V–K	3.32	–	3.31	–
$v\ sin\ i$ (km s^{-1})	3.5 ± 0.1	3.4 ± 0.6	3.2 ± 0.5	–
ϕ ($\times 10^{-3}$ arcsec)	8.03(±0.3)	3.7	8.0	11.5
$F_*/F_\odot(\times 10^{15})$	2.7	13.9	2.7	1.3
T_{eff}(K)	4340(±81)	4349	4100	4140
$R_*/R_\odot$	59(±21)	74	71	89
$M_*/M_\odot$	5.9(±2.1)	7.4	7.1	8.9
Surface gravity (cm s^{-2})	46(+29)(−16)	36	38	30
Distance (pc)	69(±22)	120	84	73

ium with respect to established evolutionary models and the origin of this barium excess is still uncertain (as for all barium stars). There is a need for more accurately determined abundances and spectroscopic gravities, since these parameters are important in the modelling of stellar atmospheres.

CHAPTER 3. OBSERVATIONAL DATA

This Chapter describes spectra of the star ι Aur obtained with IUE, and the reduction of these data. ι Aur has been observed with the IUE satellite at both high and low-resolution with the long and short wavelength cameras. For details of instrumentation and performance of the IUE satellite see Boggess *et al.* (1978a, 1978b). The hybrid bright giants have been studied by other astronomers, in particular, Hartmann, Dupree and Raymond (1981), Reimers (1982) and HJBD. The high resolution (HIRES) data for ι Aur, however, have not been reduced previously. The HIRES data enable wavelength shifts and line profiles to be measured to an accuracy of $\pm 7\ \mathrm{km\ s^{-1}}$ and some blends present in the low-resolution spectra can be resolved. These data are important in providing information about the velocity fields in the stellar atmosphere (see Chapters 4 and 7). The low resolution (LORES) short wavelength data have also been re-extracted, and are useful in determining emission line fluxes. If the lines are unblended, the fluxes obtained from low resolution spectra will be more reliable than the fluxes obtained from the high resolution spectra because of the increased signal to noise ratio. But between 1800 – 2000 Å the high resolution spectrum allows a better determination of fluxes above the level of the continuum. In Section 3-1 the reduction of the HIRES and LORES spectra is described. The results are tabulated in Section 3-3, and in Section 3-4 details of other observations are given.

3-1 IUE Data Reduction

The IUE images that have been analysed are listed in Table 3-1. The spectra were taken as part of a continuing collaborative program between research groups at Oxford, Harvard and Boulder.

Table 3-1 The IUE data for ι Aur used in this work (all exposures were taken with the large aperture, LAP). The exposure time is in minutes and the date is in year and days.

Image	Dispersion	Exposure time (Min)	Date (Year, Day)
LWP4014	HIRES	415	84-230
LWP5200	HIRES	310	85-013
LWP5199	HIRES	12	85-013
SWP15474	LORES	90	81-315
SWP17719	LORES	465	82-230
SWP16458	LORES	210	82-060
SWP15503	HIRES	887	81-319

The spectra were extracted from image files on the IUE Guest Observer tapes or from the tapes obtained from World Data Centre. The extraction was performed using the IUEDR program (Giddings, 1982) at the Rutherford-Appleton STARLINK node. A full description of the extraction techniques used in this work is given in Judge (1986a). The reductions did not employ the ***default*** set of extraction parameters because it is possible to obtain better extractions if the parameters are chosen to suit the particular nature of the spectra. For example, in the HIRES exposures the continuum signal is weak and the auto-tracking could result in contamination from nearby 'hot-spots' etc., thus this option was not used. The photowrites of the images were used extensively to distinguish between 'hot-spots', defects and stellar features.

3-1-1 Short Wavelength Spectra

The absolute flux calibration of the short wavelength LORES spectra was that of Bohlin and Holm (1980). For the HIRES spectrum (1250 – 1950 Å) the Bohlin and Holm calibration was merged with the high/low resolution ratios of Cassatella, Ponz and Selvelli (1981). The errors in this calibration are $\sim \pm 15\%$ for 1400 Å $<$

$\lambda < 1975$ Å. The lines in the following analysis lie between $1296 < \lambda < 1995$Å, so that errors from the linear extrapolation of the calibration curves are expected to be less than $\pm30\%$ (using data presented in that paper).

For the LORES spectra the wavelength calibration was determined by making least-square Gaussian fits to neutral species O I (1304.6Å), O I] (1356.6Å) and C I (1657.3Å), which are formed in similar regions of the stellar atmosphere. The resolution of the LORES images is ~ 6 Å (Cassatella *et al.*, 1985), and the main use of these spectra is to obtain well exposed emission-line fluxes. Figure 3-1 shows two SWP LORES spectra of different exposure times. The fluxes corresponding to the different emission lines measured are given in Table 3-3.

The high-resolution spectra are useful because the resolution ($\lambda/\Delta\lambda \simeq 1.05 \times 10^4$ at 2000 Å to $\sim 1.3 \times 10^4$ at 1300 Å, Imhoff, 1983) is high enough to enable wavelength shifts of $> 7\,\mathrm{km\,s^{-1}}$ to be detected. The wavelengths were calibrated by making least-square Gaussian fits to the intersystem lines O I] (1641.30Å), C I] (1993.62Å) and to S I uv9 (1295.65Å, 1296.17Åand 1302.86Å). This produces a wavelength scale which is relative to the base of the chromosphere, where the neutral atoms are located. The wavelength scale should be accurate to $\pm7\,\mathrm{km\,s^{-1}}$ with part of the error being due to internal wavelength errors of $1\sigma \leq 2-3\,\mathrm{km\,s^{-1}}$ (Harris and Sonneborn, 1986). The identifications were based on the laboratory wavelengths tabulated by Kelly (1982). The results are given in Table 3-4. Figure 3-2 and Figure 3-3 show some of the important features in SWP15503.

3-1-2 Long Wavelength Spectra

The long wavelength HIRES spectra ($\lambda/\Delta\lambda \sim 1.2 \times 10^4$) were calibrated in absolute flux using the LORES calibration of Cassatella and Harris (1983) merged

Table 3-2 List of photospheric lines suitable for calibrating the long wavelength spectra.

Fe I (λÅ)	multiplet	Cr II (λÅ)	multiplet
2767.52	46	2849.83	5
2778.22	44	2855.67	5
2788.10	44	2862.57	5
2808.33	45	2867.65	5
2813.29	44	2877.97	5
2828.81	45		
2863.86	2		
2874.17	2		

with the high/low resolution ratios of Cassatella *et al.* (1988). A reliable wavelength scale, relative to the photosphere, was established using symmetric, unblended photospheric absorption lines of Fe I and Cr II. It was not possible to use the same lines to calibrate all the spectra because only some of the lines have symmetric and unblended profiles in each spectrum (see Table 3-2). The wavelength scale should be accurate to $\pm 5\ \mathrm{km\,s^{-1}}$ in the range 2760 Å – 2880 Å. The identifications of spectral features are based on previous work on cool stars by Judge (1986a, 1986b), Carpenter *et al.* (1985) and the laboratory wavelengths from Kelly (1979).

3-2 Interstellar Extinction and Absorption

To calculate the stellar UV fluxes from the fluxes at the Earth, the effects of interstellar extinction and interstellar absorption need to be considered. Interstellar extinction is believed to be due to scattering and absorption of radiation by particles whose size is comparable to the wavelength of the radiation. Interstellar absorption is due to the absorption of radiation by the gas in the line of sight. The absorption is greatest for resonance transitions of species with large oscillator strengths and high abundances.

Since ι Aur is fairly close ($\sim$ 70 parsecs) the effects of interstellar extinction are not likely to be large. The extinction A_λ can be found if the colour excess E_{B-V} is known (Seaton, 1979). Because these stars are so near, the value E_{B-V} is too small to be directly measured. An alternative method of finding a value of E_{B-V} is to use the relationship found by Bohlin *et al.* (1978) *i.e.*,

$$< [N(\mathrm{HI} + \mathrm{H}_2)/\mathrm{E}_{B-V}] >= 5.8 \times 10^{21} \, \mathrm{atoms\, cm^{-2} mag^{-1}}. \qquad (3.1)$$

This relation is derived from studies of interstellar H Ly-α absorption features in stellar spectra. The only assumption made in reducing Ly-α profiles to values of column densities are that the interstellar line has a pure damping profile and that the stellar H Ly-α line is narrower than the interstellar absorption feature (*i.e.,* $N(\mathrm{HI}) \geq 5 \times 10^{18} \mathrm{cm}^{-2}$). Paresce (1984) has analysed available data to find a mean relation between distance and column density. The stars studied here are in regions of galactic longitude where the following relationship has been found to be valid for nearby stars;

$$N(\mathrm{HI})/r = 2 \times 10^{17} \, \mathrm{cm^{-2}\, pc^{-1}}, \qquad (3.2)$$

where r is the distance in parsecs. Using the adopted distances to ι Aur and the equations above, in the wavelength range of the IUE satellite cameras, a maximum value for A_λ of $\sim$0.04 mag is found at λ2150 and λ1200. This leads to a maximum correction of $\sim$ 6% and the corrections have, therefore, been neglected.

From the estimate of column mass it is possible to calculate the equivalent width of the interstellar absorption in lines of high opacities. Using cosmic abundances for oxygen and magnesium, and the oscillator strengths from Garstang (1961) and Froese Fisher (1976) respectively, the optical depth at line centre, τ_0, can be found from equation (4.7). For Mg II k λ2795 the optical depth at line centre is $\tau_0 \sim 1.3 \times 10^2$. Using the relationship for $\tau_0 \gg 1$ (Spitzer, 1978) where the equivalent width W is a weak function of τ (*i.e.*, $\mathrm{W}/\lambda = 2.b.\mathrm{F}(\tau_0)/c$, where $\mathrm{F}(\tau_0) = \sqrt{ln(\tau_0)}$

for $\tau_0 \gg 1$), an upper-limit of 0.2 Å to the equivalent width is calculated. The O I, $\lambda 1302 - 1306$, triplet lines have self-reversed features which cannot be explained by this amount of absorption. If the self-reversals have an interstellar origin, then the line at 1302.17 Å will have the greatest absorption, since the atoms will be in the lowest energy state and little or no absorption would be expected in the lines which originate from $^3P_1$ and $^3P_2$. Although the line at $\lambda 1302.17$ is contaminated by a reseau, the other lines also show significant absorption and asymmetry, suggesting that the reversal is due to scattering in the stellar atmosphere. The Mg II h & k lines show two absorption features, the low velocity component is believed to be partly of interstellar origin (Drake, Brown and Linsky, 1984). The velocity vector of the interstellar medium in the direction of ι Aur is $\sim 18\,\mathrm{km\,s^{-1}}$ and from this, one would expect an absorption feature to be seen blueward of the rest wavelength. This shift is consistent with the reversals in both the O I ($\lambda 1302.17$) and the Mg II lines. The depth of the absorption features in the Mg II h & k lines is consistent with the equivalent width *upper-limit.* (An accelerating stellar outflow could, of course, also produce such an effect.) The effects of interstellar absorption will be neglected so that the stellar fluxes adopted may be underestimates of the true fluxes in lines with high opacities. The absorption in the Mg II lines will be discussed further in Section 6-2, where the line profiles are compared with the results of chromospheric modelling.

3-3 RESULTS

Tables 3-4 through to Table 3-6 list lines with well established identifications. Owing to the nature of the HIRES spectra some weak features remain unidentified. The fluxes were measured using the STARLINK program DIPSO (Howarth and Maslen, 1984). Lines having profiles that are approximately Gaussian are fitted with best fit least-squares Gaussian profiles. This enables the full-width at half-maximum intensity (FWHM) to be measured. If the feature is symmetric the centroid of the profile can also be found. For asymmetric lines the fluxes are measured by integrating the area under the profile. There is no real stellar continuum in the SWP HIRES spectrum and the continuum is set from the average of the background noise level. The errors in the flux determinations are mostly due to the uncertainty in the background noise level and, in some cases, due to the poor signal to noise ratio. The likely error in the line fluxes can be found by comparing the fluxes measured with different background noise levels. The lines which have unblended profiles and a signal to noise ratio of greater than 4 should have an uncertainty in the total flux of less than 20%. The errors in the line fluxes of the lines measured above the continuum at $\lambda > 1850$Å are discussed in Section 3-3-1. The observed fluxes are converted to stellar fluxes using the scale factor discussed in Section 2-4. The wavelength shifts and FWHM values are given in $\mathrm{km\,s^{-1}}$.

3-3-1 SWP Low Resolution Data

The photowrites (photographic records of two-dimensional images) of the LORES spectra SWP17719 and SWP16458 show the spectra to be broader, in a direction perpendicular to the spectra, than in photowrites of giant stars of similar temperature. The camera focus and the satellite pointing have been checked and there is no obvious instrumental source of broadening. ι Aur is not expected to be a binary system and if there is more than one component in the image, it is not resolved. The two longest LORES exposures were taken six months apart so that the spectrum dispersion direction is the same for these exposures. Because the HIRES spectrum is perpendicular to the LORES spectrum, if high and low resolution spectra are obtained at similar times, the extension observed in the SWP photowrites could be apparent as broadening in the wavelength direction of the HIRES spectra. Exposures SWP15503 and SWP15474 were taken 4 days apart, but unfortunately the SWP15474 exposure is too short to be certain that extension is present. In the HIRES spectrum the S I and O I] lines (see Table 3-4) do not show evidence of broadening beyond the usual instrumental broadening. It is not possible to analyse the present IUE data further and an investigation of possible circumstellar scattering must await the Hubble Space Telescope. Plate 1 shows the photowrite of the 210 minute, SWP16458, exposure. The Plate shows the geocoronal H Ly-α (top centre) and towards longer wavelengths some of the features are the blended O I λ1302 multiplet plus S I (uv9), the C IV λ1550 doublet, Si II at λ1817 and the bright continuum shortward of λ1820.

Different lines have their optimum exposure in different spectra and the fluxes adopted take account of this, *e.g.,* O I (λ1304) is taken from SWP15474 and SWP16458 and Si IV ($\lambda\lambda$1394, 1403) from SWP17719. There is evidence of short term variability in the Mg II h line (Veale and Brown, 1988) of $\sim$ 12% about a mean value. Thus some other chromospheric lines may thus show variations of this order. The spectra show the presence of lines which indicate plasma at temperatures between 2×10^4 K and 10^5 K, *i.e.,* C IV λ1550, Si IV $\lambda\lambda$1394, 1403, C III] λ1909, Si III] λ1893 and C II λ1335. The O IV $\sim \lambda$1400 lines may be present but will be blended with the Si IV doublet. The deep exposure SWP17719 shows the presence of N V. The He II multiplet at $\sim \lambda$1640 may contribute to the total flux at this wavelength but He II is not observed in the SWP high-resolution spectrum, whereas a line is present at λ1641.3 which corresponds to O I]. The possibility that fluorescence by the O I resonance lines may cause emission lines in CO bands in the IUE short wavelength region was suggested by Ayres, Moos and Linsky (1981c). This could account for the signal observed at λ1380. However, the weakness of other potential CO lines suggests that the C IV flux at $\sim \lambda$1550 is not significantly contaminated by CO emission. There are weak features present at λ1713-1737 which may be blends of Fe II. N III] may contribute to the feature at

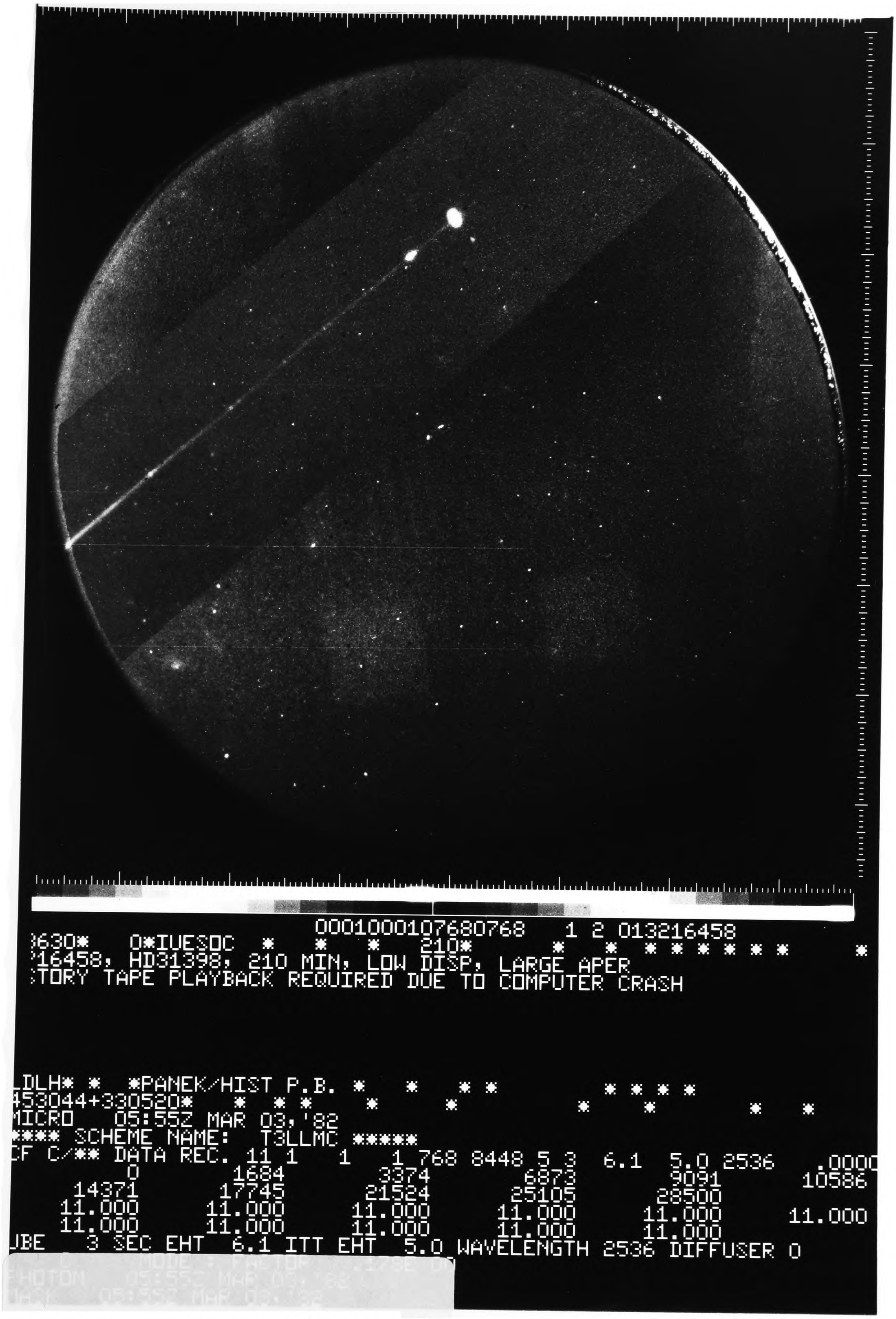

PLATE I. Photowrite of the IUE exposure SWP16458; a short wavelength, low dispersion image. The bright rectangular feature (top center) is tha geocoronal Ly-α (see text for details).

Table 3-3. Fluxes for the emission lines identified in the SWP LORES spectra, SWP15747, SWP16458 and SWP17719. The observed wavelength, identification (ID), and the flux at the star [F_*, (erg cm^{-2} s^{-1})] are tabulated. The numbers in parentheses are the indices of the power of ten, *i.e.*, $6.6 \times 10^2 = 6.6(2)$.

$\lambda_{\mathbf{Observed}}$ (Å)	ID	SWP15474	SWP16458	SWP17719
1240	N V	–	–	2.3(2)
1296	S I, Fe II	–	7.1(2)	1.0(3)
1304	O I	3.9(3)	4.1(3)	†2.5(3)
1335	C II	–	‡7.3(1)	1.4(2)
1357	O I]	–	‡7.6(1)	1.7(2)
~ 1380	CO?	–	–	2.2(2)
1394,1403	Si IV	–	–	1.1(2)
1475	S I	3.0(2)	–	1.4(2)
1549	C IV	‡1.2(2)	1.9(2)	1.5(2)
1641	O I	‡1.6(2)	‡2.5(2)	1.6(2)
1658	C I	5.4(2)	3.0(2)	2.1(2)
1718 – 1737	?	–		1.0(2)
1750	N III] + ?	–	1.2(2)	1.2(2)
1808	Si II	1.8(2)	1.5(2)	1.5(2)
1817	Si II	5.1(2)	5.9(2)	5.8(2)
1893	Si III]	–	–	‡1.5(2)
1900	S I	–	‡3.2(1)	‡1.7(2)
1909	C III]	–	‡4.6(1)	‡1.0(2)
1914	S I	–	–	‡7.7(1)

? Uncertainty in identification or reality of feature.

†Line flux estimated from symmetrical over-exposed profile.

‡Estimate of the flux (see text).

$\sim \lambda 1750$, but the upper-limit this provides to the emission measure distribution is not useful. These lines are too weak to detect in the HIRES spectrum SWP15503. The continuum flux increases above 1700 Å, but above 1820 Å the line fluxes become uncertain because it is difficult to determine the correct continuum level, given also the presence of absorption lines. Figure 3-1 shows the SWP17719 and SWP16458 spectra extracted with the *default* values of the extraction parameters. A reseau in the region off the spectrum where the background is taken causes contamination at $\sim$ 1910 Å, and care is needed in the *actual* spectrum extraction. The fluxes in the SWP17719 spectra, in this wavelength region, were measured by simultaneously fitting gaussian profiles to the lines above $\lambda 1880$ and allowing for the absorption by neutral carbon at $\lambda 1930$. Different background fits were tried for the continuum and it was found that the fluxes for lines in SWP17719 at $\lambda 1893$, $\lambda 1900$ and $\lambda 1909$ changed by less than 20%.

3-3-2 SWP High Resolution Data

The very deep exposure SWP15503 enables the optically thin intersystem lines of Si III], C I] and O I] to be observed. These lines provide valuable information on the velocity fields in the regions of line formation. The noise in the spectrum is quite high and some weak features of uncertain reality remain unidentified. The He II B-α lines at λ 1640 are not observed at high resolution. The C I line at $\lambda 1657.38$ is resolved from the rest of multiplet 2. The lines identified are listed in Table 3-4.

Figure 3-2 shows the O I and S I lines. The O I lines have blue shifted self-reversed line profiles indicative of bulk flows in the line forming regions. The rest wavelengths are indicated by tick marks.

Figure 3-3 shows profiles of the optically thin intersystem lines of Si III], C I] and O I]. The Si III] profile is broad and is contaminated by a noise spot on the

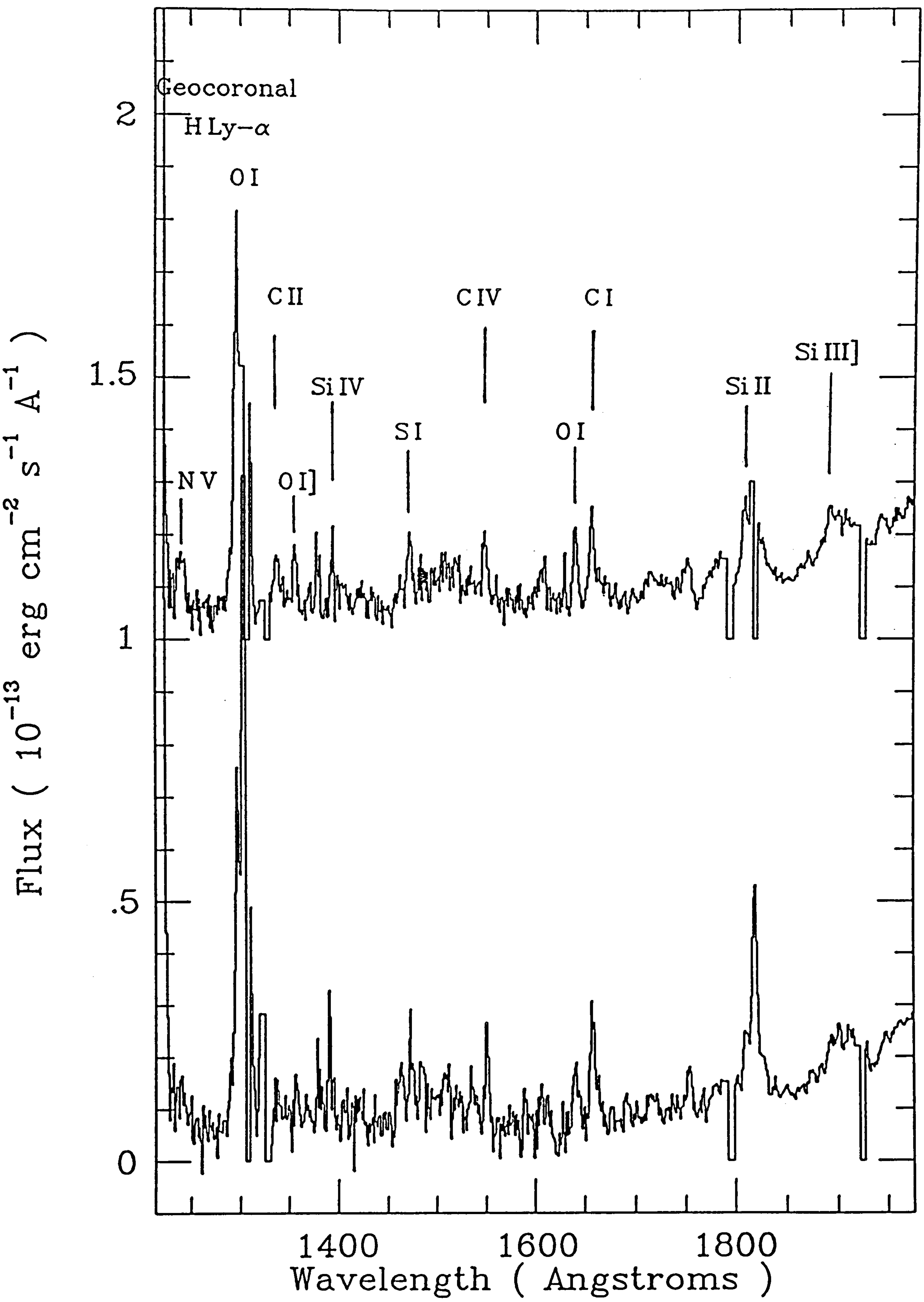

Figure 3-1 Annotated spectra of SWP17719 (top) and SWP16458 (bottom). The top spectrum is raised by 1.0 (on the axis scale) for the sake of clarity. It was previously published by HJBD. The lower spectrum corresponds to the image shown in Plate 1. The flux units are as measured at Earth and bad data points which may contaminate the spectra (*e.g.*, reseau marks and saturated pixels) are flagged to the zero flux level.

Table 3-4. Emission-line parameters for the lines identified in the HIRES SWP15503 spectrum, *i.e.*, the laboratory wavelengths (from Kelly, 1982), identification (ID), flux at the star, full width at half-maximum intensity (FWHM) and the centroid velocity of the observed lines. The velocity centroid is tabulated if the line is symmetric and unblended. The numbers in parentheses are as in Table 3-3.

λ_{Lab} (Å)	ID	F_* (erg cm^{-2} s^{-1})	FWHM km s^{-1}	Δv km s^{-1}
1215.67	H I Ly-α	–	–	–
1295.65	S I uv9	5.1(2)	‡	–
1296.17	S I uv9	4.4(2)	30	−7
1302.17	O I uv2	Reseau	–	–
1302.34	S I uv9	Blended with O I	–	–
1302.86	S I uv9	3.2(2)	< 25	+2
1304.86	O I uv2	1.4(3)	‡100	−2
1305.88	S I uv9	Blended with O I	–	–
1306.03	O I uv2	1.0(3)	‡	–
1355.60	O I]	2.5(2)	< 25	–
1358.51	O I]	ul.0(2)	–	–
1641.30	O I]	1.2(2)	‡‡29	0
1657.38	C I	8.8(1)	40	−7
1807.32	S I uv2	6.0(1)	‡	–
1808.01	Si II uvl	1.6(2)	47	0
1816.93	Si II uvl	3.7(2)	40	4
1817.45	Si II uvl	Reseau	–	–
1820.34	S I uv2	2.0(2)	‡	–
1826.24	S I uv2	8.1(1)	‡‡	–
1892.03	Si III]	4.1(1)	‡‡~ 71	+2
1900.29	S I	3.1(2)	34	+3
1908.73	C III]	ul 1.1(2)	< 107	–
1993.62	C I]	9.6(1)	35	−8

‡The line has an asymmetric profile, values of widths are estimates only.

ul Upper limit to flux measurement.

‡‡These are marginal measurements.

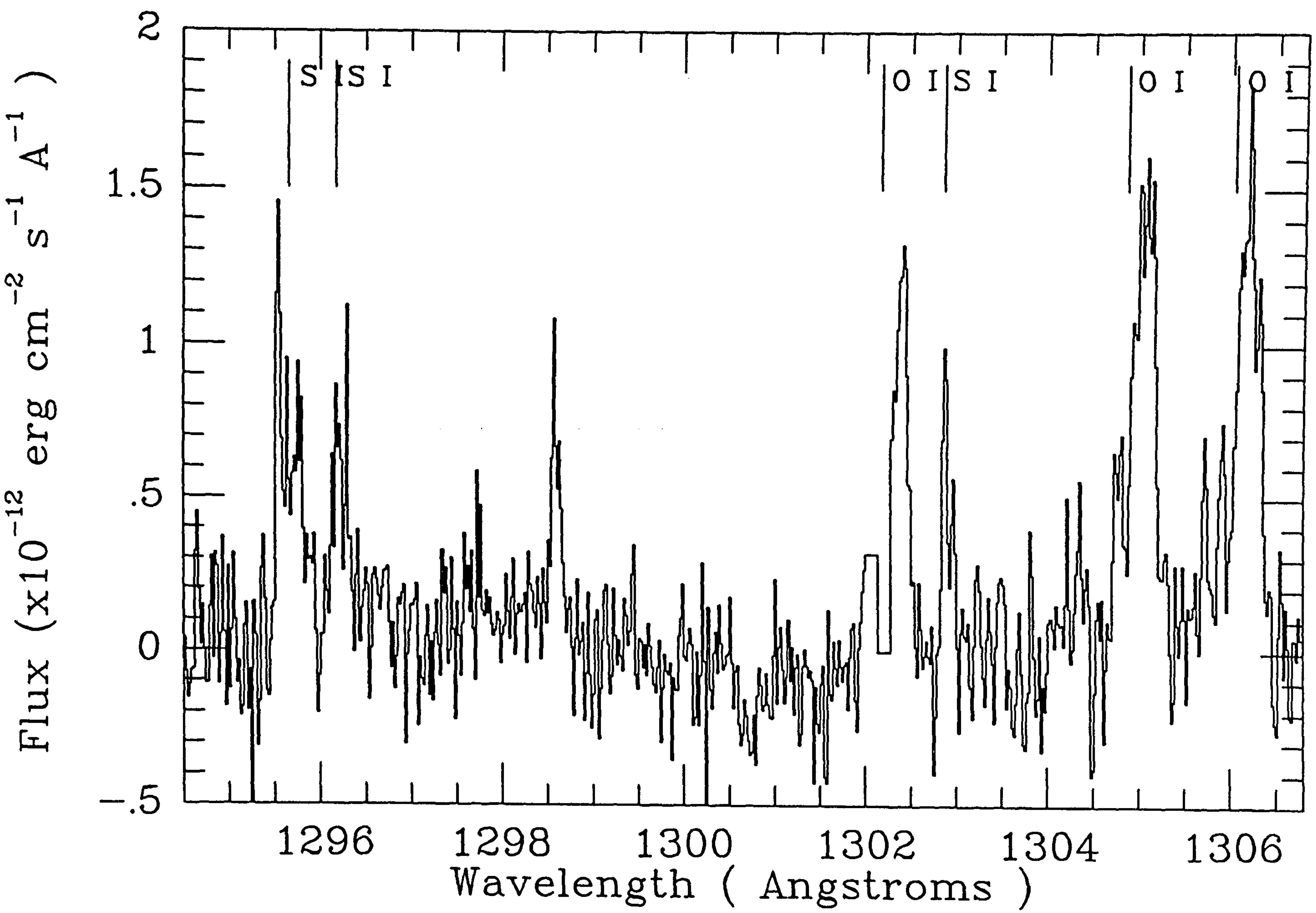

Figure 3-2 SWP15503 spectrum showing the O I triplet and S I lines. The rest wavelengths for the O I and S I lines have been marked. Note that the O I lines are self-reversed with red-wings that are much stronger than the blue wings. The bad data points are flagged to zero. The continuum signal is dominated by noise.

redward side, as is the C I] profile. (This is established from the photowrites.)

3-3-3 LWP High Resolution Data

The high resolution spectra provide good profiles of the Mg II h & k resonance lines. These profiles are useful when comparing detailed model chromospheres with the observations. The deep exposures clearly show the photospheric absorption wings and thus can provide information on the region of the temperature minimum. Figure 3-4 shows the short exposure LWP5199 and the exposure LWP4014. Two absorption components can be seen in the spectra. The long exposure spectrum is saturated in the line cores and in the far wings but the full-base line widths are still noticeably wider than those in LWP5199. Weiler and Oegerle (1979) have studied the full base widths of the Mg II k line in a sample of 73 late-type stars. They found a full base width of 215 km s^{-1} for ι Aur. The spectra clearly show that the choice of the base-width in a short exposure (with IUE) is ambiguous, because the small peak redward of the line core λ2801.7 is an underexposed part of the line core. The wind absorption trough is only clearly seen in the longer exposures. This suggests that some of the scatter in their empirical relationship between line width and stellar luminosity is due to an inappropriate choice of base-level which depends on the depth of exposure. The LWP5199 exposure enables the accurate measurement of the Mg II k/h line ratio. The observed ratio is 1.65, while the optically thin ratio is 2:1, showing that opacity effects are important.

The Fe II emission lines present between $\lambda 2700 - 2772$ are contaminated by blending, but the wavelengths of their centroids suggest that there is no systematic velocity shift from the rest-frame of the photosphere. The fluxes in these lines are upper limits owing to the problems of blending and the problems of setting a suitable continuum level. The Fe II λ2736.97 emission line is blended with Fe I (49) λ2736.96 which is in absorption. The Fe I uv44 emission lines are over-exposed,

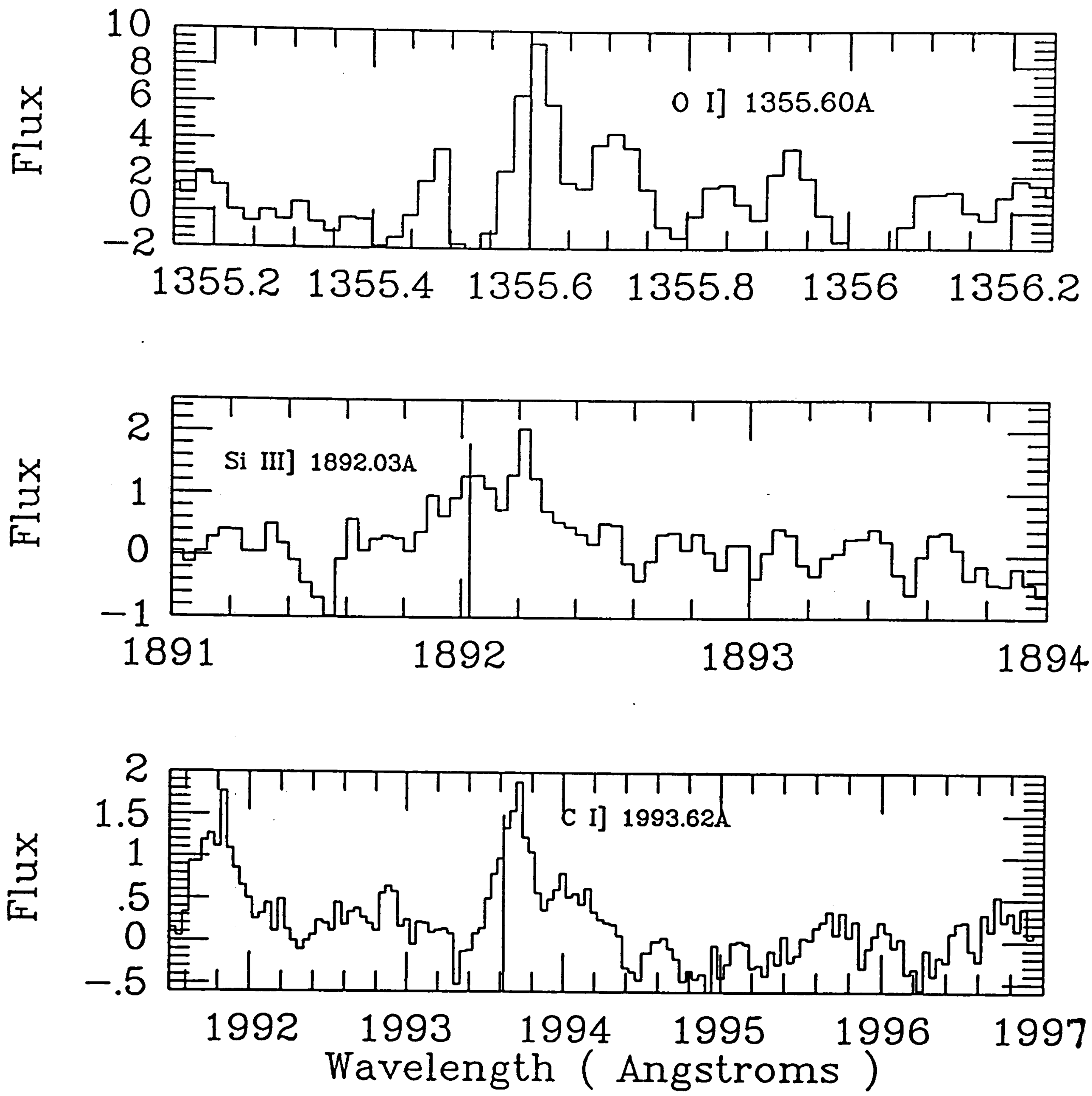

Figure 3-3 Optically thin intersystem lines from the SWP15503 spectrum.

Top: O I] λ1355.60.

Middle: Si III] λ1892.03.

Bottom: C I] λ1993.62.

Lines indicate rest wavelengths in the photospheric rest frame.

The ordinate is the flux measured at the Earth

($\times 10^{-13}$ erg cm^{-2}s^{-1}Å^{-1}).

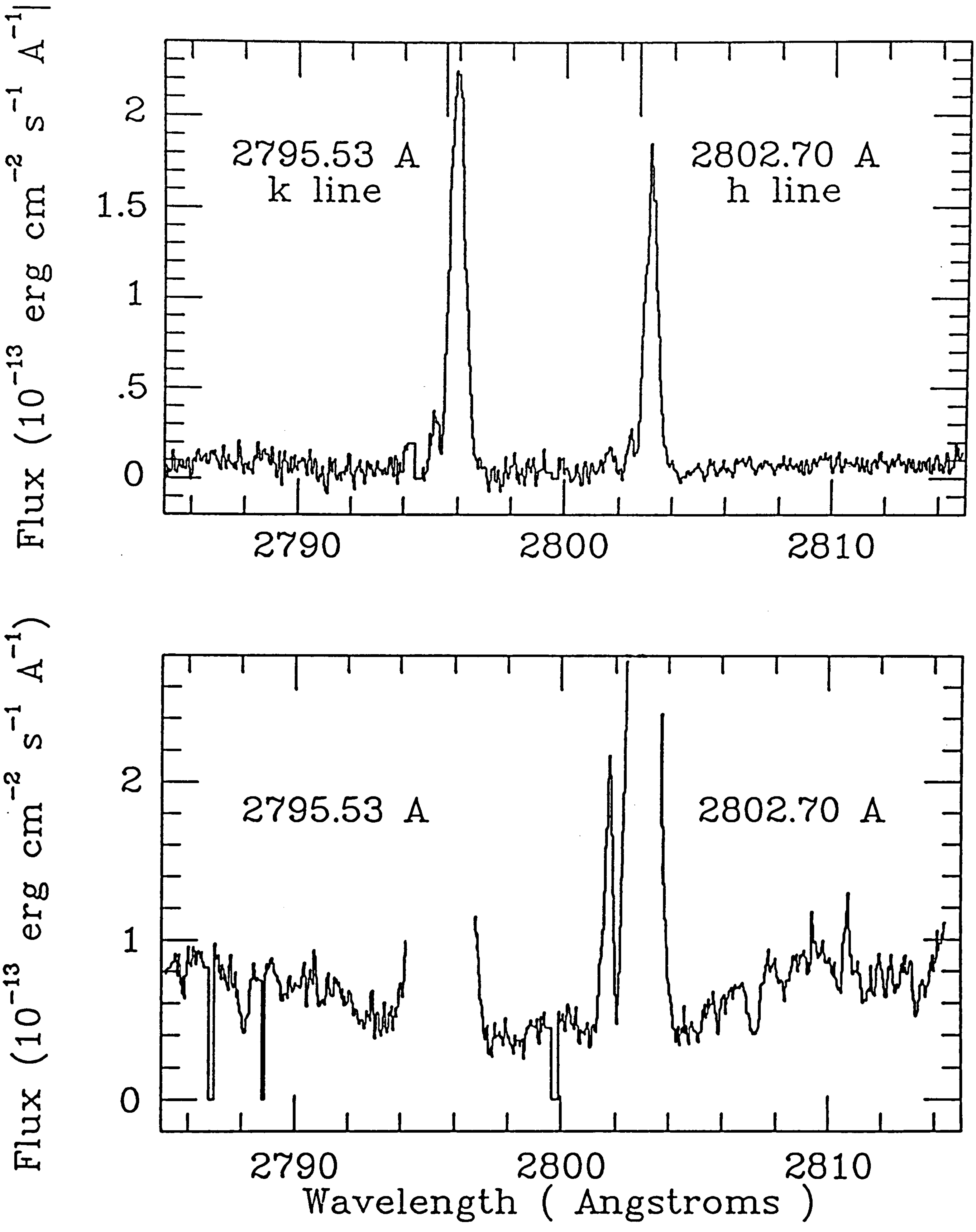

Figure 3-4 Spectra of the Mg II h & k lines. The flux at the star is in units of $\mathrm{erg\,cm^{-2}s^{-1}\AA^{-1}}$. Top: The LWP5199 spectrum k line shows the two absorption components at $v \sim -10$ and $\sim -63\mathrm{km\,s^{-1}}$. Bottom: The LWP4014 spectrum which is over exposed in the line core but shows the photospheric absorption wings.

Table 3-5. Parameters for some of the emission lines identified in the LWP4014 spectrum . The laboratory wavelength (from Kelly, 1982), identification (ID), flux at the star (F_*), full width at half-maximum intensity (FWHM) and the centroid velocity (Δv) of the observed lines are tabulated. The velocity centroid is tabulated if the line is symmetric and unblended.

$\lambda_{\rm Lab}$ (Å)	ID	F_* erg cm^{-2} s^{-1}	FWHM km s^{-1}	Δv km s^{-1}
2323.50	C II]	–	–	–
2324.69	C II]	4.6(2)	52	–
2325.40	C II]	1.3(3)	47	0
2326.93	C II]	3.3(2)	52	–
2327.40	Fe II	3.2(2)	bl	–
2328.12	C II]	5.0(2)	bl $\sim$ 58	–
2344.20	Si II]	–	–	–
2350.17	Si II]	–	–	–
2582.90	C I]	–	–	–
2709.37	Fe II (62)	bl, ul 1.1(3)	53	−8
2736.97	Fe II (63)	∗1.0(3)	br	–
2768.94	Fe II (63)	ul 2.6(3)	br	−4
2772.72	Fe II (63)	ul 2.7(3)	br	−2
2795.53	Mg II k	over-exposed	–	–
2802.70	Mg II h	over-exposed	–	–
2823.28	Fe I (44)	over-exposed	–	–
2843.98	Fe I (44)	over-exposed	–	–

bl Blended with another feature.

br Broad feature (possibly due to blending).

ul Upper limit to flux measurement.

∗ Absorption from another line superimposed near line centre.

Table 3-6. Parameters for some of the lines identified in the LWP5200 spectrum . The laboratory wavelength (from Kelly, 1982), identification (ID), flux at the star (F_*), full width at half-maximum intensity (FWHM) and the centroid velocity (Δv) of the observed lines are tabulated. The velocity centroid is tabulated if the line is symmetric and unblended. The numbers in parentheses are as in Table 3-3.

$\lambda_{\rm Lab}$ (Å)	ID	F_* erg cm^{-2} s^{-1}	FWHM km s^{-1}	Δv km s^{-1}
2323.50	C II]	–	–	–
2324.69	C II]	3.7(2)	38	–
2325.40	C II]	1.5(3)	41	–
2326.93	C II]	Reseau	–	–
2327.40	Fe II	4.3(2)	bl–	–
2328.12	C II]	6.2(2)	bl30	–
2328.51	Si II]	< 1.7(2)	bl< 30	
2334.44 2334.61	Si II]	u1.6(3)	bl50	–
2344.20	Si II]	–	–	–
2350.17	Si II]	7.6(2)	bl	–
2669.17	Al II]	ex 1.5(3)	71.4	+2
2709.37	Fe II (62)	ul 8.8(2)	br	+6
2736.97	Fe II (63)	*8.6(2)	br	–
2768.94	Fe II (63)	ul 1.8(3)	bl	0
2772.72	Fe II (63)	ul 2.2(3)	bl	+4
2795.53	Mg II k	over-exposed	–	–
2802.70	Mg II h	over-exposed	–	–
2823.28	Fe I (44)	over-exposed	–	–
2843.98	Fe I (44)	over-exposed		–

bl Blended with another feature.

ex Flux extrapolated from symmetric over-exposed feature.

br Broad Feature (possibly due to blending).

ul Upper-limit to flux measurement.

* Absorption from another line superimposed near line centre.

Table 3-7. Parameters for some of the lines identified in the LWP5199 spectrum. The laboratory wavelength (from Kelly, 1982), identification (ID), flux at the star [F_*, (erg cm^{-2}s^{-1})], full width at half-maximum intensity (FWHM) and the centroid velocity (Δv) of the observed lines are tabulated. The velocity centroid is tabulated if the line is symmetric and unblended. The numbers in parentheses are as in Table 3-3.

$\lambda_{\rm Lab}$ (Å)	ID	F_* erg cm^{-2} s^{-1}	FWHM km s^{-1}	Δv km s^{-1}
2795.53	Mg II k	4.3(4)	–	–
2802.70	Mg II h	2.6(4)	–	–
2823.28	Fe I (44)	over-exposed	–	–
2843.98	Fe I (44)	4.1(3)	< 30	-5

with one exception (λ2843.98) and this line is also at rest in the photospheric frame of reference. This line is a useful atmospheric diagnostic as the line is excited by fluorescence with the Mg II k line. This will be discussed further in Section 6-4.

Figure 3-5 shows the C II] intersystem lines which provide a measurement of the electron density. The reseau mark at λ2326 in exposure LWP5200 has been shifted to a new position in exposure LWP4014, by the different radial velocity of the camera relative to the star. These lines are discussed in more detail in Section 4-3.

3-4 Observations at Other Wavelengths

In this section observational data obtained by other observers, made at wavelengths not covered by the IUE satellite, are briefly described, since they are used in the atmospheric modelling. Some observations concern non-detections but these are potentially useful.

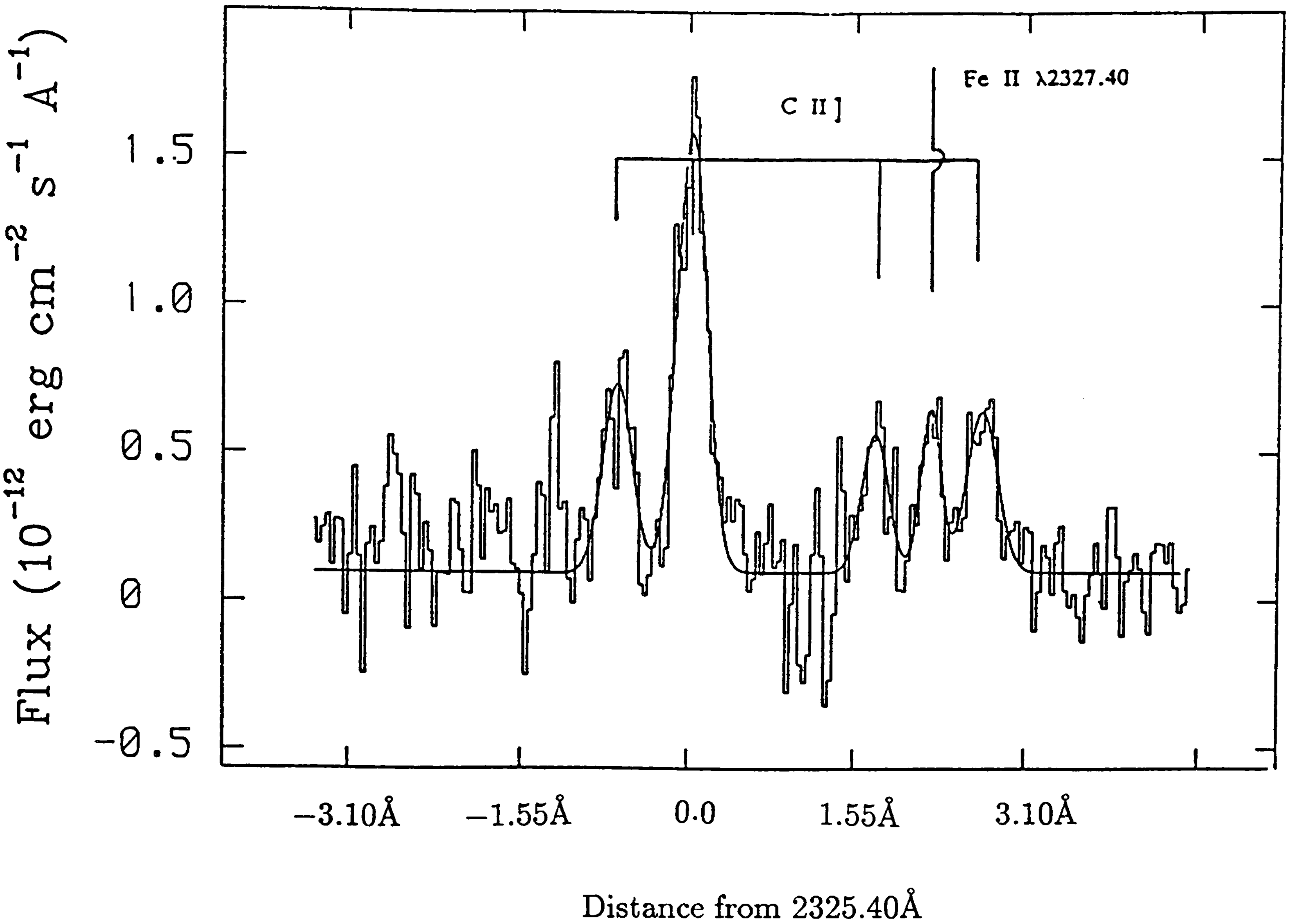

Figure 3-5 The density sensitive lines in the C II] λ2325 multiplet from LWP4014 fitted with a least squares Gaussian profile. The Fe II λ2327.40 line has also been fitted. The widths of these optically thin lines are broader than the IUE point spread function and can provide information on the turbulent motions in the line forming region.

3-4-1 Wavelengths > 3000Å

When constructing model chromospheres it is necessary to assign a temperature minimum which marks the boundary from a negative temperature gradient to a positive temperature gradient above the photosphere. It is possible to find a lower limit to T_{Min} by studying spectra of the Ca II H & K and the Mg II h & k lines. Unfortunately no *good* absolute calibrated spectra of the Ca II H & K lines are available for the stars studied here. The IUE absolute calibration is accurate to $\pm 15\%$ but the signal to noise ratio is not high (possibly $\sim$ 5 in the photospheric absorption wings for the Mg II h& k lines, see Figure 3-4). Linsky *et al.* (1979) present Ca II data which they estimate to have an uncertainty of $\pm 15\%$. The signal to noise ratio near line center approaches 100. In Section 5-1-2, data for a star of similar spectral type to that of ι Aur, *i.e.,* σ Oph, are analysed to provide a comparison of the value of T_{Min} derived from the Mg II h & k lines.

3-4-2 Radio / Microwave VLA

The radio emission from ionised stellar winds can provide an estimate of the mass loss rates of the stars. Drake and Linsky (1979) describe results of a VLA radio continuum survey of single cool giants and supergiants at 6 cm. They did not detect any of the 'hybrid' stars, *i.e.,* α Aqr, θ Her, ι Aur and γ Aql. They infer an upper limit to the ionised mass-loss rate of $\leq 2 \times 10^{-9}\, M_{\odot}\, \mathrm{yr}^{-1}$ for the bright giants and a value of $\leq 1.7 \times 10^{-9}\, M_{\odot}\, \mathrm{yr}^{-1}$ for ι Aur. This estimate can provide an upper limit to the total mass loss rate if the ionisation fraction is known. The ionisation fraction can be found from the results of wind models described in Chapter 7.

3-4-3 Infrared IRAS

Stencel, Pesce and Hagen Bauer (1988) have analysed IRAS data for red supergiants including some 'hybrid' bright giants, and have found that some stars show an infra-red excess at 60μm arising from an extended region. ι Aur and α TrA did not show the presence of infrared excess. However, δ And (K3 III), a 'hybrid' giant, was selected for observation with IUE on the basis of such excess emission (Judge *et al.*, 1987). In principle the non-detection of ι Aur can provide an upper limit to the amount of dust in the circumstellar region. This point is not pursued further here.

3-4-4 X-ray EINSTEIN and EXOSAT Data

Haisch and Simon (1982) observed the hybrid stars α Aqr, β Aqr and γ Aql with the EINSTEIN satellite but they were *not* detected as X-ray sources. The upper limit to the X-ray flux imposed on γ Aql by this observation is $f_x(\gamma \text{ Aql}) < 2 \times 10^{-13}$ erg cm^{-2}s^{-1}. Drake, Brown and Linsky (1986) also investigated G and K supergiants and giants, including ι Aur, θ Her and γ Aql. These stars were not detected at the 3σ level. Signals at $< 1.5\sigma$ were detected for ι Aur and θ Her providing upper limits to the X-ray fluxes of $f_x(\iota \text{ Aur}) < 1.7 \times 10^{-13}$ erg cm^{-2}s^{-1} and $f_x(\theta \text{ Her}) < 1.8 \times 10^{-13}$ erg cm^{-2} s^{-1} (Brown, 1986b). Caillault and Helfand (private communication reported in Brown, 1986b) suggest that θ Her was detected at 2.5σ with a flux of $f_x(\theta \text{ Her}) \simeq 2.0 \times 10^{-13}$ erg cm^{-2} s^{-1}.

In 1985, EXOSAT was used to observe α TrA, ι Aur and δ TrA. Only α TrA was detected, and Brown (1986b) found a volume emission measure of $2-4 \times 10^{52}$ cm^{-3} at $\log T_e = 6.2$. HJBD found that the upper limits for these stars are consistent with a constant ratio of the C IV/X-ray flux.

3-5 Summary

ι Aur has been observed at low and high resolution with IUE, in the SWP and LWP regions. The SWP low resolution spectra include lines which show the presence of plasma at temperatures between 2×10^4 K and 10^5 K, confirming that this star is a 'hybrid' bright giant. The low resolution spectra have been reduced to give emission line fluxes. The high resolution exposure SWP15503 includes the optically thin intersystem lines of Si III], C I] and O I] and in addition to the line fluxes these provide information on the velocity in the line forming regions (see also Section 4-4). The O I resonance lines show asymmetric self-reversed profiles which indicate mass motions in either the line forming region or in a scattering region further out from the star. In the LWP region profiles have been obtained of the Mg II h & k lines. These also show two absorption components blue shifted from line centre. The low velocity component has a blue shift (see also Table 4-5) similar to that expected from interstellar absorption. The high velocity component at $\sim 75\,\mathrm{km\,s^{-1}}$, is due to the scattering of photons in a fast moving gas.

CHAPTER 4. ANALYSIS OF EMISSION LINE FLUXES AND PROFILES

In this Chapter, the emission line fluxes and profiles are analysed to investigate the physical conditions in the line forming regions. The electron density in the high chromosphere is determined from line ratios in the C II] multiplet. Spherically symmetric, one-component models of the transition region and corona are constructed from the mean emission measure distribution for a range of boundary conditions on the pressure. The energy balance of these models is also examined.

4-1 The Emission Measures

The emission line fluxes are the basis of modelling the atmosphere in terms of physical parameters, such as the electron temperature T_e and the electron density N_e as a function of height. The techniques for analysing *effectively thin* emission lines are well established and are described in detail in Jordan and Brown (1981) and Jordan and Wilson (1971). The emission lines are effectively thin when $A_{ji}P_{ji} \gg \epsilon$, where A_{ji} is the spontaneous decay rate, P_{ji} is the escape probability and ϵ is the rate at which the atom leaves level j via a mechanism other than the radiative decay $i \rightarrow j$. The surface line flux in an effectively thin emission line can be expressed (using a two level atom for the purpose of illustration) as,

$$\mathrm{F}_* = \frac{hc}{\lambda} 8.6 \times 10^{-6} \frac{\Omega_{ij}}{\omega_i} \frac{N_E}{N_H} \int_{\Delta R} A(R) f(R) N_e N_H (\frac{R}{R_*})^2 g(T) dR. \qquad (4.1)$$

Ω_{ij} is the collision strength averaged over the Maxwellian distribution of electron energies, ω_i is the statistical weight of the lower level and N_E/N_H is the element abundance . $f(R)$ is the fraction of photons emitted between radii R and $R + dR$ which reach the observer and are not occulted by the stellar surface *i.e.*,

$$f(R) = \frac{1}{2}\left(1 + \sqrt{1 - (\frac{R_*}{R})^2}\right). \qquad (4.2)$$

$A(R)$ is the fraction of the surface from which the line is emitted and the radial term, $(R/R_*)^2$, allows for the conversion of the line flux if it is emitted from a shell of gas at $R > R_*$. The function $g(T)$ contains the temperature dependent terms and is given by,

$$g(T_e) = T_e^{-1/2} \frac{N_i}{N_{ion}} \frac{N_{ion}}{N_E} exp(\frac{-W_{ij}}{kT_e}). \tag{4.3}$$

Here W_{ij} is the excitation energy and $\frac{N_i}{N_{ion}}$ is the fractional population of the lower level. These expressions are given using the *coronal* approximation ($A_{ji} \gg N_e C_{ji}$) which is normally valid for permitted lines. In practice, full calculations of the level populations are made. It is useful to define the emission measure in the following way,

$$E_m = \int_{\Delta R} N_e N_H dR, \tag{4.4}$$

where ΔR is the region of line formation. In the following work $E_m(0.3)$ corresponds to the amount of material present in the temperature range $\Delta Log(T_e) = 0.30$ and ΔR is the corresponding distance range. This range is chosen because the lines in the transition region are typically formed over the temperature interval $\Delta Log(T_e) = 0.30$. (In Chapter 7, the emission measure $E_m(0.1)$ is used to compare wind models with the model chromospheres constructed in Chapter 6.)

The function $A(R)$ is initially taken to be unity and $f(R)$ is initially taken to be 1/2. The ion balance ratios used are an amalgamation of the low density calculations of Jordan (1969), Summers (1972), and Arnaud and Rosenflug (1985) (which take account of charge exchange). For Si III and Si IV, new calculations taking account of charge exchange and the density dependence of dielectronic recombination are used (Baliunas and Butler, (1980) and Jordan, private communication).

The usual procedure is to replace $g(T_e)$ with a constant value and then remove it from the integral. Following Jordan and Wilson (1971), the amount of flux emitted is identified with a region $\Delta log(T_e) = \pm 0.15$ dex about the optimum temperature of formation for a particular line, and hence $\int_{\Delta R} N_e N_H dR$ is found. The mean value for $g(T)$ can be found in terms of $g(T_{\max})$ (the maximum value of $g(T)$) and a normalisation constant G from the following equation,

$$\int_{log(T)-0.15}^{log(T)+0.15} g(T) dlogT = G.g(T_{\max}). \tag{4.5}$$

Then $g(T_{\max})$ and G can be iterated to allow for the distribution of material through the whole range of temperatures by considering $\int N_e N_H g(T) dR$. The correction from the iterations is important mainly where $\int_{\Delta R} N_e N_H dR$ is varying rapidly, with T_e, *e.g.,* below $\sim 2 \times 10^4$ K.

An alternative approach is to assume that all the flux is emitted at each T_e in turn. $E_m(T_e)$ is then defined as the amount of material required to produce all the observed flux, if it were all formed at a single T_e. For each line a locus of solutions can be found as a function of temperature. These loci produce an *upper limit* to the amount of material required at each temperature. This is useful when considering the amount of material needed to produce the flux in more than one line because in the one-component atmosphere assumed, $E_m(T_e)$ is single valued.

The atomic parameters adopted in calculating the emission measures are listed in Table 4-1.

The loci of $E_m(T_e)$ are plotted in Figure 4-1. At $Log(T_e) < 4.0$ the magnesium locus lies above the Al II] locus but if photoexcitation is included, magnesium and aluminium may all be in the singly ionised state. This will lower the emission measure loci. The loci for Mg II, Al II and Si II will be discussed further in the context of the chromospheric models calculated in Chapter 6. The chromospheric models can provide more accurate values of the ionisation balance, so that the emission measures can be iterated with the new values. The shape of the distribution between 10^4 and 10^5 K is constrained by the C II and C IV loci and is therefore not

Table 4-1 Atomic parameters and surface fluxes are given for ι Aur. N_i refers to the lower level population of the ground state. Fluxes for the whole multiplet are given where appropriate. The numbers enclosed by [..] in the Ω column are references which are given below.

Ion	Wavelength (Å)	Flux (erg cm^{-2} s^{-1})	$\Omega_{multiplet}$	N_E/N_H	N_i/N_{ion}
Mg II h & k	2800	6.8(4)	17.0 [1]	5.8×10^{-5}	1.0
Al II]	2670	1.5(3)	3.3 [7]	2.1×10^{-6}	1.0
Si II	1808, 1817	7.3(2)	16.0 [2]	5.4×10^{-5}	1.0
C II	1335	1.4(2)	6.2 [3][8]	1.4×10^{-4}	1.0
C II]	2325	2.6(3)	2.84 [3][8]	1.4×10^{-4}	1.0
Si III]	1892	1.5(2)	3.2 [4]	5.4×10^{-5}	0.85
Si IV	1400	1.1(2)	18.2 [6]	5.4×10^{-5}	1.0
C III]*	1908	8.6(1)	0.95 [5]	1.4×10^{-4}	0.52(a) 0.74(b)
C IV	1550	1.5(2)	11.2 [9]	1.4×10^{-4}	1.0
N V	1240	2.3(2)	7.2 [9]	2.1×10^{-4}	1.0

$*$ calculated for (a) $N_e = 10^{10}\text{cm}^{-3}$ and (b) $N_e = 10^{9}\text{cm}^{-3}$.

[1] Mendoza (1981), [2] Dufton and Kingston (1985),

[3] Hayes and Nussbaumer (1984), [4] Baluja *et al.* (1980, 1981),

[5] Dufton *et al.* (1978), [6] Dufton and Kingston (1987),

[7] Tayal *et al.* (1984), [8] Lennon *et al.* (1985),

[9] Jordan (private communication), from impact parameter calculations.

dependent on the carbon abundance. The Si IV curve is found to be higher than the other curves at the same temperature. The possible contribution from O IV] to the weak Si IV doublet flux in the LORES spectra is not expected to be more than 20%. HJBD and Jordan *et al.* (1987) have also found that the Si IV locus lies above those of other lines formed at similar temperatures. This suggests that the atomic data might be the source of discrepancy. In particular, the maximum value of $N(SiIV)/N(Si)$ is unusually low and sensitive to the uncertainties in the atomic rate coefficients. The C III] locus is density sensitive and two loci are shown

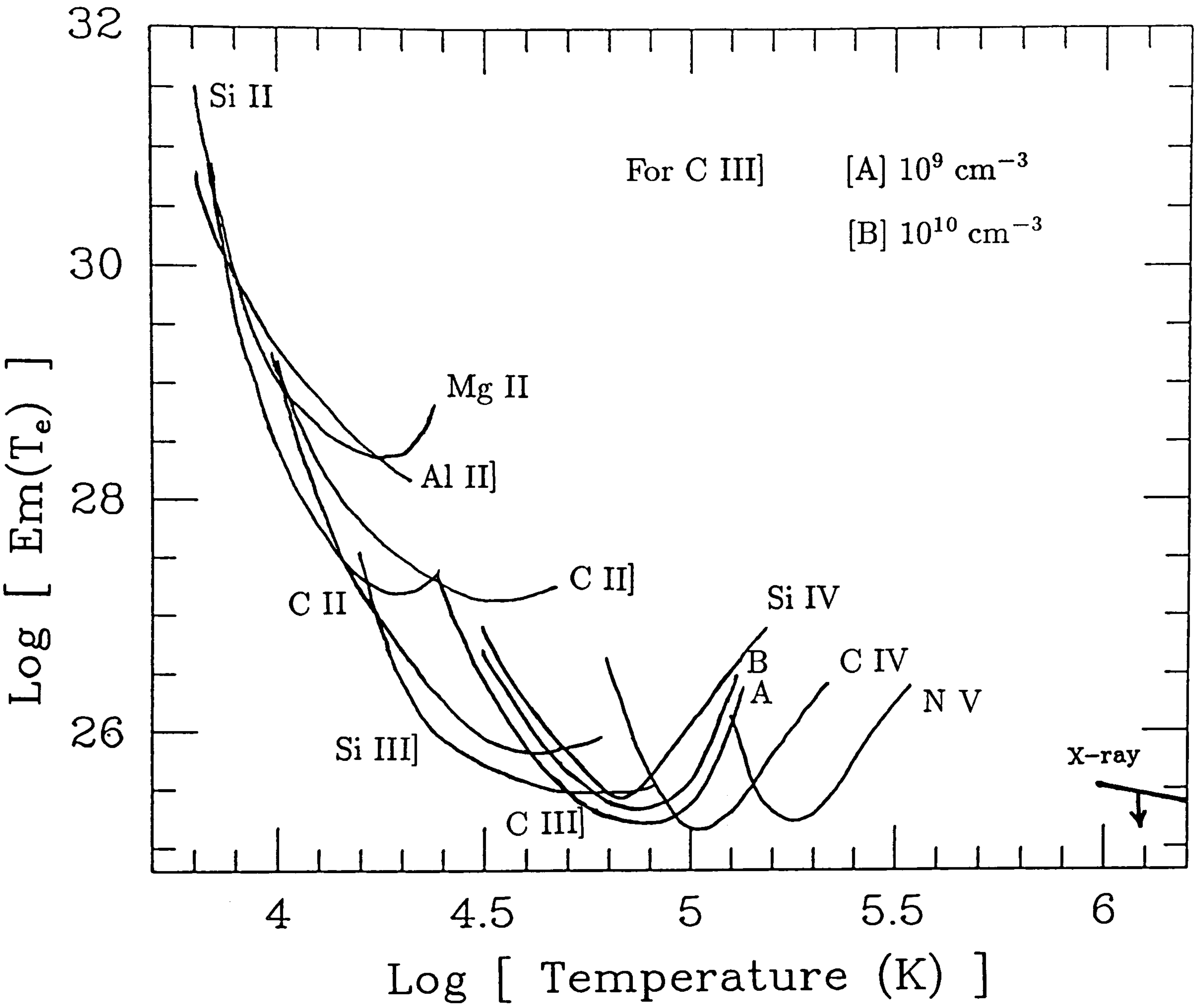

Figure 4-1 Loci of $E_m(T_e)$ for ι Aur. The solutions represent the amount of material needed if each line is formed at a single temperature in turn and therefore give upper limits. The X-ray emission measure is an upper limit.

in Figure 4-1, for $N_e = 10^9$ and 10^{10} cm^{-3}. A self-consistent emission measure distribution can be found which lies on or below the locus for $N_e = 10^9$ cm^{-3}. The X-ray upper limit is calculated from the observation of α TrA (Brown, 1986b) which is the same as the upper-limit described in Section 3-4-4. In the following modelling the emission measure above $Log(T_e) = 5.3$ is interpolated linearly between the X-ray and N V emission measures.

If solar abundances are adopted, the Si loci would be raised by 0.13 dex and the C and N loci would be lowered by 0.25 dex and 0.42 dex, respectively. Within the errors from the flux determinations ($\pm 20\%$) and the atomic parameters for these ions

Table 4-2 The Adopted Emission Measure Distribution. The units of the emission measure are cm^{-5}.

$Log(T_e)$	$E_m(0.3)$	$Log(T_e)$	$E_m(0.3)$
4.0	28.40	4.8	25.26
4.1	27.23	4.9	25.26
4.2	26.75	5.0	25.27
4.3	26.50	5.1	25.28
4.4	26.15	5.2	25.30
4.5	25.65	5.3	25.32
4.6	25.58		
4.7	25.42	6.1	25.50

($\pm 25\%$), both the evolved and the solar abundances (see Section 2-5) are consistent with the mean emission measure distribution. The mean emission measure $E_m(0.3)$ is calculated for each line using equations (4.1) and (4.5). The emission measures are then iterated using equation (4.5) and $\int N_e N_H g(T) dR$, where the contribution function $g(T)$ is weighted to make allowance for the overall distribution of material. The iterations only affect the emission measures derived below $Log(T_e) < 4.3$, where the distribution varies steeply with temperature. In Chapter 6, the change in the mean emission measure caused by the inclusion of photoionisation in the ion balance calculations is discussed. Assuming that the emission measure distribution is smooth, the shape of the mean distribution is found by requiring that it touches all the loci for permitted transitions only once (except Si IV) and that this shape is also consistent with the values of $E_m(0.3)$. The absolute scale value is established by recomputing the fluxes to ensure that all fluxes are reproduced to within 50%. At any T_e the uncertainty in the value of $E_m(0.3)$ is $\pm 50\%$.

4-2 Opacities from Line Ratios

Jordan (1967) showed that constraints on line opacities, and hence hydrogen column densities, can be found by examining the relative fluxes of emission lines

Table 4-3 Table of opacity-sensitive line ratios and optical depths. The table lists: in column 1, the ion state; in columns 2 and 3, the pair of emission lines; in column, 4 the ratio for optically thin lines based on theoretical or observed A-values; in column 5, the observed ratio and in column 6, the inferred optical depths.

Ion	Line 1 λ (Å)	Line 2 λ (Å)	Ratio$_{thin}$	Ratio$_{Observed}$	τ_0 (Line 1)
O I	1304.9	1641.3	1.0×10^5	8.1 ± 2.5	$1.6(\pm 0.5) \times 10^3$
C I	1657.4	1993.6	7.1×10^2	0.52 ± 0.2	$5.6(\pm 2.1) \times 10^2$
S I	1807.3	1820.3	1.9	~ 0.3	> 1
S I	1807.3	1826.2	5.7	~ 0.7	> 1
S I	1296.2	1302.9	2.2	1.4	≥ 1
Si II	1808.0	1817.4	6.4	~ 2.2	> 1

which share a common upper level. Following Jordan (1967), the theoretical ratio for the fluxes is given by the relationship,

$$\frac{F_1}{F_2} = (\frac{A_1 q_1}{\lambda_1})(\frac{\lambda_2}{A_2 q_2}), \tag{4.6}$$

where (for a Doppler broadened line and $\tau_0 > 1$) q is the escape probability of a photon at an optical depth τ_0 from a planar atmosphere of optical depth $2\tau_0$ and q is given by $q = erfc\left[\sqrt{ln(\tau_0)}\right]$. A is the spontaneous transition probability and λ is the wavelength. If one line is optically thin, for example line 1, then $q_1 = 1$ thus allowing the optical depth in line 2 to be found from the observed line ratio. It is then possible to estimate whether or not one of the transitions is optically thin by comparing the theoretical value of q_1/q_2 with that derived from the observed flux ratios. The value of τ_0 can be used to estimate the mean column density over which the lines are formed using,

$$\tau_0 = 1.50 \times 10^{-15} \lambda(\mathring{A}) \frac{f_{ij}}{b} \frac{N_i}{N_{ion}} \frac{N_{ion}}{N_E} \frac{N_E}{N_H} \int N_H dh, \tag{4.7}$$

where b is the Doppler line broadening parameter in the region of line formation, *i.e.*, $b = FWHM/2\sqrt{ln(2)}$. Although it is assumed that N_i/N_{ion} and N_{ion}/N_E are constant, the chromospheric models can be integrated to check τ_0. Table 4-3 gives the opacity sensitive line ratios and the inferred optical depths.

The transition probabilities for the oxygen ratio have been taken from Garstang (1961). The data for the λ 1304.86 should be reliable, while the data for the λ 1641.3 may be an underestimate. See the paper by Judge (1986) for a full discussion of the data used here. The oscillator strengths for the C I ratio have been taken from the experimental ratio of $gf(\lambda 1993.6)/gf(\lambda 1657.4)$ (with a quoted error of 33%) (Tozzi, Huber and Pauls, 1983) combined with the absolute value of $gf\lambda 1657.4$ taken from Weise, Smith and Glennon (1966). The optically thin ratios for all the sulphur line ratios have been taken from Weise, Smith and Miles (1969).

The O I and C I ratios have been used to estimate the mean hydrogen column densities in the line forming regions (these lines are formed at temperatures $\leq 10^4$ K). A Boltzmann distribution is assumed for the ground term relative populations. The ionisation balance, $N(C\ II)/N(C\ I)$, is sensitive to photoionisation by the H Ly-α radiation field. It is assumed that in the line forming region all the carbon is neutral. This will underestimate the hydrogen column density. The carbon line ratio gives $\int N_H dh = 1(\pm 0.4)10^{21}$ cm^{-2}. The oxygen ratio gives $\int N_H dh = 8(\pm 5) \times 10^{20}$ cm^{-2}. The ionisation balance for $N(O\ I)/N(O\ II)$ is dominated by charge transfer and recombination with H I and H II at temperatures $\leq 10^4$ K (Field and Steigman, 1971). It is assumed that the reaction (O II + H $\rightleftharpoons$ O I + H II) is in detailed balance and that the reaction channels are populated according to their statistical weights. Thus, the ion balance is given by,

$$\frac{N(\mathrm{O\,I})}{N(\mathrm{O\,II})} = \frac{8}{9}\frac{N(\mathrm{H\,I})}{N(\mathrm{H\,II})}. \tag{4.8}$$

The hydrogen ionisation fraction has been taken from the model chromospheres described in Chapter 6.

In the emission measure analysis it is assumed that the lines treated are *effectively thin.* Adopting the hydrogen column density above (*i.e.*, $\sim 10^{21}$ cm^{-2}), it can be shown that $A_{ji}P_{ji} \gg \epsilon$ for all the lines used, except the Mg II h & k lines

(H Ly-α also would not satisfy this condition). The formation of Mg II is discussed further in Chapter 6.

4-3 The Electron Density

It is possible to measure the electron density by examining density sensitive line ratios. The long LWP exposures both show the C II] λ2325 multiplet; line ratios within this multiplet can be used to measure the electron density (Stencel *et al.*, 1981). Lennon *et al.* (1985) have recalculated the necessary atomic data and give line flux ratios R_1, R_2 and R_3 as a function of N_e (see Table 4-4). The observed values for these ratios from the LWP exposures and the deduced electron densities are given in Table 4-4. The longest exposure, LWP4014, has the best signal to noise ratio and provides the best density measurement of $Log[N_e(\mathrm{cm}^{-3})] = 9.0 \pm 0.3$, where the error represents the spread in the electron densities from the different ratios. The density was measured by simultaneously fitting Gaussian profiles to C II] $\lambda\lambda$2325.4, 2328.1 and λ2326.9 and also to the Fe II line at λ2327.4. Studies of the region between λ2323 and λ2350 in cool giants and supergiants (*e.g.* Judge, 1886a,b) show that the contribution from potential blends with Fe II and Co II decreases with decreasing gravity and density. The lines involved in ratios R_1 and R_2 are not expected to be contaminated by blends in ι Aur. The background was then adjusted until the electron densities from the different line ratios came into closest agreement. For example, decreasing the background to zero (see Figure 3-5) would increase the scatter in the derived density measurements to $\pm$0.8 dex. The most accurate line ratios will be those involving the strongest line, λ2325, *i.e.*, R_1 and R_2. The ratio for R_1 is greater than R_2 and R_3, while R_2 is less than R_3. These trends have also been observed in other low gravity cool stars (*e.g.*, Stencel *et al.*, 1981).

Byrne *et al.* (1988) determined the electron density from the C II] multiplet in a small sample of stars with luminosity classes I–II to III. They found a relationship between the electron density and the stellar surface gravity (see Figure 3 in the paper by Byrne *et al.*, 1988), *i.e.*,

$$Log(N_e) = (0.34 \pm 0.30) Log(g_*/g_\odot) + 10.1 \pm 1.0.$$

This gives an electron density of $Log(N_e) = 9.16 \pm 1.83$ for ι Aur which is consistent to within the large uncertainty with the measured value of $Log(N_e) = 9.0 \pm 0.3$. However, the uncertainties in the density determinations for individual stars, typically 0.3 dex, are at present too large to enable the precise dependence of N_e on g_* to be found, and a larger sample of data with longer exposures is required.

Table 4-4 Electron density sensitive ratios and deduced N_e

Ion	Ratio	Observed ratio	$Log(N_e\,(cm^{-3}))$
C II	LWP5200 $R_1 = F_{2325.4}/F_{2328.1}$	2.4	9.8 High density limit
C II	LWP4014 $R_1 = F_{2325.4}/F_{2328.1}$	2.8	9.3
C II	LWP4014 $R_2 = F_{2325.4}/F_{2326.9}$	3.7	8.7
C II	LWP4014 $R_3 = F_{2324.7}/F_{2326.9}$	1.5	9.0

Some of the C II] flux is formed below $\sim 10^4$ K so that these lines limit the range of acceptable model chromospheres as developed in later chapters. The Si II] multiplet has the same term structure as C II] multiplet and can also be used to derive the electron densities if $N_e \geq 10^9$ cm^{-3}, Dufton and Kingston (1985). However, in the spectra of ι Aur the λ2334 lines of Si II] are blended with Fe II uv3 and uv35, while the Si II] λ2350.17 is contaminated by a reseau. Hence none of the density sensitive ratios can be measured. The density sensitive C III] locus can provide an estimate of the electron density at $\log(T_e) \sim 4.8$. Comparing the emission measure derived from the C III] flux with the mean emission measure from the whole distribution leads to $N_e \sim 10^9$ cm^{-3}. If the C III] flux is in error by 20% the C III] locus will be in error by 0.08 dex from the proper value so that $N_e \leq 10^{10}$ cm^{-3} is a reasonable upper limit.

However, Si III] is density sensitive above $N_e \sim 10^{10}$cm^{-3} and its locus excludes densities above $N_e \sim 10^{11}$ cm^{-3}. A lower limit to the electron density can be placed on the plasma at 5×10^4 K from the ratio of the C III] intersystem line $\lambda1909$ to C III quadrupole line at $\lambda1906.7$. The quadrapole line is not observed but an upper limit to this flux gives the ratio, $\lambda1906.7/\lambda1909 < 0.1$ showing that $N_e \geq 10^6$ cm^{-3} (Nussbaumer and Schild, 1979 and Keenan *et al.*, 1984).

4-4 Velocity Fields

The LWP exposures enable measurements to be made of the two absorption components in the Mg II h & k line profiles, which are characteristic of the 'hybrid' bright giants. The results are given in Table 4-5. It should be noted that the high velocity measurements refer to the minimum of the absorption feature. This will not necessarily represent the mean velocity of the absorbing material, as the form of the underlying profile must also be considered. This is discussed in further detail in Chapter 6. The low velocity component is associated with interstellar absorption and the observed values are consistent with the previously measured spectra of ι Aur (Drake, Brown and Linsky, 1984; HJBD). The measured values of the high velocity component, presumed to be caused by an out-flowing wind, are also within the range of previously measured values.

The observed values of the full-width at half maximum intensity (FWHM) and the line shifts (Δv) can be used to investigate the mass motions in the line forming and line scattering regions. If the lines are broader than the Gaussian point spread

Table 4-5 Mg II h & k absorption components measured relative to the photospheric wavelength scale.

Absorption component	h line $\lambda2802.70$ Δv (km s^{-1})	k line $\lambda2795.52$ Δv (km s^{-1})
Low velocity LWP5200	−6	–
High Velocity LWP5199	−63	−70
High Velocity LWP5200	−70	−79
High Velocity LWP4014	−77	−82

function of the IUE ($\mathrm{FWHM_{IUE}} \simeq 25\,\mathrm{kms^{-1}}$) then the stellar line widths can be found from the following relation, assuming the profiles are Gaussian,

$$\mathrm{FWHM_*} = \sqrt{(\mathrm{FWHM^2} - \mathrm{FWHM^2_{IUE}})}. \tag{4.9}$$

The uncertainty of FWHM and $\mathrm{FWHM_{IUE}}$ are both about ±15 per cent. Therefore, it is only meaningful to determine $\mathrm{FWHM_*}$ when FWHM$>$ 32 kms^{-1}. For values less than this only an upper limit can be placed on $\mathrm{FWHM_*}$. It is useful to work in terms of the Doppler broadening parameter b, where b$= \mathrm{FWHM_*}/2\sqrt{ln(2)}$.

The optically thin lines of neutral O I] at $\lambda1641.3$ and $\lambda1355.6$ have widths consistent with the IUE spread function, giving an upper limit of $b <$ 15km s^{-1}. The O I resonance lines are broader than the IUE spread function. Since the optically thick and optically thin lines from the same element and stage of ionisation are formed in similar regions, then the larger broadening of the resonance lines is likely to be due to opacity effects and not to non-thermal broadening, as indeed can be shown from the chromospheric models in Chapter 6. The C I] $\lambda1994$ line is slightly broader than the O I] lines but this may be due to noise. α TrA does show some non-thermal broadening in C I] (see exposure SWP15494 in HJBD). Values of b can be found from the relationship between the widths of optically thick and thin lines which are formed in identical regions, *i.e.*, $F_{\mathrm{Thick/Thin}} = 1.2\sqrt{ln(\tau_0) + 0.37}$ (Ayres *et al.*, 1982), where it is assumed that $\tau_0 \gg 1$ for the optically thick line. This relationship also assumes that the line profiles are both Gaussian. The ratio O I $\lambda1304.9/\lambda1641.3$ can then be used to calculate b for $\lambda1641.3$. The profile of the O I $\lambda1304.9$ is asymmetric, but provides an upper limit of $b \leq 17\,\mathrm{km\,s^{-1}}$ for $\lambda1641.3$, which is consistent with the direct measurement of the total line width of $\lambda1641.3$ and $\lambda1355.60$ in Table 3-4

The intersystem lines of C II and Si III are also broader than the IUE spread function. These lines are expected to be optically thin and will not be broadened by multiple scattering. The observed line broadening is greater than the local thermal broadening, b $= 12.85\sqrt{(\frac{T_{ion}}{10^4 M_{ion}})}$, where T_{ion} is the ion temperature and M_{ion} is the ion mass in AMU. This suggests that these lines are broadened by some non-thermal mechanism. (See Table 4-6 for a list of optically thin line widths of α TrA and ι Aur.) No significant line shifts have been detected in these lines for the 'hybrid' stars. This is important because if the ionised plasma is compact and near the stellar surface, it implies that there are no systematic mass motions of the gas $> 7\,\mathrm{km\,s^{-1}}$ between the low chromosphere where C I] is formed, the middle chromosphere where C II] is formed, and the transition region where Si III] is formed. The region of formation of the O I] line is chromospheric but it is pumped by sharing a common upper level with $\lambda1304$, which is itself excited via fluorescence with the H Ly-β line. These velocity constraints are discussed further in Chapter 6.

4-5 Modelling from the Emission Measure

The emission measure distribution, $E_m(0.3)$, can be used to model the transition region and corona (see Jordan and Brown, 1981 and references therein). In hydrostatic equilibrium the pressure gradient term from the momentum equation for the atmosphere can be combined with the temperature gradient derived from the emission measure. The emission measure can be re-written in terms of the tempera-

Table 4-6 Optically thin line widths for ι Aur and α TrA. The data have been taken from the HIRES spectra in Chapter 3, from the paper by HJBD and from Brown *et al.* (1986). The values for C II] in ι Aur are the mean widths of the cleanest profiles. The widths are the observed FWHM in km s^{-1} and the uncertain are about 25%.

Spectrum	O I] λ1641	Si III] λ1892	C III] λ1909	C I] λ1994	C II] λ2325
ι Aur					
LWP5200	–	–	–	–	41
LWP4014	–	–	–	–	47
SWP15503	$\sim$ 30	71	–	35	–
α TrA					
LWP13980	–	–	–	–	56
LWP13981	–	–	–	–	51
SWP8986	–	76	99	50	–
SWP15494	< 30	–	–	40	–
SWP23430	38	71	68	33	–

ture gradient if it is assumed that over the region of line formation, $\Delta log(T_e) = 0.3$, P_e^2 is constant. Then,

$$E_m(0.3) = \int_{\Delta R} N_E N_H \left(\frac{R}{R_*}\right)^2 dR = C \int_{\Delta T_e} \left(\frac{R}{R_*}\right)^2 \frac{P_e^2}{k^2 T_e^2} \frac{dR}{dT} dT. \qquad (4.10)$$

Where C is the ratio N_H/N_e. When $T_e \geq 10^4$ K hydrogen is fully ionised and $C \simeq 0.8$, is adopted in the following models. The models are only extended to temperatures $\leq 2 \times 10^4$ K for demonstration purposes, since the assumptions made concerning local mean values become unrealistic below $T_e < 2 \times 10^4$ K. Removing local mean values of dR/dT and P_e^2 from the integrand gives,

$$E_m(0.3) = C\overline{P_e^2 \frac{dR}{dT}} \frac{1}{k^2} \frac{1}{\sqrt{2}T_e} (\frac{R}{R_*})^2 . \qquad (4.11)$$

The local mean values can now be treated as variables throughout the atmosphere.

It is possible to include in the momentum equation terms that allow for the effects of wave action on the atmosphere. The momentum equation including the pressure caused by wave motions is,

$$\rho V(\frac{dV}{dR}) = -\frac{dP_T}{dR} - \frac{\rho GM}{R^2} - \frac{1}{2}\frac{d\epsilon}{dR}, \tag{4.12}$$

where P_T is the total gas pressure and ϵ is the energy density of the waves. The last term, $-1/2(d\epsilon/dR)$, is the time-averaged force per unit volume due to the waves. This pressure term has the effect of supporting the weight of the gas and hence counterbalances the gravitational attraction. The effective isothermal scale height will thus be increased and the atmosphere will be more extended than in the absence of waves.

Several cases can be considered. The first case (a) is where all the terms in equation (4.12) are important. This case will be treated in detail in the Chapter 7. The second case, (b), is where the velocity term is negligible. Case (b) can be divided into; (i) hydrostatic equilibrium, where the wind pressure is negligible and (ii) hydrostatic equilibrium including pressure support by wave motions. In a one-component model the absence of significant velocity shifts in the observed emission lines implies that case (b) is appropriate. This case is studied here. Combining equation (4.11) and (4.12) leads to,

$$P_e^2 = P_{\mathrm{Top}}^2 + 1.6 \times 10^{-8} g_* \int_{T_e}^{T_{\mathrm{Top}}} E_m(0.3)(\frac{R_*}{R})^4 \, dT_e, \tag{4.13}$$

where g_* is the surface gravity and subscript Top refers to the reference level at the top of the atmosphere. Here, P_e is in units of $\mathrm{cm}^{-3}\mathrm{K}$. From equations (4.11) and (4.13) it is possible to build up models of pressure against temperature and hence temperature against distance above a given height. The radial term $(R_*/R)^4$ makes it necessary to iterate the equations. The base height for the models is taken to be the radius of the star. It is possible to obtain convergence if the initial estimate of the total radial extent is taken to be the stellar radius. When the initial pressure

Table 4-7 Models constructed in hydrostatic equilibrium.

Model	Surface gravity (cm s^{-2})	Maximum temperature
Model A	60	2×10^5 K
Model B	45	2×10^5 K
Model C	40	2×10^5 K
Model D	45	10^6 K

$P_{\rm Top} = 0$ the model is referred to as the *minimum pressure hydrostatic model.* In practice a small pressure, which is expected to be small compared to the actual gas pressure, is included at the top of the model to improve the numerical stability in the convergence of the radial term. The models are considered to be converged when the change in the total radial extent between successive iterations is less than $10^{-4} R_{Total}$.

Table 4-7 defines a set of such models and they are shown in Figure 4-2. This range of surface gravities is chosen to cover the uncertainties in the stellar parameters as discussed in Chapter 2. Table 4-8 gives the electron pressure against temperature for these models. The models are integrated down from the maximum temperature and Model D has been constructed assuming that there is material present in the amounts suggested by the X-ray upper-limits. The emission measure, $E_m(0.3)$, in this case has been linearly interpolated between the X-ray upper-limit and the observed emission measure for the N V.

The pressures predicted by the models can now be compared with the pressure estimated from the C III] emission measure. Models A, B, C and D all have lower pressures at $\mathrm{Log}(T_e) = 4.8$ than would be expected if $N_e = 10^9$ cm^{-3} at this temperature. Model D extends to $T_e = 6.0$ and this model leads to an electron density of $N_e = 2 \times 10^8$ cm^{-3} at $\log(T_e) = 4.8$. Thus all the models are consistent with the position of the C III] locus in its low density limit of $N_e \sim 10^9$ cm^{-3}.

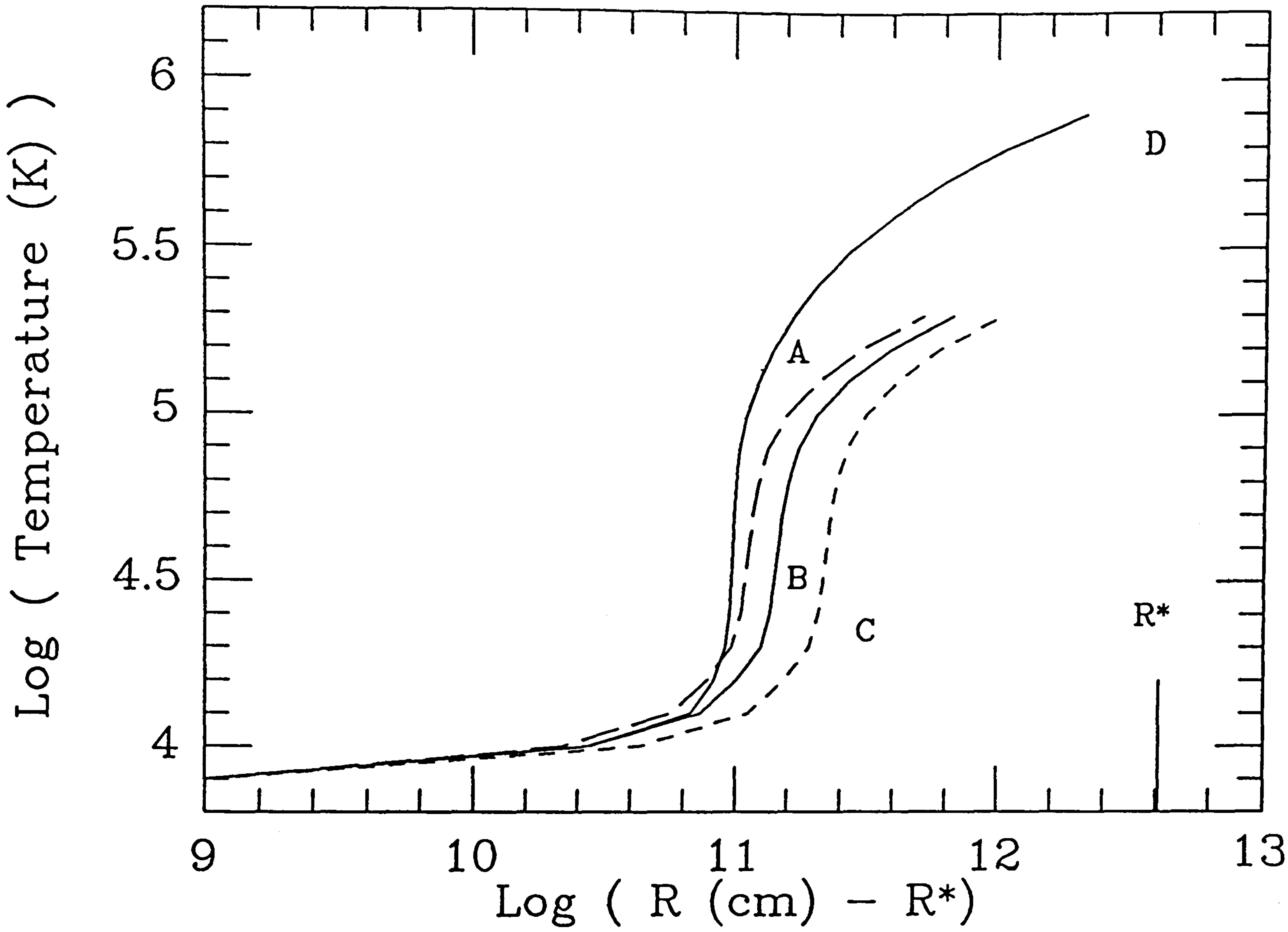

Figure 4-2 Temperature against height for ι Aur. Case (b)(i): Models A, B and C are constructed with a maximum temperature of $\mathrm{Log}(T_e) = 5.3$ and with surface gravities of $g_* = 60, 45, 40\ \mathrm{cm\,s^{-2}}$ respectively. Model D is constructed with a maximum temperature of $\mathrm{Log}(T_e) = 6.0$ and a surface gravity of $g_* = 45\ \mathrm{cm\,s^{-2}}$. The minimum temperature is $T_e = 10^4$ K and the graphs have been extended to lower temperatures for illustration purposes only.

So far a spherically symmetric, one-component model has been considered. If the emission line fluxes originated from a fraction $A(R)$ of the stellar surface then the pressures in these models would be greater by a factor of $A(R)^{-1/2}$. However, the C III] density estimate will be unchanged if all the lines which constrain the emission measure distribution around C III] are restricted to the same area. To be consistent with C III] in its low density limit this requires that $A(R) \geq 4 \times 10^{-2}$.

The electron density estimate obtained from the C II] multiplet is not able to constrain the models above 10^4 K, because the gas below $T_e = 10^4$ K becomes partially ionised and also the emission measures are not well determined at these temperatures. The radial extent of the atmosphere in these models is $\leq R_*$ above

Table 4-8 Electron pressure in units of $\mathrm{Kcm^{-3}}$ against temperature for Models A, B, C and D.

$Log(T_e)$	Model A	Model B	Model C	Model D
5.2	2.7(12)	1.7(12)	9.6(11)	1.1(13)
5.1	3.4(12)	2.4(12)	1.7(12)	1.1(13)
5.0	4.0(12)	2.9(12)	2.2(12)	1.1(13)
4.9	4.4(12)	3.3(12)	2.6(12)	1.1(13)
4.8	4.8(12)	3.6(12)	3.0(12)	1.2(13)
4.7	5.0(12)	3.9(12)	3.2(12)	1.2(13)
4.6	5.3(12)	4.1(12)	3.5(12)	1.2(13)
4.5	5.4(12)	4.3(12)	3.6(12)	1.2(13)
4.4	5.8(12)	4.6(12)	3.9(12)	1.2(13)
4.3	6.5(12)	5.3(12)	4.6(12)	1.2(13)
4.2	9.2(12)	7.7(12)	7.0(12)	1.3(13)
4.1	1.4(13)	1.2(13)	1.1(13)	1.7(13)
4.0	3.1(13)	2.7(13)	2.5(13)	3.8(13)
3.9	5.9(13)	5.1(13)	4.8(13)	7.2(13)

the surface. The pressure exerted by the material above $\mathrm{Log}(T_e) = 4.3$ is small compared to pressures at lower temperatures. As a result, the models can be approximately represented by a constant pressure above this temperature.

The next case, (b), includes the effects of wave pressure in the momentum equation. The line broadening of the optically thin lines can be used to estimate the wave pressure as a function of temperature. Equation (4.11) and (4.12) can be solved analytically to give the following equation,

$$P_e^2 = \frac{P_0^2(1+f(T_0))^2}{(1+f(T_e))^2} + \frac{g_* Const.}{(1+f(T_e))^2}\int_{T_e}^{T_0} E_m(0.3)(1+f(T_0)(\frac{R_*}{R})^4 dT, \qquad (4.14)$$

where $f(T) = \frac{\mu m_p}{2kT} < V_{turb}^2 >$ which can be measured as a function of temperature. To calculate the turbulent velocities, $< V_{turb}^2 >$, from the non-thermally broadened emission lines, it is necessary to make several assumptions. First, it is assumed that the turbulence has a Gaussian distribution and is randomly orientated. Then the most probable velocity can be found from the definition of the line broadening parameter b for a Doppler broadened line,

$$b = \sqrt{(\frac{2kT}{m} + V_{prob}^2)}. \tag{4.15}$$

The deduced root mean square turbulent velocity is thus, $V_{R.M.S.turb} = \sqrt{\frac{3}{2}V_{prob}}$ and the values are shown in Table 4-9. It can be seen immediately that if the ratio of the gas pressure to the turbulent pressure is constant, then g_* can be replaced by an effective gravity (g_{eff}) throughout the atmosphere,

$$g_{eff} = \frac{g_*}{1 + P_{turb}/P_{gas}}, \tag{4.16}$$

where P_{turb} is the turbulent gas pressure and P_{gas} is the total gas pressure. (*e.g.*, HJBD). This has the effect of turbulently expanding the atmosphere and reducing the pressure in the atmospheric models.

Because the emission lines are formed over a range of temperature and there are uncertainties in the measured line-widths, it is also useful to constrain the values of V_{turb} from energy balance arguments (see below). Until now no assumptions have been made concerning the origin of the turbulence. Hartmann and MacGregor (1980) have studied the effects of different mechanical processes which can drive the winds observed in cool stars. They found that acoustic waves dissipate in the chromosphere and do not carry sufficient momentum into the corona to drive a massive wind. The possibility of compressional waves driving the wind cannot be ruled out. However, the damping of Alfvén waves can *qualitatively* deliver sufficient momentum to drive the wind, and dissipate enough energy to account for the observed radiation losses, but the damping mechanism is unclear.

It is now assumed that the turbulent broadening is a result of the passage of Alfvén waves through the atmosphere. The energy density is associated with that of the fluctuating magnetic field *i.e.*, using the mean square velocity and magnetic field,

$$\rho < V_{turb}^2 >= \frac{< \delta B^2 >}{4\pi}. \tag{4.17}$$

It is possible to constrain the values of V_{turb} by considering the following argument. The Alfvén wave flux through a given solid angle must either be constant with no dissipation, or decrease if energy is dissipated as the waves propagate outwards from the star. Then, the Alfvén wave flux, Φ_{Alf}, must satisfy

$$\Phi_{Alf}.A \propto \frac{P_{gas}^{1/2}}{T_e^{1/2}} < V_{turb}^2 > B.A, \tag{4.18}$$

where A is the area element. From magnetic flux conservation, $B.A$ is constant; for small amounts of dissipation $\Phi_{Alf}.A$ is constant or slowly decreasing; then as P_e is nearly constant (as found from the models above) then $< V_{turb}^2 >$ cannot increase more quickly than $T_e^{1/2}$, with increasing distance from the star. This condition is used to constrain the adopted values of the turbulent velocities. The adopted values of the turbulent velocity are found assuming

$$< V_{turb}^2 >_0 T_0^{-1/2} = < V_{turb}^2 >_e T_e^{-1/2}. \tag{4.19}$$

The adopted values of the turbulent velocities are shown in Table 4-9. The C II] is adopted to set the scale of equation (4.19) and this relationship gives turbulent velocities at $Log(T_e) = 5.0, 6.0$ of 55 and 97km s^{-1}. It can be seen that the observed turbulent velocities are approximately a factor of two greater than the local sound speed.

A direct result of this argument is that the ratio of turbulent pressure to gas pressure must decrease monotonically with increasing temperature. This argument also ensures that the models do not have electron densities which fluctuate with height or temperature.

Table 4-10 defines three models which include the effects of turbulence and the results are shown in Figure 4-3. Model 1 is chosen to have an electron pressure at

Table 4-9 The measured (Obs) and adopted (Adp) values of V_{turb} derived from the emission-line widths and the approximate temperature of line formation. O I] and C I] are formed in regions where the approximations used to constrain the adopted value of $< V_{turb}^2 >$ cease to be valid as the electron densities become uncertain.

Line		Log(T_e) ± 0.15	b_{therm} (km s^{-1})	C_s (km s^{-1})	$V_{turb}(Obs)$ (km s^{-1})	$V_{turb}(Adp)$ See (4.19)
O I]	1641Å	~ 3.8	< 3	11	18	
Si III]	1892Å	~ 4.5	~ 4.8	27	49	41
C I]	1993Å	~ 3.8	~ 4.7	8	14	
C II]	2325Å	~ 3.9	< 3.7	11	29	29

the top of the model ($Log(T_e) = 5.3$) so that at $Log(T_e) = 4.8$ the electron density is $10^9\,\mathrm{cm}^{-3}$. This is to illustrate that there needs to be a large amount of gas above the top of the model to produce such electron densities. Model 2 represents a turbulently expanded model which includes material up to $Log(T_e) = 6.0$ and is consistent with the X-ray upper-limit to the X-ray emission measure. Model 3 is constructed using the *observed* emission measure and the model starts at $Log(T_e) = 5.3$. All the models shown satisfy the electron density constraint of $N_e \leq 10^9$ cm^{-3} from the C III] emission measure at $Log(T_e) = 4.8$. Including turbulence into the momentum equation gives an additional term counteracting the gravitational attraction and thus supports the atmosphere. For a given surface gravity the inclusion of a support term leads to a more extended atmosphere and lower electron densities. Model 1 is constructed to match an electron density of $N_e \sim 10^9$ cm^{-3} at $Log(T_e) = 4.8$. This requires an electron pressure of $P_e = 7.4 \times 10^{13}$ cm^{-3} K at $Log(T_e) = 5.3$. However, the pressure from the X-ray upper-limit is less than a tenth of this value, as can be seen from Model 2. Thus Models 2 and 3 show that if the electron density in the C III] line forming region *is* 10^9 cm^{-3} then the emission must be limited to a fraction $\leq 10^{-2}$ of the stellar surface. Models 2 and 3 are more extended than the equivalent non-turbulent models because the lower pressure leads to less steep temperature gradients; conversely as Model 1 has large pressures the atmosphere is more compact. The radial extent of Model 1 is $R_{extent} - R_* < 10^{11}$ cm while the extent of Models 2 and 3 are $R_{extent} - R_* \sim 10^{13}$ cm. The radial extent of Models 2 and 3 depend sensitively on the assumed turbulent velocity field, because the total pressure is dominated by the turbulence. All the models in cases (a) and (b) are consistent with the constraint on the lower limit to the electron density of $N_e > 10^6$ cm^{-3} at $Log(T_e) \simeq 4.8$.

4-6 Energy Balance

Empirical models of the atmosphere can provide information on the amount of non-thermal energy required to balance the energy losses. From the conservation of energy, the flux gradients can be written as,

$$\frac{dF_{Mech}}{dR} + \frac{dF_{Rad}}{dR} + \frac{dF_{Cond}}{dR} + \frac{dF_{Wind}}{dR} = 0, \tag{4.20}$$

where the F's are the fluxes of the mechanical energy input, radiation losses, thermal conduction and wind energy, respectively. Evaluating the last three terms can provide an estimate of the mechanical energy flux required, as a function of height or temperature. For unit surface area at the star the radiative losses, over a given temperature or height range, can be found by integrating,

$$\frac{dF_{Rad}}{dR} = -N_e N_H P_{Rad}(T_e), \tag{4.21}$$

where $P_{Rad}(T_e)$ is the power loss function (erg cm^3 s^{-1}). Then,

$$\begin{aligned} \Delta F_{Rad}(T_e) &= \int_{\Delta R} \frac{dF_{Rad}}{dR} dR, \\ &= \int_{\Delta R} N_e N_H P_{Rad}(T_e) dR, \end{aligned} \tag{4.22}$$

where ΔR is the spatial extent over which the radiation is emitted. The observations give $E_m(0.3) = \int_{\Delta R} N_e N_H (R/R_*)^2 dR$. Then the flux emitted over the line forming region defined in the emission measure can be expressed as, *i.e.*,

$$\Delta F_{Rad}(0.3) \simeq E_m(0.3)\left(\frac{R_*}{R}\right)^2 P_{Rad}(T_e). \tag{4.23}$$

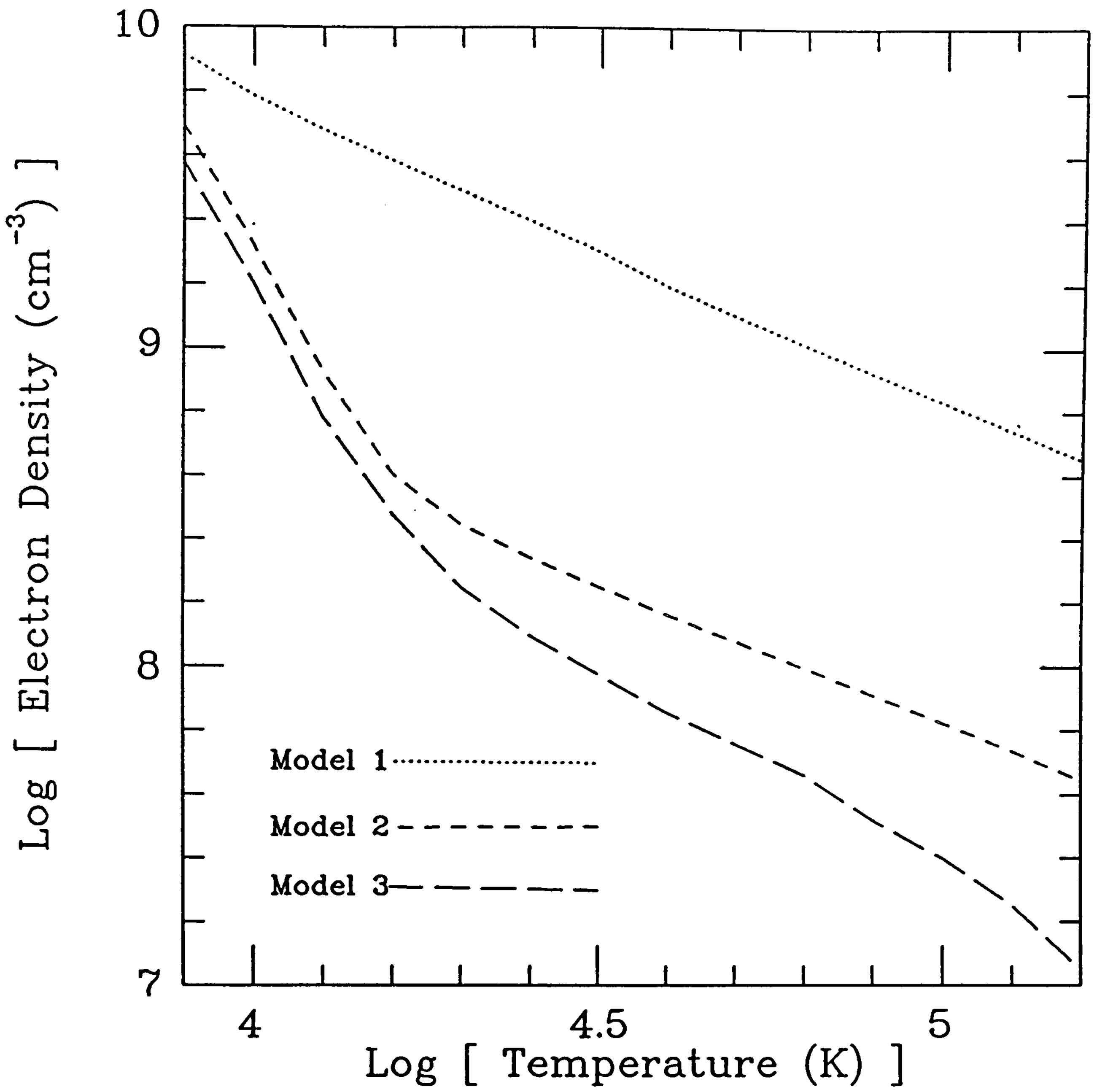

Figure 4-3 Logarithm of electron density against logarithm of temperature for three turbulently supported models. See Table 4-10 for the definition of Models 1, 2 and 3.

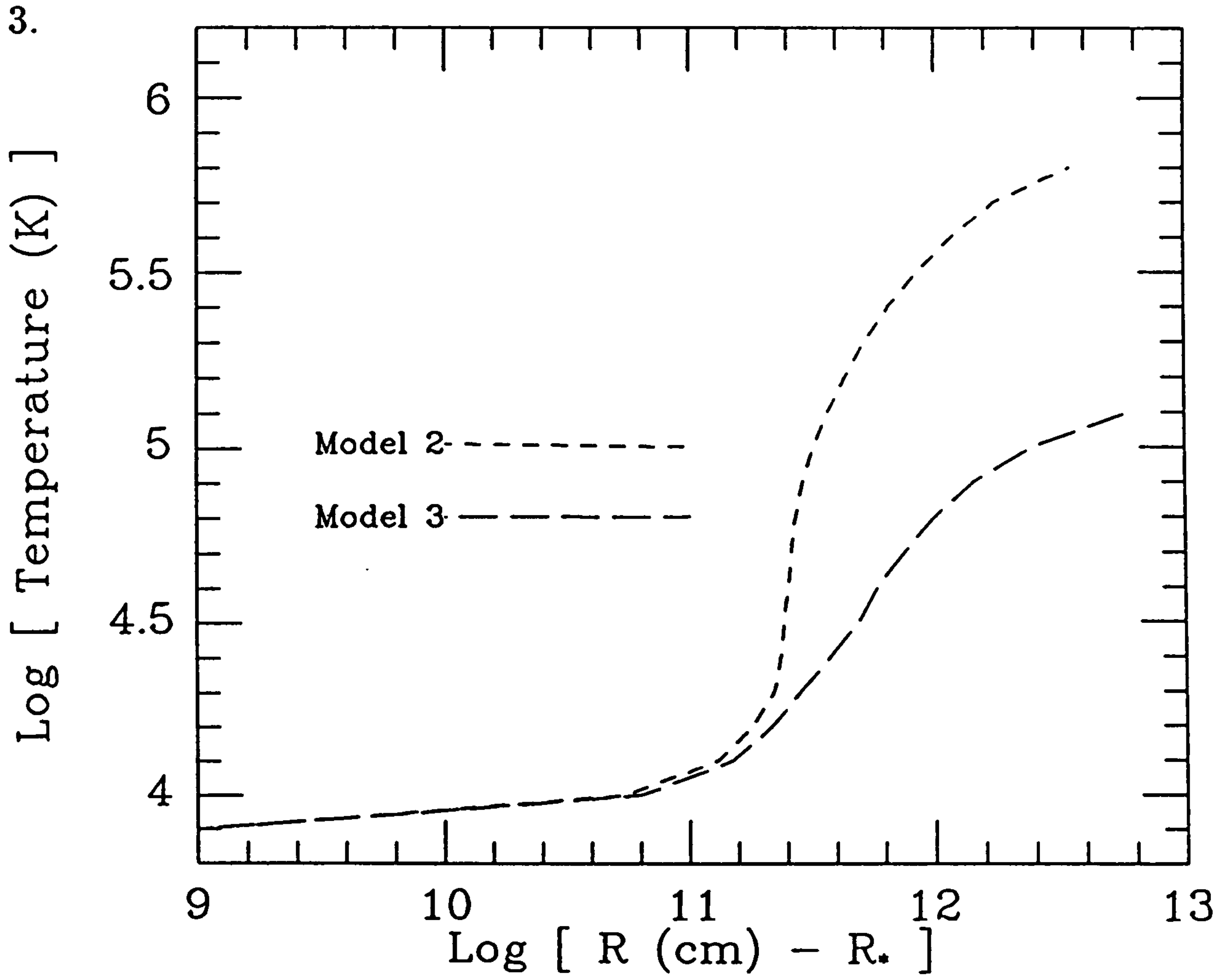

Figure 4-4 Temperature against height for turbulently supported Models 2 and 3.

Table 4-10 Turbulently supported models.

Model	Surface gravity ($\mathrm{cm\,s^{-2}}$)	Maximum temperature $Log(T_e)$	Initial pressure $P_e\,(\mathrm{cm^{-3}})$ K
Model 1	45	5.3	7.4×10^{13}
Model 2	45	6.0	$\sim 10^6$
Model 3	45	5.3	$\sim 10^6$

Table 4-11 Radiative Power Loss Function, P_{Rad} ($\mathrm{erg\,cm^3\,s^{-1}}$) for an optically thin plasma with cosmic abundances, compiled from previously published results (Hartmann *et al.* (1982) and McWhirter *et al.* (1975)).

$Log(T_e)$	$Log(P_{Rad})$	$Log(T_e)$	$Log(P_{Rad})$	$Log(T_e)$	$Log(P_{Rad})$
3.8	-26.00	4.6	-21.88	5.4	-21.80
3.9	-24.50	4.7	-21.65	5.5	-22.05
4.0	-23.60	4.8	-21.40	5.6	-22.10
4.1	-23.12	4.9	-21.25	5.7	-22.15
4.2	-22.62	5.0	-21.22	5.8	-22.20
4.3	-22.30	5.1	-21.32	5.9	-22.25
4.4	-22.18	5.2	-21.42	6.0	-22.30
4.5	-22.00	5.3	-21.52	6.1	-22.35

Here it is assumed that $E_m(0.1) \simeq 1/3E_m(0.3)$, noting that where $E_m(0.3)$ changes steeply below $Log(T_e) = 4.3$, this approach may over estimate the actual value of $E_m(0.1)$. The total radiation losses above a given level can be found from the summation,

$$F_{Rad} = \sum \Delta F_{Rad}. \tag{4.24}$$

The values of $\Delta F_{Rad}(T_e)$ and F_{Rad} are model independent apart from the $(R_*/R)^2$ term in equation (4.23). This term enables the emission measure to be calculated if the flux is emitted far from the stellar surface. The summed radiative losses are shown in Figure 4-4. Table 4-11 gives the values of P_{Rad} adopted.

Table 4-12 The energy balance for Models 1, 2 and 3. The energy terms are units of $\mathrm{erg\,cm^{-2}\,s^{-1}}$. ΔF_{Rad} is the energy radiated out of the region ± 0.05 dex about the temperature. ΔF_{Cond} is positive if energy is deposited in the temperature region and negative if energy is conducted out of the region.

$Log(T_e)$	Model 1 ΔF_{Rad}	Model 1 ΔF_{Cond}	Model 2 ΔF_{Rad}	Model 2 ΔF_{Cond}	Model 3 ΔF_{Rad}	Model 3 ΔF_{Cond}
4.0	2.1(4)	–	2.0(4)	–	2.1(4)	–
4.1	4.3(3)	1.7(0)	4.0(3)	–	3.6(3)	–
4.2	4.5(3)	1.5(1)	4.3(3)	–	4.0(3)	–
4.3	5.3(3)	6.0(1)	4.8(3)	1.7(-1)	4.5(3)	2.2(-1)
4.4	3.1(3)	1.7(2)	2.8(3)	9.0(-1)	2.6(3)	5.5(-1)
4.5	1.5(3)	2.4(2)	1.3(3)	9.0(-1)	1.2(3)	4.0(-1)
4.6	1.7(3)	2.8(2)	1.5(3)	2.4(0)	1.3(3)	4.9(-1)
4.7	2.0(3)	2.0(2)	1.8(3)	5.2(0)	1.4(3)	5.7(-1)
4.8	2.4(3)	2.5(2)	2.1(3)	5.0(0)	1.5(3)	5.8(-1)
4.9	3.4(3)	3.3(3)	3.0(3)	7.2(0)	1.9(3)	5.3(-1)
5.0	3.7(3)	6.4(2)	3.3(3)	1.0(1)	1.4(3)	3.0(-1)
5.1	3.0(3)	1.3(3)	2.7(3)	1.4(1)	4.9(2)	-1.9(-1)
5.2	2.5(3)	2.0(3)	3.3(3)	2.1(1)		-9.8(-1)
5.3			1.8(3)	3.3(1)		
5.4			9.1(2)	3.0(1)		
5.5			5.6(2)	4.2(1)		
5.6			5.0(2)	3.2(1)		
5.7			4.2(2)	2.0(1)		
5.8			3.1(2)	-3.9(1)		
5.9			2.8(2)	-1.9(2)		

With a radial magnetic field the conductive flux F_{Cond} is given by the classical equation,

$$F_{Cond}(T_e) = -\kappa T_e^{5/2} \frac{dT_e}{dR}, \tag{4.25}$$

where κ, the conductivity coefficient, is $\simeq 10^{-6}$ (Spitzer, 1978).

The radiative losses, ΔF_{Rad}, and the net conductive flux, ΔF_{Cond}, can be evaluated for the models discussed above and the results are shown in Table 4-12.

The net conductive flux at a temperature T_e is the difference between the conductive flux flowing through surface elements in the atmosphere, located at $Log(T_e) \pm 0.05$. It can be seen that the net conductive flux is small compared with the radiation terms in Models 2 and 3. In Model 1, which has larger pressures and temperature gradients, the conduction term is comparable to the radiative losses at high temperatures. The sign of the net conducted energy is such that energy is deposited in the transition region from above. In the Sun the radiative losses in the region $10^5 \rightarrow 2 \times 10^5$ K cannot remove the flux conducted down from the corona, so the energy may be converted into mass motions of some kind. This could result in the turbulent motions observed in the optically thin lines. The radiative losses in Models 1 and 2 both exceed the net conductive flux at any particular temperature, so that this problem does not occur and the non-thermal motions are not driven by energy deposited from the corona. The introduction of an area factor $(A(R))$ will not alter the estimate of the conductive flux, which depends on $P_e^2/E_m(T_e)$, but will increase the local radiation losses through the increase in the local emission measure.

The wind energy flux is given by,

$$F_{Wind} = \frac{1}{2}\rho v^3 + 5\rho\frac{k}{M_H}Tv + \rho g R v, \tag{4.26}$$

where the first term is the kinetic energy flux, the second term is the enthalpy flux and the last term is the rate at which energy is lost in moving against the gravitational field. It is not possible to calculate these terms self-consistently for wind velocities greater than the local sound speed, because the only estimates of the densities are those calculated in hydrostatic equilibrium. The presence of a momentum outflow will lead to gas pressures lower than those in the static case. However, for wind speeds of the magnitude of the sound speed, the kinetic energy and enthalpy fluxes are small compared with the energy flux required to explain the radiative losses. Thus the dominant energy losses in the atmosphere are from the radiation in emission lines and at low temperatures in continua. In Chapter 7 the full momentum equation is solved, and it is found that the total wind energy term does not dominate the radiative energy losses in the line forming region. Thus the radiation losses must be nearly equal to the rate of energy deposition by conduction and mechanical energy. In Model 1, the requirement of mechanical energy is small at the top of the transition region, however, energy must still be deposited at the top of the model to balance the energy conducted down to the region where it is deposited. In Models 2 and 3 some energy must be deposited throughout the transition region. This has important implications for the damping of mechanical waves. The empirical damping length, defined as,

$$L_{Damp} = F_{Mech}/(dF_{Mech}/dR), \tag{4.27}$$

is thus strongly dependent on the chosen model. The radiation losses for Models 1, 2 and 3 are shown in Figure 4-4. Note that the sum of the radiation losses above $Log(T_e) = 4.0$ for all three models are within 25% of each other, this is a result of the fact that most of the radiation losses occur close to the star where the radial term is ~ 1. Because in Models 2 and 3 the conduction terms are small compared to the radiative losses, Figure 4-4 represents the amount of energy which must be supplied by a non-thermal energy source. The chromospheric losses below $Log(T_e) = 4.0$ are much greater than those in the transition region and the total losses above the photosphere are $\sim 1.5(\pm 0.5) \times 10^5\,\mathrm{erg\,cm^{-2}\,s^{-1}}$ (see Section 7-3-1).

The non-thermal energy flux required can be compared with the energy carried by different wave propagation processes. The energy flux of propagating waves Φ_{Mech} is proportional to ϵC, where ϵ is the wave energy density and C is the propagation velocity. Both acoustic and MHD (*e.g.,* Alfvén) waves are likely to be

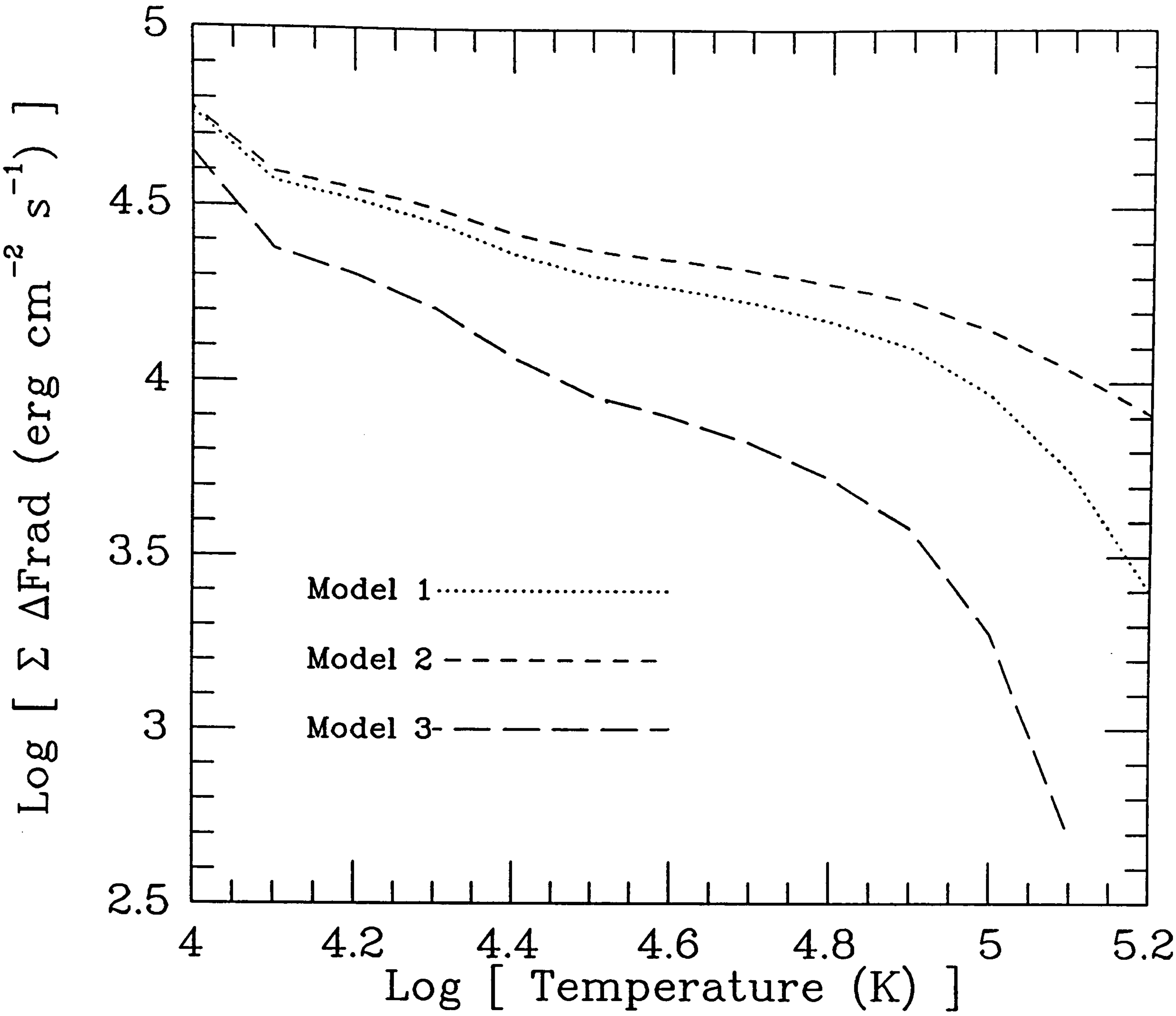

Figure 4-5 Logarithm of the total Radiative Power Loss against Logarithm of Temperature for Models 1, 2 and 3. Model 2 has an emission measure which has been extended linearly up to the value derived from the upper limit to the X-ray flux.

present in an atmosphere containing a magnetic field. The propagation velocities are, for $T_e \geq 2 \times 10^4$ K, where hydrogen is fully ionised,

$$C_{sound} = \left(\frac{\gamma P_{Tot}}{\rho}\right)^{1/2} \simeq 1.5 \times 10^4 T_e^{1/2} \,\mathrm{cm\,s^{-1}}, \qquad (4.28)$$

for sound waves and,

$$C_{Alf} = \frac{B}{\sqrt{4\pi\rho}} \simeq 2 \times 10^{11} \frac{B T_e^{1/2}}{P_e^{1/2}} \,\mathrm{cm\,s^{-1}}, \qquad (4.29)$$

for Alfvén waves. In Model 3 at $Log(T_e) = 4.0$ the energy flux of pure acoustic waves is $\sim 4.5 \times 10^3 \,\mathrm{erg\,cm^{-2}\,s^{-1}}$, and is nearly constant with temperature. Thus, acoustic waves cannot account for the observed radiation losses of 4.5×10^{4}erg cm^{-2}s^{-1} above this temperature. The same conclusion is also reached for Model 2. The energy flux carried by acoustic waves is essentially constant with temperature because the energy flux Φ_{Sound} is proportional to $N_eT^{3/2}$. And as the pressure slowly decreases with temperature, the flux is essentially constant. However, if the flux is carried by shock waves, it is in principle possible to provide sufficient energy. The energy flux carried by shock waves can be written (Kuperus, 1965) as,

$$\Phi_{Mech} = 4\rho C^3_{sound}\frac{(M^2-1)^2}{3M(\gamma+1)^2}, \tag{4.30}$$

where M is the Mach number of the shock and γ is the ratio of specific heats. In Model 3, shocks with a Mach number of ~ 3 could carry sufficient energy flux at $Log(T_e) = 4.2$. However, the non-thermal motions do not show the presence of velocities with this amplitude.

From Table 4-9 it can be seen that the turbulent velocities are a factor of ~ 2 greater than the sound speed. If the wave energy density is $\rho < V^2_{turb} >$, the mechanical energy flux can be calculated, assuming either an acoustic or a turbulent propagation velocity. The 'turbulent' energy flux will then be greater than the acoustic energy flux by a factor of ~ 4 or ~ 8 respectively. However, at the base of the model, at $Log(T_e) = 4.0$, the turbulent energy flux is also unable to carry the net energy required.

If the propagation mechanism is Alfvén waves, an estimate of the Alfvén velocity (and hence the magnetic field) necessary to carry sufficient energy flux can be made by dividing the energy flux required by $\rho < V^2_{turb} >$, where the line broadening is known from the optically thin emission lines. In Model 3, a minimum magnetic field of $\sim 1/3$ Gauss at $Log(T_e) = 4.0$ is required to match the observational constraints (using the assumptions considered so far). Because the pressure at $Log(T_e) = 4.0$ and total radiation losses are similar for Models 2 and 3 a magnetic field of this order will also satisfy Model 2. It does not seem an unreasonable value given the lower level of surface fluxes for ι Aur compared with main sequence stars, where B at $Log(T_e) = 4.0$ must be ≥ 30 Gauss.

4-7 Conclusions

Taking Models 2 and 3 as the most representative of the available data the uncertainties in the radiation losses reflect directly those in the emission measure. Even with uncertainties of $\pm 50\%$ the radiation losses suggest that deposition of Alfvén wave energy is the most likely process to provide sufficient energy. The models constructed in this chapter illustrate how the atmospheric structure depends on the surface gravity and on possible turbulent motions suggested by non-thermal broadening of optically thin lines. The models shown here are not used in further work, but provide a basis on which to build further models.

4-8 Summary

The emission line fluxes and selected line ratios have been used to investigate the physical conditions in the transition region. Briefly these are as follows; (1) The hydrogen column density in the O I] and C I] line forming region is $\int N_H dh \sim 10^{21}$ cm^{-2}. (2) The electron density determined from the density sensitive C II] multiplet is $Log(N_e) = 9 \pm 0.3$ dex. (3) The electron density estimated from the C III] loci is $N_e \leq 10^9$ cm^{-3}.

Models 2 and 3 have been calculated to include turbulent motions in the transition region models. These motions have the effect of expanding the atmospheres. At $Log(T_e) = 4.8$ Models 2 and 3 have electron densities of $Log(N_e \text{ cm}^{-3}) = 8$ and 7.6, respectively, which means that if the electron density at this temperature is

$Log(N_e) = 9$ then the observed emission must be limited to a fraction $\leq 10^{-2}$ of the stellar surface.

The line profiles have been considered, with the following conclusions; (1) ι Aurigae has two absorption components in the Mg II h & k lines. The low velocity component is consistent with the velocity vector of the local interstellar medium. (2) The O I $\lambda1304$ resonance multiplet lines are at least partially opacity broadened, while the optically thin emission lines in the transition region are broadened by some non-thermal mechanism.

The models have been used to examine the energy balance of the atmosphere and the following have been found; (1) The one component spherically symmetric models constructed show that the energy balance is model dependent, with the radiative losses being determined by the radial extent of the atmosphere. (2) The conduction terms are small compared to the radiative losses, except for Model 1 which has been constructed so that the electron density at $Log(T_e)$ is $\sim 10^9$ cm^{-3}, however this model does not match the observed pressure derived from the X-ray upper-limit. (3) The total radiation losses between $Log(T_e) = 4.0$ and $Log(T_e) = 5.2$, for Model 1 are $\sim 5.8 \times 10^4$ erg cm^{-2} s^{-1}. Model 2 and 3 also have similar total radiation losses because most of the losses occur close to stellar surface. (4) Pure acoustic waves cannot transport a sufficient energy flux to account for the observed radiation losses, however, acoustic shocks with Mach numbers ~ 3 could in provide enough energy but the line profiles do not show such large velocities. Since conduction is so small in Models 2 and 3, comparison of the total radiation losses with those carried by a Alfvén waves suggest these might be a suitable energy transport mechanism provided there is a radial magnetic field of$\sim$ 1/3 Gauss at $Log(T_e) = 4.0$.

CHAPTER 5. MODEL CHROMOSPHERES – METHODS

So far in this work the emission lines observed in the ultraviolet waveband have been analysed to produce model atmospheres starting at $\sim 10^4$K. Below this temperature the physical characteristics of the atmosphere change. In the transition region the temperature changes rapidly over the local isothermal pressure scale height, whereas in the chromosphere the temperature changes only slightly over the local isothermal scale height. In the following models the working definition of the chromosphere is as follows; it is the region between the temperature minimum and the transition region, *i.e.,* it begins where the temperature gradient becomes positive.

In the outer atmospheres of hot stars the transfer of radiation is important in determining the energy and momentum balance. In cool star chromospheres the radiation transfer is important in determining the energy balance, but is not important in determining the momentum balance, unless the star is cool enough for significant amounts of dust to be present.

The aim of the following two chapters is to produce a self-consistent model that can reproduce the observed UV emission line fluxes and also the components of the Mg II h & k line profiles which are not likely to be affected by the scattering of line photons in mass outflows. In Chapter 5, the techniques used to construct model chromospheres are discussed, then the boundary conditions of the models are derived and the initial models are constructed. The computer programme which is used to solve the radiative transfer in the chromosphere is described, with an emphasis on how the physical nature of radiation transfer in spectral lines has been used to produce a fast efficient computer code. In Chapter 6, the results of the computer models and the way in which the temperature structure determines the line fluxes and profiles are discussed. The model chromospheres are then linked to the model transition regions constructed in Chapter 4, via the emission measures $E_m(0.3)$ and $E_m(0.1)$.

In the attempt to determine the different chromospheric characteristics in the H-R diagram two approaches have been developed. The first approach is to assume some non-thermal heating mechanism and then derive theoretical models that can be compared with the observations (or semi-empirical models). For examples of this approach see the review by Ulmschneider (1979). The second approach is to derive semi-empirical models of the temperature, turbulent velocity and density, and then compare the calculated profiles of the resonance lines of Mg II and/or Ca II with the observations. The profiles are calculated using non-LTE and partial redistribution (PRD). (For a discussion of the comparison between *complete redistribution* (CRD) and *partial redistribution* (PRD) calculations for resonance line profiles, see the review by Linsky, 1985.) Systematic adjustments to the initial model are made to bring the calculated profiles into closer agreement with the observations. This model-synthesis approach relies on the qualitative understanding of the radiative transfer problems.

Almost all the model chromospheres made, to date, are one-component in the sense that the derived physical characteristics are those of an average model. In the solar case, inhomogeneities are known to exist and the emission of Ca II and Mg II resonance lines is stronger in the supergranulation cell boundaries. Thus the chromospheric mean models will not, in general, describe the real stellar chromospheres. The properties derived are therefore only averages of the physical properties in the separate components of the stellar chromosphere. It is important, however, to make quantitative studies of one-component atmospheres so that the effects of deviations from the mean chromospheric properties expected in any inhomogeneities can be understood. One test of the effects of inhomogeneities is to examine radiation transfer in emission lines excited by accidental fluorescence from strong lines. The fluorescing radiation and the excited species may not co-exist spatially and if treated in a one-component model, inconsistencies may appear between the observed line flux ratios. (See, for example, the work on CO by Ayres *et al.*, 1986)

For the first time, explicit calculations are made treating the excitation of lines in Fe I uv44 by Mg II k radiation and this will be discussed in detail in Chapter 6. This excitation path may be important in determining the energy balance of the lower chromosphere, because the observed flux in one of these lines, namely Fe I uv44 $\lambda2843.98$, has a surface flux of 4.1×10^3 erg cm^{-2} s^{-1} which is 10% of the Mg II k line flux.

In this work, semi-empirical model chromospheres are constructed using the blue inner wings of the Mg II h & k line profiles (which is justified in Section 6-2-2) and the line fluxes. To supplement this approach the line fluxes from a range of optically thin lines are also calculated and this turns out to be very important in restricting the range of acceptable models which can produce Mg II h & k line fluxes and profiles consistent with the observations. The first stage in constructing model chromosphere is to solve the hydrogen atomic model in hydrostatic equilibrium, which gives the electron densities which are then used in further atomic model calculations. The level populations in Mg II, Si II and Al II are then calculated and the results are compared with the observations. Then, the initial chromospheric model is iterated such that the next chromospheric model produces results which are in closer agreement with the observations. It is stressed that the PRD calculations may not, in detail, contain all the relevant physics involved in photon-photon correlations and thus, some uncertainties remain in calculated *profiles.*

The emission measure analysis cannot be used to model the structure below 10^4K for several reasons. In the chromosphere the total gas pressure gradient becomes steep over the line forming regions so that the approximations made in deriving equation (4.11) are no longer valid. Also it becomes difficult to calculate the product $N_e N_H$ in terms of N_H^2 because the ionisation fraction changes by several orders of magnitude and is dependent on the photoionisation of the collisionally excited $n = 2$ level by the Balmer continuum (which is not known *a priori*). However, the emission measures computed must match up with those observed at $Log(T_e) \sim 3.8$ to 4.0.

5-1 The Initial Model Chromosphere.

There are four natural variables and parameters which are often used to describe model chromospheres. The first is the height or mass column density variable. In solar work the height is often used but in stellar work (where there is no spatial resolution) it is more convenient to use the mass column density, *i.e.*, $m_{col} = \int \mu N_H m_p dh$, where μ is the mean molecular weight and m_p is the proton mass. For collisionally excited lines this is particularly useful as the optical depth, τ is $\propto m_{col}$. The other variables and parameters are the run of temperature ($dT/dLog(m_{col})$ for example), the temperature minimum T_{Min}, and m_{col} at the base of the transition region (m_{col0}). The boundary conditions on the mass column density are calculated in the following sections while the run of m_{col} with temperature is initially estimated. The following Sections describe how the various parameters and boundary conditions are chosen.

5-1-1 The Mass Column Density m_{col0}

The mass column density in the transition region is calculated from the emission measures and electron density. Three values will be adopted, the first (and initial value) corresponds to to an electron density of $N_e = 10^9\,\mathrm{cm}^{-3}$ at $Log(T_e) = 4.8$ while the other values are found by iterating the model chromosphere. The initial values are calculated with the emission measure described in Chapter 4 and the pressure is integrated down to $Log(T_e) = 3.8$ retaining a hydrogen ionisation fraction of 0.8 below $Log(T_e) = 4.0$. This provides an estimate to the run of temperature with the column mass at the top of the model. Previous workers have simply used a smooth exponential rise above a given column mass to represent the transition region. It is the aim of the present work to join the model chromosphere to the transition region models, such that the emission measures calculated from the chromosphere can be joined to the well determined emission measures above $Log(T_e) = 4.3$.

5-1-2 The Temperature Minimum T_{Min}

To find appropriate values of the temperature and mass column density at the temperature minimum for the model chromosphere, values of the above boundary conditions are found assuming that the Mg II k_{IV} feature is formed in CRD. These values are then scaled so that important effects of radiative transfer are included. This allows for the fact that the k_{IV} feature (see Figure 1-3) is formed in PRD. To constrain these values further, the scaled results are compared to flux-constant blanketed model photospheres (Gustafsson *et al.*, 1975).

A technique originally developed by Shine and Linsky (1974) to calculate the temperature and m_{col} for the upper photosphere of the Sun, is used to calculate the column mass density of the temperature minimum of ι Aur. The value of m_{col} at T_{Min}^{CRD} (the value assuming CRD) can be calculated from line wing profiles of the Ca II and Mg II resonance lines assuming LTE, which implies CRD, and that most of the opacity in the line wings comes from the first isothermal pressure scale height. Studies in radiation transfer have shown that the assumption of CRD underestimates the value $T_{Min}(i.e., T_{Min} > T_{Min}^{CRD})$ because CRD overestimates the number of photons in the line wings (*e.g.*, Milkey and Mihalas, 1974). However, the calculated temperature can be used as a lower limit. The greatest sources of error in these calculations are the absolute flux calibrations and the abundances; the uncertainties in the absolute flux in the IUE spectra can lead to errors in excess of ±150 K in the temperature. Because of this uncertainty, flux-constant blanketed photospheric models have been computed by J. Drake (private communication, 1988) which are used to constrain the values of T_{Min} and $m_{col}(T_{Min})$.

Following the method of Shine and Linsky (1972) it is necessary to assume the following;

(1) $\pi F_{\Delta\lambda} \simeq \pi B_{\Delta\lambda}$ at $\tau_{\Delta\lambda} \simeq \frac{2}{3}$ which is an Eddington-Barbier relation with $S_\nu = B_\nu$. $\pi F_{\Delta\lambda}$ is the observed flux.

(2) $Ne \ll N_H$, *i.e.,* the photospheric pressure is dominated by hydrogen.

(3) that all the ions are in the singly ionised state so $N_{MgII} = A_{Mg}N_H$, where A_{Mg} is the atomic abundance of magnesium.

(4) the opacity at the temperature minimum is dominated by that produced in the first isothermal pressure scale height above the temperature minimum.

The opacity in the line wings is given by;

$$\kappa_{\Delta\lambda} = A_{Mg}N_H\frac{h\nu_0}{4\pi}\left(\frac{g_j}{g_i}\frac{c^2}{2h\nu^3}A_{ji}\right)\frac{\Gamma\lambda^4}{4\pi c^2(\Delta\lambda)^2} + \kappa_c, \tag{5.1}$$

where g_i and g_j are the statistical weights of the lower and upper level, respectively. A_{ji} is the radiative decay rate, κ_c is the continuum opacity and Γ is given by the line broadening parameters,

$$\Gamma = \Gamma_{Rad} + \Gamma_{(vW-H)}N_H(\frac{T}{5000})^{0.4} + \Gamma_{(vW-He)}N_{He}(\frac{T}{5000})^{0.4} + \Gamma_{Stark}. \tag{5.2}$$

The contributions to the line broadening are from radiative damping, Van der Waal's broadening from hydrogen and helium, and Stark broadening respectively. The

Table 5-1 Atomic parameters adopted in determining the temperature minimum T_{Min}. The values for Ca II are from Smith and Drake (1988). The radiative rates for Mg II are from Black *et al* (1972).

Transition	A_{ji} (s^{-1})	Γ_{Rad} (s^{-1} cm^{-3})	$\Gamma_{(vW-H)}$ (s^{-1} cm^{-3})	$\Gamma_{(vW-He)}$ (s^{-1} cm^{-3})
Ca II H 3968.5Å	1.40(8)	1.5(8)	2.0(−8)	6.0(−9)
Ca II K 3933.7Å	1.47(8)	1.5(8)	2.0(−8)	6.0(−9)
Mg II h 2802.7Å	2.54(8)	2.6(8)	1.4(−8)	
Mg II k 2795.5Å	2.55(8)	2.6(8)	1.4(−8)	

Stark broadening is small because of the low particle density, and the Van der Waal's broadening is assumed to be due predominately to hydrogen and helium. The collisional broadening due to helium is approximately 3% of that due to hydrogen (assuming $N_{He} = 0.1N_H$ and Γ from Table 5-1) and is consequently neglected in the following calculations. The temperature dependence ($\propto T^{0.4}$) is different from the pure Van der Waals temperature dependence because the colliding atoms are small perturbers (see Lwin, McCartan and Lewis, 1977).

The optical depth $\Delta\lambda$ from the line centre is given by,

$$\tau_{\Delta\lambda} - \tau_c = \int (\kappa_{\Delta\lambda} - \kappa_c) dh. \tag{5.3}$$

If the opacity is due to the material in the first isothermal scale height, H, then dh can be replaced by,

$$H = \frac{kT}{g_* m_p \mu}. \tag{5.4}$$

By equating (5.1), (5.2) and (5.3) using condition (1) and neglecting the continuum opacity, it is possible to solve for N_H. In the following calculation $T_5 = T/5000$.

$$N_H \simeq \frac{T_5^{-0.4}}{2} \frac{\Gamma_{Rad}}{\Gamma_{vW}} \left\{ \left[1 + 4 \frac{\Gamma_{vW}}{\Gamma_{Rad}^2} \frac{g_i}{g_j} \frac{\Delta\lambda^2}{\lambda^6} \frac{32 g_* m_p \mu \pi^3 c^2}{k A_{ji} A_{Mg}} \frac{3}{2} T_5{}^{-0.6} \right]^{1/2} - 1 \right\}. \tag{5.5}$$

The mass column density m_{col} in hydrostatic equilibrium is given by,

$$m_{col} = \frac{P_{gas}}{g_*}, \tag{5.6}$$

where the pressure, P_{gas}, is given by the equation of state,

$$P_{gas} = N_{Tot}kT. \tag{5.7}$$

Combining (5.5) and (5.6) gives the column mass m_{col} at temperature T. When the second term in the square root bracket in equation (5.5) is small, the equation reduces to,

$$m_{col\Delta\lambda} \propto \frac{\Delta\lambda^2}{\Gamma_{Rad}A_{Mg}}, \tag{5.8}$$

which is virtually independent of g_* and Γ_{vW}. Thus pressure broadening is not the dominant process in the temperature minimum region in cool, low gravity stars. The atomic parameters adopted are shown in Table 5-1.

The deep LWP spectra of ι Aur show the photospheric wings of the Mg II h & k lines (see Figure 3-4). The intensities in these wings have been analysed to provide a minimum value of T_{Min} at a calculated value of m_{col}. As the intensity between the line cores is suppressed, due to the combined wing opacity, the outside wings are used in the calculations. The wind absorption feature, blueward of the k line, is between the k_{1V} minimum and the line core, so it will not affect the results.

To compare the results from the Mg II profiles, this method is also applied to the Ca II profiles from a star of similar spectral type (*i.e.,* σ Oph). The spectra showing the Ca II H & K lines were taken from Linksy *et al.* (1979), noting that the calibration factor quoted in their Table 1B refers to the normalised flux of 1.0 in Figure 2h in that paper. The noise and presence of extra opacity in the line wings makes the profiles irregular, so it is necessary to estimate a mean curve. The temperature minima derived from the Mg II and Ca II lines are calculated using optimum fits to the photospheric profiles. The position of the resulting temperature minima are shown in Figure 5-1. The temperatures derived from the k and K lines are greater than those derived from the h and H lines. This can be attributed to the lower opacity in the k and K lines. If the k_{1V} feature is formed in a region surrounding the temperature minimum, then there will be contributions to the flux from the material on either side of the minimum and this effect will be more pronounced for the k and K lines.

The values of T_{min}^{CRD} are expected to be lower limits to the actual T_{min}. To constrain the location of the temperature minimum further, a grid of photospheric models has been calculated. The photospheric models shown in Figure 5-2 were calculated from the computer programme MARCS. (See Appendix A for a brief description of this programme.) The Models A, B, C and D are defined as follows, where X represents the metal abundance,

(i) Model A: $[X/H] = +0.2$, $g_* = 46\,\mathrm{cm\,s^{-2}}$ and $T_{eff} = 4340$ K.

(ii) Model B: $[X/H] = -0.2$, $g_* = 46\,\mathrm{cm\,s^{-2}}$ and $T_{eff} = 4340$ K.

(iii) Model C: $[X/H] = -0.2$, $g_* = 30\,\mathrm{cm\,s^{-2}}$ and $T_{eff} = 4340$ K.

(iv) Model D: $[X/H] = -0.2$, $g_* = 60\,\mathrm{cm\,s^{-2}}$ and $T_{eff} = 4340$ K.

The values of the metallicity are chosen to span the uncertainty in the abundances. The values of gravity also reflect the uncertainty in the stellar gravity. In the temperature minimum region at a given mass column density, Models A, B, C and D are within 100 K of each other. Models A and B are the same except Model A has a larger metallicity and has a higher temperature for a given column mass. This is partly due to the increased opacity which leads to a given optical depth, at a given frequency, occurring at a lower column mass.

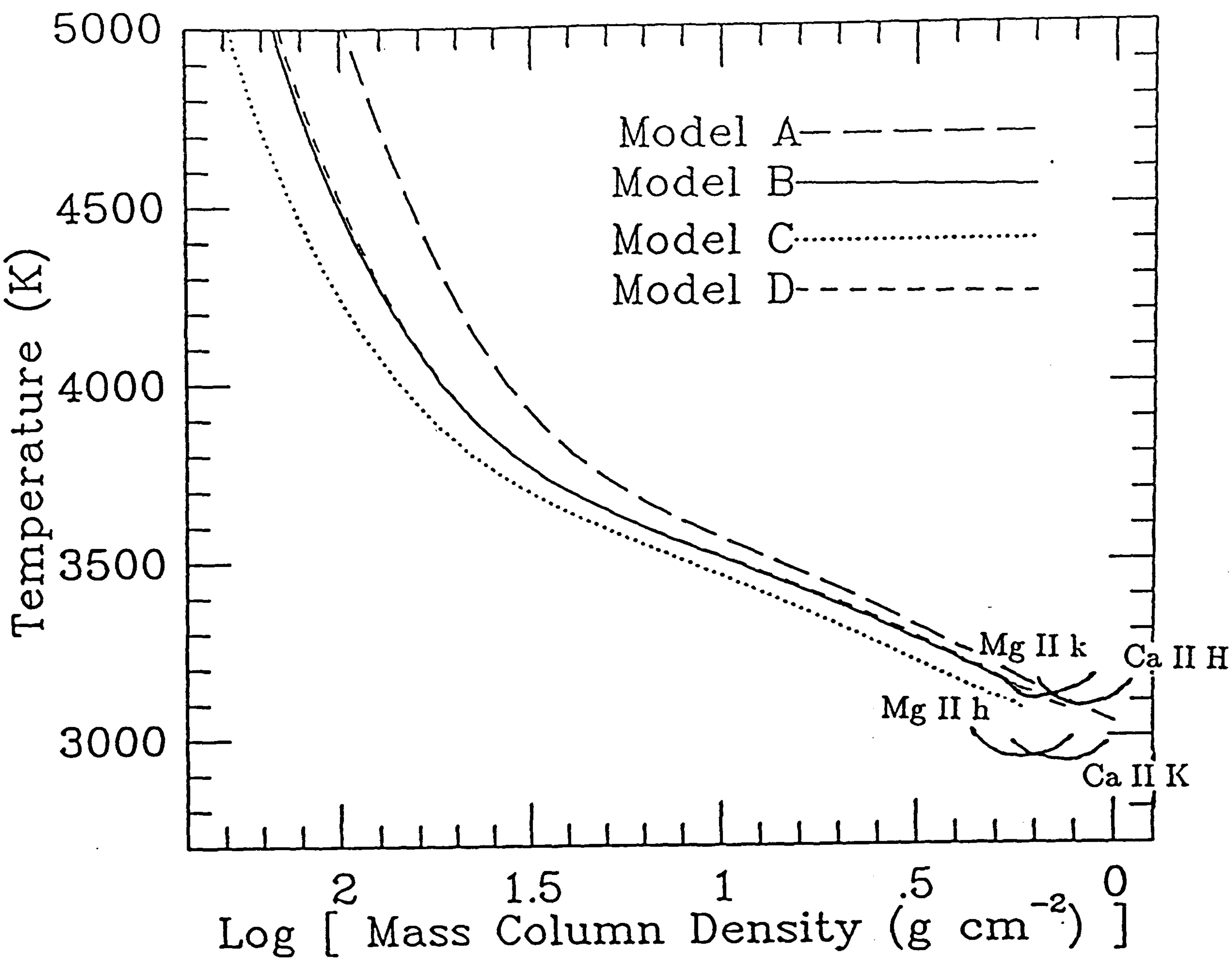

Figure 5-1 Temperature against logarithm of mass column density for the temperature minimum and photosphere of ι Aur. The four photospheric models, calculated from the programme MARCS (described in Appendix A), are Model A, long dash ($[X/H] = +0.2$, $g_* = 46\,\mathrm{cm\,s^{-2}}$ and $T_{eff} = 4340$ K), Model B, solid ($[X/H] = -0.2$, $g_* = 46\,\mathrm{cm\,s^{-2}}$ and $T_{eff} = 4340$ K), Model C, dot ($[X/H] = -0.2$, $g_* = 30\,\mathrm{cm\,s^{-2}}$ and $T_{eff} = 4340$ K) and Model D, short dash ($[X/H] = -0.2$, $g_* = 60\,\mathrm{cm\,s^{-2}}$ and $T_{eff} = 4340$ K).

The difference in temperature structure due to the uncertainty in the surface gravity of ι Aur can be seen by comparing Models B, C and D. These models have the same metallicity but different surface gravity. There are two main factors to be considered when comparing the models. First, the dependence of the mass column density on the surface gravity and second the dependence of the photospheric models on the change in gravity. The differences between Models B, C and D are mainly due to the inverse proportionality of the column mass to the surface gravity.

The locations of the temperature minima in Figure 5-1 show that the temperature minimum for ι Aur is consistent with that of σ Oph. The h (H) line minima are at a higher temperature than the k (K) line minima as discussed above. The k and K line temperature, calculated from the CRD approximation, is thus the lower bound to the real T_{Min}. The value of T_{Min}^{CRD}/T_{eff} obtained from Figure 5-1 is 0.67 ± 0.1 and this can be compared with the values shown in Figure 5-2 (which shows the ratio T_{Min}^{CRD}/T_{eff} plotted as a function of Log(T_{eff}) for a range of stars of different spectral type). It can be seen that for a given effective temperature and a given spectral type, there is a large scatter (± 0.05) in this ratio. The ratio for σ Oph is shown in Figure 5-2 and lies above that calculated for ι Aur because of the lower effective temperature. The ratio for ι Aur is at the lower limit for Figure 5-2, but considering the errors in measurement of the flux intensity (at the temperature minimum), the asymmetry in the profiles (probably due to mass motions) and the assignment of the effective temperatures, this value is consistent with previously calculated trends.

When the assumption of CRD is relaxed, it is found that T_{Min}^{CRD} underestimates the value T_{Min}. The size of $\Delta T = T_{Min} - T_{Min}^{CRD}$ has been calculated for other stellar models, spectral type V - III, and is found to be about 200 K (Ayres and Linsky, 1975). Thus the initial location of the temperature minimum for ι Aur is taken to be $0.5 > Log(m_{col}) > 0.0$ and $3150 > T_e(\mathrm{K}) > 3000$ K.

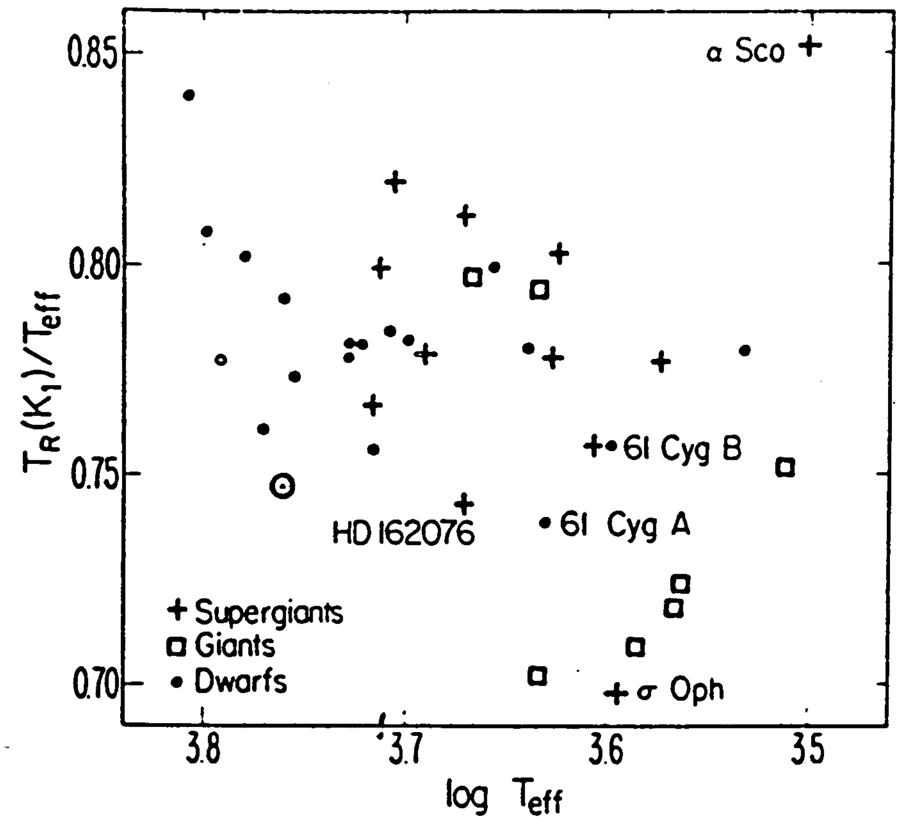

Figure 5-2 The ratios of the radiation temperature at the K_{1V} minimum feature to the effective temperature are plotted with respect to the effective temperature. From Linsky *et al.* (1980).

5-1-3 The Velocity Fields

There are two velocity fields which are needed to specify the model chromosphere: the macroscopic velocity field which is appropriate for the treatment of mass outflows and line shifts, and the microscopic velocity field which is important in determining the radiative transfer. Most of the following calculations will be carried out in hydrostatic equilibrium, where the macroscopic velocity field is set to zero at all points in the atmosphere. It is assumed that below the temperature minimum the turbulent velocity is $2\,\mathrm{km\,s^{-1}}$. This is a typical value of the photospheric microturbulence calculated from curve-of-growth analyses. The microturbulence in the transition region is taken to correspond to observed values of the line broadening in the optically thin emission lines described in Chapter 4. In the chromosphere, the turbulence is interpolated linearly in the logarithm of mass column density. The effects of changing the velocity fields are examined in Chapter 6.

5-1-4 The Electron Density

The electron densities in a model chromosphere are found by simultaneously solving the radiative transfer equations and the equation of hydrostatic equilibrium for the atomic model for hydrogen. However, to obtain a solution for the equation of hydrostatic equilibrium, a good initial estimate of the electron densities is needed. The electron densities of the initial chromospheric model are estimated as follows: In the lower transition region the electron densities were calculated from the emission measure analysis, with a crude estimate for N_e/N_H being $1.2 - 0.8$ for $Log(T_e)$ between 4.2 and 3.9. It has been found from previous calculations (*e.g.*, Vernazza *et al.*, 1973) that when hydrogen is predominately un-ionised, at high densities, $N_e \simeq 10^{-4} N_{HI}$. In the photosphere, this ratio was used to calculate the electron density. In the chromosphere an electron density of $N_e \simeq 10^9\ \mathrm{cm}^{-3}$ was adopted. This value is consistent with the electron density determined from the C II] multiplet. Where the separate approximations for the electron density come together, the values are joined together smoothly.

Working values of T_{Min}, m_{colMin}, the mass column densities in the upper chromosphere/transition region, and the variation of turbulent velocities with temperature have been discussed. The next stage in computing a chromospheric model is solving the non-LTE radiative transfer problem in the initial model.

5-2 The Computer Programme

A computer program for solving multi-level non-LTE radiative transfer problems in moving or static atmospheres, written by Mats Carlsson (1986) (hereafter known as MULTI) is used to construct the model chromosphere. This programme employs the scheme for solving the transfer problems developed by Scharmer (1981) and Scharmer and Carlsson (1985a, 1985b). For details of this scheme the reader should consult these references. The main points are described in Appendix B and they set the context for the following discussion. Some of the important features which emphasise the nature of non-LTE problems and how this has been used to advantage in the computational scheme are discussed below in the text. The effects of line blends are not included in the computer code. However, the effects of fluorescence have been included in the calculations of the iron atom, but the treatment is non self-consistent, in that the radiation field which excites the fluorescence is assumed to be unaffected by the photons leaked into the transitions of the excited atom (see the model atom for iron).

The model chromospheres have been calculated assuming plane parallel geometry and this assumption can be examined to check whether it is likely to introduce sources of error in the results. One measure of the sphericity of a stellar atmosphere is the ratio of a local isothermal scale height to the stellar radius. ι Aur has a gravity which is lower than that of the Sun by a factor of 600, thus the corresponding isothermal scale height H is 600 greater. The radius of ι Aur is $\sim 59\, R_{\odot}$ so that $(H/R)_{*} \leq 10(H/R)_{\odot}$. However, if there is significant turbulent pressure in the chromosphere the ratio of the effective scale height to the stellar radius will be increased. If the stellar and solar chromospheres extend over a similar number of scale heights the effects of sphericity in the stellar chromosphere will be less than those in the Sun. The assumption of plane parallel geometry has been demonstrated to be adequate in developing solar models, thus there is no reason to expect that it will not be valid for ι Aur.

An estimate can also be made of the geometric dilution of the radiation field expected in the bright giant chromospheres. Using the Calculus of Small Errors, to a zero order, it is possible to write a relationship between the flux in an optically thin continuum and its characteristic radiation temperature. Following Böhm-Vitense (1972),

$$4\frac{\Delta T}{T} \simeq \frac{\Delta F}{F}, \tag{5.9}$$

and if $F \propto R^{-2}$ then,

$$\frac{\Delta F}{F} \simeq 2\frac{\Delta R}{R}. \tag{5.10}$$

The radiation temperature will then vary as,

$$\frac{\Delta T}{T} \simeq \frac{1}{2}\frac{\Delta R}{R}. \tag{5.11}$$

The model chromospheres which are presented in this Chapter have $\frac{\Delta R}{R} \sim 0.05$, which represents a change in temperature of 60 K when $T_{Rad} = T_{Min}$. For radiation in an optically thick transition this temperature correction will be an overestimate. Changes in the radiation temperature of this size are found to be relatively unimportant.

The method used in the programme MULTI to solve the statistical equilibrium equations, the particle conservation equations and the radiative transfer equation is as follows. The statistical equilibrium equations and the first order form of the transfer equation are linearised with respect to the population number densities and the specific intensity (Scharmer and Carlsson, 1985). The linearised transfer equation has only one non-linear term which corresponds to the number of photons and the number of absorbing atoms. These equations are then *pre-conditioned*, *i.e.*, re-expressed in a manner which has the effect of reducing the magnitude of the non-linear terms and also removes some of the numerical problems present at large optical depths. Scattering of photons in line cores with large optical depths can lead to numerical problems because there are cancellations of large numbers which are close in value. The preconditioning reduces the magnitude of these effects.

To solve the transfer equation, an approximate *radiative transfer operator* is constructed. Following Scharmer and Carlsson (1985b), the *exact* operator is derived from the relationship (for an outgoing ray),

$$I^{+}_{\nu\mu}(\tau_{\nu\mu}) = \Lambda_{\nu\mu}[S_{\nu\mu}] \equiv e^{\tau_{\nu\mu}} \int_{\tau_{\nu\mu}}^{\infty} S_{\nu\mu}(\tau'_{\nu\mu}) e^{-\tau'_{\nu\mu}} d\tau'_{\nu\mu}. \tag{5.12}$$

If $S_{\nu\mu}$ varies slowly compared to $e^{-\tau_{\nu\mu}}$, then a significant fraction of the total integral comes from a small range in optical depth. Assuming that the source function is a linear function of optical depth, it is possible to write the approximate operator,

$$I^+_{\nu\mu}(\tau_{\nu\mu}) \simeq \Lambda^\dagger_{\nu\mu}[S_{\nu\mu}] \equiv \omega^+ S_{\nu\mu}(\tau^+_{\nu\mu}). \tag{5.13}$$

The values of ω^+ and ω^- are calculated in a straightforward manner. For example, let the source function be written as,

$$S_{\nu\mu} = a_{\nu\mu} + b_{\nu\mu}\tau_{\nu\mu}, \tag{5.14}$$

then by substituting (5.23) into (5.21) the specific intensity for the outgoing radiation in a semi-infinite atmosphere becomes,

$$I^+_{\nu\mu} = a_{\nu\mu} + b_{\nu\mu}(\tau_{\nu\mu} + 1). \tag{5.15}$$

Comparing (5.24) with (5.22), the weights ω^+ and the quadrature point $\tau^+_{\nu\mu}$ become,

$$\omega^+(\tau_{\nu\mu}) = 1; \tau^+_{\nu\mu} = \tau_{\nu\mu} + 1. \tag{5.16}$$

Expressions can also be found for the incoming ray,

$$\omega^-(\tau_{\nu\mu}) = 1 - e^{-\tau_{\nu\mu}}; \tau^-_{\nu\mu} = \frac{\tau_{\nu\mu}}{\omega^-(\tau_{\nu\mu})} - 1. \tag{5.17}$$

These relations can be used to make physical approximations to the radiation transfer. The system of equations allows for a hybrid of two well known approximation techniques to be constructed, which results in large savings in computer time and numerical stability. This 'hybrid' scheme incorporates the *core-saturation* method and the ordinary *lambda iteration* method. These are described with reference to the actual computer code. Appendix B contains a brief description of the computer scheme and describes the routines and input parameters referred to in the following text.

Rybicki's Core Saturation Method (1972)

At large optical depths there is a balance between the local emission and absorption rates. This constrains the changes in the population number densities and radiation field. The path lengths experienced by photons in the line core are short compared to the scale length of changes in the source function and population densities. Then the photons essentially experience local conditions and in the line core,

$$\kappa_{\nu\mu} I_{\nu\mu} \simeq j_{\nu\mu}. \tag{5.18}$$

Inserting large optical depths into equations (5.16) and (5.17) one finds that $\omega^+ = \omega^- = 1$ and $\tau^+ = \tau^- = \tau$ so that the result of the approximate operator method reduces to the core saturation condition. In MULTI, the input parameter DIFF controls when weights ω are set equal to 1. Typical values of DIFF are found to be in the range $5 - 10$. Obviously, if the value of DIFF is very large it will require more computing time to reach a converged solution.

Lambda Iteration

This technique uses an initial estimate of the radiation field to calculate the population number densities. These are then used to calculate the new radiation field and so on. This technique is most suitable for transitions of low optical depth, because the correction to the population number densities (at a given depth) generates a perturbation in intensity which propagates over one unit of optical depth for each iteration. Thus for lines with large optical depths, the lambda iteration method is computationally slow. This technique is incorporated into the weights ω by setting $\tau = 0$ then $\omega^- = 0$, corresponding to no incoming radiation at $\tau = 0$. In MULTI the parameter THIN sets $\omega^- = 0$ for $\tau <$ THIN. The change to the lambda iteration is useful because it is no longer necessary to solve the linearised equations (which can be unstable and produce negative populations). A value of THIN = 0.1 is found to be an optimum value in terms of saving computing time. This represents a balance of the savings due to the lambda iteration and the increased number of iterations needed to ensure convergence.

From Appendix B equations (B.13)–(B.21) it can be seen that as the iteration converges the final solution is *independent* of the assumptions made in the approximate operator. Thus the accuracy is determined by the accuracy to which the exact transfer calculation can be made (*i.e.*, the accuracy to which the intensity can be calculated from a given source function). The final accuracy in population number densities is dependent on the number of depth points per change in unit optical depth in the atmosphere. The number of depth points used is typically 50–100. To save computer time it is desirable to minimise the number of depth points, but to ensure convergence a certain number of depth points must be used. The matrix equation for the population numbers has a characteristic structure which schematically shows the nature of the radiative transfer problem. This is discussed in detail by Scharmer and Carlsson (1985), and reiterates the points discussed above. The matrix has a pronounced banded structure. The off-diagonal elements correspond to the non-local influence of the radiation field and the absence of many of these elements is due to the lambda iteration of the radiation field at small optical depths. The approximate lambda operator also reduces the number of off-diagonal elements. The banded structure of the matrix leads to savings in computer time.

Much of the time saved in MULTI, compared to other programs which solve similar problems, is due to the approximations controlled by the input parameters DIFF and THIN. The approximate lambda operator leads to the removal of non-zero elements in the matrix equations which in turn leads to large time saving. Two further MULTI parameters which affect the time taken to reach convergence are ELIM1 and ELIM2. When the maximum correction to the population numbers (EMAX) is below ELIM1, the matrix equations are not recalculated but the population numbers are back substituted. A safe value seems to be ELIM1 = 0.1. When EMAX falls below ELIM2 the iterations are stopped and the current values of the population numbers are used to calculate the final model. Values of ELIM2 $= 0.01 - 0.001$ were used in all models in this work. The difference between the population number densities and the infinitely converged solution is normally a factor of 5-10 smaller than EMAX. A value smaller than 0.01 is not normally needed since errors in the basic assumptions and depth scale are larger (Carlsson, 1986).

It has been shown how the important effects of radiative transfer have been included into the equations and how savings are made in the computing time. The next section will describe some recent modifications that have been made to the computer programme of Carlsson (1986). The rationale for these modifications is discussed in the context of particular atomic models.

5-3 Modifications to MULTI

The modifications which have been made to some of the routines in MULTI are described below. There are two main reasons for making these changes; first, the depth point grid used initially was too coarse, causing the interpolations to lead to errors in the population number densities in regions where the optical depths in the lines were changing slowly. Also there were insufficient depth points in the ionisation zone of hydrogen to obtain convergence. Second, the initial approximation of the radiation field did not lead in all cases to convergence, so more realistic starting approximations have been added. These modifications have been made by Judge (private communication, 1988) and Carlsson and Judge (private communication, 1988).

The initial depth scale is set up in the original model either by specifying the depth points (in Log($mcol$) or Log(τ_{5000})) explicitly or by a linear interpolation between the top and bottom of the model. Then the routine DSCAL2 computes a smoother grid of depth points in the sense that the change in optical depth between any two levels is not too large. This is justified by the improved convergence of the subsequent models. The original DSCAL2 routine ensured that the maximum change in the logarithm of the optical depth (taken over all transitions), $\Delta Log(\tau_{\nu\mu})$, is constant throughout the atmosphere. $Max\Delta Log(\tau_{\nu\mu})$ is defined as the change in $Log(\tau_{\nu\mu})$ from one depth point to the next, such that the maximum change in $Log(\tau_{\nu\mu})$ is calculated over all the transitions, frequencies and angles.

The first modification (Carlsson and Judge, 1988, private communication) ensures that the computer routine DSCAL2 writes a depth point grid such that maximum $\Delta Log(\tau_{\nu\mu}) = 0.3$. The second modification (Judge, 1988, private communication) adds depth points to the grid if the change in column mass between two levels is greater than the mean value of Δm_{col}.

The modifications made to the starting approximations are based on the *escape probability method* (Rybicki, 1984, 1985). The second-order escape probability method is used to obtain the starting approximation to the population densities. This is more accurate than the first order method at the atmosphere boundaries because it includes a spatial derivative. In outline, the method is as follows; the mean integrated intensity, in plane parallel geometry with no incident radiation, is

$$\bar{J}(\tau) = \int K(\tau, \tau')S(\tau')d\tau', \tag{5.19}$$

where the usual subscripts have been dropped. This equation applies to a particular transition. The kernel, $K(\tau, \tau')$, represents the probability that a photon created at τ is destroyed between τ' and $d\tau'$. The escape probability is then,

$$P(\tau) = 1 - \int K(\tau, \tau')d\tau'. \tag{5.20}$$

If the source function varies slowly compared to the variation in $K(\tau, \tau')$, then from (5.19) and (5.20),

$$\bar{J} \approx [1 - P(\tau)]S(\tau), \tag{5.21}$$

which is an equation expressed in terms of local values. This approximation fails at the boundaries because it treats the radiative transfer with local conditions. A second order approximation, which includes some non-local effects (through the change in $\bar{J}$ and S), can be written (Rybicki, 1984 - equation (6.4)),

$$\bar{J}(\tau) = [1 - P(\tau)] + \int_{\tau}^{\infty} \frac{\delta S}{\delta \tau} P(\tau) d\tau. \tag{5.22}$$

The new routine uses the second-order escape probability (5.22) for radiation transfer in the lines and the *On-the spot approximation* for the continua. This latter approximation means simply that the photons are destroyed close to where they are created, thus the escape probability is ≈ 0, so that $\bar{J}(\tau) = S(\tau)$.

5-4 Input Files and the Atomic Models

In this section a description is given of the atomic models used in MULTI to construct the model chromosphere. To run the programme, the FORTRAN code must be furnished with several input files. These files contain an atomic model (which contains the energy levels and transitions for a given atom), the depth scale, the abundances, the opacity package (as supplied with the original programme) and the initial atmospheric model.

The atomic energy levels and the transitions, which are considered in each atomic model, are described in the next subsections and Appendix C. The atomic models have been developed over a period of time, and the atomic data contained in them are believed to be the best available. The models shown in Appendix C contain the energy levels and the transitions which are included. Some atomic data have been omitted for clarity. A definition of the labels found in the atomic models is given at the beginning of the Appendix. Some references are included in the individual models.

The depth scales used in the present models were found as follows; initially the depth scale was linearly interpolated in the logarithm of the mass column density, between the top and bottom of the atmosphere. MULTI was then run using only the starting approximation. The new smooth depth scale, written with DSCAL2, was then used as the new input depth scale. This was repeated approximately three times. The necessity of having a depth scale that had sufficient points in the hydrogen ionisation zone led to the modifications described above. The abundances used are *evolved* abundances (described in Chapter 2) for C, Si, Al, N and O; other elements are assumed to have solar values. MULTI must be combined with an opacity package so that the background opacities can be calculated. The background opacities adopted in the present calculations are those supplied with MULTI.

The atmospheric model is compiled initially from the boundary conditions described in subsections 5-1-1, 5-1-2, 5-1-3 and 5-1-4. The model is extended downwards to the photosphere, just below the temperature minimum region (see below), and also upwards into the transition region. This enables the final model to be compared to the emission measure distribution described in Chapter 4. The initial model chromosphere was interpolated linearly (in Log(m_{col}) against temperature) between the lower transition region and the temperature minimum. This is shown in Figure 5-3. It was found that this initial model gave fluxes in lines of Si II, Al II and Mg II h & k which were much greater than observed. The atmospheric model was then adjusted to reduce the amount of material present in any given temperature range. It was found that the amount of material present in the initial model of the lower transition region overestimated the flux in Si II λ1816,1818 and λ1808. The pressure at the top of selected chromospheric models was reduced so that the calculated fluxes and the observed fluxes became consistent. Reducing the amount of material in the lower transition region gives emission measures which are consistent with those described in Chapter 4.

To close the set of equations needed to solve the non-LTE radiative transfer problem, the incoming and outgoing intensity at the top and bottom of the atmosphere, respectively, need to be specified. In MULTI these boundary conditions are derived from second order Taylor expansions (Carlsson, 1986). For details see Mihalas (1978).

The initial model produces continuum levels which are greater than those observed. This effect becomes important above $\lambda 1520$ (the bound–free edge of Si I) where there is no dominant source of opacity to compete with the bound–bound line blanketing. The continuum in this wavelength region is dominated by the blackbody radiation field. It has been found that in solar photospheric models the continuum fluxes are also calculated to be greater than observed, which implies that some source of line blanketing is really present (Matsushima, 1968). This high level of the calculated continuum is expected because no attempt has been made to include this line-blanketing in the computer models of the upper photosphere. The effect of increasing the opacity in the photosphere would be to force the formation of the continuum further out towards the temperature minimum region where the temperature is lower. Including additional opacity in the ultraviolet would then lower the continuum intensity. To circumvent the absence of line blanketing in the model, the photospheric structure (which is a boundary condition) is adjusted so that the temperature is reduced at a given mass column density. This ensures that the blackbody radiation field (calculated within MULTI) incident on the bottom of the chromospheric model is reduced. In the hydrogen atomic model, where the photoionisation from the $n = 2$ level by the Balmer continua is the dominant ionisation path, the photoionisation radiation field is represented by a single radiation temper-

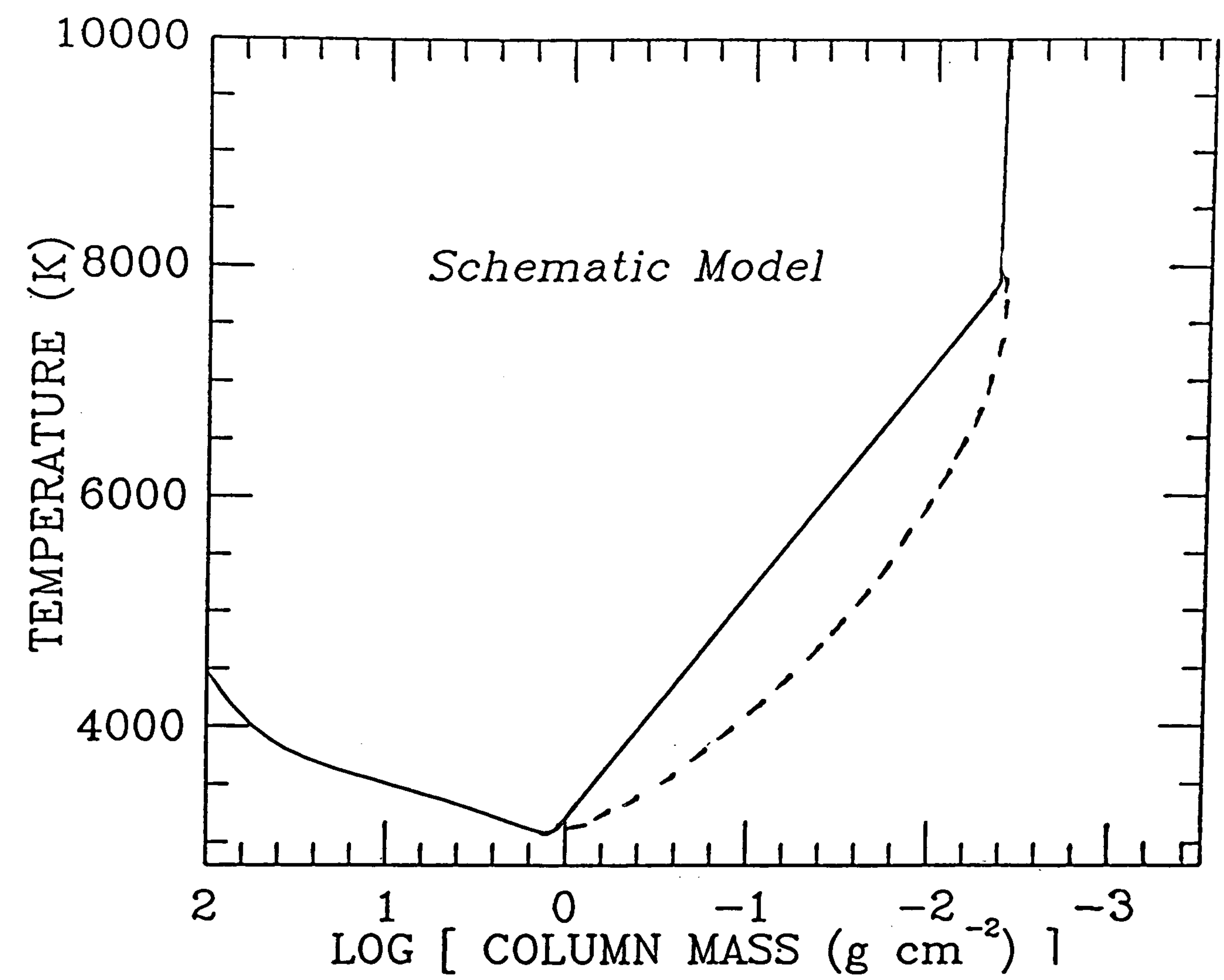

Figure 5-3 Schematic diagram showing the initial chromospheric model. The model shown by the dotted curve would produce lower calculated fluxes than the initial model.

ature, which further ensures that the effects of missing opacity do not over-estimate the photoionisation rate (for example see Ayres and Linksy, 1975).

It is also found that if the model chromosphere was terminated at the temperature minimum, then atomic models with optically thick transitions at the temperature minimum did not always converge. The photospheric part of the model is treated as a variable and is, here, used to provide numerical stability for these transitions. Because these transitions are optically thick at the temperature minimum, the line source functions should couple closely to the Planckian source function. Hence above the temperature minimum the source function will be the same as if the photospheric part of the model was absent. Therefore, this technique should not add any source of error to the chromospheric lines fluxes. The present work is concerned with photons formed above the temperature minimum and with the structure of the chromosphere and above.

5-4-1 Hydrogen

The first atom to be solved using MULTI is hydrogen because it is possible to solve the equations of hydrostatic equilibrium and the hydrogen radiative transfer problem self-consistently. First, the hydrogen atomic model is iterated to convergence, then the hydrogen model and the equation of hydrostatic equilibrium are iterated together. In MULTI, the initial model with the new calculated hydrogen and electron densities is written to the file ATHSE.DAT. The electron densities are calculated from the LTE metal ionisation and from the hydrogen ionisation. The new model (ATHSE.DAT) is then used to calculate the fluxes from the other atomic models.

Normally all the transitions included in the atomic model (see Appendix C) were solved, but sometimes it was not possible to find a converged solution, so it is necessary to 'switch off' some of the transitions, *e.g.,* Ly-α and Ly-β. The effects of these changes on the electron density are discussed in Chapter 6. The Lyman continuum is calculated in detail while the Balmer and Paschen continua are treated with a radiation temperature. The radiation temperature option, ITRAD = 3, (see Appendix C) is adopted for the Balmer continuum to simulate the effects of the ***unknown*** opacity source in the ultraviolet (and hence not included in the background opacities). The effect of changing the Balmer radiation temperature is also discussed in Chapter 6. The radiation temperatures adopted here have been scaled from the values adopted by Basri *et al.* (1981). To investigate the effects of including extra levels to this restricted 4-level atomic model, a 9-level atomic model was used to recompute the electron densities. The results of the calculations and the effect on the other computed transitions are discussed in Chapter 6.

5-4-2 Aluminium

The aluminium model has twelve energy levels, six for Al I, five for Al II and a single level for Al III. Photoionisation from the Al I ion to the Al II ground state is fixed with radiation temperatures using the photospheric option ITRAD = 2. Photoionisation is explicitly included for all levels in Al II to the Al III ground level. The aluminium lines at $\lambda\lambda$2669, 1670 are, in principle, observable with the IUE satellite. Unfortunately, only an estimate of the λ2669 flux is available for ι Aur. However, it is found that the ratios of the aluminium flux to the C II] and the Si II fluxes are similar to the ratios observed in α TrA. The λ2669 line is formed in a similar region to the Mg II h & k lines, and combined they provide a useful constraint on the chromospheric structure. This is because the Al II] λ2669 is optically thin and the flux is proportional to $\int N_e N_H dh$, whereas the Mg II h & k lines are optically thick and are sensitive to both the emission measure and the temperature structure.

5-4-3 Magnesium

Two models for magnesium are adopted to calculate the h & k lines. The first model assumes *complete redistribution* (CRD) and is used where the source function of the line core is investigated. This approximation is used because it permits great saving in computer time. The validity of the CRD approximation in the core is reasonable because within $\sim$ 3 Doppler half-widths of line centre the photons are completely redistributed in frequency (Jeffries and White, 1960). Thomas (1957) showed that although the emission line profile j_ν decreases by four orders of magnitude from line centre to three-doppler half-widths from line centre, the ratio of $\phi(\nu)$ to the absorption line profile $\phi(\nu')$ changes by only a factor of four. To a good approximation the source function in the line core is frequency independent. The second model relaxes the assumption of CRD and employs the redistribution approximation, R_{II-A} (see below), which is valid for stationary media. To illustrate how the redistribution function is employed in the present calculations, consider the isotropic source function of a two-level atom,

$$S(\nu) = \frac{4\pi(1-\epsilon)}{\phi(\nu)} \int_0^\infty R(\nu', \nu) J(\nu') d\nu' + \epsilon B, \tag{5.23}$$

where the primed quantities are for the absorbed photons (in the atom frame), $\epsilon \simeq C_{ji}/(A_{ji} + C_{ji})$ (A_{ji} and C_{ji} are the corresponding radiative and collisional de-excitation rates, respectively). ϵ physically represents the probability of a photon being destroyed after being absorbed. $R(\nu', \nu)$ represents the probability density that a photon of frequency ν' is converted to a photon of frequency ν. (Note that if $\epsilon = 1$ then $S(\nu)$ is frequency independent and equal to the Planckian source function, *i.e.*, the condition of LTE.) If the incoming and outgoing photons are un-correlated, then equation (5.23) reduces to the equation for a frequency independent source function and $R(\nu', \nu) = \phi(\nu')\phi(\nu)$ (CRD). The scattering processes which occur in a two level system have been described by Hummer (1962). If the upper and lower levels are both sharp (that is, not radiatively or collisionally broadened) then the scattering must be coherent (R_I, Hummer's notation). (See Figure 5-4.) However, if the lower level is sharp, as in resonance lines, and the upper level is broad, coherent scattering can occur between the sharp lower level and upper sub-levels (R_{II}) or completely un-correlated scattering can occur (R_{III}). This latter case is caused by the excited electron being shuffled to another sublevel during a collision. To calculate the actual redistribution, it is necessary to find what fraction of photons scatter by each process. Following the work of Omont *et al.* (1972), the PRD formulation used in the present work is,

$$R(\nu', \nu) = \gamma R_{II-A}(\nu', \nu) + (1-\gamma) R_{III}, \tag{5.24}$$

where,

$$\gamma = \frac{\Gamma_{Rad} + \Gamma_{Inel}}{\Gamma_{Rad} + \Gamma_{Inel} + \Gamma_{el}}. \tag{5.25}$$

Γ_{Rad}, Γ_{Inel} and Γ_{el} are the broadening widths due to radiative decay, inelastic collisions (*i.e.*, collisional de-excitation) and elastic collisions (*i.e.*, Stark and Van

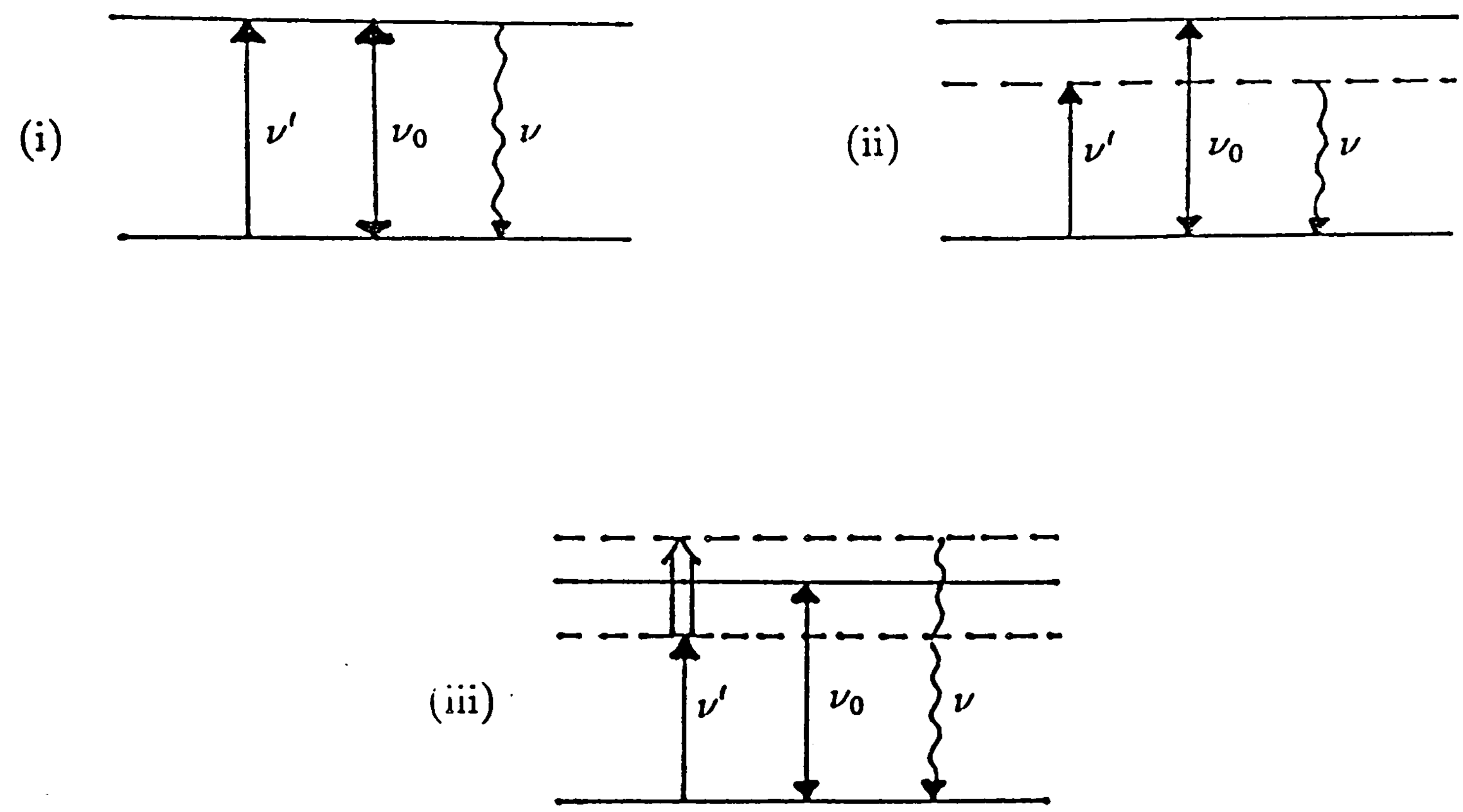

Figure 5-4 Schematic representation of the scattering of photons in a sublevel two level atom corresponding to cases R_I, R_{II} and R_{III} (Hummer's 1962 notation). ν_0 is the line centre frequency, ν and ν' are the atomic frame emission and absorption frequencies respectively. (i) The two-level atom has sharp upper and lower levels and corresponds to the case of purely coherent scattering between two sharp levels. (ii) Coherent scattering between the radiatively broadened upper level and sharp lower level. (iii) Completely non-correlated scattering (CRD) with collisions occurring during scattering. Base on Figure 1 of Heinzel (1985).

der Waals collisions) respectively. γ is the probability that the photon is scattered coherently. The angle averaged R_{II} is adopted for ease of computation and the redistribution is also assumed to be valid in the observers frame (Cooper *et al.*, 1982).

The computing time required to calculate the angle-averaged redistribution function is large. Thus these calculations were only performed to calculate the line profiles and the total fluxes of the lines. The atomic models have seven energy levels and the bound-free transitions are treated with a fixed radiation temperature. The radiation temperatures are used with the photospheric radiation option ITRAD = 2. Collisional terms have been included between all levels.

5-4-4 Silicon

The silicon model atom has eight Si I, eight Si II and one Si III levels. The bound-free transitions are treated by radiation temperatures, using the photospheric option ITRAD = 2, except the transition from level 1 to 9 (see Appendix C), which is treated with photoionisation cross-sections. Collisional excitation and ionisation terms are included between all levels. Charge transfer effects have also been included. The transitions calculated from the Si model are $\lambda 1817.5$, $\lambda 1817.0$, $\lambda 1808.1$, $\lambda 2334.7$, $\lambda 2344.3$, $\lambda 2328.6$, $\lambda 2350.2$, $\lambda 2334.5$ and $\lambda 2506.4$.

5-4-5 Iron

The iron model has been used to investigate the effects of the excitation from the fluorescence by the Mg II k line. Gahm (1974) included the fluorescence of the $y^5G_3^o$ level of the Fe I uv44 multiplet by the Mg II k line in a list of fluorescent lines excited by strong lines. (See Figure 5-5, which shows a Grotrian diagram for this process.) The emission lines from $y^5G_3^o$ were observed, prior to the IUE satellite, with the BUSS spectrograph (van der Hucht *et al.*, 1979). In previous work, the fluorescence of the Fe I $\lambda 4063$ and $\lambda 4132$ lines by Ca II and Hϵ emission has been used to infer the velocity fields and the structure of T Tauri stars (Wilson, 1974). Also, the fluorescence of Fe I $\lambda 4202$ and $\lambda 4308$ by Mg II k has been used to probe the structure of long period variable stars (Wilson, 1971).

However, no explicit calculations have been made previously for the fluorescence of the $J = 3$ level in the Fe I uv44 multiplet by Mg II k radiation. The pumping of the $J = 3$ level is due to the coincidence of the wavelength of Fe I uv44 $\lambda 2795.54$ ($y^5G_3^o - a^5F_4$) transition with the Mg II k line at $\lambda 2795.52$. The other permitted transitions from the $J = 3$ level, *i.e.*, $\lambda 2843.98$ ($y^5G_3^o - a^5F_3$) and $\lambda 2823.28$ ($y^5G_3^o - a^5F_2$) are observed in emission. The $\lambda 2823.98$ line is observed, but

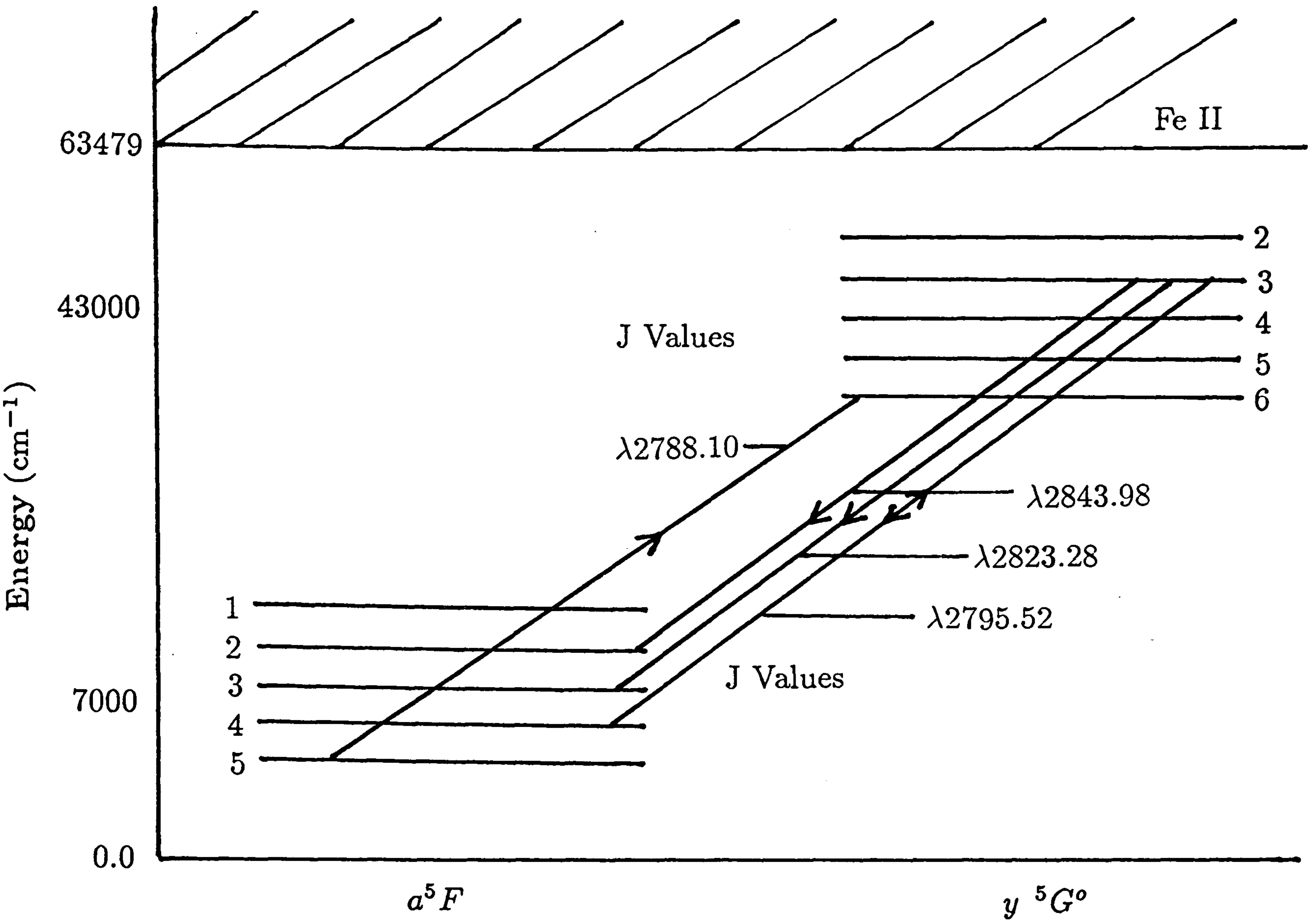

Figure 5-5 Grotrian Diagram for the Fe I uv44 y^5G^o to a^5F multiplet. Some of the observed transitions are shown.

is over-exposed and the λ2843.98 line is observed in emission with a surface flux of 4.1×10^3 erg cm^{-2}s^{-1} (see Table 3-7). Only the $^5G^o_3$ level is excited by fluorescence because the Fe I uv44 λ2788.10 line ($y^5G^o_6 - a^5F_5$) and other transitions from this multiplet are observed to be in *absorption* (see Table 3-2 and Figure 5-5).

The calculations made in Chapter 6 examine the dependence of the fluorescence on the Mg II k line source function and determine the conditions under which the profiles and fluxes of the two lines can be used as a chromospheric velocity and structural diagnostic. The model atom has eight levels. The levels 2-6 represent the fine structure of the lower level of the pumped transition. Collisional coupling is included between all levels, and photoionisation from all levels to level 8 is included.

In the computations of the Fe I transitions it is found that the continuous opacity dominates the Fe I uv44 $\lambda\lambda$2823, 2844 transitions, and the lambda iterations used to solve the scattering term of the background source function can lead to very slow convergence or even divergence of this term. Thus caution should be exercised when interpreting the computer results. In trial calculations it was found that *it is possible to obtain a converged solution for the population number densities, while the scattering part of the background source function had not converged.* The results in Chapter 6 are all free from this potential source of error.

5-5 Summary

The initial model chromosphere has been described and the boundary conditions adopted for the present work have been derived. A value for the temperature minimum has been found by scaling the temperature minimum calculated in CRD and then comparing the results with flux-constant blanketed model photospheres. The adopted value is $0.5 > Log(M_{col}) > 0.0$ for $3150 > T_e(\mathrm{K}) > 3000$. The programme MULTI is described here and in Appendix B and recent modifications to this programme have also been described. The atomic models which are used to calculated line fluxes have been briefly described, and are given in more detail in Appendix C.

CHAPTER 6. MODEL CHROMOSPHERES - RESULTS

The aim of the radiative transfer calculations is to obtain an optimum self-consistent model of the chromosphere. These calculations give the first model chromospheres for the 'hybrid' bright giant stars. The line fluxes for the transitions discussed in Chapter 5 (see Table 6-2 and Table 6-3) were calculated for the initial chromospheric model. The results of the calculations were then compared with the observations, the model was adjusted in an appropriate manner and the computations were then repeated. Five example models are discussed in detail below and these demonstrate the sensitivity of the Mg II resonance line profiles and the line fluxes to changes in the atmospheric structure.

When analysing the computed fluxes and profiles, care was taken to check the computed results for self-consistency – the computer was not regarded as a *black-box.* During the development of the final computer models, many results generated proved to be unphysical, given the independent constraints on quantities such as line optical depths.

The models discussed here produce a range of fluxes for a given transition, and some of these are consistent with the observed fluxes and are chosen (1) to illustrate the consequences of changes in the chromospheric structure on the calculated line fluxes and (2) to reproduce some of the features of the Mg II h and k line profile which are believed to be unaffected by scattering in out-flowing material (see Section 6-2-2). There must be some latitude in the selection criteria because of the uncertainties in the element abundances, atomic data and the possibility that all line fluxes cannot be reproduced with a one component model. The process of *trial and error* can lead to model chromospheres that can produce most *but not all* of the required features. There is a balance between trying to match the computed models with the observations and the stage where no more physical insight is gained from further computations with a particular model.

6-1 Hydrogen and the Initial Models

The five chromospheric structures shown in Figure 6-1 are used to produce the chromospheric models discussed in this section. The model chromospheres are specified by the run of mass column density with temperature *and* the electron density at each point in the atmosphere. Thus each chromospheric *structure* can be used to calculate several different ranges of electron densities (with different hydrogen atomic models) and hence give several different chromospheric *models*. Five of the seven model chromospheres 1(i), 2(i), 3, 4 and 5 are tabulated in detail in Appendix D. Models 1(i) and 1(ii) have the same chromospheric structure (*i. e.,* have the same run of mass column density with temperature) and the difference between the models is that they are solved with different hydrogen atomic models and hence have different electron densities. This also applies to Models 2(i) and 2(ii). The model of the hydrogen atom used to compute chromospheric Models 1(i), 2(i) and 3 included all the transitions described in Appendix C. Models 1(ii), 4 and 5 were calculated with the Ly-α and Ly-β lines omitted from the atomic model. Model 2(i) and 2(ii) were calculated with different radiation temperatures (see Section 6-1-1). The different hydrogen models adopted for the chromospheric models are shown in Table 6-1. These hydrogen atomic models have 4 levels. Model 2(i) was recalculated with a 9-level hydrogen atomic model to investigate the effects of including extra levels in the atomic model on the calculated electron densities.

Figure 6-1 shows the chromospheric structure of five models which satisfy (for the most part) the initial selection criteria and which are discussed below. Models 1(i)(ii), 2(i)(ii) and 3 have a similar structure in the upper chromosphere but different structure in the temperature minimum region. Models 1(i)(ii) and Model

Table 6-1 The 4-level hydrogen atomic models solved with the chromospheric models. The first column is the chromospheric model, the second column shows which hydrogen lines are included in the hydrogen atomic model solution for that model atmosphere and the third and fourth columns show the adopted radiation temperatures.

Model	Hydrogen Lines	Balmer Radiation Temperature (K)	Paschen Radiation Temperature (K)
1(i)	Ly-α, Ly-β and H-α	3700	3500
1(ii)	H-α	3700	3500
2(i)	Ly-α, Ly-β and H-α	3700	3500
2(ii)	Ly-α, Ly-β and H-α	3200	3000
3	Ly-α, Ly-β and H-α	3700	3200
4	H-α	3700	3200
5	H-α	3700	3200

3 have their temperature minimum located at the same point in the atmosphere *i. e.*, T_{Min} = 3060 K and $Log(mcol) = -0.25$ while Models 2(i)(ii) have a temperature minimum at T_{Min} = 3160 and is located deeper in the atmosphere at $Log(mcol) = +0.25$. At a depth of $Log(mcol) = -1.0$, Models 1(i)(ii), 2(i)(ii) and 3 have quite different temperatures (4000 K, 3500 K and 4400 K, respectively). These models serve to illustrate the sensitivity of the atomic model calculations to the lower chromospheric structure.

Models 4 and 5 have the transition region at a lower pressure than Models 1(i)(ii), 2(i)(ii) and 3. At the base of the transition region, *e.g.*, 8000 K the ratio of the total gas pressures for Model 2 : Model 4 : Model 5 is approximately 4 : 3 : 2. These models illustrate the effects of changing the structure of the upper chromosphere.

An illustration of how the temperature changes with pressure in different re-

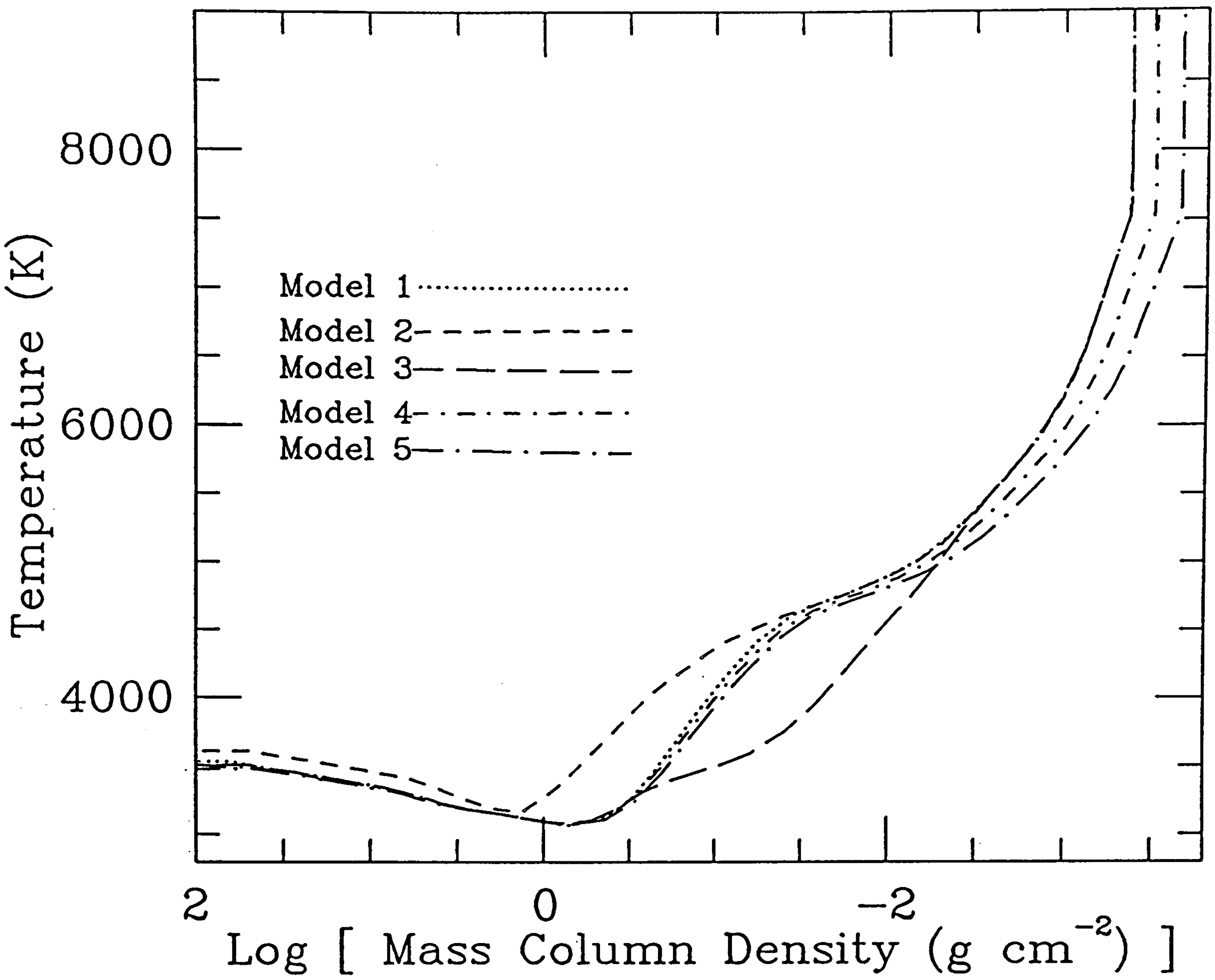

Figure 6-1 Temperature against logarithm of mass column density for Models 1(i)(ii), 2(i)(ii), 3, 4 and 5. These models will serve to illustrate the sensitivity of the model calculations to the upper and lower chromospheric structure. The models are tabulated in Appendix D.

gions of the chromosphere can be seen from the following example; In Model 4 in the lower chromosphere, the pressure increases by a factor of 20 from 4000 K to 5000 K, while at the base of the transition region the pressure increases by only a factor of 1.4 from 7000 K to 8000 K.

6-1-1 The Electron Densities

Figure 6-2 shows the electron densities for Models 1(i), 2(i)(ii) and 3. Model 2 has been calculated with two sets of radiation temperatures (i), (ii). Models 1(i), 2(i) and 3 were calculated with the same radiation temperatures (shown in the atomic model file in Appendix C (*i.e.*, a Balmer continuum radiation field TRAD = 3700 K and a Paschen continuum radiation field TRAD = 3500 K, using the chromospheric option ITRAD = 3). Model 2(ii) is chosen to show how the electron densities depend on the radiation temperatures adopted in the hydrogen atomic model. Model 2 (ii) was calculated with the same input parameters except that the radiation temperatures were arbitrarily reduced by 500 K. The direct comparison of Models 2(i) and 2(ii) show that reducing the Balmer radiation temperature by 500 K decreases the electron density by a maximum of 44% between $-3.38 < Log(mcol) < -2.1$. A more realistic error in the scaling of the radiation temperature (see Section 5-4-1) is 100 K then the error in the resulting electron density will be only 10%.

Figure 6-2 shows that the electron density initially decreases from the photosphere to the temperature minimum, where it rises and then decreases again. Note that Models 1(i) and 2(i)(ii) have different structure in the temperature minimum region. Where the gas density decreases and the hydrogen is predominantly un-ionised, the electron density is due to the ionisation of the metals. Where the temperature rises, the ionisation fraction of hydrogen increases more quickly than the total gas density decreases, and the electron density increases. When the gas density decreases more rapidly than the increase in the hydrogen ionisation fraction, the electron density decreases once more. The values for the electron density at the *top* of the chromospheric models are uncertain because the depth scale grid for the hydrogen solution does not contain many points above the hydrogen ionisation zone. The fluctuation in the electron density at the top of the chromospheres for Models 4 and 5, shown in Figure 6-3, is due to the coarse correction made to the population densities by the hydrostatic equilibrium calculations.

Model 1(i) shows a second shallow rise in electron density at $Log(mcol) = -1$. This rise corresponds to the change in the Balmer radiation temperature introduced at this point in MULTI. The effect is not as noticeable in Models 2 (i) and (ii).

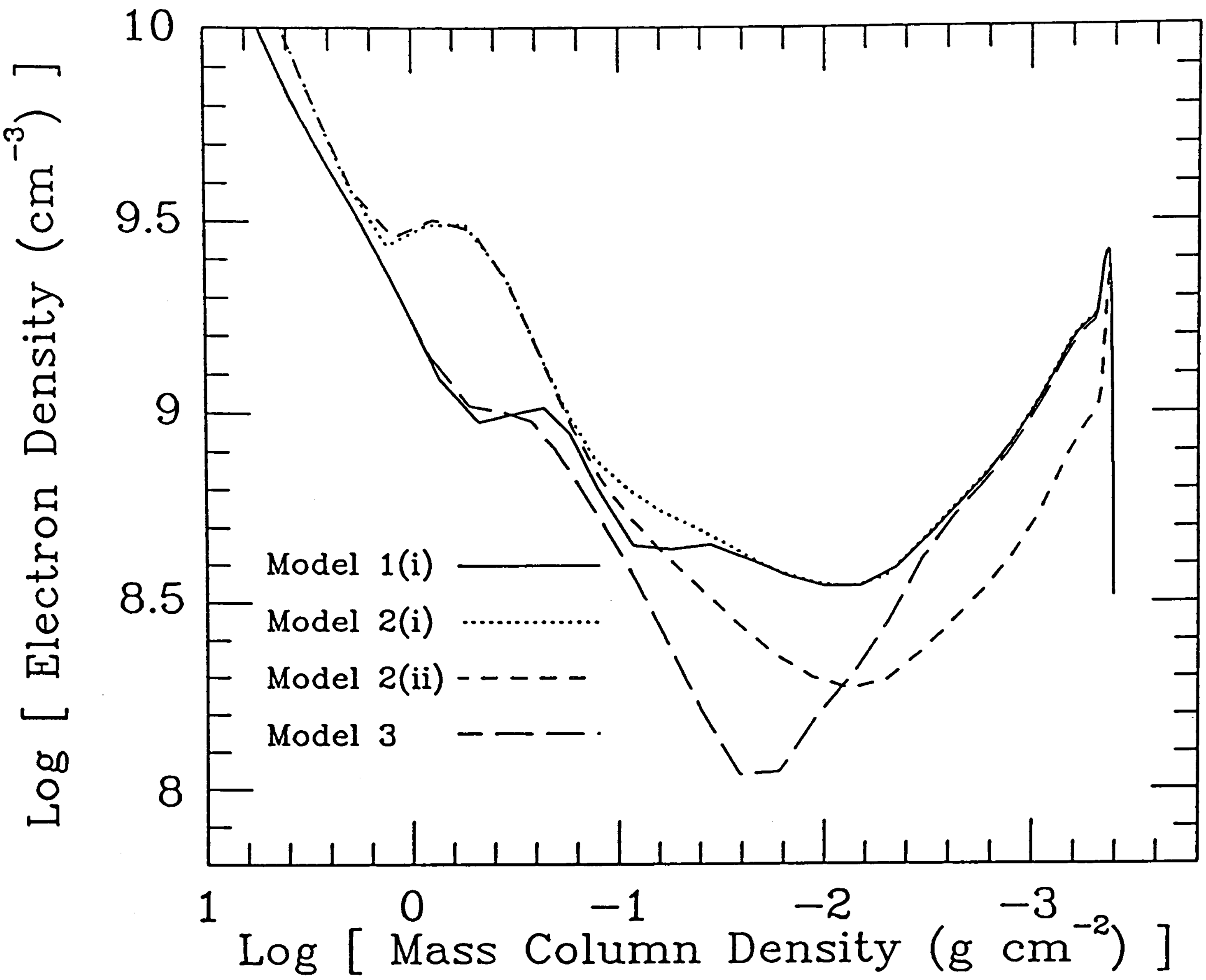

Figure 6-2 The electron densities calculated from Models 1(i), 2(i), 2(ii) and 3. Models 1(i), 2(i) and 3 are consistent with the electron density determined from the C II] line ratios described in Chapter 4.

The ionisation of hydrogen is dominated by photoionisation from the collisionally populated $n = 2$ level. This explains why Model 2(ii) has lower electron densities then the other two models. The reduction in the Balmer continuum radiation temperature results in a lower photoionisation rate. The similarity between the electron densities in Models 1(i), 2(i) and 3 above 5000 K implies that the electron density where C II] is formed will be insensitive to the structure in the region of the temperature minimum, but will be sensitive to the Balmer continuum radiation temperature. Approximate calculations show that the C II] lines are formed between $5000\,\mathrm{K} < T_e < 10000\,\mathrm{K}$, with most of the flux originating at ~ 8000 K. The electron density estimate derived in Chapter 4 was 5×10^8 cm^{-3} $< N_e <$ 2×10^9 cm^{-3}.

This range of conditions is satisfied by both Model 1 and Model 2(i), which have a range of electron densities of $Log(N_e) = 8.55$ at 5000 K to $Log(N_e) = 9.3$ at 10^4 K, with $Log(N_e) \sim 9.4$ at 8000 K. The electron density in Model 2(ii) at 5000 K is $Log(N_e) = 8.3$ and remains about 0.25 dex below the values in Model 2(i) until the transition region where hydrogen becomes fully ionised. Models 1(i), 2(i) and 3 are discussed further below.

Figure 6-3 shows the electron densities in Models 1(i)(ii), 4 and 5. Model 1 has been calculated with two sets of transitions included in the hydrogen atomic model (see Table 6-1). Model 1(i) is shown in Figure 6-1 and includes H-α, Ly-α and Ly-β, whereas Model 1(ii) has been calculated without the Ly-α and Ly-β transitions. It was found that the convergence (see Section 5-2) of the hydrogen solutions depends critically on the depth scale adopted when running MULTI. It was not possible to find a converged solution with all the hydrogen transitions included in Models 4 and 5, which have lower transition region pressures than Models 1(i)(ii), 2(i)(ii) and 3.

The electron densities for Models 4 and 5, shown in Figure 6-3, are lower than in Model 1(i) because these models have lower total gas pressures at a given temperature. It is hard to give a precise mean electron density in the C II] line forming region without explicitly calculating a full carbon model atom, but Models 4 and 5 which have electron densities at 8000 K of $Log(N_e) = 9.3 and 9.1$ respectively, and appear to be consistent with the observed electron density.

Models 1(i) and (ii) have similar electron densities in the upper chromosphere, but for $Log(mcol) \geq -1.4$ the electron densities differ by about 25%, with Model 1(ii) having the larger electron density. The Ly-α and Ly-β lines are both optically thick in this region and the H-α line becomes optically thin at $T_e \sim 7500$ K. The removal of the Ly-α transition from the hydrogen model does not significantly affect the calculated electron densities because the Ly-α line formation is dominated by

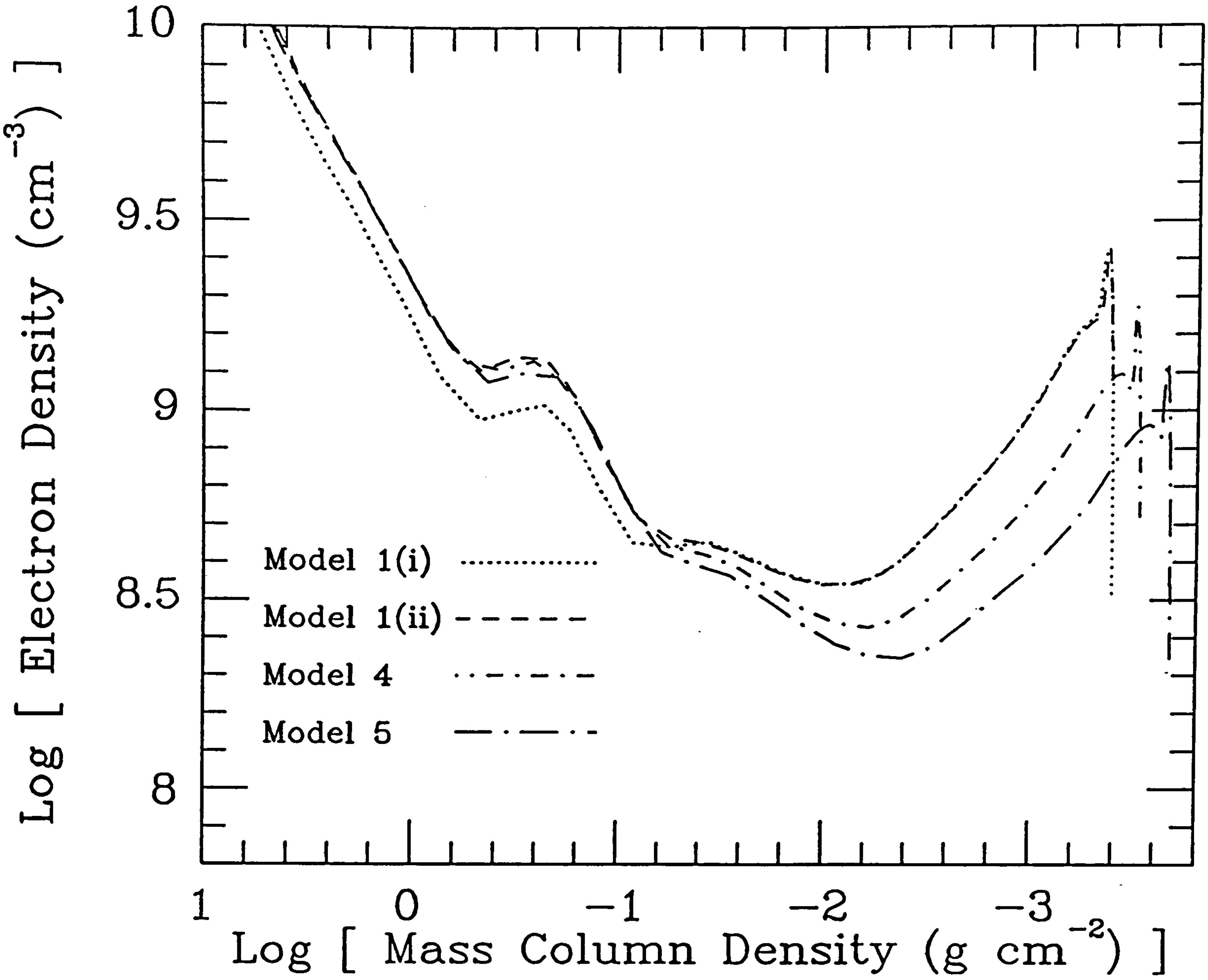

Figure 6-3 The electron densities calculated in Models 1(i), 1(ii), 4 and 5. In Model 1(i) the hydrogen model atom has been solved for all the transitions shown in Appendix C. Models 1(ii), 4 and 5 have been solved for the same hydrogen model except the Lyman lines have been omitted.

resonance scattering (Heinzel and Hubeny, 1985). The H-α (Balmer-α) and the Ly-β are interlocked because they share a common upper level, so the depopulation of level n=3 in the atomic model is affected by the removal of the Ly-β transition. The n=3 level is then depopulated by emission in H-α which tends to increase the population of the n=2 level. The ionisation path is via the photoionisation of the n=2 level, so the removal of the Ly-α line increases the photoionisation rate. Compared with the full hydrogen model, the adoption of a hydrogen atomic model with the two transitions removed leads to a small increase in the electron density in the lower chromosphere above $Log(mcol) = -1.2$. The electron densities for Models 4 and 5 were calculated with exclusion of the Lyman transitions and from a comparison of Models 1(i) and 1(ii), the electron densities are found to be not significantly different above $Log(mcol) = -1.2$.

The electron densities calculated for Model 2(i) with the 9-level hydrogen atomic model were found to be lower than those for the 4-level hydrogen model, shown in Figure 6-2, by 0.08 dex in the logarithm of the electron density between $-1.0 > Log(mcol) > -3.38$. This is a result of the reduced ionisation of hydrogen in this range of mass column density. The presence of the extra levels to some extent reduces the population number densities in lower levels. Because the collisionally excited $n = 2$ level is photoionised to produce free electrons, this will lead to a reduction in the ionisation rate. However, because the densities are not sufficiently high to cause significant additional population of the higher atomic levels, this process is relatively unimportant compared to the change in the total recombination rate. Another important process which directly affects the ionisation fraction is the recombination rate. Vernazza *et al.* (1981) show that the radiative recombination coefficient increases with the number of levels in the hydrogen atomic models. The increase in recombination in the 9-level atomic model is counteracted by the photoionisation out of these levels so that the electron density is reduced by a factor less than the factor by which the radiative recombination coefficient is underestimated. The difference by which the 9-level atomic model underestimates the total radiative recombination rate is shown by Vernazza *et al.* (1981) using data in Osterbrock (1974), and at 8×10^3 K, is $\sim 5\%$. So the maximum overestimation in the electron density by using the 4-level atomic model is 25%. The effect of the uncertainties in the electron density on the other atomic model calculations is discussed in the individual sub-sections. In the following sections Models 1(i), 2(i), 3, 4, and 5 are considered and the suffix (i) is dropped.

6-2 The Magnesium II h & k Lines

The calculations concerning the Mg II h & k lines are divided into the following Sections: in Section 6-2-1, a comparison is made between the Mg II h & k line profiles calculated in CRD and PRD; in Section 6-2-2, schematic calculations are made to investigate to effects of bulk mass motions on the line core source function of the Mg II h line; in Section 6-2-3, the effects of microturbulence on the line profiles are investigated and in Section 6-2-4, the calculated ratios of the h & k lines are compared with the observations.

6-2-1 PRD versus CRD

The difference between line profiles calculated with CRD and PRD is expected to be greater in low gravity stars than in the Sun. This is because the lower particle densities in the photon scattering region lead to the photons having a greater chance of scattering coherently, and less chance of the excited electrons having their energies reshuffled by collisions. Figure 6-4 illustrates the differences between the Mg II h line profiles calculated in CRD and PRD using Model 1 and Model 2. Figure 6-5 and Figure 6-6 show the profiles calculated with PRD together with the observed Mg II h & k line profiles. (The observed line profiles are a product of merging LWP5199 and LWP4014 weighted with their respective exposure times.) The difference between the CRD and PRD calculations is significant in all the models and the use of CRD would not give realistic results for the chromospheres of the bright giants. A similar result has been demonstrated for solar models (Athay, 1976). The line wings in the PRD calculations are less strong than in the CRD calculations, while the h_{2V} and h_{2R} peaks are much greater in the PRD calculations. This is a direct result of the photons being 'trapped' in the line core as a result of the energies of the excited electrons being less reshuffled than in the CRD case, and hence fewer photons are emitted in the line wings. As there are fewer photons in the line wings for PRD, the source function for the wings decouples from the Planck source function at higher pressures and hence the wings are formed at a lower temperature. Consequently the line centre source function thermalises at a higher temperature, because there are more photons in the line core.

The effects of the different model atmospheric structures on the Mg II line profiles can be seen in Figure 6-5 and Figure 6-6. It is useful to consider the line profile of an optically thick line as a mapping of the magnitude of the source function S_ν at an optical depth of $\tau_\nu \sim 1$, onto the intensity of the observed line profile at frequency ν. The intensity of the h_{2R} and h_{2V} peaks thus represents the magnitude of the source function at an optical depth of unity at the frequency of these features. Optical depth unity at line centre (h_3), occurs at ~ 10500 K and the optical depth of unity for the radiation at the frequencies of the h_{1V} and k_{1R} features occurs near the temperature minimum. The intensity of the h_{2R} and k_{2V} peaks decreases from Model 2 to Model 1 to Model 3. As the peaks occur at approximately the same frequency for all the models and the column mass at which optical depth unity occurs is also similar, the difference in intensity of the peaks reflects the difference in the magnitude of the source function at these wavelengths. The strength of this source function, S_ν, depends on how strongly S_ν is coupled to the Planckian source function, B_ν. The temperature rise in Model 2 occurs at a greater column mass than either Model 1 or 3. The larger particle density ensures that S_ν is more closely coupled to B_ν, so that the magnitude of S_ν is larger. Similarly the temperature rise in Model 3 occurs at lower pressures than Model 2 and hence has less enhanced h_{2R} and k_{2V} peaks.

The Model 2 Mg II h & k line profiles at $> 100\,\mathrm{km\,s^{-1}}$ from line centre have greater intensity than observed. This part of the line profile is formed in the region

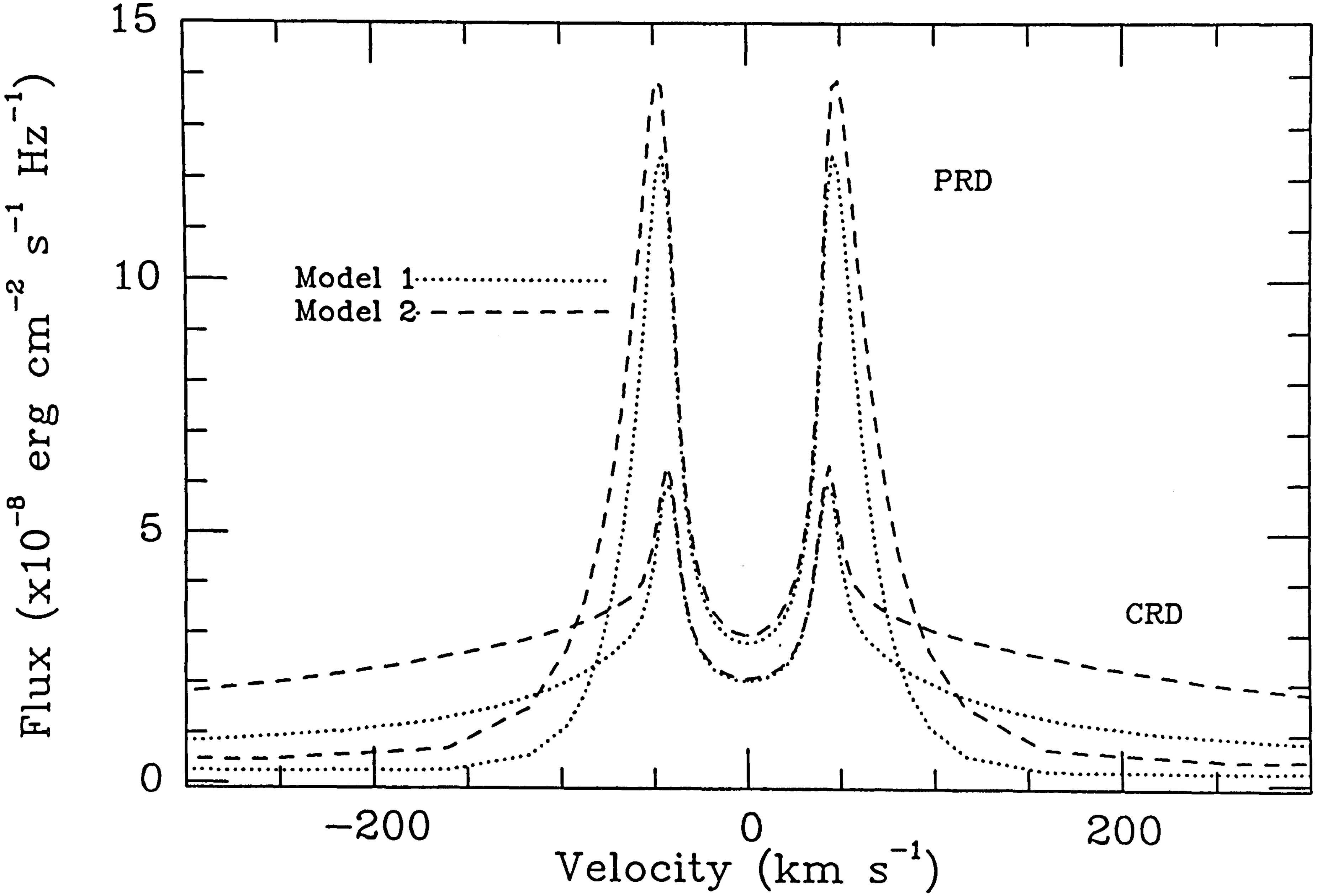

Figure 6-4 The calculated Mg II h line profiles, computed with complete redistribution (CRD) and partial redistribution (PRD), for Model 1 and Model 2.

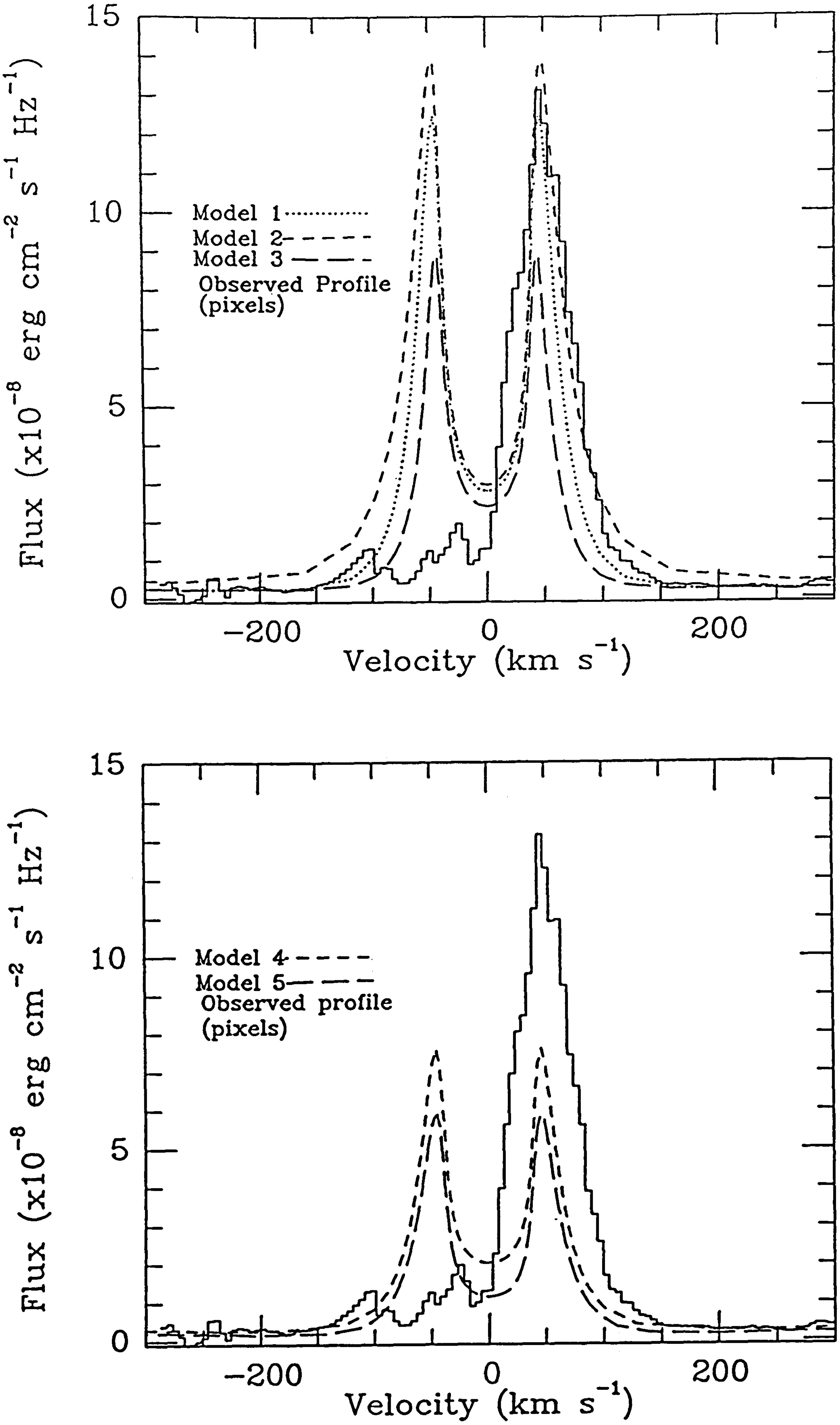

Figure 6-5 The Mg II h line profiles for Models 1–5, computed in PRD, shown with the observed line profile. Models 1, 2 and 3 are shown in the top diagram and Models 4 and 5 are shown in the bottom diagram.

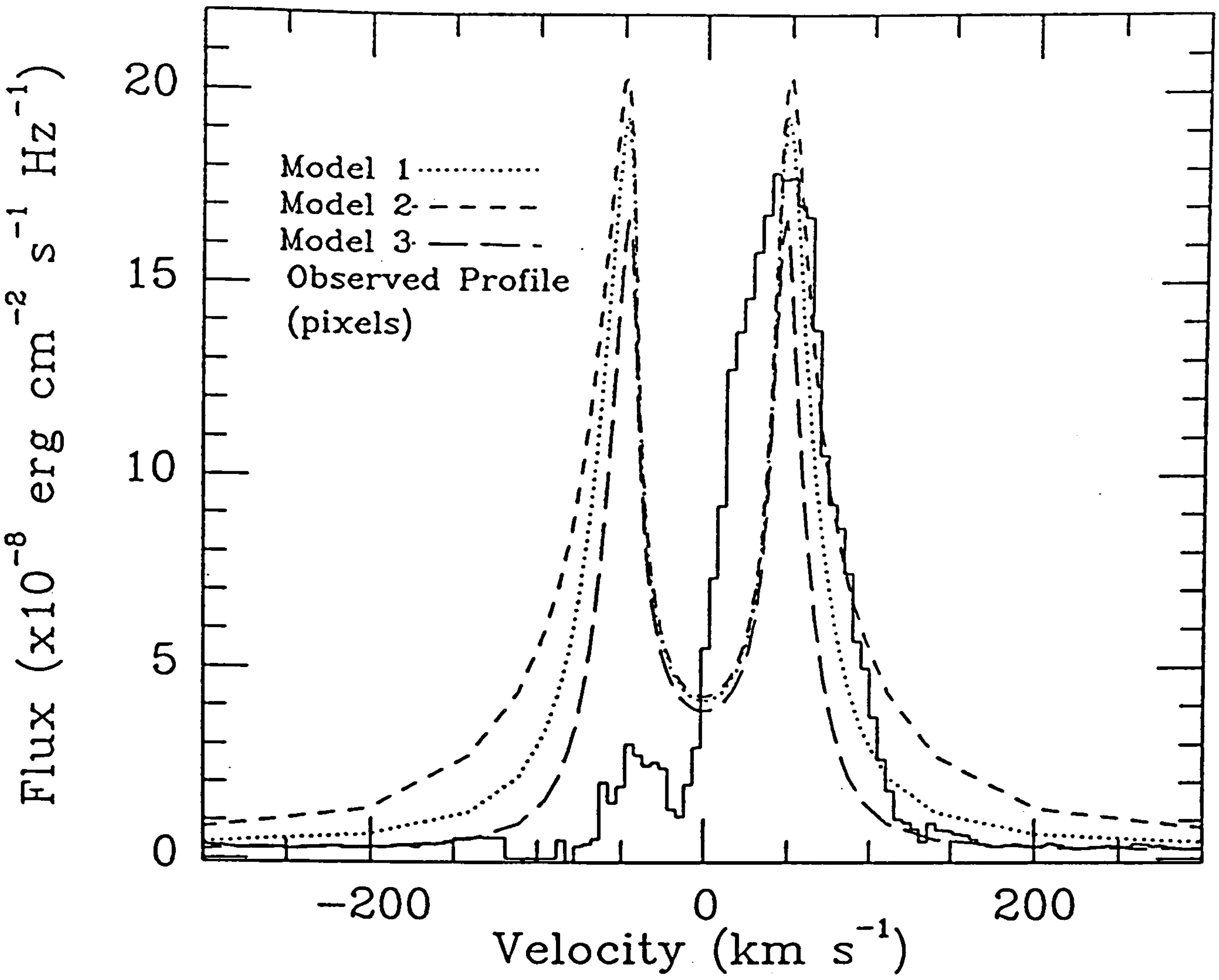

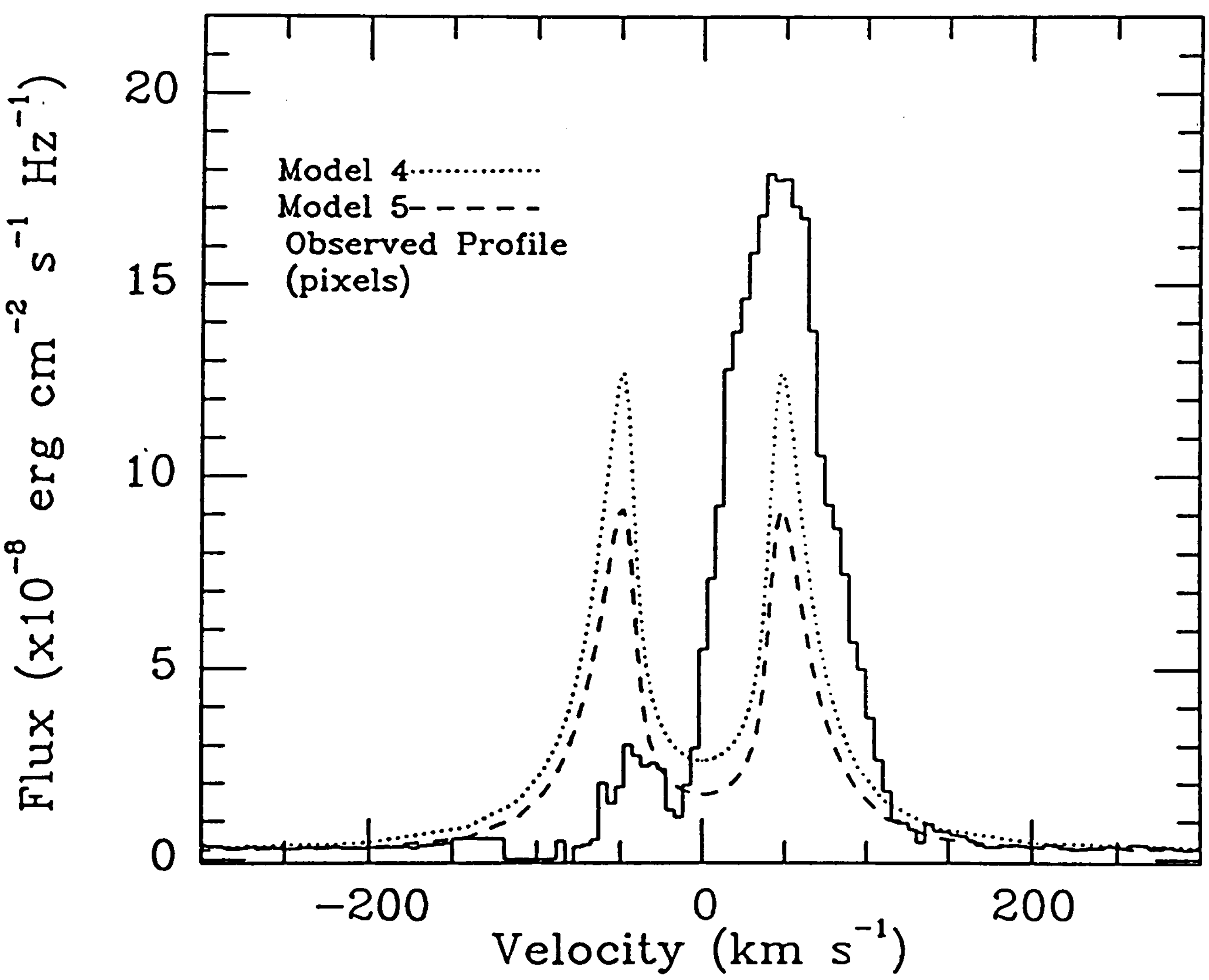

Figure 6-6 The Mg II k line profiles for Models 1–5, computed in PRD. The observed profile is also shown. Models 1, 2 and 3 are shown in the top diagram and Models 3 and 4 are shown in the bottom diagram.

where the initial chromospheric rise occurs (see Figure 6-1). This suggests that the gradiant $dT_e/dLog(mcol)$ is less than that adopted for Model 2.

Figure 6-7 shows how, in a solar model, the source function at different frequencies decouples from the chromospheric temperature rise. The source function for the far wings decouples from B_ν even below the temperature minimum, and this is reflected in the relative insensitivity of the intensity in the far wings to the different structures. This was found to be the case in the five models studied in detail. The way in which the observed line profile is related to the magnitude of source function S_ν was used to guide the iteration of the model chromospheres in the line forming region.

The Mg II h line flux was also calculated using Model 2 (Model 2(i)) with the electron densities from the 9-level hydrogen atomic model. Because the two Mg II h line fluxes are calculated using the same chromospheric structure, but different electron densities, the optical depth scale will be the same, so that the calculated differences in profile will be due to the difference in the line source function. The intensity at line centre is found to be unaltered within the errors due to depth scale interpolation. However, the h_{2R} peak is depressed by 4% relative to the profile in Figure 6-5. This shows that the h_{2R} feature is produced between $-1.00 > Log(mcol) > -3.384$ (where the electron density is reduced compared to 4-level calculations).

6-2-2 The Effects of Bulk Mass Motions

In a hydrostatic, plane parallel model atmosphere, it is not possible to produce asymmetric line profiles, because there is symmetry about line centre in the atomic processes which control the radiation transfer. To investigate the effects of bulk mass motions on the source function of the line core, the atomic model of magnesium (in

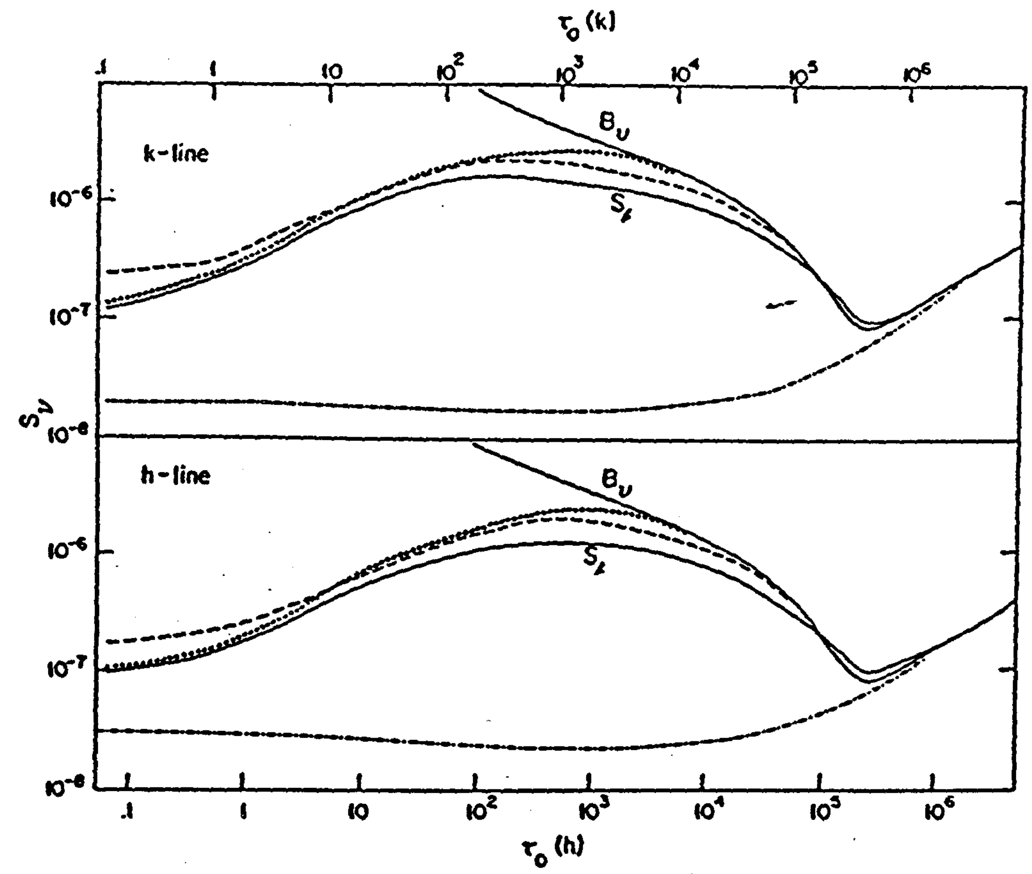

Figure 6-7 The source functions for the Mg h & k lines compared with the Planckian source function B_ν: S_l, complete redistribution; dots, line centre ($\Delta\lambda = 0$); dashes, k_{2R} ($\Delta\lambda = 0.12$Å), h_{2R} ($\Delta\lambda = 0.109$Å); dot-dashes, k_{1R} ($\Delta\lambda = 0.462$Å), h_{1R} ($\Delta\lambda = 0.365$Å). Based on the Harvard-Smithsonian Reference Atmosphere. From Milkey and Mihalas (1974).

CRD) was computed with Model 1. Several different macroscopic velocity fields were superimposed on the model atmosphere. This treatment is not self-consistent because the electron populations are calculated in hydrostatic equilibrium and the mass flux is not conserved. However, in the line forming region the macroscopic velocity field is small compared with the turbulent velocity field and of the order of the sound speed so the electron densities calculated from hydrostatic equilibrium should not be too different from the actual electron densities expected in such a wind. The following calculations are schematic and illustrate some important effects of radiative transfer which must be considered when interpreting the calculated line profiles. Ideally, one would solve the magnesium model with PRD to see what affect the velocity fields have on the line profiles, but unfortunately, the PRD formulation used in the current work is valid only for a zero macroscopic velocity field. Therefore, a second approach has been adopted. The magnesium CRD model is solved instead, noting that the source function in the *line core* should be similar for both the CRD and PRD models. Thus, the effects of the mass motions on the *line core* can still be investigated. Figure 6-8 shows the resulting magnesium h line profiles (top) calculated assuming complete redistribution, with the macroscopic velocity fields (bottom) superimposed on Model 1.

The models shown in Figure 6-8, will be referred to by the abbreviations given in that figure and are discussed below. The first model (W1, solid line) has no bulk mass motions and the line profile is symmetric about line centre. (Only the blue half is shown for clarity.) W2 has a small velocity gradient and the velocity at the top of the model is 7 km s^{-1}. (The velocity shifts observed in the optically thin transition region lines are below this value.) The change in line profile is small, with the blue h_{2V} peak being slightly depressed and the red wing being slightly higher. These effects are a consequence of the line opacity being Doppler shifted towards the blue wavelengths. W4 has a larger temperature gradient and the profile asymmetry is more pronounced.

The velocity field in W3 is chosen to schematically represent a flow pattern with upswelling and down flowing material, as suggested by Basri *et al.* (1981). To treat such a velocity field self-consistently would require a two component model to conserve mass flux. The effects of this velocity field on the line profile are quite significant. Although the absolute velocities in W3 are < 7 km s^{-1}, the line profile is similar to that of W4 (which has a larger velocity field). The reason for this can be understood in terms of the red-shifting of photons in the line wings and the blue-shifting of the overlying opacity. The greatest profile asymmetry occurs when the maximum opacity is Doppler shifted to the same wavelength as the h_{2V} emission peak. The photons in h_{2R} then experience less opacity than in the static

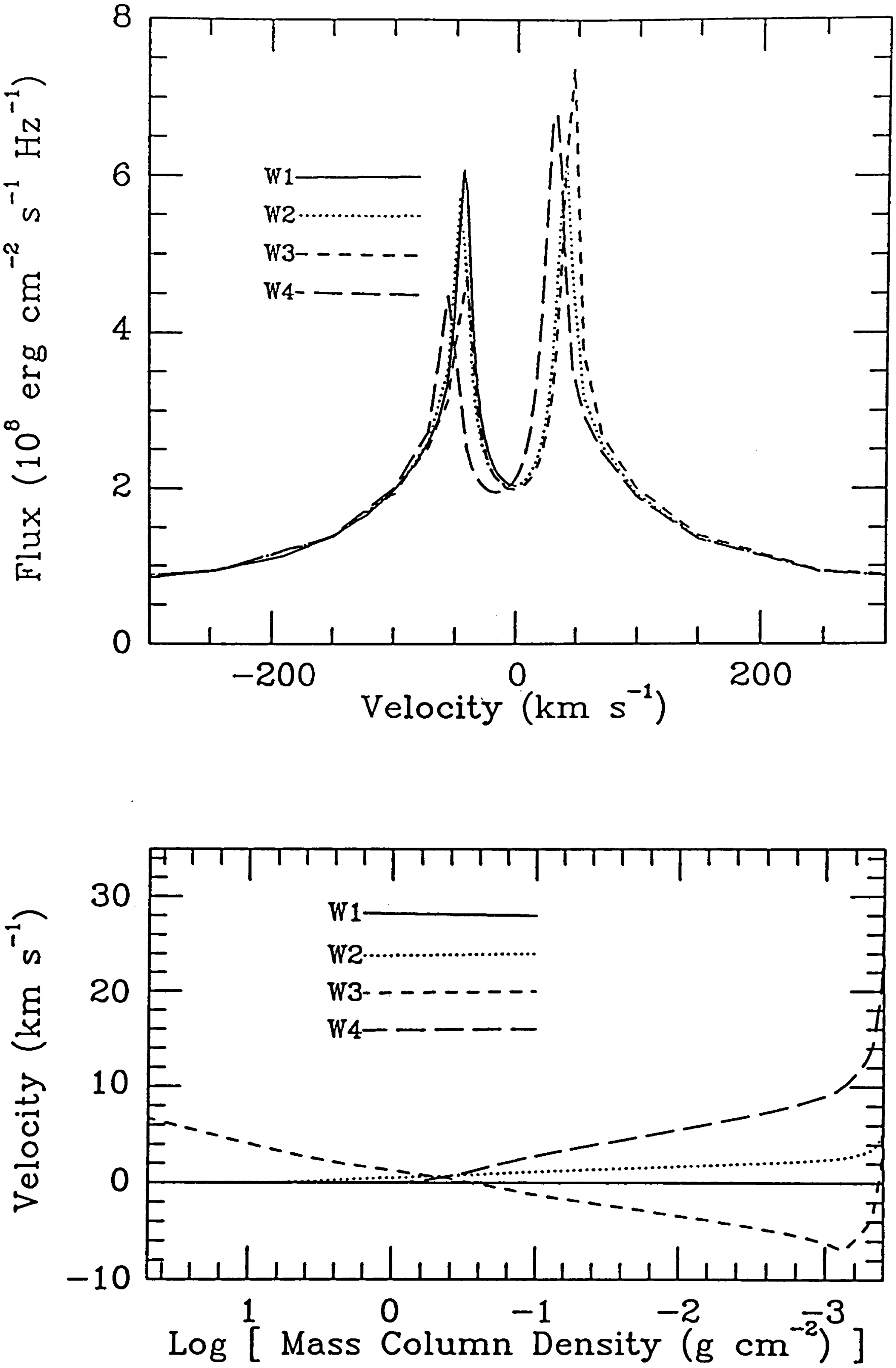

Figure 6-8 Magnesium h line profiles (top) resulting from CRD calculations with the macroscopic velocity fields (bottom) superimposed on Model 1. The line profiles are plotted as a function of the displacement from line centre in Doppler units km s^{-1}. Half of the line profile for W1 has been omitted for clarity. See text for discussion.

case (W1), and have a greater probability of escape. In W3 the velocity structure leads to photons formed just above the temperature minimum region being emitted from gas at rest in the photospheric frame. The photons emitted just above the temperature minimum are red-shifted, the violet wing photons being shifted towards line centre and the red wing photons shifted towards the h_{1R} feature. The velocity field changes are now such that in the region where the line centre photons are emitted the velocity shift is in the opposite sense (blue-shifted). The violet wing photons then experience an extra source of overlying opacity as the line centre opacity is blue-shifted. This reduces the intensity in the h_{2V} peak. Thus, the effects of red-shifting the photons in the line wings and blue-shifting the line opacity produce a distinct asymmetric profile.

There are two factors excluded from the calculations of the line profiles, which may also be present in the observed line profile. First, the effects of interstellar absorption have not been included (the absorption will occur at $\sim -18\mathrm{km\,s^{-1}}$) and, second, any effects of absorption and scattering in the circumstellar environment have been neglected. The estimate of interstellar absorption made in Chapter 3 show that this can account for the observed depression in the line profile at $v \sim -6\mathrm{km\,s^{-1}}$. The effects of any scattering in the circumstellar region are harder to quantify. Optical depth unity at the line centre occurs at $\sim 1.1 \times 10^4$ K for the chromospheric models presented here. However, if the star has been losing mass to the interstellar medium (with velocities comparable to $-50\mathrm{km\,s^{-1}}$), then there may be a sufficiently large Mg II column density for scattering, to be able to modify the underlying h_{2V} intensity. This is not unreasonable because there must be material moving with a velocity of $\sim -75\ \mathrm{km\,s^{-1}}$, scattering the photons from the blue wings to form the observed wind absorption feature. The absorption feature is likely to be formed by the conservative scattering of photons so that the *total* flux observed in the h & k lines still represents the flux emitted in the chromosphere (see Table 6-2).

If there is a significant velocity shift between the photosphere and the location at which the optical depth is unity for the Mg II h & k lines centres, then in an outwardly accelerating wind, the transition region line profiles also would be expected to show some velocity shifts. The observations constrain any such velocity field to $< 7\,\mathrm{km\,s^{-1}}$. So the important question is 'are the Mg II h & k line profiles modified above the chromosphere by scattering material such as that which produces the observed wind absorption feature?'. If the answer is 'no', then this suggests either there exists two physically distinct regions (one which emits transition line radiation, the other having a bulk mass outflow), or that the observed profiles are generated by the convolution of profiles from upward and downward flowing elements occurring below the transition region material. If the answer is 'yes', then it is not possible to determine the emergent profiles between the chromosphere and the scattering region, whereas it is these profiles which should be compared with the calculated line profiles.

In the schematic wind calculations the red wings beyond $100\,\mathrm{km\,s^{-1}}$ were not significantly affected by the velocity fields. It is then reasonable to assume that the PRD line profiles beyond $100\,\mathrm{km\,s^{-1}}$ redward of line centre are relatively unaffected by bulk mass motions. Fitting the calculated profiles from the PRD atomic model to the observed profile is meaningful if the wind motions do not significantly affect the atmospheric structure. The observed wing profile for the h line lies between that in Models 1 and 2, while the red wing of the k line lies between that in Models 2 and 3. Model 2 over-estimates the flux in the line wings at $200\,\mathrm{km\,s^{-1}}$ from line centre by a factor of 4 for the k line and a factor of 2 for the h line. This part of the line profile is formed above the temperature minimum region and suggests that the temperature in this region, for Model 2, is too high. The observed h_{2R} feature is much broader than any of the models predict. If a wind model had a velocity field greater than those discussed in this section, then the line centre opacity would be blue-shifted to a greater extent than W4 and the line centre intensity would be increased (however, this has the effect of moving the h_{2R} feature bluewards but not broadening it). It seems that the asymmetry observed in the Mg II h & k lines is expected if a wind with a significant velocity ($\sim 50\,\mathrm{km\,s^{-1}}$) exists at the location of the optical depth unity at line centre, but that there must be other processes which produce the observed width of the h_{2R} and k_{2R} features.

Owing to the uncertainties in the calculated continuum flux at these wavelengths and the insensitivity of the wing source function to the temperature structure, it is not possible to use a comparison of calculated *far* wing intensities with the observations to infer the atmospheric structure.

At the present time it is not possible to determine if the asymmetric Mg II h & k line profiles are formed by bulk mass motions in the line forming region or whether there is scattering of the Mg II h & k photons above the chromosphere in an out-flowing wind.

6-2-3 The Effects of Microturbulence

The microturbulence is poorly constrained observationally in all stars but the Sun. The measurement of microturbulence from the abundance determinations of evolved stars seems to suggest that $2\,\mathrm{km\,s^{-1}}$ is a reasonable value for the photospheric microturbulence. In the chromosphere it is necessary to assume a particular velocity field. The turbulent velocity field adopted in this work has been described in Section 5-1-3.

To investigate the sensitivity of the line profiles to the chosen turbulence field, Model 1 was recomputed with smaller values of turbulent velocities. Figure 6-9 shows the Mg II h line profiles (upper part) resulting from the different turbulent velocity fields (lower part).

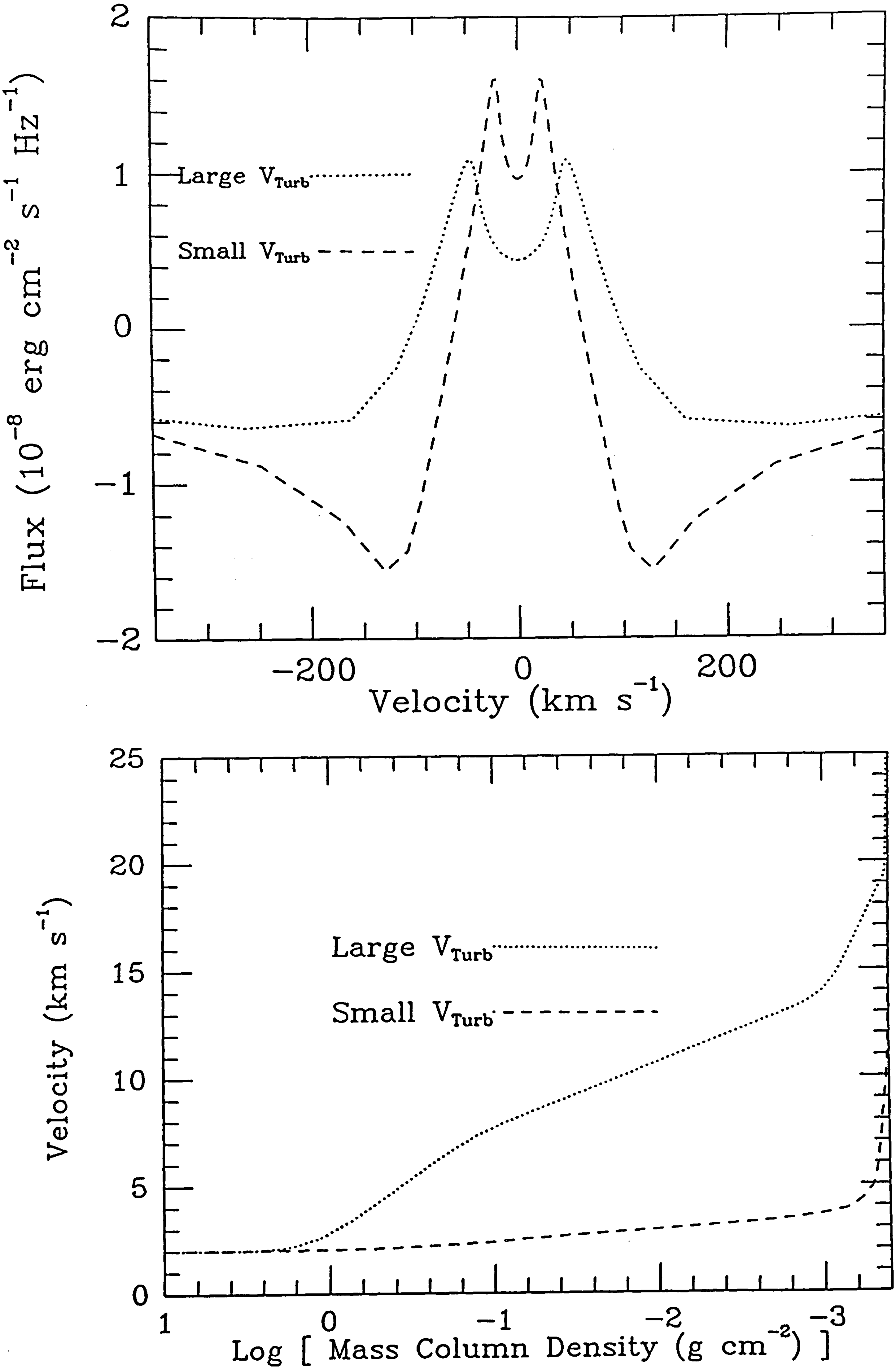

Figure 6-9 Two h line profiles calculated from Model 1 (PRD) with different turbulent velocity fields (shown in the lower diagram).

The decrease in turbulence leads to the h_{2R} and k_{2V} peaks moving towards line centre and increasing in intensity, whereas the intensity in the wings is reduced. The line wings are formed far from the Doppler core and the decrease in intensity is a result of the reduced photon redistribution from the line core to the Lorentzian wings. The reduction of the redistribution of core photons leads to a decrease in the non-coherent scattering term in equation (5.24). The observed separation of the h_2 features is reproduced with the adopted microturbulent velocity field. The profile produced using low values of microturbulence has a much narrower profile and much more intense h_2 peaks.

It has been demonstrated that the width of the Mg II h & k line profiles can be changed either by increasing the mass column density of the line wing forming region or by changing the values of the microturbulent velocities. However, changing the mass column density in the line wing forming region does not significantly change the separation of the h_2 features.

6-2-4 Comparison of the h & k Ratios

Because the Mg II h & k lines have different opacities, their profiles will be controlled by the temperature structure in slightly different parts of the atmosphere. The ratio of the fluxes in the h & k lines, and the ratio of the peak intensities have been calculated and compared with the observed ratios. Table 6-2 shows the results of these calculations.

If the observed line profile is due to conservative scattering of line photons then it is useful to compare the *total* fluxes in the calculated models with those observed. Although the profiles seen in Figures 6-5 and 6-6 are symmetric about line centre, scattering may redistribute the photons into profiles similar to those observed. From Table 6-2 it can be seen that Models 1 and 2 both overestimate

Table 6-2 Observed and calculated fluxes of the Mg II h & k lines. The calculated fluxes are computed using the electron densities from the 4-level hydrogen atomic model. The units for the first two columns are erg cm^{-2} s^{-1}. The third column is the ratio of the total flux in the line and the fourth column is the ratio of the intensities at the $_{2R}$ feature.

	Flux(k)	Flux(h)	Flux(k)/Flux(h)	Flux(k_{2R})/Flux(h_{2R})
Observed	4.3(4)	2.6(4)	1.65	1.38
Model 1	5.9(4)	2.9(4)	2.00	1.55
Model 2	7.2(4)	4.1(4)	1.75	1.48
Model 3	4.5(4)	2.3(4)	1.92	1.89
Model 4	4.2(4)	2.4(4)	1.76	1.68
Model 5	2.7(4)	1.5(4)	1.80	1.58

the total flux in the h and k lines. Model 1 has Mg II h & k line fluxes too large by factors of 1.6 and 1.7, respectively, the corresponding values for Model 2 are 1.1 and 1.4. Model 5 underestimates the total flux in these lines by factors of 1.7 and 1.6, respectively. The total fluxes for both lines in Models 3 and 4 agree within 10% with the observed values. The Model 2 Mg II h line was calculated with the electron densities from the 9-level atom. The total flux of the computed line was 5% less than the flux calculated above which gives agreement with the observed flux to within 15%.

The ratio of the total fluxes calculated in the models are all between the observed value 1.65 and the optically thin value of 2.0. There are two likely explanations for this result; first, the k line may be losing flux through the photo-excitation of other lines, and second, the model chromospheres may not be reproducing the correct opacity in the line forming regions. The first explanation is suggested by the presence of very strong Fe I uv44 emission, which is pumped by the k line centre radiation field. This leads to photons leaking out of the k line into other transitions, resulting in a decrease in the total k line flux. (This is considered in more detail below.)

The second possible explanation is harder to quantify, as the total line fluxes are formed over a range of optical depths. If most of the flux comes from the line core then the k line source function must be reduced relative to that of the h line at the point in the atmosphere where the photons escape, $\tau \sim 1$. Because the h line is less opaque than the k line, the photons at a given frequency from line centre are emitted from deeper in the atmosphere for the h line. This effect could be incorporated in the chromospheric models by reducing the temperature gradient in the line forming region. If the temperature gradient is reduced in the temperature minimum region, then S_ν will decouple more quickly from B_ν and the profile intensities will be reduced. However, considering the uncertainties in the calculations and in the true nature of the line profile, no further modifications were made to the models. The ratio of the calculated peak intensities is also less than that observed, and the above explanations are also possible. The photons lost by fluorescence may not occur at the h_{2R} frequency but the removal of photons in the line centre will reduce the redistribution of photons to this frequency. However, of the two models (Models 3 and 4) which reproduce the observed fluxes, Model 4 gives the best agreement with the k/h ratio and the k_{2R}/h_{2r} ratio.

The results of the Mg II h line profile analysis suggest that there may be bulk mass motions present in the h line forming region and, therefore, the observed lines whose profiles show no velocity shifts would be formed in a physically separate region. This implies that the temperature at the top of the stellar chromosphere does not rise up to transition region temperatures but levels out at some lower temperature. Another possible reconciliation of the calculated line profiles with the observations would be if sufficient material has been ejected into the circumstellar region for scattering to modify the line profile as 'seen' at the top of the chromosphere.

6-3 Aluminium and Silicon

Model chromospheres which are constructed purely on the basis of matching the calculated and observed profiles of the Mg II or Ca II resonance lines, cannot provide information on the structure above the temperature, $\sim 1.1 \times 10^4$ K, where the photons escape from the atmosphere. In the present work, transitions from aluminium and silicon ions have also been calculated to constrain the models at temperatures $< Log(T_e) = 4.3$. The calculated fluxes in the aluminium and silicon transitions in Models 1–5 are shown in Table 6-3. The results are discussed in the following subsections. The effects of the reduced electron density in Model 2 (Model 2(i)), resulting from the inclusion of extra levels in the hydrogen atomic model, is to slightly reduce the calculated line fluxes. The Al II λ2669 is reduced by about 5%, while the Si lines are reduced by $\sim$ 20%. This difference reflects the amount of the total line flux formed in the region where the electron density is reduced. The Al II] λ2669 line is formed in a wide range of temperatures (see 6-3-1) while the Si II lines have most of the flux formed over the interval $-1.0 < Log(mcol) < -3.384$ (where the reduction in electron density occurs).

6-3-1 Aluminium

The transitions calculated for the aluminium atomic model are λ2669 and λ1670. The aluminium is in the singly ionised state throughout most of the chromosphere, with the aluminium becoming doubly ionised at $\sim 1.1 \times 10^4$ K. The λ2669 transition is optically thin in the line forming region, whereas λ1670 is optically thick (optical depth unity occurring at $\sim 10^4$ K). The calculated fluxes for λ2669 are all within a factor of four of the estimated observed flux. As λ2669 is formed over a large temperature range, *i.e.*, $4000 < T_{\rm Form} < 14000$ K, it is sensitive to the chromosphere as a whole. However, the difference between the observed flux

Table 6-3 Comparison of calculated and observed line fluxes for transitions of aluminium and silicon. All the fluxes are calculated with the electron densities from the 4-level hydrogen atomic model. Fluxes at the star are in units of erg $cm^{-2}s^{-1}$.

Transition	Model 1	Model 2	Model 3	Model 4	Model 5	Observed Flux
Al II 2669.2Å	3.4(3)	5.4(3)	2.5(3)	2.6(3)	2.0(3)	$\sim$ 1.5(3)
Al II 1670.8Å	1.1(2)	1.2(2)	4.8(1)	4.4(1)	1.2(1)	–
Si I 2506.4Å	1.1(3)	1.0(3)	1.0(3)	4.6(2)	4.7(2)	–
Si II 2334.5Å and 2334.7Å	2.8(3)	3.4(3)	1.9(3)	1.1(3)	8.4(2)	< 1.6(3)
Si II 2350.2Å	4.0(2)	5.8(2)	3.0(2)	2.0(2)	1.2(2)	*7.6(2)
Si II 2328.6Å	1.3(1)	2.9(1)	6.0(0)	7.5(0)	4.1(0)	< 2.7(2)
Si II 2344.7Å	1.4(3)	1.7(3)	1.1(3)	6.8(2)	4.4(2)	–
Si II 1808.1Å	1.1(3)	1.2(3)	1.2(3)	2.3(2)	1.2(2)	1.6(2)
Si II 1817.0Å and 1817.5Å	2.8(3)	2.9(3)	2.8(3)	6.1(2)	3.3(2)	5.8(2)

* See text.

and that calculated in Models 3–5 is less than a factor of 1.8. Comparing Models 4 and 5 with Model 1 shows that reducing the pressure (and the electron density) at the top of the model reduces the emitted flux. The optically thick line at λ1670 has similar fluxes in Model 3 and Model 4. This means that the flux emitted in the upper chromosphere of Model 4 (which is at a lower pressure than Model 3) is compensated by the flux emitted in the lower chromosphere (which has higher temperatures for a given column mass than Model 3). In this way, the total flux for both models can be similar.

Unfortunately the λ1670 transition is too weak to observe in the IUE spectra of ι Aur but the low calculated flux is consistent with a non-detection in the LORES spectra. In the future, the Hubble Space Telescope may be able to detect λ1670 and this will be able to constrain the model chromospheres further. It can be seen that Model 4, which gave the best overall fit to the Mg II line fluxes, gives a reasonable fit (to within a factor of 1.7) to the Al II] flux.

6-3-2 Silicon

Neutral silicon starts to become singly ionised in the upper photosphere and becomes doubly ionised above 10^4 K. The initial upper chromosphere substantially over-estimated the flux in the Si II λ1816, 1818 and λ1808 lines. The temperature gradient was increased to obtain a broad agreement between the calculated fluxes and the observed fluxes. The resonance line of Si I at λ2500 is not observed in the IUE spectra of ι Aur, but the calculated fluxes are at the detection threshold and the line is observed in even cooler stars.

The fluxes in the optically thin lines of Si II ($\lambda\lambda\lambda$2334, 2350, 2328 and λ2344) all reflect the amount of emitting material in the whole chromosphere, and again the fluxes do not vary greatly between the models. The differences in flux for Models 1–3 result from the different amounts of material, at a given temperature, below 5200 K. The different calculated fluxes for Models 1, 4 and 5 reflect the lower pressures above this temperature.

The calculated fluxes of Si II] are consistent with the observed fluxes except λ2350 which is anomalously low. The ratio of the fluxes in λ2334.5 + 2334.7 and λ2350 has been observed for several cool giants and is also found to be smaller than that predicted by the atomic model used here. Judge (1986a,b) has found that this ratio is 2.5 for α Boo (K2 III), 2.9 for α Tau (K5 III) and 2.3 for β Gru (M5 III). The value from the observations and those calculated from the atomic model are 2.1 and $\sim$ 6, respectively. Judge (1986a) considers that the probable source of this discrepancy is in the atomic data (Dufton and Kingston, 1985) rather than in a blend because the observed λ2350 line in the giants discussed above is not broadened at the IUE resolution. Any blend must lie close to the central wavelength λ2350.17. An Fe II line lies close to this wavelength, but a line which shares the same upper level is absent. It is likely, therefore, that the atomic data used in the model is the source of discrepancy and not the chromospheric model.

The calculated fluxes in the transitions at $\lambda\lambda 2334.5$, 2334.7 in Models 1–3 are slightly in excess of the observed flux, but Model 4 gives an acceptable fit. The transition at $\lambda 2328$ has small calculated fluxes, but the observed line is blended with the C II] multiplet and thus the tabulated flux represents an upper limit.

The fluxes calculated for the transitions at $\lambda 1808, 1817.0$ and $\lambda 1817.5$ are insensitive to the lower chromosphere, implying that they are formed above 5200 K. The $\lambda 1817.0, 1817.5$ lines for Models 1–3 have calculated fluxes five times those observed, and the $\lambda 1808$ transition is in excess by an even greater factor. The presence of an excess of emitting material in the upper chromosphere can be removed in one of two ways. First, by increasing the temperature gradient the amount of material between two given temperatures is reduced, but the pressure at the top of the model is increased. Second, the temperature gradient can be kept constant and the upper chromosphere shifted to a lower pressure. In order to maintain the structure in the lower chromosphere, the middle chromosphere must also be adjusted by having a lower temperature gradient between $5000\mathrm{K} < T_e < 8000\mathrm{K}$. If there was a structural diagnostic sensitive to this middle region, then it may be possible to decide which of the approaches should be adopted. The computer calculations show that most of the excess emission in these lines occurs at $\sim 10^4$ K, so Models 4 and 5 have been constructed using the second approach. One of the effects of lowering the pressure at the top of the model is to reduce the electron density at a given temperature, thus if there is a tight constrain on the electron density it could restrict the range of acceptable models. The fluxes calculated for Model 4 are in good agreement with the observations, while Model 5 produces fluxes which are lower than observed. Other line fluxes are changed by a small amount because the electron density and the temperature minimum regions are slightly different.

The results for all the above lines suggest that Model 4 gives the best representation of the lower, middle and upper chromosphere.

6-4 Fe I uv44 Fluorescence by the Mg II k Line

The transitions described above have line forming regions which cover different temperature ranges and can provide information on the amount of material in their respective emission regions. However, the flux from these transitions has been calculated using one atomic model at a time. The presence of transitions whose rates are also determined by the presence of another atom's emission feature, *e.g.*, fluorescence, can provided sensitive information on the chromospheric structure, because generally, the two atomic species will exist in different temperature ranges which overlap. Thus, information on a more limited temperature range is available. The Fe I uv44 multiplet $J = 3$ level, which is photo-excited by the Mg II k line flux, is one such example. See the Grotrian diagram in Figure 5-5. The Fe I uv44 line at $\lambda 2843.98$ is observed in the LWP5199 spectrum while the $\lambda 2823.28$ line is over-exposed. The observed line flux is large (see Table 3-7) and suggests the presence of an exciting mechanism beyond collisional excitation. The conclusive evidence for fluorescence is that the lines observed in emission come from only the excited $J = 3$ level, while the lines from the other excited levels in the Fe I uv44 y^5G^o term are seen in ***absorption***. Thus the $J = 3$ level is photo-excited via pumping of the $\lambda 2795.54$ transition (the rest wavelength of the Mg II k line is $\lambda 2795.52$).

The initial calculations of the Fe I uv44 multiplet show that the transitions at $\lambda 2843$ and $\lambda 2823$ have optical depths ($\tau \leq 10$) in the line forming region 3600 K $< T_e <$ 5800 K. In this region, the Mg II k line is also optically thick ($\tau > 1000$), thus the source function $S_{\lambda 2795.52} \simeq J_{\lambda 2795.52}$. The Fe I uv44 transition to $J = 3$ is completely dominated by the Mg II k line fluorescence. The approximations used in the following calculations are that J_λ is constant over the λ2795.54 Fe I line profile, *i.e.*, $J_\lambda = J^{CRD}_{\lambda 2795.52}$, and that J_λ is unaffected by the photoexcitation.

From the calculations above it was shown that in the more realistic PRD formulation the line centre source function couples more closely to the Planckian source function (B_ν) than in the CRD formulation, thus, $J^{CRD}_{\lambda 2795.52} \leq J^{PRD}_{\lambda 2795.52}$. This will mean that the calculations may underestimate the true Fe I uv44 line fluxes. The assumption that the mean intensity, $\bar{J}$, is the same over the Fe Iλ2795.54 line profile is probably accurate as λ2843.98 is observed to be narrow. However, in these initial calculations the important features of this fluorescence can still be seen. The effect of the leakage of photons out of the Mg II k line into the Fe I uv44 lines can be judged by the emergent flux in these lines. Figure 6-10 shows where in the chromosphere the fluorescence occurs for λ2843.98.

The source of continuous opacity at these wavelengths and depths is dominated by the Rayleigh scattering of neutral hydrogen. The photons in the Fe I $\lambda\lambda$2823, 2843 lines do not escape directly but are Rayleigh scattered by neutral hydrogen. As the density decreases and the temperature increases, the continuous opacity becomes dominated by hydrogen bound-free transitions and photons in the λ2823 λ2844 lines escape. The photons in the Fe I uv 44 λ2795 line are still dominated by the Mg II k line opacity as the latter remains optically thick. Thus the line formation is very sensitive to the amount of material below the temperature for ionising neutral iron. The resultant Fe I uv44 line formation is then sensitive to *photospheric* conditions *and* the presence of the Mg II k line radiation.

The fluxes calculated from these models are shown in Table 6-4. The difference in the fluxes between Models 1, 2, 3 and 4 is quite large and some of this will be due to the different continuum levels in each model. It is possible to estimate the magnitude of the absorption underlying the emission lines by examining the

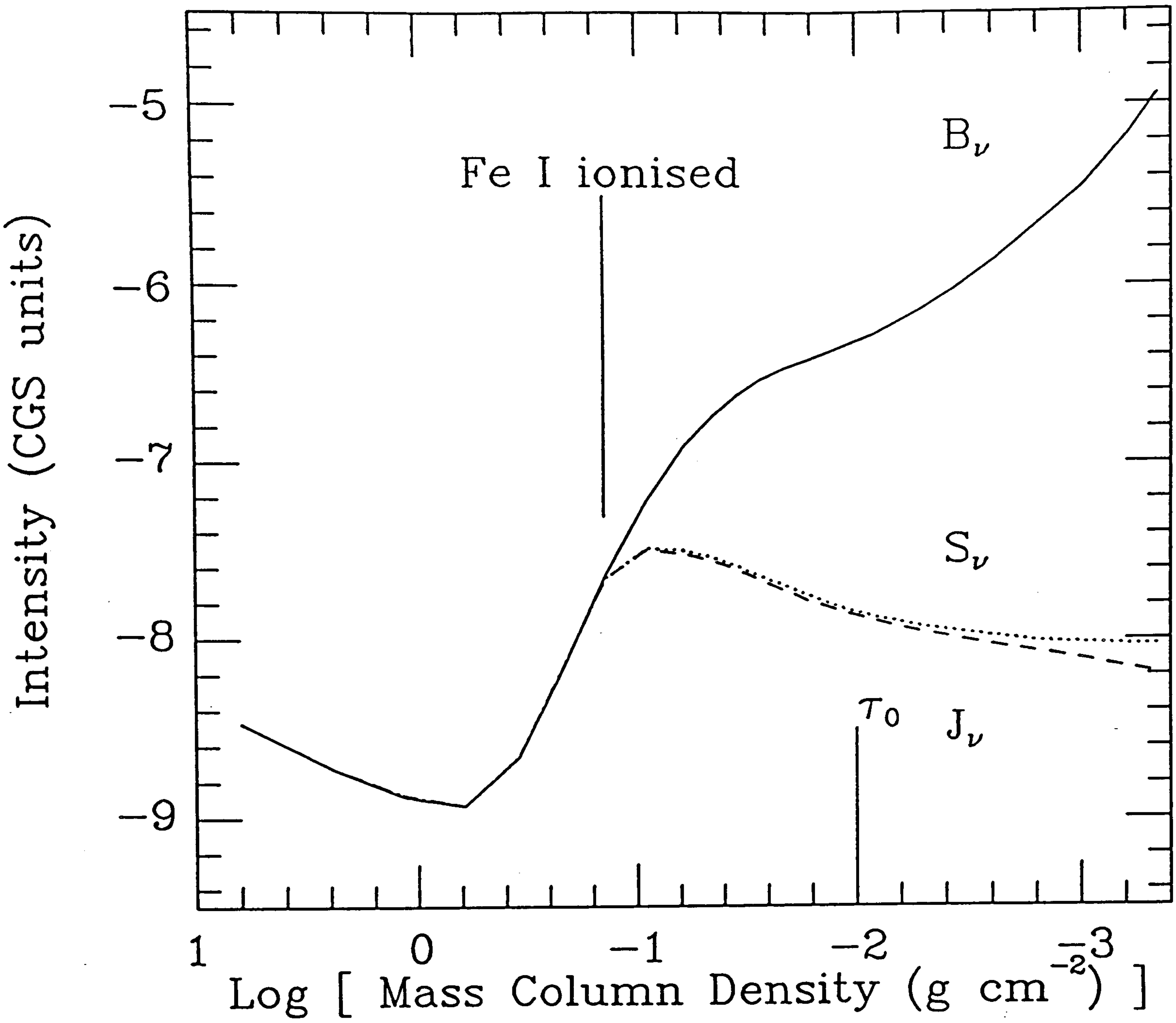

Figure 6-10 Diagram showing the Planck source function, B_ν, the line source function, S_ν, and intensity of the Fe I uv44 λ2843.98 line, J_ν, against the logarithm of mass column density. Note that S_ν decouples from B_ν as the neutral iron becomes ionised. The optical depth reaches unity as the continuous opacity decreases and the intensity in the line decouples from S_ν as photons escape in the line.

Fe I uv44 photospheric absorption line at λ2788. The energy removed from the continuum is $\sim 10^3$ erg cm^{-2} s^{-1}. The fluxes in Table 6-4 suggest that the flux lost from the Mg II k line is $\leq 10^4$ erg cm^{-2} s^{-1}. This represents an upper-limit of 20% of the observed k line flux. The observed Mg II h & k line ratios are less than those calculated with the magnesium atomic model (PRD). However, if photons are lost from the k line via the Fe I uv44 $J = 3$ fluorescence, then one would expect the observed ratio to be less than that calculated initially. Because the leakage of photons in the Fe I lines occurs at large optical depths the effects on the Mg II k line will be related to how its source function is modified by the photon loss and will not merely result in a reduction in the k line flux. One would expect that the removal of photons from the line core would inhibit photon redistribution within the line itself. To investigate the effects of photon loss from the k line source function requires a simultaneous treatment of the lines involved, but this requires a substantial amount of further work. In this respect the treatment of the Fe I and Mg II atomic models separately may be inadequate for these types of stars.

The ratio of the calculated Fe I fluxes is not as expected from an optically thin gas but the transition with the larger oscillator strength, $\lambda 2843$, is calculated to be the weaker line. The calculated line fluxes are the sum of the photospheric absorption and chromospheric emission fluxes. Thus, if $\lambda 2843$ has a larger photospheric absorption feature, the emission must fill the absorption trough before being seen in emission. The Mg II resonance lines also sit on photospheric absorption but the emission there is relatively strong. Since the observed line width of Fe I $\lambda 2843$ is similar to the IUE point spread function, the emission line cannot have a very large optical depth at line centre otherwise there would be opacity broadening; this is consistent with the models which predict $\tau_0 < 10$. In spite of the above uncertainties Model 4 gives a calculated flux in $\lambda 2843.97$ which is in good agreement with the observations.

Calculations of the fluorescent excitation of lines in the Fe I uv44 multiplet by the Mg k line have been made for the first time and the lines have been shown to provide an important structural diagnostic below 5500 K. The Mg II k line is optically thick in the region of fluorescence so that the photon leakage may play an important role in the radiation transfer in the Mg II k line. The estimated flux loss in $\lambda\lambda 2844$, 2823 is a significant proportion of the Mg k line flux. The need for the simultaneous solution of atomic models for both atoms is demonstrated.

Table 6-4 The calculated fluxes in the Fe I uv44 multiplet when the λ2795.54 transition is excited by the Mg II k line. The observed flux for λ2843.97 is 4.1 $\times$ 10^3 erg cm^{-2} s^{-1}. The fluxes given below are in the same units. The fluxes were calculated with the electron densities from the 4-level hydrogen atomic model.

Model	λ2843.97	λ2823.27
Model 1	6.6(2)	3.0(3)
Model 2	* 4.2(3)	2.1(2)
Model 3	1.8(3)	3.6(3)
Model 4	4.0(3)	5.4(3)

* Absorption feature, *i.e.*, flux removed from the continuum.

The importance of making models with the continuum levels in agreement with the observations is also highlighted.

6-5 Joining the Chromospheric and Transition Region Models

The emission measures derived in Chapter 4 did not have photoionisation included in the ionisation balance values. The ion balances calculated in MULTI show that both the magnesium and the aluminium are in the singly ionised state below $\sim$ 9000 K. The initial emission measure in Chapter 4 (Table 4-2) overestimated the amount of material needed to produce the observed fluxes from Al II] and Mg II. A reduction in the calculated emission measure loci below $Log(T_e) = 4.0$, to allow for a greater ion fraction, also leads to the Si II lines being formed at a higher temperature than first expected. The emission measure distribution has been recalculated with the ionisation balances from the model chromospheres. The emission measure below 10^4 K is reduced and the emission measure $\geq 10^4$ is raised by a small amount. The original emission measure, $E_m(0.3)$, and the emission measure iterated from the chromospheric ion balance calculations are shown in Table 6-5. The emission measures $E_m(0.3)$ and $E_m(0.1)$, which have been calculated from Model 4

Table 6-5 The emission measure from Chapter 4, $E_m(0.3)$, and the iterated emission measure, $E_m^*(0.3)$, (calculated using the ion balance results from Model 4) compared to the emission measure calculated directly from Model 4. Also shown is the emission measure, $E_m(0.1)$, for Model 4.

$Log(T_e)$	Initial $E_m(0.3)$ (cm^{-5})	Iterated $E_m^*(0.3)$ (cm^{-5})	Model 4 $E_m(0.3)$ (cm^{-5})	Model 4 $E_m(0.1)$ (cm^{-5})
3.7	–		–	30.9
3.8	–		–	29.5
3.9	–		29.60	28.7
4.0	28.40	28.65	28.70	27.4
4.1	27.32	27.50	27.55	27.1
4.2	26.75	26.80	26.85	26.5
4.3	26.50	26.50	–	26.2
4.4	26.15	26.15	–	–
4.5	25.65	25.65	–	–

are also shown. The emission measure ($E_m(0.3)$) for Model 4 does not extend above $Log(T_e) = 4.2$ (*i.e.*, the final $E_m(0.3)$ covers the temperature range in $Log(T_e)$ of 4.05 – 4.35) because the lines treated are not formed beyond this temperature. The calculated emission measure $E_m(0.1)$, which is more sensitive to the variation of T_e with height, is also shown. This emission measure will be used in Chapter 7 to compare the wind model solutions with the observations. (The emission measure $E_m(0.1)$ would be equal to a third of $E_m(0.3)$ if the emission measure distribution were constant with temperature.)

The values of $E_m(0.3)$ from Model 4 are consistent with those derived from the observations, which is to be expected if they both represent the amount of material needed to form the Si II line fluxes. The chromospheric model is then joined to the transition region at $Log(T_e) \sim 4.2$. It is then possible to attach a model transition region to the model chromosphere using the techniques described in Chapter 4.

6-6 Summary

Five chromospheric structures have been discussed and line fluxes for the chromospheric models 1(i), 2(i), 3, 4 and 5 have been calculated for transitions in the following species; Si II, Al II, Mg II h & k and Fe I uv44.

It has been found that it is not possible to distinguish which of the models is most appropriate to describe the Mg II line profiles, however, Models 3 and 4 produce line fluxes which are within 9% of the observed fluxes. In addition to changing the velocity fields, a small increase in the magnesium abundance would bring the line profile in the red wing for Model 4 into close agreement with the observations. The 'hybrid' bright giant, α TrA, has a magnesium abundance which is a factor ~ 1.5 greater than the solar abundance (used here). This highlights the importance of obtaining accurate abundance determinations. The importance of using the partial redistribution formulation when solving the radiation transfer in the resonance lines has been demonstrated. The difference between the Mg II h & k line profiles calculated in CRD and PRD is pronounced, so it is essential to adopt the PRD formulation when constructing model chromospheres in low gravity stars.

Models 1, 2 and 3 overestimate the flux in the Si II $\lambda\lambda$1816,1818 and λ1808 lines, while the reduced pressure models give better agreement. Model 4 gives the best agreement between the observed and calculated fluxes for these lines. Model 5, which has a lower pressure in the upper chromosphere, yields lower fluxes and has electron densities which are at the lower limit of that determined from the C II] multiplet. This then constrains the range of acceptable models to have pressures greater or equal to those in Model 5. This implies that in hydrostatic equilibrium, the electron density at $Log(T_e) = 4.8$ is not more than an order of magnitude less than 10^9 cm^{-3}. Model 4 produces the best agreement between the observed and calculated line fluxes, with all the fluxes except for Si II λ2350 being within a factor of 1.8 of the observed values. The atomic data for the Si II atomic model produces $\lambda 2350$ fluxes which are about a factor of two too small.

The electron densities in most of these models are broadly consistent with those measured from the C II] multiplet, *i.e.*, $Log(N_e) = 9.0(\pm 0.3)$. However, the electron density in Model 2(ii) is below the observed value. In particular, Model 4 which gives the best overall fit to all the line fluxes, gives an electron density which is consistent with the observed value. The effects of changing the radiation temperatures and the number of levels in the hydrogen atomic model have been examined and it is found that increasing the number of levels may reduce the calculated electron density between $-1.0 > Log(mcol) > -3.38$ by up to 25%.

The calculations of the Al II flux show that Model 4 gives the best overall agreement with the observations.

Calculations of the fluorescent excitation of the Fe I uv44 $J = 3$ level by the Mg II k line have been made for the first time and show that this process is sensitive to the atmospheric structure near the temperature minimum. Model 4 gives a good fit to the observed flux of the $\lambda 2843$ transition.

The emission measures have been calculated for Model 4 up $Log(T_e = 4.2$ and the model chromosphere has been joined on to the emission measures derived from the other line fluxes discussed in Chapter 4. Thus for the first time for a 'hybrid' bright giant a model has been made from the low chromosphere through to the transition region ($\sim 2 \times 10^5$ K).

CHAPTER 7. WIND MODELS

In this Chapter, a constant damping length Alfvén-driven wind formulation is investigated in the context of ι Aur. The passage of Alfvén waves through a gas can deposit energy and momentum to the gas and thus may be able to drive a wind and heat gas (such as that observed as transition region material). This formulation has been applied to another 'hybrid' star α TrA by Hartmann *et al.* (1981) and by Mendoza (1984). In this work the base gas density of the wind model is constrained by the model chromospheres described in Chapter 6 and also has the gas ionisation fraction included so that the temperature of the wind can be determined where the gas is not fully ionised. A brief review of cool stellar winds is given below.

Good reviews on the theory of stellar winds have been given by Cassinelli (1979), Castor (1981) and Holzer, Flå and Leer (1983). For steady state radial flows, the momentum equation can be written,

$$v\frac{dv}{dr} + \frac{GM}{r^2} + g_{Therm} + g_{Rad} + g_{Wave} = 0, \tag{7.1}$$

where v is the wind velocity, r is the radial distance, GM/r^2 is the gravitational attraction, and g_{Therm}, g_{Rad} and g_{Wave} are the accelerations due to the thermal pressure, radiation pressure and wave pressure, respectively. The mechanisms proposed to explain the observed mass-loss rates can be divided into three classes which depend on the relative magnitudes of the different acceleration terms in equation (7.1). The three classes are:

(i) When $g_{Therm} > g_{Rad}$, g_{Wave}, the wind is driven by the thermal pressure. This is a Parker-type wind and was originally proposed to explain the solar wind. The thermal pressure acceleration is given by $g_{Therm} = \frac{1}{\rho}\frac{dP}{dr}$, where P and ρ are the gas pressure and density, respectively.

(ii) When $g_{Rad} > g_{Therm}$, g_{Wave}, the wind is driven by radiation pressure. In cool (M-type) giants and supergiants it has been proposed that winds can be driven by the radiation pressure on circumstellar dust grains.

(iii) When $g_{Wave} > g_{Therm}$, g_{Rad}, the winds are driven by waves or periodic shocks.

The first class of wind mechanisms, that of thermal winds, assumes energy is deposited above the photosphere of the star and that the thermal pressure is large enough to cause the gas to flow out against the gravitational attraction of the star. This process is essentially a Parker type solar wind.

Combined, the mass and momentum equations for stellar winds leads to several families of solutions each having different mathematical behaviour and physical significance. The equation for the velocity gradient can be written in the general form,

$$\frac{dv}{dr} = \frac{A - B}{C - D}, \tag{7.2}$$

where A, B, C and D are terms found by combining the equations for the conservation of momentum and mass. The different families of solutions come from the different behaviour of the numerator and denominator terms, which in turn depend on the sources of momentum in the wind. Not all the possible solutions to equation (7.2) are physically realistic, *e.g.*, if $C = D$ and $A \neq B$ the velocity gradient becomes infinite. When $A = B$ and $C \neq D$ the velocity gradient becomes zero, and if the initial velocity is increasing before this condition is reached, then the velocity will begin to decrease pass this point. The solutions to equation (7.2) which are physically realistic must satisfy the observed boundary conditions, *i.e.*, the wind must have a subsonic flow speed near the stellar surface and a pressure which tends to zero at very large distances. This latter boundary condition ensures that the wind solution is compatible with the pressure of the interstellar medium. These solutions are those which pass through the *critical point*, *i.e.,* when $A = B$ and $C = D$ simultaneously. Physically, the critical point is the point where the wind flow speed goes from subsonic to supersonic and hence no disturbance downstream of the critical point can flow upstream through it.

The mass loss for thermal winds can be found by evaluating the mass conservation equation, assuming that the flow is spherically symmetric and comes from the whole stellar surface.

$$\dot{M} = 4\pi\rho_{Crit}R_{Crit}^2 V_{Crit}, \tag{7.3}$$

where the subscript *Crit* denotes the values of the parameters at the critical point. To account for the mass-loss from stars exhibiting circumstellar absorption ($10^{-5}\ M_{\odot}\mathrm{yr}^{-1} < \dot{M} < 10^{-10}\ M_{\odot}\mathrm{yr}^{-1}$) requires that the critical point be in a region of high density, *i.e.,* the chromosphere. But to get the critical radius near to the stellar surface (and hence a large critical density), the critical temperature must be $\sim 10^6$ K. Cool low gravity stars are not observed to have high density coronae, thus mass loss in the cool stars and 'hybrid' bright giants is not due to thermal pressure.

The second class of wind mechanisms, radiation driven winds, is based on the transfer of momentum from the radiation to the gas surrounding the star. In very luminous stars, radiation can accelerate the gas if there is sufficient opacity in the waveband where there is a peak in the stellar flux. In early-type stars, the opacity sources are the resonance lines in the ultraviolet. In late-type stars, if the stars are cool enough (≤ 3000 K) the opacity source is in the infrared waveband. This is due to the presence of dust grains, with the momentum being transferred to the gas from the dust grains via gas-grain collisions. This mechanism is unlikely to be able to drive massive winds in the 'hybrid' bright giants, because the temperatures are too large in the regions near to the star for grains to form. Further from the star, where dust grains may condense, the radiation field will be diluted and the density will be too low for significant mass losses to occur. If the 'hybrid' bright giants have transition region material formed in a region which is physically distinct from the wind, and if the wind is cool enough, dust grains may form near the star. But given the presence of absorption in ionised species such as Mg II, this is unlikely.

The class of wave-driven winds includes Alfvén wave and periodic shock driven winds. It was shown in Chapter 4 that acoustic shocks with Mach numbers $\simeq 3$ could carry sufficient energy flux above $Log(T_e) = 4.0$ to account for the observed radiative losses in ι Aur, but flows at this speed are not observed. Wilson and Hill (1979) made hydrodynamical studies of the effects of periodic isothermal and adiabatic shocks in stellar atmospheres. They found that isothermal shocks produce negligible mass loss rates but adiabatic shocks can produce mass-loss rates of $10^{-6} M_{\odot}/yr^{-1}$ for stars with the physical parameters of Mira variables. The mass-loss rates are sensitive to the gas cooling rates. In these stars, the cooling rates seem to be large enough to ensure that the shocks are isothermal and hence the mass-loss is very small. There is no evidence that 'hybrid' bright giants have photospheric oscillations, but the amplitude of the pulsations does not need to be large as the shock will reach its maximum strength further out from the star.

In this Chapter, models of Alfvén wave-driven winds are investigated in the context of the 'hybrid' bright giant ι Aur, since these seem to be the most appropriate class of wind solution for this star.

7-1 Alfvén Wave-Driven Winds.

It can be shown that Alfvén waves can deposit momentum into the atmospheres of stars by considering the energy flux and energy density of the waves. The energy density of the Alfvén waves is

$$\epsilon = \frac{1}{2}\rho\delta v^2 = \frac{\delta B^2}{8\pi}, \tag{7.4}$$

where δv is the transverse velocity of the Alfvén wave and δB is the corresponding change in the magnetic field. The energy flux is

$$F_A = \epsilon V_A = \frac{\delta B^2}{8\pi}\frac{B}{\sqrt{4\pi\rho}}, \tag{7.5}$$

where V_A is the Alfvén velocity. If the magnetic field decreases slowly as the distance from the star increases (*e.g.,* radial $B \propto R^{-2}$), while the density ρ falls quickly near the star, the Alfvén velocity increases with radial distance. In a flux tube of area A, $B.A$ is constant, and if there is negligible wave dissipation, $F_A.A \simeq$ constant, then the energy density decreases outwards. The energy density is proportional to the wave pressure, so there is a pressure gradient and hence an outwards force. There are two separate effects on the gas due to the presence of propagating waves. The first, which occurs even if there is no damping, is the stress (or pressure) exerted on the gas to drive a wind. The second is the heating of the atmosphere by the dissipation of wave energy into thermal energy.

When constructing the model chromospheres in Chapter 6, the temperature structure was initially specified and then adjusted so that the calculated emission line fluxes and the magnesium line profiles were in broad agreement with the observations. This approach does not assume any specific heating mechanism. In this Chapter, the effects of damped Alfvén waves on the temperature and velocity structure of the atmosphere are examined, the assumption of hydrostatic equilibrium being relaxed.

Hartmann and MacGregor (1980) have calculated the response of the outer atmospheres of cool, low gravity stars to the passage of mechanical energy fluxes. They found that Alfvén wave fluxes could produce mass-loss rates ($6 \times 10^{-11}\, M_\odot\, \mathrm{yr}^{-1} <$

$\dot{M} < 3 \times 10^{-5}\ M_{\odot}\ \mathrm{yr}^{-1}$) which are consistent with the observations of luminous late-type stars. They also found that the acoustic or magnetic fast mode waves dissipated through shock formation in the chromosphere. These processes have damping lengths that are too short to drive a significant mass-loss rate. The ability of damped Alfvén waves to drive massive winds and also to heat the gas to transition region temperatures makes it an attractive theory. If the damping length is the order of the stellar radius $L_{Damping} \sim R_*$, then the heating of the gas increases with increasing gravity. A range of models exists, from cool, low velocity winds for the supergiants to hot *coronal* winds for stars with $Log(g) \geq 2$. Thus, for stars with intermediate gravities there are solutions which have relatively high temperature material and high velocity winds ($V \sim 150\,\mathrm{km\,s^{-1}}$ and $T_e \sim 10^5$ K). This work has been extended to simple models of Alfvén wave-driven winds for α TrA (Hartmann, Dupree and Raymond, 1981; Mendoza, 1984), α Ori (Hartmann and Avrett, 1984) and T Tauri stars (Hartmann, Edwards and Avrett, 1982). A comparison with the results calculated for α TrA is given in Section 7-3-1.

The 'hybrid' bright giants have gravities which are between those of supergiants and giant stars with hot coronae, and, as discussed in Chapter 1, they are located at effective temperatures in the H-R diagram where giant stars with hot coronae are not usually found. The giant stars in this region show the presence of only low velocity winds from circumstellar absorption features in the spectra of the Ca II resonance lines. A mechanism (such as the passage of Alfvén waves) that can drive a wind and heat the gas to temperatures of 10^5 K is of interest in understanding the observations of the 'hybrid' stars. The observational evidence for bulk motions in the chromosphere comes from the asymmetries in the Mg II h & k and O I λ1304 line profiles and the evidence for hot plasma comes from the presence of the transition region lines, formed up to $\sim 10^5$ K. In particular, the high velocity absorption component observed in the Mg II h & k lines could result from line scattering in fast, cool ($\leq 2 \times 10^4$ K) outflowing gas. This is the motivation for studying the 'hybrid' bright giants with models which have Alfvén wave damping as a heating and wind-driving mechanism.

7-2 Alfvén Wave-Driven Wind Theory

The basic theory for Alfvén wave-driven winds has been discussed extensively in the literature and the detailed background is not repeated here. Section 1-3 lists some of the more important references. The original Alfvén wave-driven formulation was based on solar work. Building on this, Hartmann and MacGregor (1980) formulated Alfvén wave-driven winds, adopting a constant damping length for the Alfvén waves and an isothermal atmosphere. Later, Hartmann, Edwards and Avrett (1982) (hereafter HEA) included the effects of the wave dissipation on the heating of the gas. The derivation of the basic equations is given in Appendix E. In Sections 7-2-1 and 7-2-2 some of the important features of these equations are discussed.

7-2-1 The Inner Wind Region

In Chapter 4, it was shown that near the star the energy balance is dominated by heating and radiative cooling of the gas. In this case $P_{Rad} = Q$, where Q is the heating rate. This approximation is used to simplify the momentum equation in the inner wind region. When this approximation is no longer valid (See Section 7-2-2) the full energy equation (neglecting conduction) is solved with the appropriate momentum equation.

The radiative losses can be written in terms of the power loss function, Λ,

$$P_{Rad} = N_e N_H \Lambda(T) = \frac{\rho^2}{(\mu M_H)^2 F(T)} \Lambda(T) = Q, \qquad (7.6)$$

where $F(T) = N_T^2/N_eN_H$ (N_T is the total number of particles per unit volume). F can be written in terms of the ionisation fraction defined as $f_{ion}(T) = N_e/N_H$. Assuming that $N_{He} = 0.1N_H$ then,

$$F(T) = \frac{(1.1 + f_{ion}(T))^2}{f_{ion}(T)}. \tag{7.7}$$

It is important to take account of the ionisation fraction at the base of the wind if the temperature is to be determined properly. This is the first time that a variable ionisation fraction has been used to determined the temperature in Alfvén driven winds. $f_{ion}(T)$ has been taken from the model chromospheres described in Chapter 6 and the adopted values are listed in Table 7-1. Further from the star, where the gas cools again, the values of $f_{ion}(T)$ will not be accurate but most of the radiation originates closer to the star where the densities are much greater. Thus the emission measures derived for the wind near the star will be close to the total emission measures in a given temperature range. The adopted radiative power loss function is also shown in Table 7-1, and is a combination of the values in Table 4-11 and those given by HEA (their Table 1). The power loss function for $T_e < 10^4$ K is quite uncertain but the temperature of the gas has little dynamical effect at these temperatures. The optically thin power losses above this temperature should be accurate to within a factor of two. The Ly-α peak in the power loss curve (cf. Rosner, Tucker and Vaiana, 1978) has been removed so that no instability due to a negative gradient of the function occurs (HEA). This will lead to a small overestimate of the material present at $\sim Log(T_e) = 4.3$. To calculate a power loss function which does not assume an optically thin gas (most of the energy losses in the chromosphere of ι Aur occur in the optically thick resonance lines), detailed Lyman line and resonance line calculations will need to be made, but these require a substantial amount of further work.

The momentum in the inner wind region, given by equation (E.15) in Appendix E, can be integrated with equation (E.13) as the auxiliary equation. The approximation to the energy equation in the inner wind region makes the momentum equation flexible and easy to integrate. The solutions to this set of equations, which satisfy the physical boundary conditions of subsonic flow at the stellar surface and vanishing pressure at large radial distances, pass through an X-type critical point (see Figure 7-1). Hartmann and MacGregor (1980) have discussed the nature of the critical points for isothermal wind models. When there are sources of momentum other than thermal pressure, more than one critical point may exist. The flow speed at the critical points then becomes 'sonic' points, in the sense that the 'sonic' speed is now related to the momentum source. For Alfvén driven winds the 'sonic' speed is no longer the local sound speed but a modified sound speed which includes terms which contain the Alfvén velocity. Figure 7-1 shows schematic curves for when the numerator, N, and denominator D, of equation (E.10) (when expressed as an equation for du/dz) are equal to zero. Wind solutions which pass through the inner critical point (X-type), satisfy the physical boundary conditions. The second critical point causes the wind solutions to spiral about this point.

With reference to Figure 7-1, the wind solutions initially have a positive velocity gradient. When the solution passes through the $N = 0$ line, the velocity gradient must change sign and the velocity decreases. If the wind solution reaches the $D = 0$ line the gradient becomes infinite and the solution is not physical.

In the text below the following terms which are defined in Appendix E are used: λ is the Alfvén wave damping length L normalised to the stellar radius R_*, such that $\lambda = L/R_*$. ξ is a dimensionless gravitational term defined in terms of the sound speed a and the stellar radius, such that $\xi = GM/(2R_0 a_0^2)$ where the subscript 0 refers to the base of the wind model and here $R_* = R_0$. z is the dimensionless radius $z = r/R_*$ and u is the dimensionless flow velocity of the wind $u = v/a_0$.

For solutions with $\lambda \rightarrow \infty$, the $N = 0$ curve is a monotonically decreasing

Table 7-1 The adopted values of $Log(f_{ion}(T_e))$ and $Log(\Lambda(T_e))$.

$Log(T_e(\mathrm{K}))$	$Log(f_{ion}(T))$	$Log(\Lambda(\mathrm{erg\,cm^3\,s^{-1}}))$
3.70	-2.657	-28.30
3.75	-1.708	-27.25
3.80	-0.476	-26.00
3.85	-0.055	-25.25
3.90	-0.029	-24.50
3.95	0.000	-24.10
4.00	0.020	-23.60
4.10	0.028	-23.12
4.20	0.032	-22.62
4.30	0.036	-22.30
4.40	0.040	-22.18
4.50	0.041	-22.00
4.60	0.042	-21.88
4.70	0.042	-21.65
4.80	0.042	-21.40
4.90	0.042	-21.30
5.00	0.042	-21.28
5.10	0.042	-21.26
5.20	0.042	-21.24
5.30	0.042	-21.22
5.40	0.042	-21.20

function and crosses the z axis at $z = \xi/2$, while the $D = 0$ curve remains qualitatively the same, so there is only one critical point. When $\lambda \to 0$ the $N = 0$ curve minimum moves upwards and the $D = 0$ curve moves closer to the star. For the models calculated here, when $\lambda \leq 0.85$, the inner critical point vanishes and no wind solutions exist. At large distances from the star, in the case of damped Alfvén waves, there will be a point where gravitational forces dominate the wave forces and the wind is decelerated. There may also be a point where thermal forces begin to dominate the gravitational forces and the wind is then thermally re-accelerated. This latter point corresponds to the Parker critical point.

The inner-critical point was found for a given set of fixed initial conditions (magnetic field, density, temperature and wave amplitude). The initial flow velocity

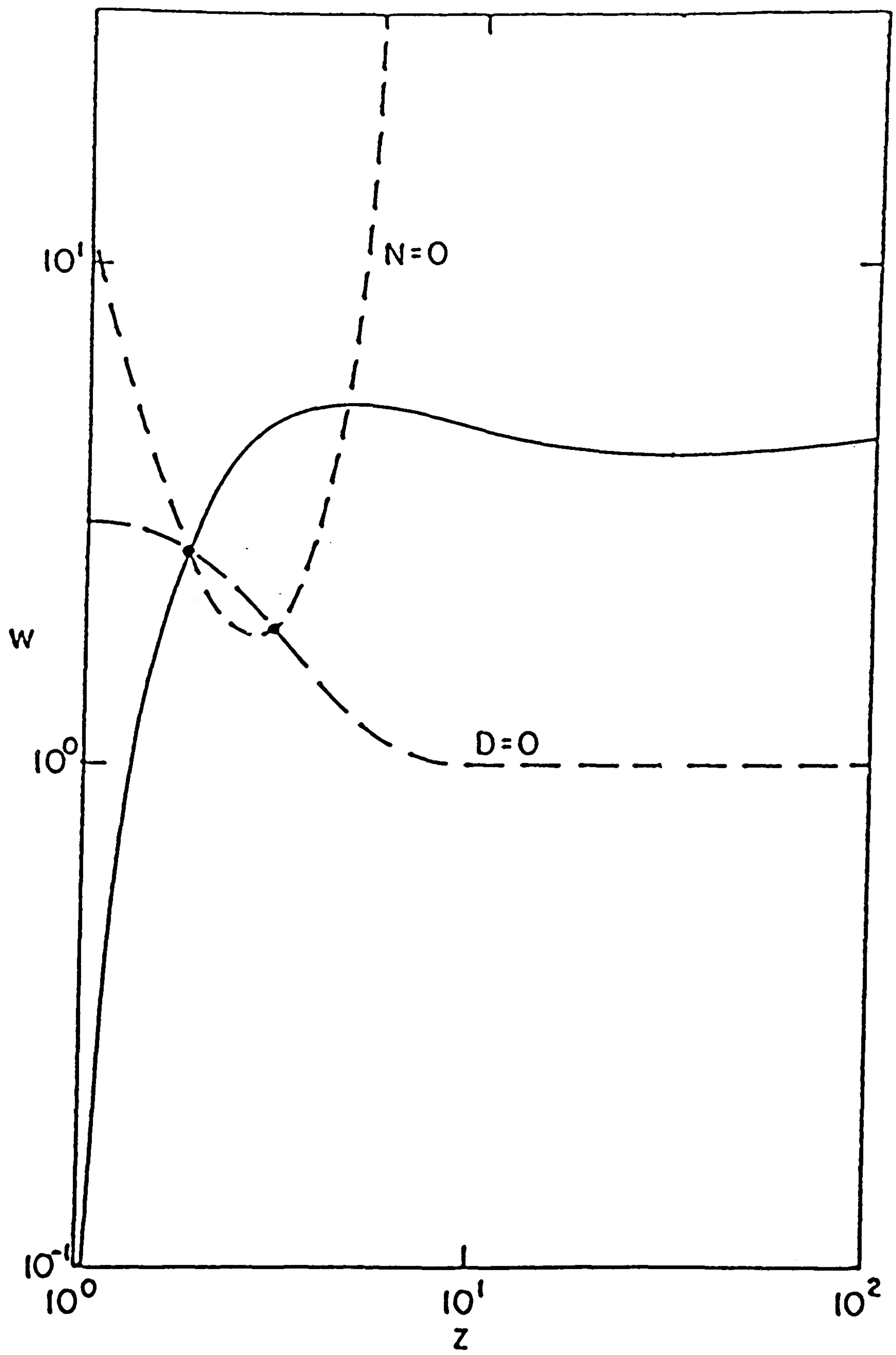

Figure7-1 Schematic representation of the critical points of the wind solutions (based on Hartmann and MacGregor, 1980). The curves w(z) correspond to N=0, D=0. The numerator and denominator of equation (E.10) (when expressed as an equation for du/dz) can be solved separately. When the numerator, N, (denominator, D) is zero the velocity gradient becomes zero (infinite). The curves, $N = 0$ and $D = 0$ refer to these solutions. The critical points are marked by heavy dots. The critical point closest to the stellar surface is an X-type point while the other critical point is an attractor (Hartmann and MacGregor, 1980). The wind solutions which pass through the inner critical point, satisfy the physical boundary conditions of sub-sonic flow at the stellar surface and vanishing wind pressure at large radial distances. The wind models discussed here satisfy these conditions.

is estimated and then wind solutions are examined. If the solution is subcritical (supercritical) the initial velocity is increased (decreased) until the critical point is found. To obtain the solution beyond the critical point, a 'shooting method' is used (in order to avoid numerical problems inherent in the nature of critical points). This produces a small discontinuity, and some information is lost in the 'jump' region. The approximation to the energy equation in the inner region makes the critical point 'jump' numerically more stable.

7-2-2 The Outer Wind Region

The approximation in the energy equation assumes that near the surface the wave heating term and the radiative cooling term dominate over the wind expansion terms. Further from the stellar surface this is no longer true and it is necessary to solve the full energy equation. The transition between solving the approximate and complete energy equations is determined by the dimensionless energy parameter,

$$\zeta = \frac{\rho a_0^3 u}{r_0 z P_{Rad}} \left(\frac{T}{T_0}\right) \left(2 + \frac{dLn(u)}{dLn(z)}\right), \tag{7.8}$$

which indicates when the wave heating and radiative cooling terms become comparable with the wind expansion terms in the energy equation. The wind models are started by solving equations (E.10) and (E.8), then when ζ exceeds a certain value ζ_{Crit}, the integration is continued with equations (E.11) and (E.12). The discontinuity in the wind solution can be made negligible if ζ_{Crit} is made to be of the order of 1%. The models were typically calculated from $z = 1 \rightarrow 50$.

The numerical integration was performed with a fourth order Runge-Kutta method with variable stepsize (Montesinos, private communication, 1988). (For a description, see Press *et. al.,* 1986.)

Table 7-2 The adopted initial conditions for the base of the wind model solutions.

Parameter	Value	Units
Radius	59	Solar Radii
Mass	5.9	Solar Masses
Base temperature	5480	Kelvin
Base particle density	5.5×10^{10}	cm^{-3}
Base density	1.08×10^{-13}	$g\ cm^{-3}$

7-3 Wind Model Solutions

Once the stellar radius and gravity are known, the wind models are defined by the initial atmospheric conditions and the velocity that takes the wind solution through the inner critical point. The mass and radius adopted have been discussed in Chapter 2, and are given in Table 7-2. Because it is not possible to determine which of the chromospheric models in Chapter 6 can best reproduce the Mg II h & k line profiles, the initial density and temperature are taken from Model 1. Because the total gas density at 5480 K changes by less than 25% between Models 1–4 this is not expected to be a significant source of uncertainty. Thus, the free parameters are the base magnetic field, B_0, the initial wave amplitude, and the damping length, L. The relevant parameter space can be constrained by comparing the conditions in the wind models with the observational constraints described in Chapter 4. The magnetic fields for bright giants have never been measured, so the magnetic field must be a free parameter. However, a lower limit can be placed on the magnetic field by considering the energy flux required to produce the observed radiation losses and the estimated mass-loss rate.

The initial wave amplitude is specified by the parameter $\alpha_0 = \left(\frac{\delta B_0}{B_0}\right)^2$. Alfvén wave damping is non-linear and becomes stronger as α becomes larger and this will tend to restrict α to some limiting value. The damping will become non-linear as α_0 becomes the order of unity. A maximum value of $\alpha = 1$ is therefore adopted. A value as large as this is sometimes observed in the solar wind at 1 A.U. (Hollweg, 1973).

The damping length is assumed to be constant in each model but can be varied as a free parameter. When $\lambda \rightarrow \infty$, this corresponds to undamped Alfvén waves. In this case the Alfvén waves still have significant amplitude in the low density material surrounding the star. The result is an acceleration of the wind to velocities much greater than are observed in cool giants and supergiants. It is then necessary to include wave damping which leads to a depletion of the energy wave flux in the high density gas near the star, and gives rise to terminal wind velocities an order of magnitude smaller than in the undamped wave case. It is found that for $\lambda \leq 0.85$, no wind occurs because the wave force becomes small compared to the thermal or gravitational forces near the stellar surface. This case corresponds to where the inner critical point vanishes.

7-3-1 Observational Constraints on Wind Models

The calculated wind models are now examined to see whether or not they provide a suitable description of the atmosphere of ι Aur, by satisfying the observational constraints. It is not known *a priori* whether or not the wind forming region is the same as that giving rise to the transition region lines, but this possibility must be included in the range of wind models considered. If the transition region material, such as that emitting in C IV, originates in the wind then the heating by the Alfvén waves must lead to temperatures $Log(T_e) \geq 5.0$, and perhaps $Log(T_e) \simeq 5.25$ to account for the N V. This could then produce the observed C IV radiation. A more stringent constraint is that the amount of material in a given temperature range agrees with the emission measure derived from the observed fluxes. It is convenient to compare the wind models with the emission measure distribution integrated over 0.10dex in $Log(T_e)$, *i.e.,* $E_m(0.1)$ as described in Chapter 6. The use of the $E_m(0.1)$

is preferable to $E_m(0.3)$ because it is more sensitive to the structure in the regions where the emission measure changes rapidly with temperature.

The initial Alfvén wave flux can be written in terms of α_0, *i.e.*,

$$F_{A0} = \frac{\delta B_0{}^2}{8\pi} V_{A0} = 1.12 \times 10^{-2} \alpha_0 B_0^3 \rho_0^{-1/2} \mathrm{erg\,cm^{-2}\,s^{-1}}. \qquad (7.9)$$

The radiation losses from the chromosphere and transition region can be found adding the contributions from the different temperature regions (0.1 dex in the logarithm of T_e) using equation (4.23). Using the emission measure $E_m(0.1)$ from Model 4 (Table 6-5) and the power loss function for $Log(T_e) > 3.85$ the contribution to the radiative losses can be found for this temperature range. Below this temperature most of the radiative losses occur from optically thick lines, so the observed Mg II h and k line fluxes have been used to estimate the radiation losses between the base of the wind models ($\sim Log(T_e) = 3.74$) and $Log(T_e) = 3.85$. Linsky and Ayres (1978) estimate that the Mg II h & k lines represent about 30% of identifiable emission-line cooling in the solar chromosphere, so as an approximation the fraction of Mg II h & k line formed in the above temperature range is scaled by this factor to find the total radiation losses. The total radiation losses are found to be $1.5 \pm 0.5 \times 10^5$ erg cm^{-2} s^{-1}.

The radiation losses suggest that the initial Alfvén wave flux must be $> 1.5 \pm 0.5 \times 10^5$ erg cm^{-2} s^{-1}. However, most of the energy lost is from the H Ly-α and Mg II h & k lines, formed below $T_e \leq 2 \times 10^4$ K, so this constraint is common to all models with $T_{Max} \geq 6000$ K. To match the radiation losses alone the initial Alfvén wave flux requires $B_0 \geq 1.6$ Gauss.

The models will produce a small overestimate in the amount of material in the temperature range where the radiative loss curve has been smoothed out to remove numerical instabilities caused by the H Ly-α peak and negative gradients. The radiative power loss as a function of T_e below $Log(T_e) \simeq 4.0$ is uncertain, mainly because the assumption of an optically thin plasma becomes inappropriate. Thus it is useful to compare the emission measure distribution above $Log(T_e) \simeq 3.9$, bearing in mind that below $\sim 2 \times 10^4$ K the wind models will overestimate the emission measure.

The line shifts and profiles can also constrain the velocity fields in the wind, provided, of course, that the line features are formed within the wind. The Si III] line is broad and appears to be at rest compared to the photosphere. This broadening could result from 'turbulence' in the line forming region or from the emission being from an optically thin expanding shell of gas. The shell would need to be far away from the star ($R \sim 2\,R_*$) so that it does not occult redward emission, thus giving a broad profile. The S I, C II] and O I] lines are formed at lower temperatures but have cleaner profiles. These lines also appear to be formed at the rest frame of the photosphere. The C II] lines are broader than the IUE point spread function, and the broadening could again be due to turbulence. The line broadening, due to the passage of Alfvén waves in the wind, can be calculated (under certain assumptions, see below) and compared with the observations. The asymmetries in the Mg II h & k lines and the O I resonance lines can result from a wind flow in the line forming region.

As discussed earlier, the 'hybrid' giants are characterised by double absorption features in the Mg II and Ca II resonance lines. The low velocity component can be accounted for by interstellar absorption, while the high velocity absorption troughs occur mostly at $\leq 100\,\mathrm{km\,s^{-1}}$ (towards the observer). This velocity must be reproduced somewhere in the wind model where there is sufficient opacity to scatter the photons in the Mg II h & k lines.

Another constraint on the wind models is the estimated mass-loss rate. Drake and Linsky (1979) infer an upper-limit to the ionised mass-loss rate of $\leq 2 \times$

10^{-9} $M_\odot$ yr^{-1} for 'hybrid' stars, from the non-detection of ι Aur, θ Her, γ Aql and α Aqr in the 6 cm radio continuum survey. A value of $\leq 1.7 \times 1\bar{0}^9$ $M_\odot$ yr^{-1} is found for ι Aur. However, since the ionisation fraction is not known, a further constraint is required. An estimate of the mass-loss rate can be found from the requirement of a sufficiently high column mass of N_{MgII} to scatter the wind, *i.e.,* the optical depth in the wind must be $\tau_0 > 1$ in each part of the line scattering profile. However, it is not possible to unambiguously determine which part of the asymmetric profile is due to bulk mass motions in the line forming region and which part is due to scattering in the overlying wind. If one assumes that the wind scattering is centered on the middle wavelength of the absorption trough, then the line must also be optically thick out to at least the edges of the observed absorption trough. If one assumes a Doppler width for the absorption profile of 10 km s^{-1} (a value found for the interstellar medium, Anderson *et. al.*, 1978) then the relation,

$$\tau = \tau_0 exp\left[-(\frac{\Delta V}{\Delta V_{Dopp}})^2\right], \tag{7.10}$$

gives the optical depth at line centre of $\geq 5 \times 10^2$. For the Mg II h & k lines this implies a column density of $\int N_H dh > 4 \times 10^{19}$ cm^{-2}. Now the mass-loss rate can be evaluated from the wind models in the region where the material is in the Mg II state, so that the gas can scatter the radiation. Then assuming that the scattering region covers the entire stellar surface,

$$\dot{M} \sim 4\pi\mu M_H V_{Abs} \bar{N}_{Scat} R^2_{Scat}, \tag{7.11}$$

where the subscript refers to the region of line scattering and the bar to the mean density in the scattering region. As the wind velocity reaches an asymptotic limit the velocity is essentially constant, so the density decreases with the radius squared. Most of the scattering will occur where the contributions to the column density are greatest, *i.e.,* between $R_{Scat} < R < 3R_{Scat}$, so that the spatial extent of the scattering region is $\sim 2R_{Scat}$. Thus the column density can be written in terms of the mean density and spatial extent of the region of scattering. The mass-loss rate is then approximately,

$$\dot{M} \simeq 3 \times 10^{-30} \int N_H dh \left(\frac{R_{Scat}}{R_*} \right) \mathrm{M}_\odot \, yr^{-1}. \tag{7.12}$$

Now if the wind is cool and the scattering occurs just above the line forming region $R_{Scat} > R_*$, taking a lower limit with $R_{Scat} \simeq R_*$, leads to a lower limit to the mass-loss rate in ι Aur of $\dot{M} \geq 1 \times 10^{-10}\,\mathrm{M}_\odot\, yr^{-1}$. For the models calculated here $R_{Scat} \geq 6R_*$, thus the estimate of the mass loss becomes $\dot{M} \geq 8 \times 10^{-10}\,\mathrm{M}_\odot\,\mathrm{yr}^{-1}$.

The two inequalities for the observed mass-loss rate are in close agreement to each other and provide a good estimate for the ionised mass-loss rate because one estimate is a lower limit and the other is an upper limit. The uncertainty in the derived mass-loss rate from the Mg II line scattering argument arises from the uncertainty in the opacity in the scattering region and also from the uncertainty of the line broadening parameter b. A further estimate of the total mass loss rate expected from ι Aur can be found from the semi-empirical relationship of Reimers (1975, 1977). This relationship for cool luminous stars is based on dimensional arguments, *i.e.*,

$$\dot{M}(M_\odot\,\mathrm{yr}^{-1}) = \mathrm{Constant}\frac{(L/L_\odot)}{(g/g_\odot)(R_*/R_\odot)}, \tag{7.13}$$

where L is the luminosity, g is the surface gravity and R is the radius. The constant of proportionality is determined by comparing this relationship with spectroscopically determined mass-loss rates and other indirect methods and a range of values from $1 - 6 \times 10^{-13}\, M_\odot \mathrm{yr}^{-1}$ has been determined by Reimers. This relationship will be uncertain by a factor of $2 - 3$ owing to the uncertainties in the parameters in equation (7.13). Taking the adopted values from Table 2-3 and a value for the constant of 3×10^{-13}, gives a mass-loss rate of $3 \times 10^{-9}\, M_\odot\,\mathrm{yr}^{-1}$, which is within a factor of 2 of the upper-limit for the ionised mass-loss rate found by Drake and Linsky (1979). In the following work the lowest estimate of the mass-loss rate is adopted *i.e.*, $\geq 8 \times 10^{-10}\, M_\odot\,\mathrm{yr}^{-1}$.

Also, an estimate of the mass-loss rate in a given model can be found analytically from the Alfvén wave-driven wind formulation. It can be shown that at the base of the wind, the wave force is essentially unchanged for values of $\lambda > 1$ (Hartmann and MacGregor, 1980). This implies that the mass-loss rate is relatively unaffected by the damping length adopted (as long as $\lambda > 1$). At the critical point the thermal pressure is still expected to be small compared to the wave pressure ($M_A \ll 1$) so that,

$$\frac{GM}{2r_{Crit}^2} \simeq \frac{\epsilon_{Crit}}{4\rho_{Crit}} \text{ and } V_{Crit} \simeq \frac{\epsilon_{Crit}}{4r_{Crit}^2}. \tag{7.14}$$

The location of the critical point for the models here varies only a little, taking values between $1.4 < z_{Crit} < 1.7$. Assuming $z_{Crit} = 1.5$ then from equation (E.6),

$$\epsilon_{Crit} \simeq 0.6\epsilon_0\left(\frac{\rho_{Crit}}{\rho_0}\right)^{1/2}. \tag{7.15}$$

Equation (7.14) becomes

$$\frac{GM}{2r_{Crit}^2} = \frac{0.6\epsilon_0}{4(\rho_0\rho_{Crit})^{1/2}} = \frac{0.6\pi^{1/2}F_{A0}}{2B_0\rho_{Crit}^{1/2}}, \tag{7.16}$$

so that,

$$\rho_{Crit} = \frac{0.37\pi}{GM^2}\left(\frac{F_{A0}}{B_0}\right)^2 r_{Crit}^2. \tag{7.17}$$

Since the mass-loss rate (if the wind covers the whole star) at the critical point is,

$$\dot{M} = 4\pi r_{Crit}^2 \rho_{Crit} V_{Crit}, \tag{7.18}$$

one finds,

$$\dot{M} = \frac{4\pi^2}{\sqrt{2}(GM)^{3/2}} z_{Crit} r_0{}^{7/2}\left(\frac{F_{A0}}{B_0}\right)^2. \tag{7.19}$$

Assuming $z_{Crit} = 1.5$ then equation (7.19) becomes,

$$\dot{M} = 3.9 \times 10^{-26}\left(\frac{M_*}{M_\odot}\right)^{-3/2}\left(\frac{R_*}{R_\odot}\right)^{7/2}\left(\frac{F_{A0}}{B_0}\right)^2 M_\odot \mathrm{yr}^{-1}, \tag{7.20}$$

which, using the values in Table 7-2, gives

$$\dot{M} = 4.9 \times 10^{-12}\alpha_0^2 B_0^4 \, M_\odot \, \mathrm{yr}^{-1}. \tag{7.21}$$

This shows that B_0 must be $\geq$ 3.6 Gauss to give a mass-loss rate sufficient to produce the observed scattering in the Mg II resonance lines. Note that this value of B_0 corresponds to the lowest mass-loss rate estimate given above. The equation for the initial energy flux can be written,

$$F_{A0} = 3.42 \times 10^4 \alpha_0 B_0^3 \,\mathrm{erg\,cm^{-2}\,s^{-1}}, \tag{7.22}$$

and as discussed above, the radiation losses alone require $F_{A0} \geq 1.5 \pm 0.5 \times 10^5 \,\mathrm{erg\,cm^{-2}\,s^{-1}}$, *i. e.*, $B_0 \geq 1.6$ Gauss. The minimum value of B_0 required to reproduce the mass-loss rate gives an initial wind energy flux a factor of ten larger than the minimum required to reproduce the observed radiation losses. In section 7-4-1(a) it is shown that this results in wind model emission measures which are larger than those observed. If the wind region is confined to a fraction A of the stellar surface, and extends radially (effectively channeled by the strong magnetic field, which dominates the gas pressure) the estimate of the minimum magnetic field required to produce the observed mass-loss rate is unchanged because both estimates have the same dependence on the area factor. But if the chromospheric and transition region material in the wind are confined to a fraction A of the stellar surface, then the estimate for the observed radiative losses (or the observed emission measure distribution) must be increased by a factor A^{-1}. With an area factor of $\sim 1/10$ the mass-loss rates and radiative losses above $Log(T_e) = 4.0$ can be brought into broad agreement with the observations.

Previous studies of Alfvén wave-driven winds on the 'hybrid' bright giant α TrA have been modelled with lower magnetic fields than 3.5 Gauss. Mendoza (1984) adopted variable gas densities at the base of her models which are a factor of 20 less than that adopted in this work from the chromospheric models in Chapter 6. Mendoza's wind models also produced mass-loss rates which are at the lower limit to the expected mass-loss rates. Because of the higher base gas densities and the lower radiation losses for ι Aur (see HJBD) compared with α TrA, and allowing for the different stellar parameters, it is found that it is *not* possible to produce a one component model wind, that covers the entire surface of the star which can produce the observed mass-loss rate and have an initial Alfvén wave energy flux that gives emission measures consistent with the observations.

7-4 Wind Model Results

A grid of Alfvén wave-driven winds has been calculated for $B_0 \geq 3$ Gauss. The models are specified by the damping length, L, the initial magnetic field, B_0, and the initial wave amplitude α_0. The grid of models calculated covers the parameter space; 3 Gauss $< B_0 <$ 10 Gauss, $0.2 < \alpha_0 < 1.0$ and $0.9 < \lambda < 2.0$. A summary of the wind models is given in Table 7-3 and the results are discussed below.

The results in Table 7-3 can be compared with the theoretical predictions and the observational constraints. The ways in which the free parameters affect the models are now examined. From Models 1, 4, 5, 6 and 7 it can be seen that increasing the damping length and holding the other two parameters constant increases the maximum temperature and increases the maximum velocity, while the mass-loss rates are relatively unchanged. This is a result of the balance between the wave forces and the gravitational forces in the lower part of the atmosphere which is not sensitive to the damping length if $\lambda > 1$. As the damping length increases, the energy is deposited further from the star where the densities get progressively smaller. Thus for a given amount of energy dissipation the gas can reach larger temperatures. Also the momentum deposition at lower densities leads to larger terminal velocities. Figure 7-2 shows the temperature and velocity profiles for Models 1, 4, 5 and 6. Models 12, 15 and 16 also have variable damping lengths and show the same trends.

Table 7-3 A summary of the results from the Alfvén wave-driven wind models. Because the area factor, A, is unknown, the values for the mass-loss rates assume $A = 1$. The values of B are in Gauss, the mass-loss rates are given in terms of solar masses per year and the terminal wind velocity is given in km s^{-1}. T_{Max} is the maximum temperature of the wind. The initial temperature and density are given in Table 7-2. The model parameters are described in the text.

Model	F_{A0}	B	α_0	λ	$\dot{M}$	$Log(T_{Max})$	$V_{Terminal}$
1	6.8(6)	10.0	0.2	1.0	9.3(-9)	4.57	1.0(2)
2	1.0(7)	10.0	0.3	1.0	2.0(-8)	4.25	7.8(1)
3	1.4(7)	10.0	0.4	1.0	3.3(-8)	4.15	6.3(1)
4	6.8(7)	10.0	0.2	0.9	8.8(-9)	4.47	7.4(1)
5	6.8(6)	10.0	0.2	1.5	9.9(-9)	4.53	1.8(2)
6	6.8(6)	10.0	0.2	1.7	1.0(-8)	4.77	2.0(2)
7	6.8(6)	10.0	0.2	2.0	1.0(-8)	4.80	2.3(2)
8	5.8(6)	7.5	0.4	1.0	1.1(-8)	4.32	7.5(1)
9	4.3(6)	7.5	0.3	1.0	6.6(-9)	4.60	1.0(2)
10	2.9(6)	7.5	0.2	1.0	2.8(-9)	5.52	1.8(2)
11	3.0(6)	6.0	0.4	1.0	4.8(-9)	4.65	9.8(1)
12	2.1(6)	5.0	0.5	1.0	3.3(-9)	4.77	1.2(2)
13	1.7(6)	5.0	0.4	1.0	2.2(-9)	5.23	2.0(2)
14	2.6(6)	5.0	0.6	1.0	5.4(-9)	4.55	1.0(2)
15	2.1(6)	5.0	0.5	1.5	4.2(-9)	4.83	1.8(2)
16	2.1(6)	5.0	0.5	2.0	4.2(-9)	5.25	2.6(2)
17	2.2(6)	4.0	1.0	1.0	5.4(-9)	4.41	6.4(1)
18	1.8(6)	4.0	0.8	1.0	3.7(-9)	4.61	8.6(1)
19	1.5(6)	4.0	0.7	1.0	2.7(-9)	4.77	1.2(2)
20	1.1(6)	4.0	0.5	1.0	1.5(-9)	5.22	1.9(2)
21	9.2(5)	3.0	1.0	1.0	1.8(-9)	4.80	1.3(2)

The change in the velocity and temperature structure due to the change in the initial magnetic field can be investigated if the values of λ and α_0 are kept constant. Models 3, 8 and 13 show that as the magnetic field decreases, the mass-loss rate decreases in the way predicted by equation (7.21). The maximum temperature and terminal velocity increase with decreasing magnetic field strength, with Model 11 having gas at temperatures comparable with those observed, but with a terminal

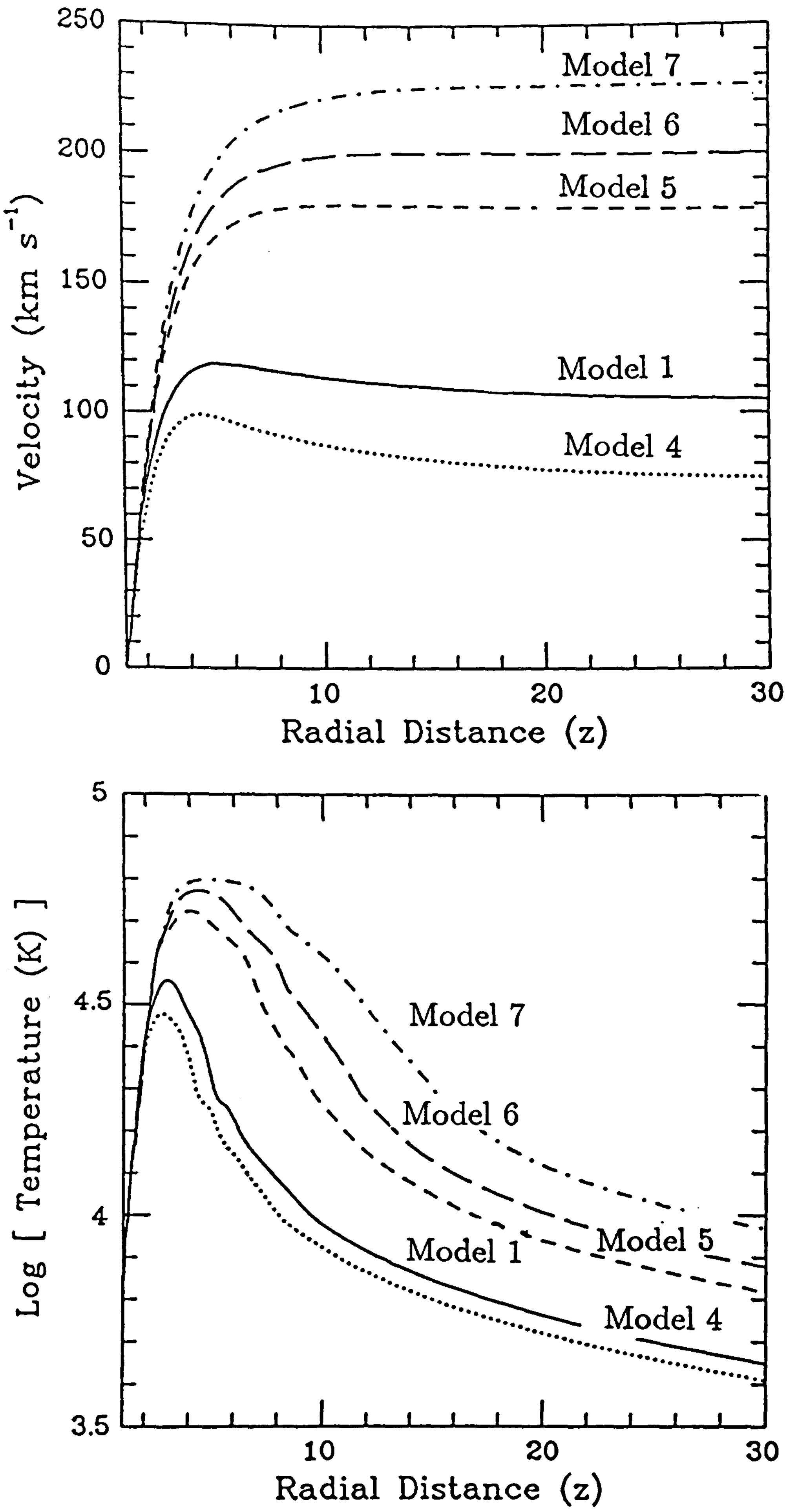

Figure 7-2 The temperature and velocity profiles for Models 1, 4, 5, 6 and 7. Increasing λ increases the distance where the energy and momentum deposition occurs. This results in larger maximum terminal velocities and larger maximum temperatures. Models 1, 4, 5, 6 and 7 all have $B_0 = 10$ Gauss and $\alpha = 0.2$ and have λ values of 1.0, 0.9, 1.5, 1.7, 2.0, respectively.

Top: The velocity distribution plotted as a function of radial distance z.

Bottom : The temperature distribution also plotted against z.

velocity that is too large. The models which have the highest mass-loss rates have lower maximum temperatures. This is due to the fact that the radiative cooling controls the wind temperature. As the velocity profiles are similar in these models the wind density will be proportional to the mass-loss rate, so the radiative cooling will be proportional to the mass-loss rate squared. As B_0 is decreased, with $\alpha = constant$, the cooling rate falls more quickly than the heating rate. The heating of the waves is still balanced by the radiative cooling, but it is the density profile which determines the temperature structure at the base of the wind.

The change in the velocity and temperature profiles when α_0 is decreased are shown in Figure 7-4 from Models 12, 13 and 14. The trends are the same as those when B_0 is decreased, *i.e.,* the heating is $\propto \alpha_0 B_0^3$ and the cooling is $\propto \alpha_0^4 B_0^8$ so that as either B_0 or α_0 are decreased, the heating decreases more slowly than the cooling.

7-4-1 Further Comparison with Observations

The initial constraints placed on the models by the observations are that there is gas at temperatures in excess of $Log(T_e) = 5.0$ and that the gas which scatters the radiation in the Mg II h & k lines is travelling at $< 100 \text{ km s}^{-1}$. It can be seen from Table 7-3 that both the terminal velocity and the maximum temperature increase as the initial energy flux decreases. However, when the gas has reached the maximum temperature constraint the terminal velocity is in excess of that observed.

For example, Model 21 has a terminal velocity of $1.3 \times 10^2 \text{ km s}^{-1}$ and a maximum temperature of $Log(T_e) = 4.80$. From the trends discussed above, lowering α_0, with λ held constant, will raise the maximum temperature but also the terminal velocity. The terminal velocity for $\alpha_0 = 1$ is already in excess of the velocity seen in the wind scattering.

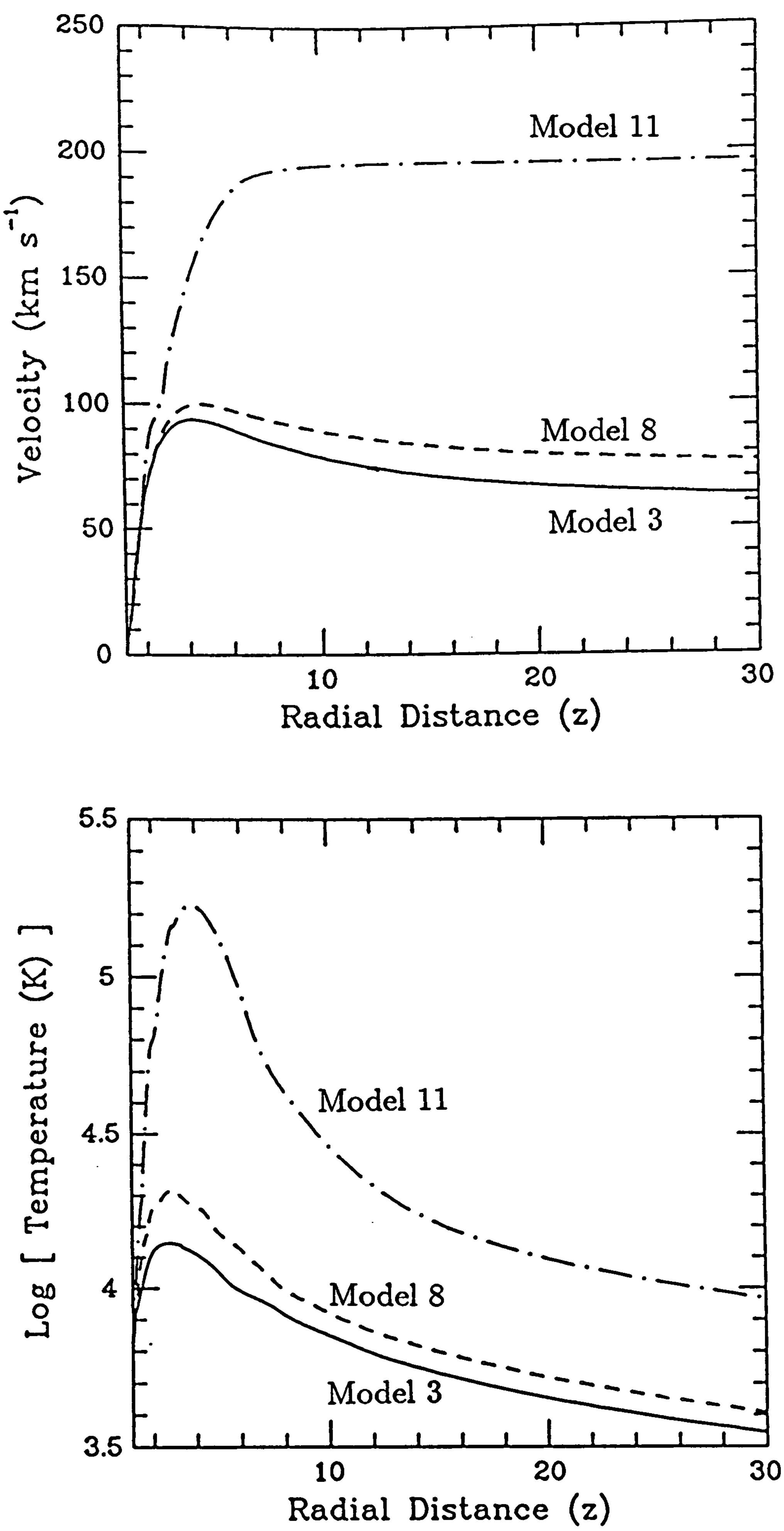

Figure 7-3 The temperature and velocity structure of Models 3, 8 and 11. α and λ have values of 0.4 and 1 respectively. Models 3, 8 and 11 have initial magnetic fields of 10.0, 7.5 and 6 Gauss respectively.

Top : The terminal velocities increase with decreasing magnetic field.

Bottom: The maximum temperature increases as the magnetic field decreases.

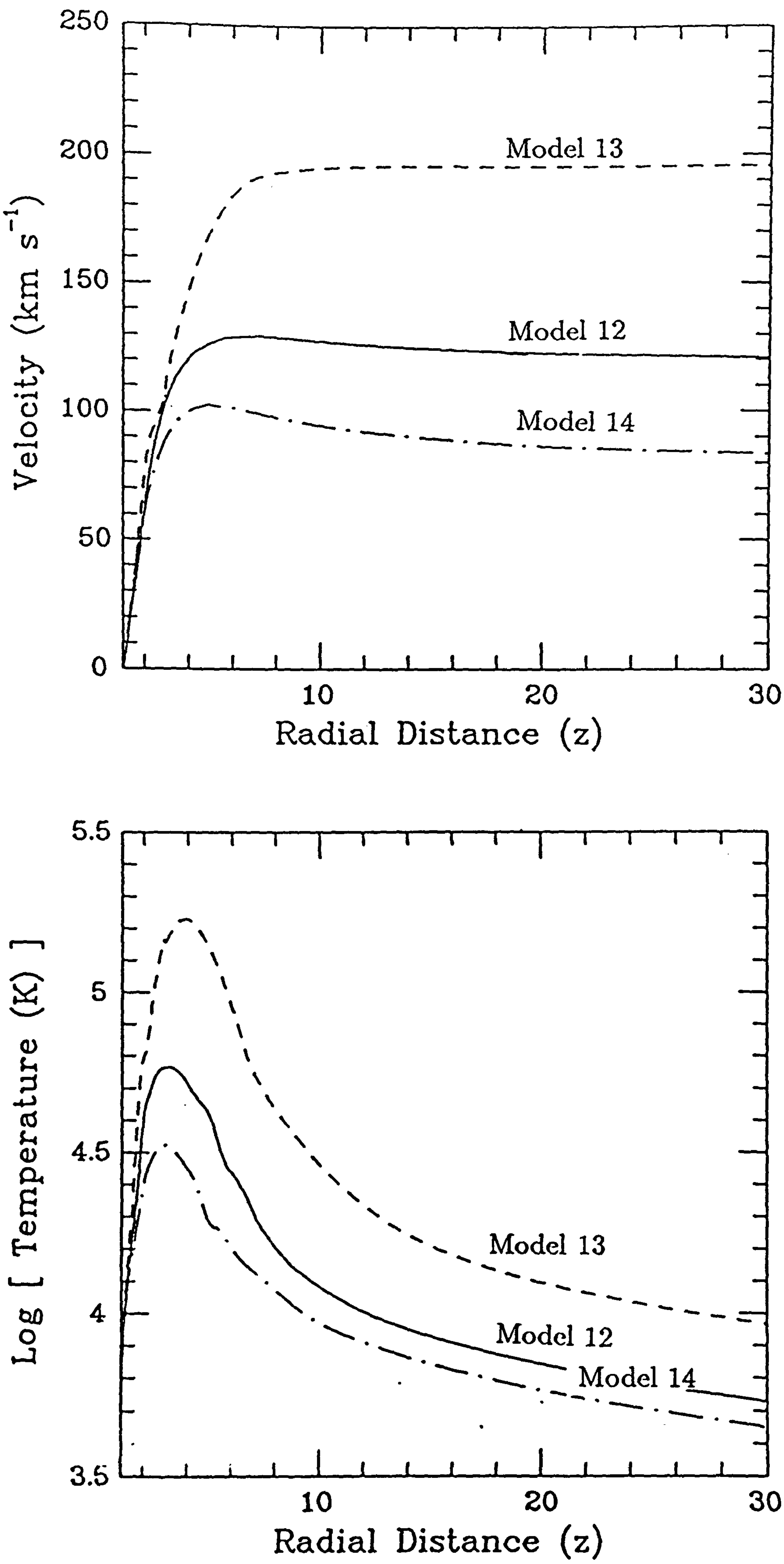

Figure 7-4 The temperature and velocity structures of Models 12, 13 and 14. These models have $B_0 = 5$ Gauss and $\lambda = 1$. The values of α_0 for models 12, 13 and 14 are 0.5, 0.4, 0.6 respectively. The trends in the maximum temperature and terminal velocity are the same as those in Figure 7-3.

7-4-1(a) Emission Measures

If the wind models are to be consistent with the observations, then not only must there be a sufficient energy flux at the base of the wind to be able to produce the observed radiation losses but also the wind models must reproduce the detailed energy losses over a restricted range of temperature. The wind models can be compared directly with the observations via the calculated and observed emission measures (or that from Model 4 in Chapter 6). Figure 7-5 shows the emission measure distribution, $E_m(0.1)$, for models 17 and 19. These models have similar *forms* of the emission measure distributions because above $\sim 2 \times 10^4$ K the shape is determined by the power loss function (Jordan *et al.,* 1987). To compare the models with the observed emission measure distribution, the area factor must be taken into account. If the actual emission lines formed above $Log(T_e) = 3.7$ are restricted to a surface factor A, then the values of the observed emission measures (calculated assuming that the ultraviolet emission lines are formed over the whole star) must be increased by A^{-1}. This explicitly assumes that the emission lines are formed in the wind. If this is *not* the case and the lines are *not* formed in the wind then the observed emission measure distribution should be increased by $(1 - A)$.

Figure 7-5 shows that the emission measures for the wind Models 17 and 19 have emission measures above $Log(T_e) = 4.0$ which are a factor ~ 15 larger than those from the static model (assuming that the emission comes from the majority of the stellar surface). Model 17 which has an emission measure which lies just above that of Model 19 and this reflects the fact that the energy flux for Model 17 is larger than for Model 19 and some of this extra energy flux is deposited at the base of the model which then leads to higher emission measures. The models can be reconciled with the observations if the observed emission is restricted to an area factor, A, then the observed emission measure distribution will be increased by a factor A^{-1}. Note that if the geometry of the wind is included in the static

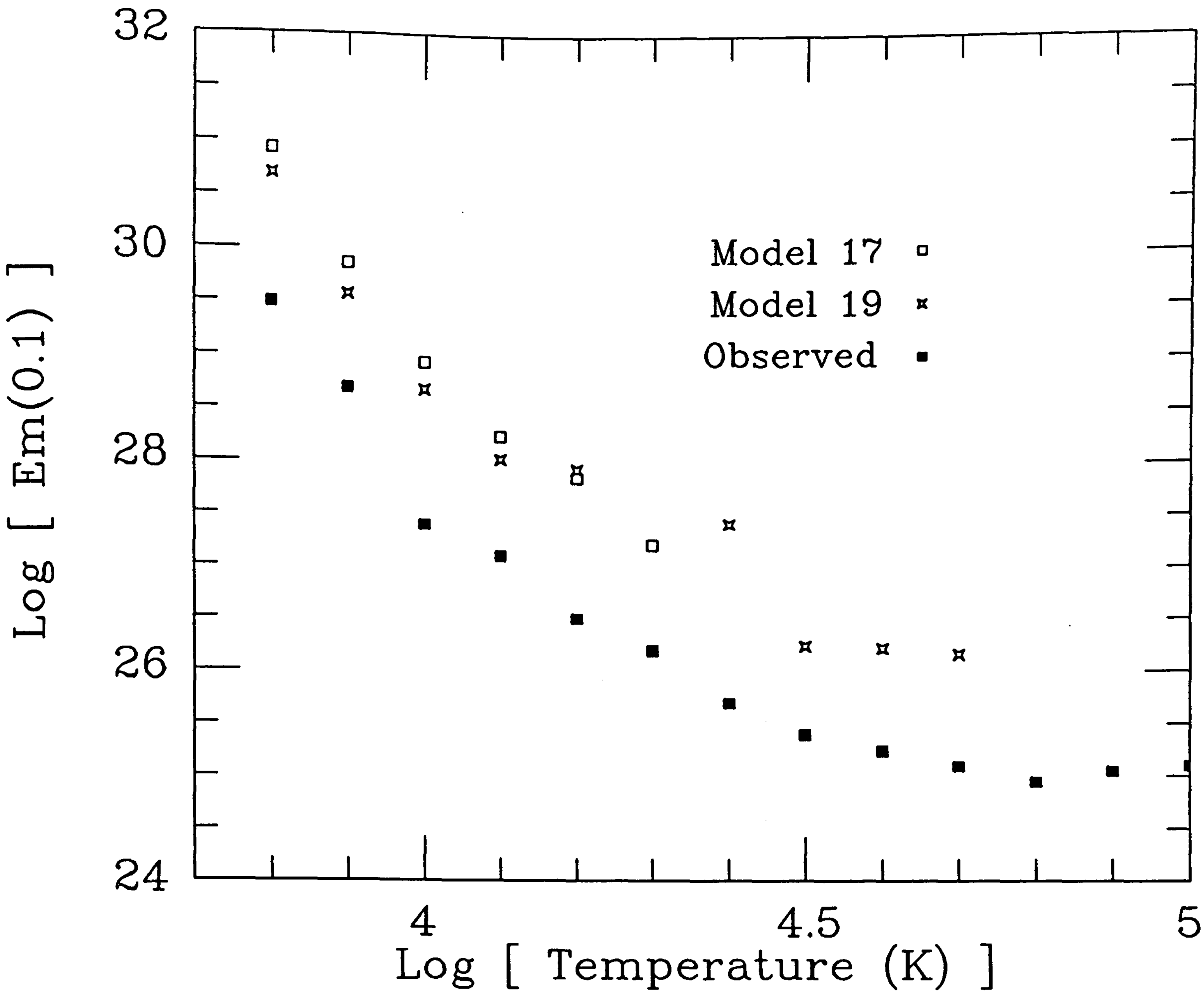

Figure 7-5 The observed emission measure distribution, $E_m(0.1)$, compared with those calculated from Models 17 and 19.

emission measure distribution, via the $(R_*/R)^2$ term, the static emission measure will be slightly lower at higher temperatures *e.g.*, ~ 0.5 dex at $Log(T_e) = 4.5$.

7-4-1(b) Velocity Fields

So far the observational constraints provided by the line profiles have not been used. It is difficult to interpret the line profiles unambiguously. For instance if an optically thin emission line is formed in an outflowing wind far from the star, the radiation from the near and far side would create a broad emission peak which is still centred on the photospheric rest frame velocity. If the emission comes from near the star ($R_{Formation} \sim 1 - 2R_*$), the occulted redshifted line emission from the far side will lead to an observed blueshifted emission feature. The line widths may also be affected by turbulence associated with the deposition of energy from the magnetic field. The effects of turbulence are important in determining the line profiles close to the star, but further out into the wind the expansion controls the line width. The 'hybrid' stars do not show any significant line shifts ($> 7\,\mathrm{km\,s^{-1}}$) for the Si III], C II] and O I] lines compared with the neutral species used to calibrate the wavelength scales. Thus if the lines *are* all formed in the wind, the wind velocity cannot be large where the temperature reaches its peak (at $\sim 10^5$ K), or that the high temperature line Si III] is formed out in the wind, where the lines are broadened by the wind but are symmetrical. If the Si III] and C IV lines are formed in this outer region, the line profiles would be flat topped and have a FWHM of twice the wind velocity. The Si III] line has a FWHM of $\sim 72\,\mathrm{km\,s^{-1}}$ so it is unlikely that it is formed in this outer region. Then by examining the velocity of the gas in the temperature region where the Si III] is formed, the models predict velocities of $\sim 50\,\mathrm{km\,s^{-1}}$. Since this line appears to be at rest in the photospheric frame, this further suggests that the Si III] is not formed in the wind.

In Chapter 4, the line broadening was associated with the magnetic turbulence. Table 7-4 shows the turbulent broadening predicted by Model 21, assuming that $1/2\rho V_{Turb}^2 = \delta B^2/8\pi$ and that V_{Turb} is related to the observed line widths via equation (4.15) (see Section 4-5). It can be seen that the observed turbulent velocities are less than those predicted by the model.

The magnetic turbulent velocities can be reduced by reducing α_0 and/or B_0, but this would lead to mass-loss rates which are too low. The turbulent velocities initially increase as the density falls more rapidly than the wave energy density decreases. The situation is reversed, however, as the density begins to fall off more slowly than the wave energy density. For Model 21 this occurs at $\sim Log(T_e) = 4.6$.

Table 7-4 The wind velocity and magnetic turbulent broadening for Model 21 and the observed line broadening. The velocities are measured in km s^{-1}. The missing data point at $Log(T_e) = 4.5$ is due to the absence of information caused by making a 'jump' at the critical point.

$Log(T_e)$	V_{wind}	Distance z	$V_{Turb}^{Magnetic}$	$V_{Turb}^{Observed}$
3.8	0.3	1.02	11.3	~ 14
3.9	2.8	1.09	55.2	~ 24
4.0	7.8	1.17	72.4	–
4.1	13.0	1.24	86.2	–
4.2	22.9	1.38	104	–
4.3	32.1	1.51	119	–
4.4	40.0	1.59	121	–
4.5	–	–	–	49
4.6	56.3	1.80	124	–
4.7	68.5	1.97	122	–
4.8	98.1	2.62	104	72

7-4-1(c) Gas Densities

Constraints on the electron density can also be used to restrict the range of acceptable wind models. The electron density in the C II] line forming region can be used to constrain the gas pressure below $Log(T_e) = 4.0$. The C III] line density estimate is $6 < Log(N_e) < 9$ at $Log(T_e) = 4.8$. The models in Table 7-4 have electron densities in the range, $8.7 < Log(N_e) < 9.3$ below 10^4 K and $6 < Log(N_e) < 8$ at $Log(T_e) = 4.8$. The electron density, therefore, cannot be used to limit the range of acceptable model solutions.

7-5 Cool Wind Solutions

It has been shown that for the Alfvén wave-driven wind models to satisfy the observations, the wind must originate from a fraction of the surface area < 0.1. It has also been found that it is not possible to reconcile the observations with the wind models which produce the transition region emission lines and the wind in the same region. If the high temperature material is formed in a physically separate region, then one can ask whether cool wind solutions exist which can reproduce the observed Mg II h & k scattering. It was shown in Chapter 6 that in hydrostatic models, the transition region lines are produced from a small amount of material which lies above the Mg II h & k line forming region. Assuming that the photosphere is not affected by the wind, the initial conditions for the base of the wind should still be applicable to a cool wind model. If the wind is cool there are at present few observations which can be used to constrain the range of acceptable wind solutions. Improved exposures of the Al II] line, to give both the flux and the line profile, would be particularly useful since this line has a low temperature of formation but is optically thin. Similarly exposures to optimise both optically thick and thin lines of Fe II are potentially useful.

One constraint is that if the wind *is* cool, it does not have an emission measure which is greater than observed at a given temperature. Radiation is emitted from a continuous range of temperatures so the observed emission measure will become the sum of the emission measures from the two separate regions. As discussed previously, the wind solutions with lower maximum temperature have lower terminal velocities. All the models in Table 4-7 which satisfy the cool wind criterion have terminal velocities below 100 $\mathrm{km\,s^{-1}}$ and these are then possible wind solutions. Without further observations it is not possible to restrict the range of viable wind solutions.

If cool wind solutions prove to be unacceptable, another possible alternative would be that the mass-loss rates are time-dependent. The variation in the wind absorption for the similar 'hybrid' star α TrA suggests that the wind is not in a steady state. Further simultaneous observations of the optically thin transition region line profiles and the Mg II h & k line profiles could show the wind variability and test whether or not the transition region lines are emitted in a region physically separate from the wind.

7-6 Summary

A brief review of wind mechanisms has been given with an emphasis on Alfvén wave-driven winds. Alfvén wave driven winds can potentially drive massive winds and also heat gas to transition region/coronal temperatures, and this makes the mechanism attractive in the context of the 'hybrid' stars. A constant damping length Alfvén wave formulation has been applied to ι Aur. An ionisation fraction has been included below $\sim 10^4$ K for the first time so that the temperature of the gas is determined at the base of the wind where the gas is not fully ionised. It is found that if the wind and observed transition region material both come from the whole stellar surface then there is a massive wind of $> 8 \times 10^{-10}\ M_{\odot}\ \mathrm{yr}^{-1}$. The Alfvén wave flux then produces radiation losses an order of magnitude greater than observed, unless area factors are invoked.

The results show that none of the models in Table 7-3 satisfy the joint constraint of having a wind with a velocity $\sim 75\ \mathrm{km\ s}^{-1}$ and having a maximum temperature of 10^5 K or higher. Also it is found that the wind models predict velocity shifts for the Si III] which are not observed and the predicted non-thermal motions are greater than observed.

This strongly suggests that the wind is formed in a region separate from that which produces the emission lines above $T_e \sim 2 \times 10^4$. However the present observations do not allow a description of the conditions within.

CHAPTER 8. CONCLUSIONS AND FUTURE WORK

The 'hybrid' bright giants, which show evidence of both material at $\sim 10^5$ K and the presence of high velocity blue-shifted absorption in the Mg II h & k line profiles, provide an interesting test for theories concerning the development of coronae and winds in the context of the H-R diagram.

The bright giant ι Aur (K3 II) was recognised as a 'hybrid' by Reimers (1982). Since it is one of the few examples that can be observed at both low and high resolution with IUE it was chosen for study in this Thesis.

The evolutionary status of ι Aur has been discussed in Chapter 2. On the basis of theoretical evolutionary tracks for intermediate mass stars and simple arguments regarding the onset of activity from dynamo action, ι Aur is probably between the base of the RGB and the point on the evolutionary track where the helium core has been ignited (but before the point where the convective envelope disappears as the star moves on to the blue loop phase of its evolution). The mass of ι Aur is estimated to be $\sim 6\,M_{\odot}$. Abundances appropriate to the first dredge-up phase have been adopted on the basis of studies of ι Aur and other hybrids.

IUE low resolution spectra have been used to determine fluxes in lines formed in the transition region; high resolution spectra supplement these fluxes and allow the widths of a few lines to be measured. The high resolution observations show that profiles of strong lines such as the O I resonance multiplet and the Mg II h & k are asymmetric and self-reversed. This asymmetry exists in all members of the O I multiplet and must therefore be due to bulk mass motions in the line forming (or scattering) region and not to interstellar absorption. There are two absorption features in the wings of the Mg II h & k lines. The low velocity feature, at $\sim -6\mathrm{km\,s^{-1}}$ relative to the photosphere, is consistent with interstellar absorption while the high velocity component at $\sim 75\,\mathrm{km\,s^{-1}}$ is due to scattering of the line photons in a fast moving wind. The optically thin lines from the transition region do not show significant velocity shifts with respect to the photospheric rest frame. They are also broader than the IUE point spread function, indicating the presence of non-thermal motions in excess of the local sound speed.

The line fluxes in the effectively thin lines formed above $\sim$ 8000 K and an upper-limit to the X-ray flux, have been used to derive the emission measure distribution. This is combined with the equation of hydrostatic equilibrium to make static models of the outer atmosphere. The electron density has been measured from the C II] lines, but C III] provides only an upper-limit of $N_e \leq 10^9$ cm^{-3} at $\sim 6.3 \times 10^4$ K.

The energy balance of the static models in Chapter 4 shows that thermal conduction is not likely to be important below $\sim 10^5$ K. Between $\sim 10^4$ K and $\sim 10^5$ K the energy input is balanced by radiation. By considering acoustic waves, shock waves and MHD waves, it is shown that the most probable mechanism for transporting the energy from below $Log(T_e) = 4.0$ to the regions where the energy is radiated away is via magnetic disturbances propagating with the Alfvén velocity. If the magnetic field is radial then the magnetic field strength must be at least $\sim 1/3$ Gauss. Thus a much lower field is required than in the case of the Sun.

One component model chromospheres for the 'hybrid' bright giant, ι Aur, have been constructed as described in Chapters 5 and 6, assuming a plane parallel geometry. This is the first time that a model chromosphere has been constructed for a 'hybrid' bright giant. Model 4 accounts satisfactorily for the line fluxes in lines formed over a range of chromospheric temperatures, *i.e.*, the fluxes in Mg II, Al II] and Si II. The models also match the electron density derived for the C II] lines as well as reproducing the observed widths of the Mg II h & k lines. This result suggests that the width of the resonance lines is partly controlled by the increased column density of the line forming region. The microturbulence also plays a role in determining the line width.

For the first time, calculations have been made of the excitation of the Fe I uv44 $y^5G_3^0$ level by the Mg II k line. The calculations show that the emission in the Fe I lines $\lambda\lambda$2844, 2823 is very sensitive to the structure of the atmosphere near the temperature minimum region. Further calculations are needed to examine the effects of photon loss in the Mg II k line on the observed profile.

The effects of a constant damping length, Alfvén wave-driven wind on the atmosphere of ι Aur have been investigated. For the first time a variable ionisation fraction has been included into the wind formulation and this is important in determining the temperature at the base of the winds. For the wind models to be consistent with the observations of the transition region line fluxes the wind must originate from a small fraction (< 0.1) of the stellar surface. Overall it has been found that it is unlikely that the transition region lines are formed in a warm ($\sim 10^5$ K) wind. It is more likely that the wind is cool, with $T_{Max} \leq 2 \times 10^4$ K. Beyond this it is not possible at present to further determine the conditions in the cool wind. The hybrid giants contrary to the earlier suggestions by Hartmann *et al.* (1981, 1982), do not seem to require high velocity, warm wind.

Further observations are required to enable better measurements to be made of the physical properties of the outer atmospheres of the 'hybrid' bright giants. The Hubble Space Telescope shall be able to provide higher resolution than the IUE satellite and this will allow more accurate determinations of the line profiles. The greater sensitivity should allow improved measurements of the line fluxes. In particular, more accurate observations of the transitions of Al II, λ1670 and the optically thin λ2669, could provide tighter constraints on the wind region because these lines are formed in similar regions of the atmosphere as the Mg II h & k lines.

Ground based observations of the Ca II H & K and the infrared triplet lines are underway. These together with the Mg II h & k lines will be able to constrain the lower part of the chromospheric models because the Ca II lines are formed deeper into the atmosphere than the Mg II h & k lines.

The proposed Lyman satellite and EUV satellite should be able to observe the O VI $\lambda1032$ and $\lambda1038$, lines, which are formed at $\sim 3.5 \times 10^5$ K. These lines could then be used to constrain the emission measure distribution between N V and the X-ray upper-limit (see Byrne and Rodono, 1988). Future X-ray satellites such as ROSAT may also provide useful data.

Regarding the treatment of the radiative transfer, it is important to obtain fast PRD computer codes which can be used in *moving* atmospheres, in order that the asymmetric line profiles of the resonance lines can be treated self-consistently. The possibility of solving non-LTE problems in spherical symmetry would enable the chromospheric modelling to be extended further into the wind.

The Alfvén wave-driven wind models could be improved by a specific treatment of the wave damping. Also a self-consistent power loss function for temperatures $Log(T_e) < 4.0$ is needed, taking opacities into account.

Finally, given the geometry indicated, *i.e.*, spatially separate wind and transition regions, long term studies to examine variability may be able to distinguish between this type of solution and the alternative of intermittent episodes of mass loss.

REFERENCES

Anderson, R. C., Henry, R. C., Moos, H. W. and Linsky, J. L., 1978. *Astrophys. J.,* **226**, 883.

Antiochos, S. K., Haisch, B. M. and Stern, R. A., 1986. *Astrophys. J.,* **307**, L55.

Arnaud and Rosenflug, 1985, *preprint.*

Athay, R. G., 1976, *The Solar Chromosphere and the Corona: Quiet Sun* , D. Reidel, Dordrecht, 384.

Avrett, E. H., 1981, *Solar Phenomena in Stars and Stellar Systems*, Eds. Bonnet, R. M. and Dupree, A. K., D. Reidel, Dordrecht, 173.

Ayres, T. R., 1975. *Astrophys. J.,* **200**, 660.

Ayres, T. R., 1985. *Astrophys. J.,* **291**, L7.

Ayres, T. R., Judge, P. G., Jordan, C., Brown, A. and Linsky, J. L., 1986. *Astrophys. J.,* **311**, 947.

Ayres, T. R. and Linsky, J. L., 1975. *Astrophys. J.,* **200**, 660.

Ayres, T. R., Linsky, J. L., Basri, G. S., Landsman, W., Henry, R. C., Moos, H. W. and Stencel, R. E., 1982. *Astrophys. J.,* **256**, 550.

Ayres, T. R., Linsky, J. L., Vaiana, G. S., Golub, L. and Rosner, R., 1981a. *Astrophys. J.,* **250**, 293

Ayres, T. R., Marstad, N. C. and Linsky, J. L., 1981b. *Astrophys. J.,* **247**, 545.

Ayres, T. R., Moos, H. W. and Linsky, J. L., 1981c. *Astrophys. J.,* **248**, L137.

Baluja, K. L., Burke, P. G. and Kingston, A. E., 1980, *J. Phys. B.* , **13**, L543

Baluja, K. L., Burke, P. G, and Kingston, A. E., 1981, *J. Phys. B.* , **14**, 1333.

Barnes, T. G., Evans, D. S. and Moffett, T. J., 1978. *Mon. Not. R. astr. Soc.,* **183**, 285..

Basri, G. S., Linsky, J. L. and Ericksson, K, 1981. *Astrophys. J.,* **251**, 162.

Beckers, J. M., 1972. *Ann. Rev. Astr. Astrophys.,* **10**, 73.

Belcher, J. W., 1971. *Astrophys. J.,* **168**, 509.

Belvedere, G., 1983. *Activity in Red-Dwarf Stars*, Ed. Byrne, P. B. and Rodono, M., 579

Bernat, A. P., Honeycutt, R. K., Kephart, J.E., Cow, C.E., Sandford, M. T., II and Lambert, D. L., 1978. *Astrophys. J.,* **219**, 532..

Baliunas, S. L. and Butler S. E., 1980. *Astrophys. J.,* **235**, L45.

Blackwell, D. E. and Shallis, M. J., 1977. *Mon. Not. R. astr. Soc.,* **180**, 177.

Boggess, A., *et al.*, 1978a. *Nature,* **275**, 372.

Boggess, A., *et al.*, 1978b. *Nature,* **275**, 377.

Bohlin, R. C. and Holm, A.V., 1983. IUE NASA Newsletter, **10**, 3.

Bohlin, R. C., Savage, B. D. and Drake, J. F., 1978. *Astrophys. J.,* **224**, 132..

Böhm-Vitense, E., 1972. *Astr. Astrophys.,* **17**, 335.

Bonnell, J. and Bell, R. A., 1982. *Mon. Not. R. astr. Soc.,* **201**, 253.

Brosius, J. W., Mullan, D. J. and Stencel, R. E., 1985. *Astrophys. J.,* **288**, 310.

Brown, A., 1986a, *4th Cambridge Workshop on Cool Stars and Stellar Systems and the Sun*, Springer-Verlag, 454

Brown, A., 1986b. *Advances in Space Research*, **6**, No. 8, 195..

Brown, A., Jordan, C. and Wilson, R., 1979, *The First Year of IUE*, Ed. Willis, A. (UCL).

Brown, A., Ferraz, M. C. de M. and Jordan, C., 1984. *Mon. Not. R. astr. Soc.,* **207**, 831..

Burton, W. M., Jordan, C., Ridgeley, A. and Wilson, R., 1971, *Phil. Trans. Roy. Soc. Lond.*, **A. 270**, 81

Brown, A., Jordan, C., Stencel, R. E., Linsky, J. L. and Ayres, T. R., 1984. *Astrophys. J.,* **283**, 731..

Byrne, P. B., Dufton, P. L., Kingston, A. E., Lennon, D. J. and Murphy, H. M., 1988. *Astr. Astrophys.,* **197**, 205.

Byrne, P. B. and Rodono, M., 1988, *Gemini Suppl.*, **No. 21** , 4

Carlsson, M., 1986, *Uppsala Astronomical Observatory*, Report No. 33 .

Carpenter, K. G. and Wing, R. F., 1979, *Bull. Am. Astr. Soc.* **11**, 419.

Carpenter, K. G., Wing, R. F. and Stencel, R. E., 1985. *Astrophys. J. Suppl.,* **57**, 405..

Cassatella, A., Barbero, J., and Benvenuti, P., 1985. *Astr. Astrophys.,* **144**, 335.

Cassatella, A. and Harris, A. W., 1983. IUE ESA Newsletter, **17**, 12

Cassatella, A., Ponz, D. and Selvelli, P.L., 1981. ESA IUE Newsletter, **10**, 31.

Cassatella, A., Ponz, D. and Selvelli, P.L., In Press, 1988.

Cassinelli, J. P., 1979. *Ann. Rev. Astr. Astrophys.,* **17**, 275..

Cassinelli, J.P. and MacGregor, K. B., 1986, *Physics of the Sun*, Eds. Sturrock, P. A., Holzer, T. E., Mihalas, D. M. and Ulrich, R. K., D. Reidel, Dordrecht, 47

Castor, J., 1981, *Physical Processes in Red Giants*, Eds. Iben, I. and Renzini, A., D. Reidel.,285.

Cooper, J., Ballagh, R. J., Burnett, K, and Hummer, D. G., 1982. *Astrophys. J.,* **260**, 299..

Cox, D. P. and Tucker, W. H., 1969. *Astrophys. J.,* **157**, 1157.

Cram, L., 1987, *Cool Stars, Stellar Systems, and the Sun*, Eds. Linsky, J. L. and Stencel, R. E., Springer-Verlag, 123

Deutsch, A. J., 1956. *Astrophys. J.,* **123**, 210..

Drake, S. A., Brown, A. and Linsky, J. L., 1984. *Astrophys. J.,* **284**, 774.

Drake, S. A. and Linsky, J. L., 1986. *Astronomical Journal,* **91**, 602.

Dufton, P. L., Berrington, K., A., Burke, P. G. and Kingston, A. E., 1978. *Astr. Astrophys.,* **62**, 111.

Dufton, P. L. and Kingston, A. E., 1985. *Astrophys. J.,* **289**, 844.

Dupree, A. K., Black, J. H., Hartmann, L. and Raymond, J. C., 1979, *The first Year of IUE*, Ed. Willis, A., UCL.

Dupree, A. K. and Reimers, D., 1987, *Exploring the Universe with the IUE Satellite*, Ed. in Chief Kondo, Y., 321.

Endal, A. S. and Sofia, S., 1979. *Astrophys. J.,* **232**, 531..

Egret, D., Keenan, P. C. and Heck, A., 1982. *Astr. Astrophys.,* **106**, 115.

Evans, R. G., Jordan, C. and Wilson, R., 1975. *Mon. Not. R. astr. Soc.,* **172**, 585.

Feild, G. B. and Steigman, G., 1971. *Astrophys. J.,* **166**, 59.

Froeses Fisher, C., 1976. Can. J. Phys., **54**, 1465

Gahm, G. F., 1974, *Astron. Astrophys. Suppl.*, **18**, 259.

Garstang, R. H., 1961. Proc. Camb. Phil. Soc., **57**, 115.

Gerola. H., Linsky, J. L., Shine, R., McClintock, R. C., Henry, R. C. and Moos, H. W., 1974. *Astrophys. J.,* **193**, L107..

Giddings, J. R., 1982. *IUEDR: A program for IUE Data Reduction*, Starlink User Note **37**

Gray, D. F., 1982. *Astrophys. J.,* **262**, 682..

Gray, D. F. and Nagar, P., 1985. *Astrophys. J.,* **298**, 765.

Gray, D. F. and Toner, P., 1986. *Astrophys. J.,* **310**, 277.

Gustafsson, B., Bell, R. A., Eriksson, K, and Nordlund, Å, 1975. *Astr. Astrophys.,* **42**, 407.

Haisch, B. M., 1986. *Irish Astronomical Journal,* **17**, 200.

Haisch, B. M., 1987, *Cool Stars, Stellar Systems, and the Sun* Eds. Linsky, J. L, and Stencel, R. E., Springer-Verlag, **291**, 269

Haisch, B. M. and Linsky, J. L., Weinstein, A. and Shine, R. A., 1977. *Astrophys. J.,* **214**, 785..

Haisch, B. M. and Simon, T., 1982. *Astrophys. J.,* **263**, 252.

Harris, A. W. and Sonneborn, G., 1986, *How to use IUE Data*, **RAL-86-105**, 36

Hartmann, L. and Avrett, E. H., 1984. *Astrophys. J.,* **284**, 238..

Hartmann, L., Dupree, A. K. and Raymond, J. C., 1980. *Astrophys. J.,* **236**, L143.

Hartmann, L., Dupree, A. K. and Raymond, J. C., 1981. *Astrophys. J.,* **246**, 193.

Hartmann, L., Edwards, S. and Avrett, E., 1982. *Astrophys. J.,* **261**, 279.

Hartmann, L., Jordan,C., Brown, A. and Dupree, A. K., 1985. *Astrophys. J.,* **296**, 576.

Hartmann, L. and MacGregor, K. B., 1980. *Astrophys. J.,* **242**, 260.

Hayes, M. A. and Nussbaumer, H., 1984. *Astr. Astrophys.,* **134**, 193.

Hearn, A. G., 1967. *Mon. Not. R. astr. Soc.,* **136**, 417.

Heinzel, P., 1985. Preprint No. 12 *Astron. Inst. Czech. Acad. Sci.*, Ondřejov Observatory

Hollweg, J. V., 1973. *Astrophys. J.,* **181**, 547..

Holzer, T. E., 1980, *Cool Stars, Stellar Systems, and the Sun* Ed. Dupree, A. K., Smithsonian Astrophysical Special Report No.389, 153

Holzer, T. E., Flå , T. and Leer, E, 1983. *Astrophys. J.,* **275**, 808..

Howarth, I. D. and Maslen D., 1984. *DIPSO - a friendly spectrum analysis program*, Starlink User Note **50**

Hummer, D. G., 1962. *Mon. Not. R. astr. Soc.,* **125**, 21..

Hummer, D. G., 1969. *Mon. Not. R. astr. Soc.,* **145**, 95.

Iben, I. Jr., 1967. *Ann. Rev. Astr. Astrophys.,* **5**, 425.

Iben, I. Jr., 1972. *Astrophys. J.,* **178**, 433.

Iben, I. Jr., 1981, *Physical Processes in Red Giants*, Eds. Iben, I. Jr. and Renzini, A., D. Reidel, Dordrecht, 3

Jacques, S. A., 1977. *Astrophys. J.,* **215**, 942..

Jamar, C., Macon-Hercot, P., Praderie, F., 1976. *Astr. Astrophys.,* **52**, 373.

Jefferies, J. T. and White, O. R., 1960. *Astrophys. J.,* **132**, 767.

Jordan, C., 1967., *Solar Physics*, **2**, 441

Jordan, C., 1969. *Mon. Not. R. astr. Soc.,* **142**, 501..

Jordan, C., 1980. *Astr. Astrophys.,* **86**, 355.

Jordan,C., 1986. *Irish Astronomical Journal,* **17**, 227.

Jordan, C., Ayres, T. R., Brown, A., Linsky, J. L. and Simon, T., 1987. *Mon. Not. R. astr. Soc.,* **225**, 903.

Jordan, C., and Brown, A., 1981, *Solar Phenomena in Stars and Stellar Systems*, Eds. Bonnet, R. M. and Dupree, A. K., D. Reidel, Dordrecht, 199

Jordan, C., Brown, A., Walter, F. M. and Linsky, J. L., 1986. *Mon. Not. R. astr. Soc.,* **218**, 465..

Jordan, C. and Judge, P. G., 1984, *Physica Scripta*, **T8**, 43

Jordan, C., Judge, P. M. and Johansson, S., 1985, *IAU Colloq.*, **86**, Ed. Doschek, G. A., Washington D. C., 51.

Jordan, C., and Linsky, J. L., 1987, *Exploring the Universe with the IUE Satellite* ed Kondo, Y., D. Reidel, Dordrecht, 259.

Judge, P. G., 1986a. *Mon. Not. R. astr. Soc.,* **221**, 119..

Judge, P. G., 1986b. *Mon. Not. R. astr. Soc.,* **223**, 239.

Judge, P. G., Jordan, C. and Rowan-Robinson, M, 1987. *Mon. Not. R. astr. Soc.,* **224**, 93.

Kahler, J. B., Iben, I. and Becker, S. A., 1978. *Astrophys. J.,* **224**, L63.

Keenan, F. P.,Berrington, K. A., Burke, P. G., Kingston, A. E. and Dufton, P. L., 1984. *Mon. Not. R. astr. Soc.,* **207**, 459.

Kelch, W. L., Linsky, J. L. and Worden, W. P., 1979. *Astrophys. J.,* **229**, 700.

Kelly, R. L., 1979. *Atomic Emission Lines in the Near Ultravioltet: Hydrogen Through Krypton: Section I*, NASA TM-80268

Kelly, R. L., 1982. *Atomic and Ionic Emission Lines Below 2000 Angstroms-Hydrogen Through Argon*, ONRL Report 5922.

Kjærgaard, P., Gustafsson, B., Walker, G. A. H. and Hultqvist, L, 1982. *Astr. Astrophys.,* **115**, 145..

Kovács, N., 1983. *Astr. Astrophys.,* **120**, 21.

Kuperus, M., 1965, *Rech. Astron. Obs. Utrecht*, **17**, 1

Kuperus, M., 1969, *Space Sci. Rev.*, **9**, 713..

Lambert, D. L., 1981, *Physical Processes in Red Giants*, Eds. Iben, I. Jr. and Renzini, A., D. Reidel, Dordrecht, 115.

Lambert, D. L. and Ries, L. M., 1981. *Astrophys. J.,* **248**, 228..

Lennon, D. J., Dufton, P. L., Hibbert, A. and Kingston, A. E., 1985. *Astrophys. J.,* **294** , 200.

Linsky, J. L., 1980. *Ann. Rev. Astr. Astrophys.,* **18**, 439.

Linsky, J. L., 1981, *Physical Processes in Red Giants*, Eds. Iben, I. Jr. and Renzini, A., D. Reidel, Dordrecht, 247

Linsky, J. L., 1985, *Progress in Stellar Spectral Line Formation Theory*, Eds. Beckman, J. E. and Crivellari, L., D.Reidel, Dordrecht, 1.

Linsky, J. L. and Ayres, T. R., 1978. *Astrophys. J.,* **220**, 619..

Linsky, J. L. and Haisch, B. M., 1979. *Astrophys. J.,* **229**, L27.

Linsky, J. L. and Worden, S. P., MacClintock, W. and Robertson, R. W., 1979. *Astrophys. J. Suppl.,* **41**, 47.

Luck, R. E., 1978. *Astrophys. J.,* **219**, 148.

Luck, R. E. and Lambert, D. L., 1981. *Astrophys. J.,* **245**, 1018.

Lwin, N., McCartan, D. G. and Lewis, E. L., 1977. *Astrophys. J.,* **213**, 599.

MacGregor, K. B., 1987, *Cool Stars, Stellar Systems, and the Sun*, Eds. Linksy, J. L., and Stencel, R.E., Springer-Verlag, 250

Mangeney, A. and Praderie, F., 1984. *Astr. Astrophys.,* **130**, 143..

Marilli, E. and Catalano, S., 1984. *Astr. Astrophys.,* **133**, 57.

Matsushima, S., 1968. *Astrophys. J.,* **154**, 715.

McWhirter, R. W. P., Thonemann, P. C. and Wilson, R., 1975. *Astr. Astrophys.,* **40**, 63.

Mendoza, B. E., 1984, *Oxford University D.Phil Thesis*

Mendoza, C., *J. Phys. B.*, 1981, **2465**.

Mihalas, D., 1978, *Stellar Atmospheres*, Freeman, San Francisco.

Milkey, R. W. and Mihalas, D., 1974. *Astrophys. J.,* **192**, 769..

Morrison, N. D. and Linsky, J. L., 1978. *Astrophys. J.,* **222**, 723.

Mullan, D. J., 1978. *Astrophys. J.,* **226**, 151.

Nussbaumer, H. and Schild, H., 1979. *Astr. Astrophys.,* **75**, L17.

Omont, A., Smith, E. W. and Cooper, J., 1972. *Astrophys. J.,* **175**, 185.

Oranje, B. J., Zwaan, C. and Middlekoop, F., 1982. *Astr. Astrophys.,* **110**, 30.

Osterbrock, D. E., 1974, *Astrophysics of Gaseous Nebulae*, (San Fransisco: Freeman)

Parker, E. N., 1958. *Astrophys. J.,* **128**, 664..

Paresce, F., 1984. *Astronomical Journal,* **89**, 1022.

Press, W. H., Flannery, B. P., Teukolsky, S. A. and Vetterling, W. T., 1986, *Numerical Recipes*, Cambridge University Press, 547

Priest, E. R., 1982, *Solar Magneto-hydrodynamics*,D.Reidel, Dordecht,26.

Reeves, E. M., Vernazza, J. E. and Withbroe, G. L., 1976, *Phil. Trans. Roy. Soc. Lond.*, A. **281**, 293.

Rego, M. E., Williams, P. M. and Peat, D. W., 1972. *Mon. Not. R. astr. Soc.,* **160**, 129..

Reimers, D., 1975, *Problems in Stellar Atmospheres and Envelopes*, Ed. Baschek, B., Kegel, W. H. and Traving, G., (Springer, Berlin),229

Reimers, D., 1977a. *Astr. Astrophys.,* **57**, 395..

Reimers, D., 1977b. *Astr. Astrophys.,* **61**, 217.

Reimers, D., 1978. *Astr. Astrophys.,* **67**, 161.

Reimers, D., 1982. *Astr. Astrophys.,* **107**, 292.

Ridgeway, S. T., Joyce, R. R., White, N. M. and Wing, R. F., 1980. *Astrophys. J.,* **235**, 126.

Rosner, R., Tucker, W. H. and Vaiana, G. S., 1978. *Astrophys. J.,* **220**, 643.

Rybicki, G. B., 1984, *Methods in Radiative Transfer*, Ed. Kalkofen, CUP. 21

Rybicki, G. B., 1985,*Progress in Stellar Spectral Line Formation Theory*, Eds. J. Beckman and L. Crivellari, D. Reidel, Dordrecht, 199.

Scalo, J. M., 1976. *Astrophys. J.,* **206**, 474..

Schrijver, C.J ., 1987, *Cool Stars, Stellar Systems, and the Sun*, Eds. Linsky, J. L. and Stencel, R. E., Springer-Verlag 135

Schwarzschild, M. and Eberhard, G., 1913. *Astrophys. J.,* **38**, 292..

Seaton, M. J., 1979. *Mon. Not. R. astr. Soc.,* **187**, 73p.

Sharmer, G. B., 1981. *Astrophys. J.,* **249**, 720

Scharmer, G. B. and Carlsson, M., 1985a, *J. Comput. Phys*,**59**, 56

Scharmer, G. B. and Carlsson, M., 1985b, *Progress in Stellar Spectral Line Formation Theory*, Eds. J Beckman and L. Crivellari, D.Reidel, Dordrecht, 189

Shine, R. A. and Linksky, J. L., 1974, *Solar Physics*, **37**, 145 .

Simon, T., 1984. *Astrophys. J.,* **279**, 738..

Simon. T, Herbig, G. and Boesgaard, A. M., 1985. *Astrophys. J.,* **293**, 551..

Simon, T., Kelch, W. L. and Linsky, J. L., 1980. *Astrophys. J.,* **237**, 72.

Smith, G. and Drake, J. J., 1988. *Mon. Not. R. astr. Soc.,* **231**, 115.

Sneden, C., Lambert, D. L. and Pilachowski, C. A., 1981. *Astrophys. J.,* **247**, 1052.

Spitzer, L. Jr., 1978. *Physical Processes in the Interstellar Medium* (Wiley)

Stencel, R. E., 1978. *Astrophys. J.,* **233**, L37.

Stencel, R. E., Linsky, J. L., Brown, A., Jordan, C., Carpenter, K. G., Wing, R. F. and Czyzak, S., 1981. *Mon. Not. R. astr. Soc.,* **196**, p47..

Stencel, R. E. and Mullan,D.J.,1980a. *Astrophys. J.,* **238**, 221.

Stencel, R. E. and Mullan,D.J.,1980b. *Astrophys. J.,* **240**, 718.

Stencel, R. E., Pesce, J. H. and Hagen Bauer, W., 1988. *Astronomical Journal,* **95**, 141.

Summers, H. P, 1972, *Culham Internal Report*

Thomas, R. N., 1957. *Astrophys. J.,* **125**, 260.

Tozzi, G. P., Huber, M. C. E. and Pauls, U., 1983. *Astr. Astrophys.,* **126**, 320..

Ulmschneider, P., 1979. *Astr. Astrophys.,* **74**, 229

Van der Hucht, K. A., Stencel, R.E., Haisch, B. M. and Kondo, Y., 1979, *Astron. Astron. Astrophys. Suppl.*, **36**, 377

Veale, A. and Brown, A., 1988, *A Decade of UV Astronomy with the IUE satellite*, ESA SP-281 Vol. 1, 335

Vernazza, J. E., Avrett, E. H. and Loeser, R., 1976. *Astrophys. J.,* **184**, 605..

Vernazza, J. E., Avrett, E. H. and Loeser, R., 1981. *Astrophys. J. Suppl.,* **45**, 635..

Vilhu, O., 1987, *Cool Stars, Stellar Systems, and the Sun*, Eds. Linsky, J. L. and Stencel,R . E., Springer-Verlag, 110

Weiler, E. J. and Oegerle, W. R., 1979. *Astrophys. J. Suppl.,* **39**, 537.

Weise, W. L., Smith, M. W. and Glennon, B. M., 1966, *Atomic Transition Probabilities, Vol I, Hydrogen Through Neon*, NSRDDS-NBS 4.

Weise, W. L., Smith, M. W. and Miles, B. M., 1969, *Atomic Transition Probabilities, Vol II, Sodium Through Calcium*, NSRDS-NBS 22

Williams, P. M., 1971. *Mon. Not. R. astr. Soc.,* **155**, 215..

Williams, P. M., 1975. *Mon. Not. R. astr. Soc.,* **170**, 343..

Willson, L. A., 1972. *Astr. Astrophys.,* **17**, 354.

Willson, L.A., 1974. *Astrophys. J.,* **191**, 143.

Willson, L. A. and Hill, S. J., 1979. *Astrophys. J.,* **228**, 854.

Wilson, O. C., 1976. *Astrophys. J.,* **205**, 823.

Wilson, O. C. and Bappu, M. K. V., 1957. *Astrophys. J.,* **125**, 661.

Withbroe, G. L. and Noyes, R. W., 1977. *Ann. Rev. Astr. Astrophys.,* **15**, 363.

Zeippen, C. J., Seaton, M. J., and Morton, D. C., 1977. *Mon. Not. R. astr. Soc.,* **18**, 527.

APPENDIX A

The programme MARCS is based on the flux-constant models described by Gustafsson *et al.* (1975). The models assume plane-parallel stratification, hydrostatic equilibrium and LTE. The equation of radiative transfer, the conservation of total flux, and hydrostatic equilibrium are solved simultaneously. The opacity in the stellar atmosphere due to line blanketing is treated with opacity distribution functions (ODFs), which are described in detail by Kurucz (1979). The programme was run on the Oxford University's Department of Astrophysics Micro-VAX. The input parameters which were used to specify the models in this present work are;

(1) The surface gravity.

(2) The effective temperature.

(3) The stellar abundances. The abundances are scaled relative to the solar abundances by a constant factor.

No turbulent pressure term is included in the model calculations. Gustafsson *et al.* (1975) find that including the effects of turbulent pressure changes the temperature structure little (except in the convection zone) and the gas pressures and densities by less than 10%. The uncertainties in the model temperature structure arising from the poor knowledge of line opacities in the ultraviolet are found to be small at the surface. Arbitrarily increasing the opacity in the ultraviolet by an order of magnitude increases the effects of back-warming, at $\bar{\tau} = 10^{-2}$ is found to increase T_e by about 10K. The temperature minimum is at a smaller $\bar{\tau}$ so the corresponding error in temperature will be small.

The approximation of LTE will be least valid at the surface layers where photons can escape and the detailed balance is no longer obtained. The radiation field decouples from the particles and the radiation temperature no longer equals the electron temperature (in the LTE photosphere the radiation temperature $T_{Rad} = T_e$, the electron temperature, everywhere). In the corona and transition region the plasma is usually described using the electron temperature as this is the appropriate quantity to use for calculating collisionally excited line fluxes. Whereas the radiation field is described by T_{rad} and is the appropriate quantity used to describe photo-processes. The radiation field will decouple from the particles when the optical depth for a certain frequency becomes of the order unity. At some frequencies in the photosphere the optical depth is of the order of unity and the model is no longer in LTE. The temperature structure obtained from the photospheric models is taken to be that described by the electron temperature.

APPENDIX B

The Radiation Transfer Problem

The solution of a multi-level atom which is not in LTE involves the simultaneous solution of the statistical equilibrium equations,

$$n_i \sum_{j \neq i}^{N_L} P_{ij} - \sum_{j \neq i}^{N_L} n_j P_{ji} = 0, \qquad (B.1)$$

the particle conservation equation,

$$\sum_{j=1}^{N_L} n_j = n_{tot}, \qquad (B.2)$$

and the radiative transfer equation,

$$\mu \frac{dI_{\nu\mu}}{dz} = -\kappa_{\nu\mu} I_{\nu\mu} + j_{\nu\mu}, \qquad (B.3)$$

where n_i is the number of atoms per unit volume in level i, N_L is the total number of energy levels, and n_{tot} is the total number of atoms per unit volume (this is specified by m_{col}). P_{ij} is the total probability per unit time that an atom in level i will make a transition to level j. $I_{\nu\mu}$ is the specific intensity, $\kappa_{\nu\mu}$ is the absorption coefficient, $j_{\nu\mu}$ is the emissivity coefficient, and μ is the cosine of the angle between the ray and the normal of the atmosphere. The total transition probabilities can be written in terms of radiative R_{ij} and collisional C_{ij} terms,

$$P_{ij} = R_{ij} + C_{ij}. \qquad (B.4)$$

These terms can be written as follows,

$$R_{ij} = \begin{cases} \frac{1}{2}\int_{-1}^{1}\int_{0}^{\infty} \frac{4\pi}{h\nu}\alpha_{ji} G_{ji} \left(I_{\nu\mu} + \frac{2h\nu^3}{c^2} \right) d\nu d\mu, & \text{if } i > j; \\ \frac{1}{2}\int_{-1}^{1}\int_{0}^{\infty} \frac{4\pi}{h\nu}\alpha_{ij} I_{\nu\mu} d\nu d\mu, & \text{if } i < j, \end{cases} \qquad (B.5)$$

where the expressions for α_{ij} and G_{ij} for bound-bound (b–b) and bound-free (b–f) are given by,

$$\alpha_{ij} = \begin{cases} B_{ij}\phi_{\nu\mu}\frac{h\nu_{ij}}{4\pi} & \text{(b–b)}; \\ \alpha_c(\nu) & \text{(b–f)}. \end{cases} \qquad (B.6)$$

and,

$$G_{ij} = \begin{cases} \frac{g_i}{g_j} & \text{(b–b);} \\ \frac{n_i^*}{n_j^*} e^{\frac{-h\nu}{kT}} & \text{(b–f).} \end{cases} \qquad (B.7)$$

B_{ij} is the Einstein coefficient for stimulated emission ($i > j$) and absorption ($i < j$), $\phi_{\nu\mu}$ is the normalized absorption profile, $\alpha_c(\nu)$ is the bound–free absorption cross-section, $g_{i,j}$ are the statistical weights, and $n_{i,j}^*$ are the LTE-populations of the levels. The expressions for the absorption and emission coefficients (in CRD) are as follows,

$$\kappa_{\nu\mu} = \kappa_{\nu c} + \alpha_{ij}(n_i - G_{ij}n_j), \qquad (B.8)$$

and,

$$j_{\nu\mu} = j_{\nu c} + \frac{2h\nu^3}{c^2} G_{ij}\alpha_{ij}nj. \qquad (B.9)$$

Here the subscript c refers to the background opacity and emissivity.

The mean intensity $\bar{J}_{ij}$ is defined as,

$$\bar{J}_{ij} = \frac{1}{2}\int_{-1}^{1}\int_{0}^{\infty} \phi_{\nu\mu} I_{\nu\mu} d\nu d\mu. \qquad (B.10)$$

It is the mean intensity of the radiation field which couples the statistical equilibrium equations to the radiation field. The radiation field at any point in the atmosphere is coupled to the population densities in a region within the distance over which the photons scatter without being thermalised. The transfer problem is then *non-local* and *non-linear.* The dependence of the radiation field on the population densities in a non-local region arises from the expression for the emissivities and absorption coefficients. For completeness, the definitions of the source function and the monochromatic optical depth are, respectively,

$$S_{\nu\mu} = \frac{j_{\nu\mu}}{\kappa_{\nu\mu}}, \qquad (B.11)$$

and

$$d\tau_{\nu\mu} = -\frac{\kappa_{\nu\mu} dz}{\mu}. \qquad (B.12)$$

To complete the transfer problem, the outgoing intensity at the bottom of the atmosphere and the incoming intensity at the top of the atmosphere must be specified. In MULTI these boundary conditions are derived from second order Taylor expansions.

The method used in the program MULTI to solve these equations is as follows. The statistical equilibrium equations and the first order form of the transfer equation are linearised with respect to the population number densities and the specific intensity (Scharmer and Carlsson, 1985). The linearised transfer equation has only one nonlinear term which corresponds to the number of photons and the number of absorbing atoms.

These equations are then ***pre-conditioned***, ***i.e.***, re-expressed in a manner which has the effect of reducing the magnitude of the non-linear terms and also remove some of the numerical problems due to large optical depths. Scattering of photons in line cores with large optical depths can lead to numerical problems because there are cancellations of numbers which are close in value. The preconditioning reduces the magnitude of these effects.

Iteration Scheme used in MULTI

A multi-dimensional Newton-Raphson iterative scheme is used to solve the linearised equations and the approximate operator, $\Lambda^{\dagger}$, corresponding to the weights ω (see Section 5-2). Following Carlsson (1986), the scheme can be represented as follows. Let the equations (B.1)–(B.3) be written as the operator equation,

$$W[n] = b. \tag{B.13}$$

The current estimate of the population numbers $n^{(n)}$ leads to an error $E^{(n)}$,

$$W[n^{(n)}] = b + E^{(n)}. \tag{B.14}$$

If $\delta^{(n)}n$ is the correction needed to get the solution n, then

$$W[n^{(n)} + \delta^{(n)}n] = b. \tag{B.15}$$

Subtracting (B.14) from (B.15) gives,

$$W[n^{(n)} + \delta^{(n)}n] - W[n^{(n)}] = -E^{(n)}. \tag{B.16}$$

The operator W (including the approximate radiative operator $\Lambda^{\dagger}_{\nu\mu}$ which is conditioned in the optically thin and optically thick cases and the linearised equations) is constructed such that,

$$W^{\dagger(n)}[\delta^{(n)}n] \simeq W[n^{(n)} + \delta^{(n)}n] - W[n^{(n)}], \tag{B.17}$$

for small $\delta^{(n)}$. This leads to,

$$W^{\dagger(n)}[\delta^{(n)}n] \simeq -E^{(n)}, \tag{B.18}$$

which can be used to define the correction $\delta n^{(n)}$. Then the iterative scheme is,

$$E^{(n)} = W[n^{(n)}] - b \tag{B.19}$$

$$\delta n^{(n)} = {W^{\dagger(n)}}^{-1}[-E^{(n)}] \tag{B.20}$$

$$n^{(n+1)} = n^{(n)} + \delta n^{(n)}. \tag{B.21}$$

It can be seen that as the iteration converges the final solution is *independent* of the assumptions made in the approximate operator. Thus the accuracy is determined by the accuracy to which the exact transfer calculation can be made (*i.e.*, the accuracy to which the intensity can be calculated from a given source function).

MULTI

A brief description of the parameters used in MULTI, which are referred to in the text, is given. A simple flow diagram shows how these are related to the running of the programme. The numbers before the subsection headings refer to the location on the flow diagram.

1) The Input Files

The programme MULTI must be supplied with several input files; ATMOS.DAT: This file contains the atmospheric model. The model is given in terms of the temperature, electron density, macroscopic velocity, and the turbulent velocity for a given logarithm of the mass column density. DSCALE.DAT: Contains the atmospheric depth scale to be used to solve the atomic models. INPUT.DAT: Contains the input parameters which control the approximations used in radiative transfer calculations, the starting approximations for the population number densities and the parameters which control the output from the computer. ATOM.DAT: This file contains the atomic model. The atomic models described in Chapter 5 are given in Appendix C. ABUND.DAT: Contains the abundances.

2) Starting Approximations

The starting approximations for the population number densities are controlled by the input parameters ISTART and ILAMBD. The starting approximations provided in the original programme are;

(1) ISTART=1; Initialise the population number densities to LTE.

(2) ISTART=0; Calculates the population densities with a zero radiation field.

(3) ISTART=-1; The population densities from the previous calculation are used as the starting approximation.

These starting approximations are then lambda iterated by the number of times specified by ILAMBD before the main programme starts. A value of ILAMBD

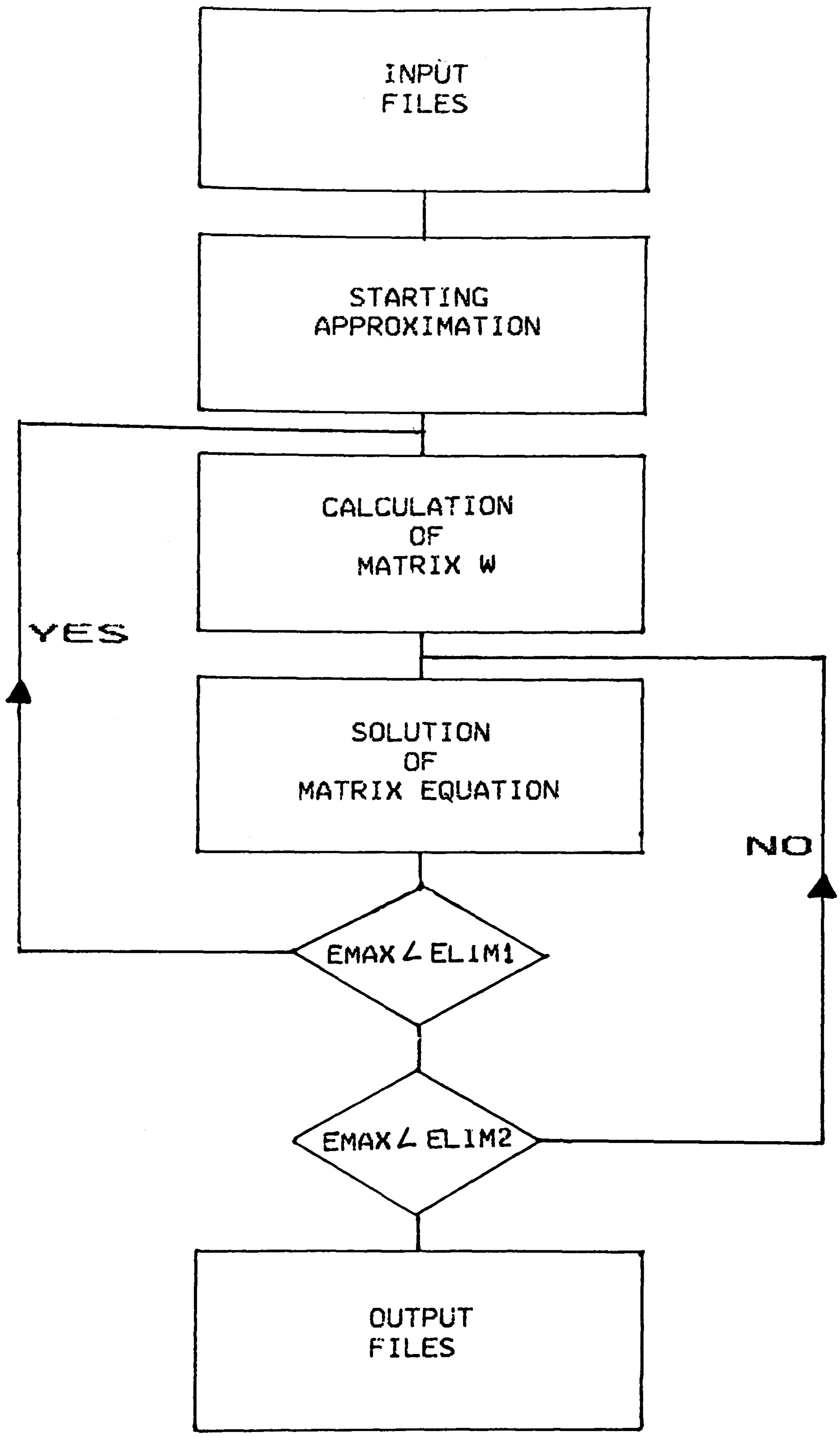

Figure B1 Flow diagram showing how some of the input parameters are used within the programme MULTI. The numbers in the boxes refer to the numbered subsections.

greater than one was not found to be necessary. The modifications to the starting approximations described in the text are initiated when,

(4) ISTART= $N \leq -2$. The second order escape-probability approximation is used for the radiation transfer in the lines and the *On-the-spot* approximation is used for the continua (see text for details). For ISTART=N, $N-2$ lambda iterations are made before the main programme starts.

3) Solution of the Radiative Transfer Equations

The matrix W (see equation (B.18)) is constructed as described in the text. The implementation of the transfer approximation, which helps make this programme efficient, is controlled by the input parameters DIFF and THIN. When the change in opacity between the depth points exceeds DIFF, then the transition is treated with the approximation equivalent to the core-saturation method. A value of between 5–10 was found to be suitable. When the optical depth of a transition at a given level is less than THIN, the solution for the number densities is lambda iterated. A value of THIN= 0.1 is used in the following work.

Once the matrix has been constructed the change in population densities is calculated. To save computing time, if the maximum relative correction to the population number densities (EMAX) is less than a value given in the input file by ELIM1, then on the next iteration the matrix W is not recalculated and the new population densities are substituted back into the previous matrix W. This saves much computer time but ELIM1 must be small for convergence to occur. Values of ELIM1= $0.1-0.001$ have been adopted. The computer then continues to iterate the population densities until EMAX is less than a chosen value. This value is assigned to ELIM2 and when this has occurred the solution has converged and the computer writes the results to an output file. A value of ELIM2 is adopted.

Appendix C

The model atoms used to calculate the results shown in Chapter 6 are summarised below. The energy levels and the lines for which fluxes can be calculated are included. A brief description of the terms is given below.

ABUND; atomic abundance in a logarithmic scale with hydrogen=12.

NK; number of levels in atom (including the continuum levels).

NLIN; number of radiative bound-bound transitions.

NCNT; number of continua treated in detail.

NFIX; number of fixed transitions (treated by radiation temperatures).

E; energy of the level (in units of cm^1).

G; statistical weight of the level.

F; the absorption oscillator strength

NQ; number of frequency points used to calculate the transition.

QMAX; maximum frequency width in units of kilometers per second.

QO; frequency within which the quadrature points are distributed linearly rather than logarithmically.

IW; =0 for line where the background source function is treated as constant =1 treated fully for wide lines.

GA; radiative damping parameter.

GVW; Van der Waals damping parameter.

GS; stark damping parameter.

Radiation Temperatures

The radiative transitions can be solved either by using a photoionisation cross-section, or by using a fixed transition rate which is controlled by the radiation temperature T_{Rad}. The radiation temperature is specified by the parameter TRAD in the atomic models. MULTI provides three options (ITRAD) which can be used to treat the radiation temperatures. These options are;

(i) ITRAD=1 The radiation temperature option, $T_{Rad} = T_e$.

(ii) ITRAD=2 The photospheric option, $T_{Rad} = T_e$ until $T_e <$ TRAD then $T_{Rad} =$ TRAD.

(iii) ITRAD=3 The chromospheric option, $T_{Rad} = T_e$ except when $T_e <$ TRAD AND T_e is increasing, then $T_{Rad} =$ TRAD.

Hydrogen

```
H
* ABUND   AWGT
 12.0000  1.008
*
* NK IS NUMBER OF LEVELS, CONTINUUM LEVELS INCLUDED,
* NLIN IS NUMBER OF LINES IN DETAIL
* NCONT IS NUMBER OF CONTINUA IN DETAIL
* NRFIX IS NUMBER OF FIXED TRANSITIONS
*
*NK NLIN NCONT NFIX
  4   3    1    2
*    E (CM-1)       G    LABEL    ION
      0.000         2    'N=1 '    1
  82259.070         8    'N=2 '    1
  97492.230        18    'N=3 '    1
1.0967875E5         1    'CONT'    2
*
*.LYMAN-ALPHA AND LYMAN-BETA WITH FREQUENCIES DETERMINED IN FREQ
* H-ALPHA WITH FREQUENCIES GIVEN EXPLICITLY IN DOPPLER UNITS (Q0<0)
*
* J  I       F         NQ  QMAX Q0 IW     GA        GVW      GS
  2  1  0.41600000 20     6.  6. 0  4.7E008       1.0      1.0
  3  1  0.07910000 20     6.  6. 0  5.57E07      1.0      1.0
  3  2  0.64080000 23    50. -2. 0   4.97E07   1.0      1.0
  0.000E+00 2.219E-01 4.452E-01 6.708E-01 9.001E-01
  1.136E+00 1.200E+00 1.260E+00 1.320E+00 1.382E+00
  1.645E+00 1.937E+00 2.276E+00 2.694E+00 3.243E+00
  4.009E+00 5.134E+00 6.855E+00 9.566E+00 1.392E+01
  2.099E+01 3.259E+01 5.167E+01
* 7.2E+1     1.0E+2  2.0E2      5.0E2
*
* LYMAN CONTINUUM CALCULATED IN DETAIL
*
  4  1  6.5400E-18 10  600.  0.
*
* BALMER AND PACHEN CONTINUA TREATED WITH RADIATION TEMPERATURES
*
* J  I  P    A0          TRAD ITRAD
  4  2  1  1.4100E-17  3700.  3
  4  3  1  2.1800E-17  3500.  3
```

Iron

```
Einstein Coefficients from Spectroscopic Data for Iron, Weise, W. L. (ed)
  NBS, 1985.
Atomic Data from PANDORA

IRON I & II


E 1
 ABUND     AT WT
  7.50     55.85
    NK          NL       NCNT   NFIX
    8           2        7      1
    E           G         ID          ION
       0.000 25.00     'A-5DE'       1
    6928.266 11.00     'A-5F5'       1
    7376.766  9.00     'A-5F4'       1
    7728.056  7.00     'A-5F3'       1
    7985.710  5.00     'A-5F2'       1
    8154.710  3.00     'A-5F1'       1
   43136.800  7.00     'Y-5G3'       1
   63479.988 30.00     'A-6DE'       2

** BOUND-BOUND TRANSITIONS TREATED IN DETAIL ***

   UP    LO      F      NQ   QMAX    Q0  IW      GA          GVW          GS
   7      5  0.2089     15  300.0    3.0  0   2.030E+08   0.000E+00   0.000E+00
   7      4  0.0861     15  300.0    3.0  0   2.030E+08   0.000E+00   0.000E+00

** BOUND-FREE TRANSITIONS TREATED IN DETAIL ***
```

Magnesium

```
   M A G N E S I U M   I I ,   6   L E V E L S
 Mg II h and k rad. rates from Black et al., ApJ Vol. 177,
 p. 567 (1972). Coll. rates from Mendoza, J.Phys.B Vol. 14,
 p. 2465 (1981 )
  MAGNESIUM
 PRD VERSION WITH 35 FREQUENCY POINTS AND FIXED B-F TRANSITIONS
 MGII/PRD
 ABUND     AWGT
 7.59E+00  24.12
 NK  NLIN  NCNT  NFIX
 7    2     0     6
    E          G              ION
       0.000  2.00  'MGII'    2
   35698.504  2.00  'N/A '    2
   35760.039  4.00  'N/A '    2
   69803.383  2.00  'N/A '    2
   71489.438  6.00  'N/A '    2
   71490.313  4.00  'N/A '    2
  121267.375  1.00  'CONT'    3
 NEED DATA FOR GVW
 UP  LO       F      NQ   QMAX      Q0   IW     GA          GVW          GS
  2   1  2.990E-01 50  300.0      10.0  0    2.540E+08   1.000E+00   3.183E-05
  3   1  5.982E-01 40  300.0      10.0  0    2.550E+08   1.000E+00   3.194E-05
   4   2  1.431E-01 15   30.0      0.3  0    5.880E+08   0.000E+00   2.905E-05
   4   3  1.443E-01 15   30.0      0.3  0    5.890E+08   0.000E+00   2.895E-05
   5   3  8.425E-01 15  300.0      3.0  0    7.330E+08   0.000E+00   3.189E-05
   6   2  9.227E-01 15  300.0      3.0  0    7.260E+08   0.000E+00   3.200E-05
   6   3  9.165E-02 15   30.0      0.3  0    7.270E+08   0.000E+00   3.189E-05
  FIXED TRANSITIONS FOR PRD FORMULATION:

7   1   1    2.70E-19      4000.  2
7   2   1    4.50E-19      4000.  2
7   3   1    4.50E-19      4000.  2
7   4   1    6.17E-20      4000.  2
7   5   1    1.99E-18      4000.  2
7   6   1    1.99E-18      4000.  2
```

Silicon

```
* PART ( 6. )
* CP1, CP2: Travis & Matsushima (1968, Ap.J. 134, 689)
* A51: Wiese & Martin (1980, NBS)
  SI   1
* ABUND     AWGT  ** ABUNDANCE FOR BETA GEM
   7.73    28.00
* NK  NLIN  NCNT  NFIX
  17    9     9    7
*     E          G                ION
        0.000  9.00  'SI I 3P2 3PE            '   1
     6303.202  5.00  'SI I 3P2 1DE            '   1
    15404.270  1.00  'SI I 3P2 1SE            '   1
    33348.234  5.00  'SI I 3S 3P3 5SO         '   1
    39886.590  9.00  'SI I 3S 3P 4S 3PO       '   1
    41019.348  3.00  'SI I 3P 4S 1PO          '   1
    45333.223 15.00  'SI I 3S 3P3 3DO         '   1
    49160.773 27.00  'SI I 3P2 4P 3SPDE       '   1
    65792.836  2.00  'SI II 3S2 3P 2PO 1/2'       2
    66080.148  4.00  'SI II 3S2 3P 2PO 3/2'       2
   108616.117  2.00  'SI II 3S 3P2 4PE 1/2'       2
   108724.461  4.00  'SI II 3S 3P2 4PE 3/2'       2
   108899.742  6.00  'SI II 3S 3P2 4PE 5/2'       2
   121101.039  4.00  'SI II 3S 3P2 2DE 3/2'       2
   121116.891  6.00  'SI II 3S 3P2 2DE 5/2'       2
   131291.938  2.00  'SI II 3S2 4S 2SE 1/2'       2
   197631.234  1.00  'SI III GROUND TERM    '     3
* NEED DATA FOR GVW
* UP   LO      F        NQ    QMAX    Q0  IW      GA     GVW    GS
   5  1   4.394E-02 15  300.0     3.0  0    4.660E+07   0.000E+00   4.915E-06
*   8  5   1.015E+00 15  300.0     3.0  0    6.600E+07   0.000E+00   6.416E-05
  11  9   3.722E-06 15   30.0     0.3  0    7.550E+03   0.000E+00   0.000E+00
  11 10   1.244E-06 15   30.0     0.3  0    7.550E+03   0.000E+00   0.000E+00
  12  9   2.149E-08 15   30.0     0.3  0    1.633E+03   0.000E+00   0.000E+00
  12 10   1.336E-06 15   30.0     0.3  0    1.633E+03   0.000E+00   0.000E+00
  13 10   2.945E-06 15   30.0     0.3  0    2.400E+03   0.000E+00   0.000E+00
  14  9   3.717E-03 15   30.0     0.3  0    4.536E+06   0.000E+00   1.007E-05
  14 10   3.696E-04 15   30.0     0.3  0    4.536E+06   0.000E+00   9.968E-06
  15 10   3.328E-03 15   30.0     0.3  0    4.480E+06   0.000E+00   9.974E-06
*  16  9   1.182E-01 15  300.0     3.0  0    1.009E+09   0.000E+00   5.010E-06
*  16 10   1.183E-01 15  300.0     3.0  0    1.009E+09   0.000E+00   4.967E-06
```

Aluminium

```
  A L U M I N U M   I ,   6   L E V E L S
  A L U M I N I U M   I I ,   5   L E V E L S
A21, A41 from Wiese & Martin (1980, NBS); P. Mauas 5/87
  A T O M I C   D A T A   F R O M   P A N D O R A
Philip Judge, 29 July 1986
Includes 2669 and 2670 Angstrom transitions
Bound-bound rates from Tayal et al., J.Phys.B Vol. 17, p. 3847 (1984)
Vol. 18, p. 4321 (1985), B. C. Johnson, PhD Thesis Harvard 1985
A(3P1-1S0) = 3.33E+03 S-1 Johnson et al 1988.
Coulomb photoionization data supplied by Kurucz
Coll. ionization data from Allen, Astrophys. Quant., 3rd Ed., p. 42
Ignore quadrupole line - gf is given by B. C. Johnson - see thesis
AL   1
ABUND      AWGT
 6.32      26.98
NK  NLIN  NCNT  NFIX
 12    2     5    4
   E          G                              ION
      0.000  6.00  'AL I 3S2 3P 2PO        '   1
  25363.576  2.00  'AL I 3S2 4S 2SE        '   1
  29072.715 12.00  'AL I 3S 3P2 4PE        '   1
  32457.639 10.00  'AL I 3S2 3D 2DE        '   1
  32975.316  6.00  'AL I 3S2 4P 2PO        '   1
  51787.527  2.00  'AL I 3S 3P2 2SE        '   1
  48312.414  1.00  'AL II 2P6 3S 1SE       '   2
  85705.344  1.00  'AL II 2P6 3S 3P 3PO    '   2
  85766.214  3.00  'AL II 2P6 3S 3P 3P1    '   2
  85890.084  5.00  'AL II 2P6 3S 3P 3P2    '   2
 108162.914  3.00  'AL II 2P6 3S 3P 1PO    '   2
 200172.797  2.00  'AL III GROUND TERM     '   3
NEED DATA FOR GVW
UP   LO      F        NQ    QMAX    Q0   IW      GA     GVW    GS
  2  1   3.832E-02 15  300.0     3.0  0    4.930E+07   0.000E+00   3.151E-05
  4  1   1.495E-01 15  300.0     3.0  0    6.300E+07   0.000E+00   1.191E-04
  5  2   1.414E+00 15  300.0     3.0  0    6.750E+07   0.000E+00   1.550E-04
  6  1   7.756E-02 15  300.0     3.0  0    4.160E+08   0.000E+00   0.000E+00
  9  7   1.068E-05 15   30.0     0.3  0    3.330E+03   0.000E+00   0.000E+00
 11  7   1.796E+00 15  300.0     3.0  0    1.430E+09   0.000E+00   0.000E+00
```

APPENDIX D

The five chromospheric models described in Chapter 6 are tabulated below. For each model two sets of numbers are given. The first describe the chromospheric model and, the second, are the hydrogen population densities. The hydrogen solutions are described in detail in Chapter 6. The columns of numbers are as follows:

Chromospheric Models

The first item in the header of the chromospheric models calculated with MULTI is normally is the name of the model (this have been excluded for these models). The second item in the header defines which depth scale is to be used. If the first letter of the second item begins with an M *e.g.,* MASS SCALE, then depth scale is defined in terms of the logarithm of the mass column density. If the first letter is a T, the depth scale is defined in terms of $log(\tau_{5000})$. The third item in the header is the logarithm of the surface gravity (cm s^{-2}). The final number in the header is the number of depth points in the atmosphere.

The first column in the logarithm of the mass column density (g cm^{-2}); the second column is the temperature (K); the third column is the electron density (cm^{-3}); the fourth column is the macroscopic velocity field (km s^{-1}); and the last, fifth, column is the microturbulent velocity ($km\, s^{-1}$).

Hydrogen population densities

The columns in this section are the hydrogen population densities. The different rows correspond to the depth points in the chromospheric model. The numbers are the population densities at each level in the atom. The hydrogen atom has four levels, so that columns 4 and 5 are empty. The first column is the $n = 1$ level, the second column is the $n = 2$ level and the third column is the $n = 3$ level and the fourth column is ionised hydrogen.

Model 1: Chromospheric Model

MASS SCALE
1.6700002
80

-3.395000E+00	8.883259E+04	3.277393E+08	0.000000E+00	5.519626E+01
-3.394055E+00	5.469597E+04	4.587314E+08	0.000000E+00	4.907701E+01
-3.393552E+00	4.033439E+04	5.645093E+08	0.000000E+00	4.544006E+01
-3.393291E+00	3.404534E+04	6.338689E+08	0.000000E+00	4.343461E+01
-3.393101E+00	3.060802E+04	6.813134E+08	0.000000E+00	4.220284E+01
-3.392925E+00	2.859247E+04	7.164443E+08	0.000000E+00	4.129556E+01
-3.392745E+00	2.679039E+04	7.519933E+08	0.000000E+00	4.041933E+01
-3.392557E+00	2.512666E+04	7.886304E+08	0.000000E+00	3.955913E+01
-3.392345E+00	2.395969E+04	8.216820E+08	0.000000E+00	3.876879E+01
-3.392090E+00	2.286123E+04	8.590908E+08	0.000000E+00	3.789547E+01
-3.391859E+00	2.191744E+04	8.943267E+08	0.000000E+00	3.712082E+01
-3.391645E+00	2.112548E+04	9.273135E+08	0.000000E+00	3.643060E+01
-3.391398E+00	2.029085E+04	9.656221E+08	0.000000E+00	3.567247E+01
-3.391108E+00	1.939743E+04	1.010809E+09	0.000000E+00	3.483661E+01
-3.390761E+00	1.840887E+04	1.066197E+09	0.000000E+00	3.388969E+01
-3.390342E+00	1.730767E+04	1.135158E+09	0.000000E+00	3.281511E+01
-3.389823E+00	1.619230E+04	1.214969E+09	0.000000E+00	3.169356E+01
-3.389157E+00	1.530204E+04	1.291205E+09	0.000000E+00	3.071738E+01
-3.388269E+00	1.450161E+04	1.373222E+09	0.000000E+00	2.974517E+01
-3.387086E+00	1.347589E+04	1.492345E+09	0.000000E+00	2.846055E+01
-3.385562E+00	1.215963E+04	1.679385E+09	0.000000E+00	2.667801E+01
-3.383735E+00	1.066311E+04	1.950917E+09	0.000000E+00	2.442004E+01
-3.381663E+00	9.587292E+03	2.104304E+09	0.000000E+00	2.272510E+01
-3.379160E+00	8.799496E+03	2.257999E+09	0.000000E+00	2.144522E+01
-3.376232E+00	7.961222E+03	2.505882E+09	0.000000E+00	2.007885E+01
-3.372584E+00	7.610242E+03	2.619798E+09	0.000000E+00	1.948640E+01
-3.368022E+00	7.519194E+03	2.639292E+09	0.000000E+00	1.930232E+01
-3.362314E+00	7.499608E+03	2.614206E+09	0.000000E+00	1.922291E+01
-3.357485E+00	7.482510E+03	2.574893E+09	0.000000E+00	1.915288E+01
-3.352942E+00	7.466221E+03	2.519066E+09	0.000000E+00	1.908589E+01
-3.348398E+00	7.449929E+03	2.443464E+09	0.000000E+00	1.901888E+01
-3.343980E+00	7.433479E+03	2.352408E+09	0.000000E+00	1.895046E+01
-3.339609E+00	7.416964E+03	2.250434E+09	0.000000E+00	1.888146E+01
-3.335239E+00	7.400453E+03	2.144706E+09	0.000000E+00	1.881251E+01
-3.330868E+00	7.383938E+03	2.043872E+09	0.000000E+00	1.874353E+01
-3.323425E+00	7.355204E+03	1.914973E+09	0.000000E+00	1.862290E+01
-3.315235E+00	7.323496E+03	1.827230E+09	0.000000E+00	1.848972E+01
-3.303792E+00	7.279130E+03	1.770269E+09	0.000000E+00	1.830334E+01
-3.286905E+00	7.213591E+03	1.734500E+09	0.000000E+00	1.802800E+01
-3.265936E+00	7.132203E+03	1.699203E+09	0.000000E+00	1.768600E+01
-3.243175E+00	7.043860E+03	1.654158E+09	0.000000E+00	1.731471E+01
-3.218546E+00	6.948265E+03	1.595653E+09	0.000000E+00	1.691291E+01
-3.191447E+00	6.843083E+03	1.521035E+09	0.000000E+00	1.647089E+01
-3.161046E+00	6.725085E+03	1.427575E+09	0.000000E+00	1.597497E+01
-3.124914E+00	6.588716E+03	1.312081E+09	0.000000E+00	1.540603E+01
-3.075488E+00	6.420435E+03	1.167415E+09	0.000000E+00	1.472675E+01
-2.998285E+00	6.212656E+03	9.977419E+08	0.000000E+00	1.400699E+01
-2.900234E+00	5.995216E+03	8.295900E+08	0.000000E+00	1.346980E+01
-2.785050E+00	5.788918E+03	6.904532E+08	0.000000E+00	1.307802E+01
-2.653212E+00	5.588622E+03	5.767153E+08	0.000000E+00	1.267654E+01
-2.506741E+00	5.383423E+03	4.744355E+08	0.000000E+00	1.223346E+01
-2.347464E+00	5.181779E+03	3.918429E+08	0.000000E+00	1.175159E+01
-2.177515E+00	5.015275E+03	3.506639E+08	0.000000E+00	1.123731E+01
-2.000427E+00	4.893229E+03	3.496287E+08	0.000000E+00	1.070137E+01
-1.819413E+00	4.784662E+03	3.724404E+08	0.000000E+00	1.015357E+01
-1.634049E+00	4.707569E+03	4.135220E+08	0.000000E+00	9.592632E+00
-1.445282E+00	4.603698E+03	4.522861E+08	0.000000E+00	9.026018E+00
-1.256514E+00	4.423440E+03	4.393148E+08	0.000000E+00	8.473186E+00
-1.068473E+00	4.159940E+03	4.513511E+08	0.000000E+00	7.906775E+00
-9.017490E-01	3.895892E+03	6.336610E+08	0.000000E+00	7.317628E+00
-7.645450E-01	3.657485E+03	8.912580E+08	0.000000E+00	6.719376E+00
-6.369800E-01	3.444786E+03	1.038610E+09	0.000000E+00	6.076694E+00
-4.872740E-01	3.243447E+03	1.004372E+09	0.000000E+00	5.336504E+00
-3.242950E-01	3.097360E+03	9.514870E+08	0.000000E+00	4.407055E+00
-1.355280E-01	3.064932E+03	1.235704E+09	0.000000E+00	3.402043E+00
5.323900E-02	3.104030E+03	1.886245E+09	0.000000E+00	2.593069E+00
2.420060E-01	3.149134E+03	3.131396E+09	0.000000E+00	2.158167E+00
4.307730E-01	3.183618E+03	4.653970E+09	0.000000E+00	2.022511E+00
5.870520E-01	3.223645E+03	6.646146E+09	0.000000E+00	2.001127E+00
7.030610E-01	3.272321E+03	9.145789E+09	0.000000E+00	2.000000E+00
8.143191E-01	3.311785E+03	1.211264E+10	0.000000E+00	2.000000E+00
9.236280E-01	3.340594E+03	1.546707E+10	0.000000E+00	2.000000E+00
1.032437E+00	3.365007E+03	1.945995E+10	0.000000E+00	2.000000E+00
1.141049E+00	3.388998E+03	2.442117E+10	0.000000E+00	2.000000E+00
1.249428E+00	3.412972E+03	3.060428E+10	0.000000E+00	2.000000E+00
1.357659E+00	3.435592E+03	3.816298E+10	0.000000E+00	2.000000E+00
1.465927E+00	3.456561E+03	4.733485E+10	0.000000E+00	2.000000E+00
1.574230E+00	3.477917E+03	5.873080E+10	0.000000E+00	2.000000E+00
1.682310E+00	3.501641E+03	7.325135E+10	0.000000E+00	2.000000E+00
1.790000E+00	3.526419E+03	9.147885E+10	0.000000E+00	2.000000E+00

Model 1: Hydrogen Populations

7.4085E+03	3.5289E-03	6.5090E-05	0.0000E+00	0.0000E+00	2.9755E+08
5.9605E+04	3.0440E-02	2.9367E-04	0.0000E+00	0.0000E+00	4.1647E+08
3.0037E+05	1.7933E-01	9.5658E-04	0.0000E+00	0.0000E+00	5.1249E+08
8.3971E+05	6.0775E-01	2.1107E-03	0.0000E+00	0.0000E+00	5.7541E+08
1.6722E+06	1.5129E+00	3.7457E-03	0.0000E+00	0.0000E+00	6.1841E+08
2.6382E+06	3.0674E+00	5.7893E-03	0.0000E+00	0.0000E+00	6.5021E+08
4.0786E+06	6.2375E+00	9.3844E-03	0.0000E+00	0.0000E+00	6.8235E+08
6.1827E+06	1.2643E+01	1.6076E-02	0.0000E+00	0.0000E+00	7.1542E+08
8.2572E+06	2.2765E+01	2.6100E-02	0.0000E+00	0.0000E+00	7.4524E+08
1.0687E+07	3.9622E+01	4.2438E-02	0.0000E+00	0.0000E+00	7.7898E+08
1.3122E+07	6.0501E+01	6.2254E-02	0.0000E+00	0.0000E+00	8.1074E+08
1.5362E+07	8.3639E+01	8.3775E-02	0.0000E+00	0.0000E+00	8.4049E+08
1.7881E+07	1.1375E+02	1.1127E-01	0.0000E+00	0.0000E+00	8.7503E+08
2.0721E+07	1.5204E+02	1.4559E-01	0.0000E+00	0.0000E+00	9.1580E+08
2.4091E+07	2.0080E+02	1.8851E-01	0.0000E+00	0.0000E+00	9.6577E+08
2.8276E+07	2.6264E+02	2.4207E-01	0.0000E+00	0.0000E+00	1.0280E+09
3.3100E+07	3.3557E+02	3.0518E-01	0.0000E+00	0.0000E+00	1.1000E+09
3.7506E+07	4.0561E+02	3.6822E-01	0.0000E+00	0.0000E+00	1.1688E+09
4.2695E+07	4.7777E+02	4.3693E-01	0.0000E+00	0.0000E+00	1.2428E+09
5.2599E+07	5.8099E+02	5.3828E-01	0.0000E+00	0.0000E+00	1.3501E+09
7.2986E+07	7.4791E+02	7.0576E-01	0.0000E+00	0.0000E+00	1.5183E+09
1.1381E+08	1.0280E+03	9.9547E-01	0.0000E+00	0.0000E+00	1.7729E+09
1.6006E+08	1.2612E+03	1.2796E+00	0.0000E+00	0.0000E+00	2.0267E+09
2.1638E+08	1.4852E+03	1.6065E+00	0.0000E+00	0.0000E+00	2.2475E+09
3.1082E+08	1.8748E+03	2.1891E+00	0.0000E+00	0.0000E+00	2.5024E+09
3.9108E+08	2.0672E+03	2.6787E+00	0.0000E+00	0.0000E+00	2.6163E+09
4.6476E+08	2.0875E+03	3.0386E+00	0.0000E+00	0.0000E+00	2.6358E+09
5.6581E+08	2.0290E+03	3.3266E+00	0.0000E+00	0.0000E+00	2.6106E+09
6.7489E+08	1.9536E+03	3.4772E+00	0.0000E+00	0.0000E+00	2.5712E+09
8.0138E+08	1.8585E+03	3.5320E+00	0.0000E+00	0.0000E+00	2.5153E+09
9.5256E+08	1.7391E+03	3.4967E+00	0.0000E+00	0.0000E+00	2.4396E+09
1.1226E+09	1.6051E+03	3.3806E+00	0.0000E+00	0.0000E+00	2.3485E+09
1.3067E+09	1.4637E+03	3.2047E+00	0.0000E+00	0.0000E+00	2.2464E+09
1.4965E+09	1.3254E+03	2.9994E+00	0.0000E+00	0.0000E+00	2.1406E+09
1.6818E+09	1.2009E+03	2.7958E+00	0.0000E+00	0.0000E+00	2.0396E+09
1.8504E+09	1.0508E+03	2.5472E+00	0.0000E+00	0.0000E+00	1.9106E+09
2.1860E+09	9.5389E+02	2.3994E+00	0.0000E+00	0.0000E+00	1.8227E+09
2.4447E+09	8.9225E+02	2.3450E+00	0.0000E+00	0.0000E+00	1.7655E+09
2.7861E+09	8.5298E+02	2.3697E+00	0.0000E+00	0.0000E+00	1.7294E+09
3.2298E+09	8.1531E+02	2.4031E+00	0.0000E+00	0.0000E+00	1.6937E+09
3.7616E+09	7.7022E+02	2.3980E+00	0.0000E+00	0.0000E+00	1.6481E+09
4.4036E+09	7.1523E+02	2.3410E+00	0.0000E+00	0.0000E+00	1.5889E+09
5.1961E+09	6.4938E+02	2.2249E+00	0.0000E+00	0.0000E+00	1.5135E+09
6.2015E+09	5.7244E+02	2.0448E+00	0.0000E+00	0.0000E+00	1.4191E+09
7.5487E+09	4.8473E+02	1.8003E+00	0.0000E+00	0.0000E+00	1.3023E+09
9.5978E+09	3.8536E+02	1.4886E+00	0.0000E+00	0.0000E+00	1.1557E+09
1.3066E+10	2.8300E+02	1.1399E+00	0.0000E+00	0.0000E+00	9.8301E+08
1.8119E+10	1.9678E+02	8.2034E-01	0.0000E+00	0.0000E+00	8.1127E+08
2.5442E+10	1.3701E+02	5.8607E-01	0.0000E+00	0.0000E+00	6.6867E+08
3.6895E+10	9.6049E+01	4.1868E-01	0.0000E+00	0.0000E+00	5.5213E+08
5.5406E+10	6.5265E+01	2.8863E-01	0.0000E+00	0.0000E+00	4.4751E+08
8.5908E+10	4.4273E+01	1.9770E-01	0.0000E+00	0.0000E+00	3.6015E+08
1.3670E+11	3.4450E+01	1.5491E-01	0.0000E+00	0.0000E+00	3.0767E+08
2.2126E+11	3.2385E+01	1.4643E-01	0.0000E+00	0.0000E+00	2.8614E+08
3.6184E+11	3.3557E+01	1.5246E-01	0.0000E+00	0.0000E+00	2.7553E+08
5.9914E+11	3.6273E+01	1.6544E-01	0.0000E+00	0.0000E+00	2.6566E+08
1.0040E+12	3.5165E+01	1.6070E-01	0.0000E+00	0.0000E+00	2.3253E+08
1.6957E+12	2.0761E+01	9.4758E-02	0.0000E+00	0.0000E+00	1.3796E+08
2.9007E+12	5.9533E+00	2.7120E-02	0.0000E+00	0.0000E+00	3.7085E+07
4.7670E+12	1.2783E+00	5.8207E-03	0.0000E+00	0.0000E+00	5.4515E+06
7.3525E+12	2.6129E-01	1.1898E-03	0.0000E+00	0.0000E+00	6.9166E+05
1.1196E+13	5.3636E-02	2.4418E-04	0.0000E+00	0.0000E+00	7.1371E+04
1.7880E+13	1.0136E-02	4.6148E-05	0.0000E+00	0.0000E+00	7.5602E+03
3.1561E+13	3.1983E-03	1.4561E-05	0.0000E+00	0.0000E+00	1.5865E+03
5.6685E+13	3.8344E-03	1.7456E-05	0.0000E+00	0.0000E+00	1.3193E+03
9.5763E+13	1.0541E-02	4.7986E-05	0.0000E+00	0.0000E+00	2.5590E+03
1.5281E+14	2.9059E-02	1.3227E-04	0.0000E+00	0.0000E+00	5.1670E+03
2.3667E+14	6.7651E-02	3.0791E-04	0.0000E+00	0.0000E+00	9.0266E+03
3.3599E+14	1.5243E-01	6.9370E-04	0.0000E+00	0.0000E+00	1.6149E+04
4.3295E+14	3.3926E-01	1.5437E-03	0.0000E+00	0.0000E+00	3.0385E+04
5.5326E+14	6.6729E-01	3.0356E-03	0.0000E+00	0.0000E+00	5.0953E+04
7.0602E+14	1.1591E+00	5.2714E-03	0.0000E+00	0.0000E+00	7.5678E+04
9.0101E+14	1.9129E+00	8.6977E-03	0.0000E+00	0.0000E+00	1.0690E+05
1.1495E+15	3.1309E+00	1.4233E-02	0.0000E+00	0.0000E+00	1.4988E+05
1.4659E+15	5.1029E+00	2.3205E-02	0.0000E+00	0.0000E+00	2.0950E+05
1.8694E+15	8.1772E+00	3.7237E-02	0.0000E+00	0.0000E+00	2.8820E+05
2.3853E+15	1.2860E+01	5.8778E-02	0.0000E+00	0.0000E+00	3.8948E+05
3.0436E+15	2.0249E+01	9.3301E-02	0.0000E+00	0.0000E+00	5.2818E+05
3.8794E+15	3.2503E+01	1.5207E-01	0.0000E+00	0.0000E+00	7.3321E+05
4.9391E+15	5.2474E+01	2.5203E-01	0.0000E+00	0.0000E+00	1.0293E+06

Model 2: Chromospheric Model

MASS SCALE
1.6700002
80

-3.394989E+00	8.841530E+04	3.284282E+08	0.000000E+00	5.519300E+01
-3.393952E+00	5.056115E+04	4.797764E+08	0.000000E+00	4.845545E+01
-3.393631E+00	4.222689E+04	5.463462E+08	0.000000E+00	4.603338E+01
-3.393338E+00	3.503033E+04	6.214301E+08	0.000000E+00	4.378060E+01
-3.393141E+00	3.184213E+04	6.652203E+08	0.000000E+00	4.257304E+01
-3.392951E+00	2.896525E+04	7.101901E+08	0.000000E+00	4.144495E+01
-3.392760E+00	2.694728E+04	7.487098E+08	0.000000E+00	4.049903E+01
-3.392569E+00	2.530071E+04	7.851523E+08	0.000000E+00	3.963299E+01
-3.392387E+00	2.404359E+04	8.173226E+08	0.000000E+00	3.888737E+01
-3.392219E+00	2.334687E+04	8.410342E+08	0.000000E+00	3.831875E+01
-3.392051E+00	2.264916E+04	8.658790E+08	0.000000E+00	3.774933E+01
-3.391857E+00	2.190066E+04	8.947608E+08	0.000000E+00	3.711410E+01
-3.391614E+00	2.105513E+04	9.309770E+08	0.000000E+00	3.635452E+01
-3.391372E+00	2.021291E+04	9.695533E+08	0.000000E+00	3.559793E+01
-3.391046E+00	1.924089E+04	1.019620E+09	0.000000E+00	3.468069E+01
-3.390691E+00	1.822286E+04	1.077492E+09	0.000000E+00	3.370713E+01
-3.390229E+00	1.709915E+04	1.149881E+09	0.000000E+00	3.260041E+01
-3.389716E+00	1.592212E+04	1.235347E+09	0.000000E+00	3.142787E+01
-3.388958E+00	1.514670E+04	1.307349E+09	0.000000E+00	3.052040E+01
-3.387991E+00	1.426058E+04	1.399748E+09	0.000000E+00	2.944909E+01
-3.386734E+00	1.317064E+04	1.532449E+09	0.000000E+00	2.805679E+01
-3.385139E+00	1.179862E+04	1.740529E+09	0.000000E+00	2.614565E+01
-3.383251E+00	1.038868E+04	2.001179E+09	0.000000E+00	2.398943E+01
-3.381101E+00	9.392426E+03	2.131577E+09	0.000000E+00	2.241076E+01
-3.378529E+00	8.606512E+03	2.310911E+09	0.000000E+00	2.113110E+01
-3.375555E+00	7.713899E+03	2.588706E+09	0.000000E+00	1.967727E+01
-3.371777E+00	7.558027E+03	2.639680E+09	0.000000E+00	1.939605E+01
-3.366654E+00	7.514521E+03	2.640038E+09	0.000000E+00	1.928340E+01
-3.361443E+00	7.496542E+03	2.615535E+09	0.000000E+00	1.921037E+01
-3.356995E+00	7.480690E+03	2.578871E+09	0.000000E+00	1.914531E+01
-3.352547E+00	7,464838E+03	2.524733E+09	0.000000E+00	1.908024E+01
-3.348100E+00	7.448990E+03	2.451773E+09	0.000000E+00	1.901519E+01
-3.343286E+00	7.431043E+03	2.354195E+09	0.000000E+00	1.894051E+01
-3.338267E+00	7.411924E+03	2.238951E+09	0.000000E+00	1.886045E+01
-3.333248E+00	7.392804E+03	2.121900E+09	0.000000E+00	1.878038E+01
-3.328230E+00	7.373688E+03	2.015567E+09	0.000000E+00	1.870033E+01
-3.321995E+00	7.349780E+03	1.911957E+09	0.000000E+00	1.860016E+01
-3.309545E+00	7.301467E+03	1.815150E+09	0.000000E+00	1.839717E+01
-3.297095E+00	7.253144E+03	1.773530E+09	0.000000E+00	1.819418E+01
-3.277906E+00	7.178663E+03	1.740914E+09	0.000000E+00	1.788123E+01
-3.256911E+00	7.097174E+03	1.704832E+09	0.000000E+00	1.753880E+01
-3.233500E+00	7.006307E+03	1.655907E+09	0.000000E+00	1.715687E+01
-3.208104E+00	6.907735E+03	1.592398E+09	0.000000E+00	1.674259E+01
-3.180351E+00	6.800016E+03	1.512543E+09	0.000000E+00	1.628989E+01
-3.148722E+00	6.677251E+03	1.411779E+09	0.000000E+00	1.577395E+01
-3.109831E+00	6.532872E+03	1.286398E+09	0.000000E+00	1.517424E+01
-3.056164E+00	6.353605E+03	1.129908E+09	0.000000E+00	1.445514E+01
-2.972385E+00	6.143039E+03	9.611501E+08	0.000000E+00	1.373774E+01
-2.868602E+00	5.922998E+03	7.884828E+08	0.000000E+00	1.333041E+01
-2.747036E+00	5.725081E+03	6.638084E+08	0.000000E+00	1.296011E+01
-2.609343E+00	5.523081E+03	5.524435E+08	0.000000E+00	1.254387E+01
-2.457896E+00	5.314906E+03	4.512590E+08	0.000000E+00	1.208601E+01
-2.295669E+00	5.109006E+03	3.691313E+08	0.000000E+00	1.159492E+01
-2.124085E+00	4.867513E+03	3.487662E+08	0.000000E+00	1.107560E+01
-1.946540E+00	4.860109E+03	3.696143E+08	0.000000E+00	1.053827E+01
-1.765082E+00	4.763025E+03	3.849959E+08	0.000000E+00	9.989166E+00
-1.577155E+00	4.683595E+03	4.367422E+08	0.000000E+00	9.420452E+00
-1.389323E+00	4.598607E+03	4.969328E+08	0.000000E+00	8.855944E+00
-1.211090E+00	4.498407E+03	5.530705E+08	0.000000E+00	8.340694E+00
-1.044749E+00	4.396487E+03	6.337811E+08	0.000000E+00	7.850227E+00
-8.804420E-01	4.262877E+03	7.549439E+08	0.000000E+00	7.310101E+00
-7.523270E-01	4.144399E+03	1.008502E+09	0.000000E+00	6.675507E+00
-6.325460E-01	4.033702E+03	1.388292E+09	0.000000E+00	6.066187E+00
-4.452350E-01	3.797811E+03	2.315352E+09	0.000000E+00	5.059692E+00
-2.560660E-01	3.558618E+03	3.131481E+09	0.000000E+00	4.039706E+00
-6.689599E-02	3.324599E+03	3.094626E+09	0.000000E+00	3.035748E+00
1.222730E-01	3.165093E+03	2.747880E+09	0.000000E+00	2.258763E+00
3.114420E-01	3.189071E+03	3.971127E+09	0.000000E+00	2.035116E+00
4.949130E-01	3.274634E+03	6.786665E+09	0.000000E+00	2.001810E+00
6.127871E-01	3.332683E+03	9.580008E+09	0.000000E+00	2.000004E+00
7.243680E-01	3.381291E+03	1.296707E+10	0.000000E+00	2.000000E+00
8.331311E-01	3.417667E+03	1.683906E+10	0.000000E+00	2.000000E+00
9.412130E-01	3.444730E+03	2.126308E+10	0.000000E+00	2.000000E+00
1.049419E+00	3.468653E+03	2.659987E+10	0.000000E+00	2.000000E+00
1.157740E+00	3.492724E+03	3.326219E+10	0.000000E+00	2.000000E+00
1.266017E+00	3.516983E+03	4.157012E+10	0.000000E+00	2.000000E+00
1.374345E+00	3.539085E+03	5.161798E+10	0.000000E+00	2.000000E+00
1.482887E+00	3.559647E+03	6.380694E+10	0.000000E+00	2.000000E+00
1.591550E+00	3.581122E+03	7.900876E+10	0.000000E+00	2.000000E+00
1.700000E+00	3.605634E+03	9.847348E+10	0.000000E+00	2.000000E+00

Model 2: Hydrogen Populations

7.5334E+03	3.6487E-03	6.7070E-05	0.0000E+00	0.0000E+00	2.9818E+08
8.7334E+04	4.6742E-02	3.9689E-04	0.0000E+00	0.0000E+00	4.3558E+08
2.3080E+05	1.3532E-01	8.2270E-04	0.0000E+00	0.0000E+00	4.9600E+08
7.0134E+05	4.9439E-01	1.9542E-03	0.0000E+00	0.0000E+00	5.6413E+08
1.2935E+06	1.1117E+00	3.2740E-03	0.0000E+00	0.0000E+00	6.0383E+08
2.4191E+06	2.6691E+00	5.8754E-03	0.0000E+00	0.0000E+00	6.4455E+08
3.9211E+06	5.7795E+00	1.0085E-02	0.0000E+00	0.0000E+00	6.7939E+08
5.9151E+06	1.1708E+01	1.7438E-02	0.0000E+00	0.0000E+00	7.1229E+08
8.0856E+06	2.0870E+01	2.8351E-02	0.0000E+00	0.0000E+00	7.4130E+08
9.5425E+06	3.0530E+01	3.9553E-02	0.0000E+00	0.0000E+00	7.6269E+08
1.1186E+07	4.2997E+01	5.3864E-02	0.0000E+00	0.0000E+00	7.8509E+08
1.3126E+07	6.0399E+01	7.3525E-02	0.0000E+00	0.0000E+00	8.1114E+08
1.5496E+07	8.5754E+01	1.0164E-01	0.0000E+00	0.0000E+00	8.4380E+08
1.8051E+07	1.1580E+02	1.3430E-01	0.0000E+00	0.0000E+00	8.7859E+08
2.1127E+07	1.5804E+02	1.7936E-01	0.0000E+00	0.0000E+00	9.2376E+08
2.4654E+07	2.0848E+02	2.3213E-01	0.0000E+00	0.0000E+00	9.7598E+08
2.8933E+07	2.7306E+02	2.9892E-01	0.0000E+00	0.0000E+00	1.0413E+09
3.4318E+07	3.5018E+02	3.7805E-01	0.0000E+00	0.0000E+00	1.1184E+09
3.8174E+07	4.1510E+02	4.4969E-01	0.0000E+00	0.0000E+00	1.1834E+09
4.4473E+07	4.9527E+02	5.4158E-01	0.0000E+00	0.0000E+00	1.2667E+09
5.6217E+07	6.0897E+02	6.7585E-01	0.0000E+00	0.0000E+00	1.3862E+09
8.0511E+07	7.9700E+02	9.0188E-01	0.0000E+00	0.0000E+00	1.5735E+09
1.2378E+08	1.0725E+03	1.2501E+00	0.0000E+00	0.0000E+00	1.8305E+09
1.7069E+08	1.2881E+03	1.5773E+00	0.0000E+00	0.0000E+00	2.0810E+09
2.3379E+08	1.5385E+03	2.0116E+00	0.0000E+00	0.0000E+00	2.3041E+09
3.4351E+08	1.9974E+03	2.8226E+00	0.0000E+00	0.0000E+00	2.5853E+09
4.0404E+08	2.0660E+03	3.2549E+00	0.0000E+00	0.0000E+00	2.6362E+09
4.8078E+08	2.0454E+03	3.6493E+00	0.0000E+00	0.0000E+00	2.6365E+09
5.7537E+08	1.9863E+03	3.9294E+00	0.0000E+00	0.0000E+00	2.6119E+09
6.7670E+08	1.9154E+03	4.0791E+00	0.0000E+00	0.0000E+00	2.5752E+09
7.9987E+08	1.8225E+03	4.1336E+00	0.0000E+00	0.0000E+00	2.5210E+09
9.4652E+08	1.7078E+03	4.0879E+00	0.0000E+00	0.0000E+00	2.4479E+09
1.1301E+09	1.5655E+03	3.9373E+00	0.0000E+00	0.0000E+00	2.3502E+09
1.3398E+09	1.4091E+03	3.7002E+00	0.0000E+00	0.0000E+00	2.2349E+09
1.5534E+09	1.2607E+03	3.4318E+00	0.0000E+00	0.0000E+00	2.1177E+09
1.7560E+09	1.1339E+03	3.1817E+00	0.0000E+00	0.0000E+00	2.0113E+09
1.9763E+09	1.0170E+03	2.9463E+00	0.0000E+00	0.0000E+00	1.9075E+09
2.2940E+09	9.1158E+02	2.7838E+00	0.0000E+00	0.0000E+00	1.8105E+09
2.5566E+09	8.6631E+02	2.7654E+00	0.0000E+00	0.0000E+00	1.7686E+09
2.9462E+09	8.2989E+02	2.8101E+00	0.0000E+00	0.0000E+00	1.7356E+09
3.4068E+09	7.9184E+02	2.8339E+00	0.0000E+00	0.0000E+00	1.6991E+09
3.9767E+09	7.4394E+02	2.8060E+00	0.0000E+00	0.0000E+00	1.6496E+09
4.6683E+09	6.8599E+02	2.7141E+00	0.0000E+00	0.0000E+00	1.5854E+09
5.5182E+09	6.1802E+02	2.5529E+00	0.0000E+00	0.0000E+00	1.5047E+09
6.6168E+09	5.3858E+02	2.3143E+00	0.0000E+00	0.0000E+00	1.4029E+09
8.1359E+09	4.4812E+02	1.8987E+00	0.0000E+00	0.0000E+00	1.2760E+09
1.0492E+10	3.4720E+02	1.6069E+00	0.0000E+00	0.0000E+00	1.1174E+09
1.4463E+10	2.5243E+02	1.2138E+00	0.0000E+00	0.0000E+00	9.4534E+08
1.8997E+10	1.7087E+02	8.4641E-01	0.0000E+00	0.0000E+00	7.6925E+08
2.8345E+10	1.2164E+02	6.1609E-01	0.0000E+00	0.0000E+00	6.4128E+08
4.1687E+10	8.4684E+01	4.3598E-01	0.0000E+00	0.0000E+00	5.2740E+08
6.3392E+10	5.6664E+01	2.8507E-01	0.0000E+00	0.0000E+00	4.2357E+08
9.8116E+10	3.7484E+01	1.9668E-01	0.0000E+00	0.0000E+00	3.3527E+08
1.5818E+11	3.2260E+01	1.7020E-01	0.0000E+00	0.0000E+00	3.0082E+08
2.5617E+11	3.2175E+01	1.7056E-01	0.0000E+00	0.0000E+00	2.8765E+08
4.1960E+11	3.3353E+01	1.7758E-01	0.0000E+00	0.0000E+00	2.7560E+08
6.8952E+11	3.7283E+01	1.8931E-01	0.0000E+00	0.0000E+00	2.6924E+08
1.1679E+12	3.9289E+01	2.1073E-01	0.0000E+00	0.0000E+00	2.4695E+08
1.8014E+12	3.5608E+01	1.9131E-01	0.0000E+00	0.0000E+00	1.9858E+08
3.0079E+12	2.9526E+01	1.5860E-01	0.0000E+00	0.0000E+00	1.4173E+08
4.6850E+12	1.8684E+01	1.0022E-01	0.0000E+00	0.0000E+00	7.3870E+07
7.1254E+12	1.2175E+01	6.5210E-02	0.0000E+00	0.0000E+00	3.5407E+07
1.0364E+13	7.7996E+00	4.1733E-02	0.0000E+00	0.0000E+00	1.6205E+07
1.9012E+13	2.2397E+00	1.1969E-02	0.0000E+00	0.0000E+00	2.6899E+06
3.5262E+13	5.0731E-01	2.7085E-03	0.0000E+00	0.0000E+00	3.1996E+05
6.5159E+13	9.0059E-02	4.8052E-04	0.0000E+00	0.0000E+00	3.0336E+04
1.1434E+14	2.6259E-02	1.4006E-04	0.0000E+00	0.0000E+00	6.1429E+03
1.7933E+14	5.4582E-02	2.9110E-04	0.0000E+00	0.0000E+00	9.5108E+03
2.6788E+14	2.1520E-01	1.1476E-03	0.0000E+00	0.0000E+00	2.8454E+04
3.4587E+14	5.2167E-01	2.7818E-03	0.0000E+00	0.0000E+00	5.8130E+04
4.4131E+14	1.1094E+00	5.9149E-03	0.0000E+00	0.0000E+00	1.0543E+05
5.6137E+14	2.0487E+00	1.0921E-02	0.0000E+00	0.0000E+00	1.6676E+05
7.1481E+14	3.4249E+00	1.8252E-02	0.0000E+00	0.0000E+00	2.3881E+05
9.1126E+14	5.5342E+00	2.9486E-02	0.0000E+00	0.0000E+00	3.3050E+05
1.1620E+15	8.9287E+00	4.7575E-02	0.0000E+00	0.0000E+00	4.5694E+05
1.4816E+15	1.4383E+01	7.6707E-02	0.0000E+00	0.0000E+00	6.3143E+05
1.8904E+15	2.2645E+01	1.2110E-01	0.0000E+00	0.0000E+00	8.5342E+05
2.4143E+15	3.5085E+01	1.8877E-01	0.0000E+00	0.0000E+00	1.1364E+06
3.0835E+15	5.4699E+01	2.9786E-01	0.0000E+00	0.0000E+00	1.5271E+06
3.9334E+15	8.7356E+01	4.8595E-01	0.0000E+00	0.0000E+00	2.1128E+06

Model 3: Chromospheric Model

MASS SCALE
1.6700002
80

-3.395000E+00	8.883259E+04	3.277393E+08	0.000000E+00	5.519626E+01
-3.394055E+00	5.469597E+04	4.587314E+08	0.000000E+00	4.907701E+01
-3.393552E+00	4.033439E+04	5.645093E+08	0.000000E+00	4.544006E+01
-3.393291E+00	3.404534E+04	6.338689E+08	0.000000E+00	4.343461E+01
-3.393101E+00	3.060802E+04	6.813134E+08	0.000000E+00	4.220284E+01
-3.392925E+00	2.859247E+04	7.164443E+08	0.000000E+00	4.129556E+01
-3.392745E+00	2.679039E+04	7.519933E+08	0.000000E+00	4.041933E+01
-3.392557E+00	2.512666E+04	7.886304E+08	0.000000E+00	3.955913E+01
-3.392345E+00	2.395969E+04	8.216820E+08	0.000000E+00	3.876879E+01
-3.392090E+00	2.286123E+04	8.590908E+08	0.000000E+00	3.789547E+01
-3.391859E+00	2.191744E+04	8.943267E+08	0.000000E+00	3.712082E+01
-3.391645E+00	2.112548E+04	9.273135E+08	0.000000E+00	3.643060E+01
-3.391398E+00	2.029085E+04	9.656221E+08	0.000000E+00	3.567247E+01
-3.391108E+00	1.939743E+04	1.010809E+09	0.000000E+00	3.483661E+01
-3.390761E+00	1.840887E+04	1.066197E+09	0.000000E+00	3.388969E+01
-3.390342E+00	1.730767E+04	1.135158E+09	0.000000E+00	3.281511E+01
-3.389823E+00	1.619230E+04	1.214969E+09	0.000000E+00	3.169356E+01
-3.389157E+00	1.530204E+04	1.291205E+09	0.000000E+00	3.071738E+01
-3.388269E+00	1.450161E+04	1.373222E+09	0.000000E+00	2.974517E+01
-3.387086E+00	1.347589E+04	1.492345E+09	0.000000E+00	2.846055E+01
-3.385562E+00	1.215963E+04	1.679385E+09	0.000000E+00	2.667801E+01
-3.383735E+00	1.066311E+04	1.950917E+09	0.000000E+00	2.442004E+01
-3.381663E+00	9.587292E+03	2.104304E+09	0.000000E+00	2.272510E+01
-3.379160E+00	8.799496E+03	2.257999E+09	0.000000E+00	2.144522E+01
-3.376232E+00	7.961222E+03	2.505882E+09	0.000000E+00	2.007885E+01
-3.372584E+00	7.610242E+03	2.619798E+09	0.000000E+00	1.948640E+01
-3.368022E+00	7.519194E+03	2.639292E+09	0.000000E+00	1.930232E+01
-3.362314E+00	7.499608E+03	2.614206E+09	0.000000E+00	1.922291E+01
-3.357485E+00	7.482510E+03	2.574893E+09	0.000000E+00	1.915288E+01
-3.352942E+00	7.466221E+03	2.519066E+09	0.000000E+00	1.908589E+01
-3.348398E+00	7.449929E+03	2.443464E+09	0.000000E+00	1.901888E+01
-3.343980E+00	7.433479E+03	2.352408E+09	0.000000E+00	1.895046E+01
-3.339609E+00	7.416964E+03	2.250434E+09	0.000000E+00	1.888148E+01
-3.335239E+00	7.400453E+03	2.144706E+09	0.000000E+00	1.881251E+01
-3.330868E+00	7.383938E+03	2.043872E+09	0.000000E+00	1.874353E+01
-3.323425E+00	7.355204E+03	1.914973E+09	0.000000E+00	1.862290E+01
-3.315235E+00	7.323496E+03	1.827230E+09	0.000000E+00	1.848972E+01
-3.303792E+00	7.279130E+03	1.770269E+09	0.000000E+00	1.830334E+01
-3.286905E+00	7.213591E+03	1.734500E+09	0.000000E+00	1.802800E+01
-3.265936E+00	7.132203E+03	1.699203E+09	0.000000E+00	1.768600E+01
-3.243175E+00	7.043860E+03	1.654158E+09	0.000000E+00	1.731471E+01
-3.218546E+00	6.948265E+03	1.595653E+09	0.000000E+00	1.691291E+01
-3.191447E+00	6.843083E+03	1.521035E+09	0.000000E+00	1.647089E+01
-3.161046E+00	6.725085E+03	1.427575E+09	0.000000E+00	1.597497E+01
-3.124914E+00	6.588716E+03	1.312081E+09	0.000000E+00	1.540603E+01
-3.075488E+00	6.420435E+03	1.167415E+09	0.000000E+00	1.472675E+01
-2.998285E+00	6.212656E+03	9.977419E+08	0.000000E+00	1.400699E+01
-2.900234E+00	5.995216E+03	8.295900E+08	0.000000E+00	1.346980E+01
-2.785050E+00	5.788918E+03	6.904532E+08	0.000000E+00	1.307802E+01
-2.653212E+00	5.588622E+03	5.767153E+08	0.000000E+00	1.267654E+01
-2.506741E+00	5.383423E+03	4.744355E+08	0.000000E+00	1.223346E+01
-2.347464E+00	5.081779E+03	3.918429E+08	0.000000E+00	1.175159E+01
-2.177515E+00	4.780275E+03	3.506639E+08	0.000000E+00	1.123731E+01
-2.000427E+00	4.580229E+03	3.498287E+08	0.000000E+00	1.070137E+01
-1.819413E+00	4.284662E+03	3.724404E+08	0.000000E+00	1.015357E+01
-1.634049E+00	3.997569E+03	4.135220E+08	0.000000E+00	9.592632E+00
-1.445282E+00	3.783698E+03	4.522861E+08	0.000000E+00	9.026018E+00
-1.256514E+00	3.603440E+03	4.393148E+08	0.000000E+00	8.473186E+00
-1.068473E+00	3.520940E+03	4.513511E+08	0.000000E+00	7.906775E+00
-9.017490E-01	3.450892E+03	6.336610E+08	0.000000E+00	7.317628E+00
-7.645450E-01	3.400085E+03	8.912580E+08	0.000000E+00	6.719376E+00
-6.369800E-01	3.354786E+03	1.038610E+09	0.000000E+00	6.076694E+00
-4.972740E-01	3.243447E+03	1.004372E+09	0.000000E+00	5.336504E+00
-3.242950E-01	3.097360E+03	9.514870E+08	0.000000E+00	4.407055E+00
-1.395280E-01	3.064932E+03	1.235704E+09	0.000000E+00	3.402043E+00
5.323900E-02	3.104030E+03	1.986245E+09	0.000000E+00	2.593069E+00
2.420060E-01	3.149134E+03	3.131396E+09	0.000000E+00	2.158167E+00
4.307730E-01	3.183618E+03	4.653970E+09	0.000000E+00	2.022511E+00
5.870520E-01	3.223645E+03	6.646146E+09	0.000000E+00	2.001127E+00
7.030610E-01	3.272321E+03	9.145789E+09	0.000000E+00	2.000000E+00
8.143191E-01	3.311785E+03	1.211264E+10	0.000000E+00	2.000000E+00
9.236280E-01	3.340594E+03	1.546707E+10	0.000000E+00	2.000000E+00
1.032437E+00	3.365007E+03	1.945995E+10	0.000000E+00	2.000000E+00
1.141049E+00	3.388996E+03	2.442117E+10	0.000000E+00	2.000000E+00
1.249428E+00	3.412972E+03	3.060428E+10	0.000000E+00	2.000000E+00
1.357659E+00	3.435592E+03	3.816298E+10	0.000000E+00	2.000000E+00
1.465927E+00	3.456561E+03	4.733485E+10	0.000000E+00	2.000000E+00
1.574230E+00	3.477917E+03	5.873080E+10	0.000000E+00	2.000000E+00
1.682310E+00	3.501641E+03	7.325135E+10	0.000000E+00	2.000000E+00
1.780000E+00	3.526418E+03	8.147885E+10	0.000000E+00	2.000000E+00

Model 3: Hydrogen Populations

7.4085E+03	3.5289E-03	6.5090E-05	0.0000E+00	0.0000E+00	2.9755E+08
5.9605E+04	3.0440E-02	2.9367E-04	0.0000E+00	0.0000E+00	4.1647E+08
3.0037E+05	1.7933E-01	9.5658E-04	0.0000E+00	0.0000E+00	5.1249E+08
8.3971E+05	6.0775E-01	2.1107E-03	0.0000E+00	0.0000E+00	5.7541E+08
1.6722E+06	1.5129E+00	3.7457E-03	0.0000E+00	0.0000E+00	6.1841E+08
2.6382E+06	3.0674E+00	5.7893E-03	0.0000E+00	0.0000E+00	6.5021E+08
4.0786E+06	6.2376E+00	9.3844E-03	0.0000E+00	0.0000E+00	6.8235E+08
6.1827E+06	1.2643E+01	1.6076E-02	0.0000E+00	0.0000E+00	7.1542E+08
8.2572E+06	2.2765E+01	2.6100E-02	0.0000E+00	0.0000E+00	7.4524E+08
1.0687E+07	3.9622E+01	4.2438E-02	0.0000E+00	0.0000E+00	7.7898E+08
1.3122E+07	6.0501E+01	6.2254E-02	0.0000E+00	0.0000E+00	8.1074E+08
1.5362E+07	8.3639E+01	8.3775E-02	0.0000E+00	0.0000E+00	8.4049E+08
1.7881E+07	1.1375E+02	1.1127E-01	0.0000E+00	0.0000E+00	8.7503E+08
2.0721E+07	1.5204E+02	1.4559E-01	0.0000E+00	0.0000E+00	9.1580E+08
2.4091E+07	2.0080E+02	1.8851E-01	0.0000E+00	0.0000E+00	9.6577E+08
2.8276E+07	2.6264E+02	2.4207E-01	0.0000E+00	0.0000E+00	1.0280E+09
3.3100E+07	3.3557E+02	3.0518E-01	0.0000E+00	0.0000E+00	1.1000E+09
3.7506E+07	4.0561E+02	3.6822E-01	0.0000E+00	0.0000E+00	1.1688E+09
4.2695E+07	4.7777E+02	4.3693E-01	0.0000E+00	0.0000E+00	1.2428E+09
5.2599E+07	5.8099E+02	5.3828E-01	0.0000E+00	0.0000E+00	1.3501E+09
7.2986E+07	7.4791E+02	7.0576E-01	0.0000E+00	0.0000E+00	1.5183E+09
1.1381E+08	1.0280E+03	9.9547E-01	0.0000E+00	0.0000E+00	1.7729E+09
1.6006E+08	1.2612E+03	1.2796E+00	0.0000E+00	0.0000E+00	2.0267E+09
2.1638E+08	1.4852E+03	1.6065E+00	0.0000E+00	0.0000E+00	2.2475E+09
3.1082E+08	1.8748E+03	2.1891E+00	0.0000E+00	0.0000E+00	2.5024E+09
3.9108E+08	2.0672E+03	2.6787E+00	0.0000E+00	0.0000E+00	2.6163E+09
4.6476E+08	2.0875E+03	3.0386E+00	0.0000E+00	0.0000E+00	2.6358E+09
5.6581E+08	2.0290E+03	3.3266E+00	0.0000E+00	0.0000E+00	2.6106E+09
6.7489E+08	1.9536E+03	3.4772E+00	0.0000E+00	0.0000E+00	2.5712E+09
8.0138E+08	1.8585E+03	3.5320E+00	0.0000E+00	0.0000E+00	2.5153E+09
9.5256E+08	1.7391E+03	3.4967E+00	0.0000E+00	0.0000E+00	2.4396E+09
1.1226E+09	1.6051E+03	3.3806E+00	0.0000E+00	0.0000E+00	2.3485E+09
1.3067E+09	1.4637E+03	3.2047E+00	0.0000E+00	0.0000E+00	2.2464E+09
1.4965E+09	1.3254E+03	2.9994E+00	0.0000E+00	0.0000E+00	2.1406E+09
1.6818E+09	1.2009E+03	2.7958E+00	0.0000E+00	0.0000E+00	2.0396E+09
1.8504E+09	1.0508E+03	2.5472E+00	0.0000E+00	0.0000E+00	1.9106E+09
2.1860E+09	9.5389E+02	2.3994E+00	0.0000E+00	0.0000E+00	1.8227E+09
2.4447E+09	8.9225E+02	2.3450E+00	0.0000E+00	0.0000E+00	1.7655E+09
2.7861E+09	8.5298E+02	2.3697E+00	0.0000E+00	0.0000E+00	1.7294E+09
3.2298E+09	8.1531E+02	2.4031E+00	0.0000E+00	0.0000E+00	1.6937E+09
3.7616E+09	7.7022E+02	2.3980E+00	0.0000E+00	0.0000E+00	1.6481E+09
4.4036E+09	7.1523E+02	2.3410E+00	0.0000E+00	0.0000E+00	1.5889E+09
5.1961E+09	6.4938E+02	2.2249E+00	0.0000E+00	0.0000E+00	1.5135E+09
6.2015E+09	5.7244E+02	2.0448E+00	0.0000E+00	0.0000E+00	1.4191E+09
7.5487E+09	4.8473E+02	1.8003E+00	0.0000E+00	0.0000E+00	1.3023E+09
9.5978E+09	3.8536E+02	1.4886E+00	0.0000E+00	0.0000E+00	1.1557E+09
1.3066E+10	2.8300E+02	1.1399E+00	0.0000E+00	0.0000E+00	9.8301E+08
1.8119E+10	1.9679E+02	8.2034E-01	0.0000E+00	0.0000E+00	8.1127E+08
2.5442E+10	1.3701E+02	5.8607E-01	0.0000E+00	0.0000E+00	6.6867E+08
3.6895E+10	9.6049E+01	4.1888E-01	0.0000E+00	0.0000E+00	5.5213E+08
5.5406E+10	6.5265E+01	2.8863E-01	0.0000E+00	0.0000E+00	4.4751E+08
8.5908E+10	4.4273E+01	1.9770E-01	0.0000E+00	0.0000E+00	3.6015E+08
1.3670E+11	3.4450E+01	1.5491E-01	0.0000E+00	0.0000E+00	3.0767E+08
2.2126E+11	3.2385E+01	1.4643E-01	0.0000E+00	0.0000E+00	2.8614E+08
3.6184E+11	3.3557E+01	1.5246E-01	0.0000E+00	0.0000E+00	2.7553E+08
5.9914E+11	3.6273E+01	1.6544E-01	0.0000E+00	0.0000E+00	2.6566E+08
1.0040E+12	3.5165E+01	1.6070E-01	0.0000E+00	0.0000E+00	2.3253E+08
1.6957E+12	2.0761E+01	9.4758E-02	0.0000E+00	0.0000E+00	1.3796E+08
2.9007E+12	5.9533E+00	2.7120E-02	0.0000E+00	0.0000E+00	3.7085E+07
4.7670E+12	1.2783E+00	5.8207E-03	0.0000E+00	0.0000E+00	5.4515E+06
7.3525E+12	2.6129E-01	1.1898E-03	0.0000E+00	0.0000E+00	6.9166E+05
1.1196E+13	5.3636E-02	2.4418E-04	0.0000E+00	0.0000E+00	7.1371E+04
1.7880E+13	1.0136E-02	4.6148E-05	0.0000E+00	0.0000E+00	7.5602E+03
3.1561E+13	3.1983E-03	1.4561E-05	0.0000E+00	0.0000E+00	1.5865E+03
5.6685E+13	3.8344E-03	1.7456E-05	0.0000E+00	0.0000E+00	1.3193E+03
9.5763E+13	1.0541E-02	4.7986E-05	0.0000E+00	0.0000E+00	2.5590E+03
1.5281E+14	2.9059E-02	1.3227E-04	0.0000E+00	0.0000E+00	5.1670E+03
2.3667E+14	6.7651E-02	3.0791E-04	0.0000E+00	0.0000E+00	9.0266E+03
3.3599E+14	1.5243E-01	6.9370E-04	0.0000E+00	0.0000E+00	1.6149E+04
4.3295E+14	3.3926E-01	1.5437E-03	0.0000E+00	0.0000E+00	3.0385E+04
5.5328E+14	6.6729E-01	3.0356E-03	0.0000E+00	0.0000E+00	5.0953E+04
7.0602E+14	1.1591E+00	5.2714E-03	0.0000E+00	0.0000E+00	7.5678E+04
9.0101E+14	1.9129E+00	8.6977E-03	0.0000E+00	0.0000E+00	1.0690E+05
1.1495E+15	3.1309E+00	1.4233E-02	0.0000E+00	0.0000E+00	1.4988E+05
1.4659E+15	5.1029E+00	2.3205E-02	0.0000E+00	0.0000E+00	2.0950E+05
1.8694E+15	8.1772E+00	3.7237E-02	0.0000E+00	0.0000E+00	2.8820E+05
2.3853E+15	1.2860E+01	5.8778E-02	0.0000E+00	0.0000E+00	3.8948E+05
3.0436E+15	2.0249E+01	9.3301E-02	0.0000E+00	0.0000E+00	5.2818E+05
3.8794E+15	3.2503E+01	1.5207E-01	0.0000E+00	0.0000E+00	7.3321E+05
4.9391E+15	5.2474E+01	2.5203E-01	0.0000E+00	0.0000E+00	1.0293E+06

Model 4: Chromospheric Model

MASS SCALE
1.6700001
80

-3.528800E+00	3.028936E+04	5.032243E+08	0.000000E+00	4.205938E+01
-3.527244E+00	2.091414E+04	6.946812E+08	0.000000E+00	3.623864E+01
-3.526349E+00	1.830391E+04	7.985313E+08	0.000000E+00	3.378725E+01
-3.525664E+00	1.669657E+04	8.783457E+08	0.000000E+00	3.220063E+01
-3.525016E+00	1.567862E+04	9.385489E+08	0.000000E+00	3.113036E+01
-3.524315E+00	1.494982E+04	9.893820E+08	0.000000E+00	3.028962E+01
-3.523515E+00	1.426401E+04	1.043710E+09	0.000000E+00	2.944764E+01
-3.522600E+00	1.350095E+04	1.110195E+09	0.000000E+00	2.849197E+01
-3.521569E+00	1.264732E+04	1.196617E+09	0.000000E+00	2.733849E+01
-3.520409E+00	1.171003E+04	1.306851E+09	0.000000E+00	2.599967E+01
-3.519107E+00	1.068451E+04	1.445339E+09	0.000000E+00	2.445230E+01
-3.517618E+00	9.931497E+03	1.535263E+09	0.000000E+00	2.326739E+01
-3.516022E+00	9.312148E+03	1.585308E+09	0.000000E+00	2.227809E+01
-3.514508E+00	8.853459E+03	1.649396E+09	0.000000E+00	2.153287E+01
-3.513354E+00	8.531279E+03	1.708515E+09	0.000000E+00	2.100803E+01
-3.512601E+00	8.324265E+03	1.749625E+09	0.000000E+00	2.067062E+01
-3.512057E+00	8.174788E+03	1.780211E+09	0.000000E+00	2.042699E+01
-3.511630E+00	8.057420E+03	1.804594E+09	0.000000E+00	2.023570E+01
-3.511263E+00	7.959630E+03	1.825039E+09	0.000000E+00	2.007622E+01
-3.510855E+00	7.921854E+03	1.831642E+09	0.000000E+00	2.001245E+01
-3.510430E+00	7.882511E+03	1.838312E+09	0.000000E+00	1.994603E+01
-3.509985E+00	7.841291E+03	1.845043E+09	0.000000E+00	1.987644E+01
-3.509519E+00	7.798149E+03	1.851765E+09	0.000000E+00	1.980362E+01
-3.509024E+00	7.752292E+03	1.858500E+09	0.000000E+00	1.972620E+01
-3.508498E+00	7.703587E+03	1.865130E+09	0.000000E+00	1.964398E+01
-3.507927E+00	7.650710E+03	1.871639E+09	0.000000E+00	1.955472E+01
-3.507163E+00	7.603975E+03	1.873594E+09	0.000000E+00	1.947373E+01
-3.505146E+00	7.565312E+03	1.852277E+09	0.000000E+00	1.939556E+01
-3.502383E+00	7.518011E+03	1.799798E+09	0.000000E+00	1.929752E+01
-3.498487E+00	7.505147E+03	1.653217E+09	0.000000E+00	1.924536E+01
-3.492900E+00	7.486317E+03	1.332538E+09	0.000000E+00	1.916849E+01
-3.484917E+00	7.458839E+03	1.120440E+09	0.000000E+00	1.905554E+01
-3.473518E+00	7.418150E+03	1.132598E+09	0.000000E+00	1.888647E+01
-3.457261E+00	7.358546E+03	1.213925E+09	0.000000E+00	1.863694E+01
-3.435172E+00	7.276264E+03	1.251565E+09	0.000000E+00	1.829126E+01
-3.415271E+00	7.201988E+03	1.241125E+09	0.000000E+00	1.797925E+01
-3.395642E+00	7.128737E+03	1.218907E+09	0.000000E+00	1.767144E+01
-3.375157E+00	7.052284E+03	1.189574E+09	0.000000E+00	1.735011E+01
-3.353294E+00	6.970672E+03	1.153054E+09	0.000000E+00	1.700710E+01
-3.329555E+00	6.882089E+03	1.108161E+09	0.000000E+00	1.663483E+01
-3.303216E+00	6.783791E+03	1.053052E+09	0.000000E+00	1.622171E+01
-3.272746E+00	6.671587E+03	9.655123E+08	0.000000E+00	1.575176E+01
-3.234558E+00	6.538456E+03	9.030467E+08	0.000000E+00	1.520314E+01
-3.179552E+00	6.371372E+03	8.022116E+08	0.000000E+00	1.455684E+01
-3.099731E+00	6.173238E+03	6.900119E+08	0.000000E+00	1.390961E+01
-3.006503E+00	5.978452E+03	5.863962E+08	0.000000E+00	1.343795E+01
-2.900432E+00	5.795778E+03	5.022252E+08	0.000000E+00	1.309102E+01
-2.782489E+00	5.622438E+03	4.355329E+08	0.000000E+00	1.274429E+01
-2.654494E+00	5.447385E+03	3.740150E+08	0.000000E+00	1.237159E+01
-2.518020E+00	5.275095E+03	3.204557E+08	0.000000E+00	1.197462E+01
-2.373675E+00	5.118013E+03	2.832401E+08	0.000000E+00	1.155464E+01
-2.222054E+00	4.987065E+03	2.681938E+08	0.000000E+00	1.111345E+01
-2.064729E+00	4.885003E+03	2.759104E+08	0.000000E+00	1.065568E+01
-1.903894E+00	4.800789E+03	3.012857E+08	0.000000E+00	1.018766E+01
-1.740904E+00	4.726315E+03	3.425247E+08	0.000000E+00	9.713373E+00
-1.576051E+00	4.642303E+03	3.903189E+08	0.000000E+00	9.236597E+00
-1.411198E+00	4.519325E+03	4.220411E+08	0.000000E+00	8.767256E+00
-1.246345E+00	4.342022E+03	4.413989E+08	0.000000E+00	8.298176E+00
-1.081492E+00	4.114684E+03	5.351918E+08	0.000000E+00	7.805796E+00
-9.166390E-01	3.860504E+03	8.005387E+08	0.000000E+00	7.228830E+00
-7.517850E-01	3.588002E+03	1.181615E+09	0.000000E+00	6.509416E+00
-5.869321E-01	3.340129E+03	1.357826E+09	0.000000E+00	5.691923E+00
-4.220790E-01	3.166233E+03	1.288603E+09	0.000000E+00	4.845234E+00
-2.572260E-01	3.084138E+03	1.349210E+09	0.000000E+00	3.897296E+00
-9.237202E-02	3.074605E+03	1.761166E+09	0.000000E+00	3.201868E+00
7.248099E-02	3.107961E+03	2.631224E+09	0.000000E+00	2.555161E+00
2.373340E-01	3.145833E+03	3.885715E+09	0.000000E+00	2.189964E+00
4.016900E-01	3.175483E+03	5.470957E+09	0.000000E+00	2.054514E+00
5.474790E-01	3.208114E+03	7.524054E+09	0.000000E+00	2.009425E+00
6.731880E-01	3.248920E+03	1.028974E+10	0.000000E+00	2.000543E+00
7.864560E-01	3.291175E+03	1.384067E+10	0.000000E+00	2.000000E+00
8.924711E-01	3.323337E+03	1.779234E+10	0.000000E+00	2.000000E+00
9.947391E-01	3.347963E+03	2.218389E+10	0.000000E+00	2.000000E+00
1.095001E+00	3.369527E+03	2.729233E+10	0.000000E+00	2.000000E+00
1.193981E+00	3.390551E+03	3.343208E+10	0.000000E+00	2.000000E+00
1.292021E+00	3.411399E+03	4.084336E+10	0.000000E+00	2.000000E+00
1.389433E+00	3.431061E+03	4.963831E+10	0.000000E+00	2.000000E+00
1.486505E+00	3.449472E+03	6.003378E+10	0.000000E+00	2.000000E+00
1.583372E+00	3.467713E+03	7.250338E+10	0.000000E+00	2.000000E+00
1.679999E+00	3.486952E+03	8.773222E+10	0.000000E+00	2.000000E+00

Model 4: Hydrogen Populations

4.9070E+04	7.6239E+01	1.0052E-01	0.0000E+00	0.0000E+00	4.5685E+08
5.2369E+05	1.8456E+02	2.2865E-01	0.0000E+00	0.0000E+00	6.3062E+08
1.4091E+06	2.5975E+02	3.1511E-01	0.0000E+00	0.0000E+00	7.2482E+08
2.8491E+06	3.2272E+02	3.8718E-01	0.0000E+00	0.0000E+00	7.9715E+08
4.6245E+06	3.7031E+02	4.4273E-01	0.0000E+00	0.0000E+00	8.5164E+08
6.6596E+06	4.0935E+02	4.9014E-01	0.0000E+00	0.0000E+00	8.9761E+08
9.4870E+06	4.4942E+02	5.4014E-01	0.0000E+00	0.0000E+00	9.4667E+08
1.4138E+07	4.9510E+02	5.9777E-01	0.0000E+00	0.0000E+00	1.0066E+09
2.2173E+07	5.5137E+02	6.6868E-01	0.0000E+00	0.0000E+00	1.0844E+09
3.6215E+07	6.2116E+02	7.5692E-01	0.0000E+00	0.0000E+00	1.1835E+09
6.0974E+07	7.2078E+02	8.8319E-01	0.0000E+00	0.0000E+00	1.3129E+09
8.9141E+07	8.0890E+02	1.0054E+00	0.0000E+00	0.0000E+00	1.4302E+09
1.1925E+08	9.1460E+02	1.1590E+00	0.0000E+00	0.0000E+00	1.5472E+09
1.4980E+08	1.0167E+03	1.3161E+00	0.0000E+00	0.0000E+00	1.6383E+09
1.7704E+08	1.1089E+03	1.4607E+00	0.0000E+00	0.0000E+00	1.7034E+09
1.9751E+08	1.1756E+03	1.5670E+00	0.0000E+00	0.0000E+00	1.7460E+09
2.1396E+08	1.2271E+03	1.6499E+00	0.0000E+00	0.0000E+00	1.7771E+09
2.2798E+08	1.2694E+03	1.7189E+00	0.0000E+00	0.0000E+00	1.8017E+09
2.4063E+08	1.3060E+03	1.7794E+00	0.0000E+00	0.0000E+00	1.8223E+09
2.4915E+08	1.3194E+03	1.8119E+00	0.0000E+00	0.0000E+00	1.8289E+09
2.5844E+08	1.3334E+03	1.8460E+00	0.0000E+00	0.0000E+00	1.8356E+09
2.6868E+08	1.3480E+03	1.8822E+00	0.0000E+00	0.0000E+00	1.8424E+09
2.8000E+08	1.3633E+03	1.9205E+00	0.0000E+00	0.0000E+00	1.8491E+09
2.9278E+08	1.3794E+03	1.9615E+00	0.0000E+00	0.0000E+00	1.8559E+09
3.0725E+08	1.3964E+03	2.0053E+00	0.0000E+00	0.0000E+00	1.8625E+09
3.2413E+08	1.4146E+03	2.0531E+00	0.0000E+00	0.0000E+00	1.8690E+09
3.4575E+08	1.4274E+03	2.1015E+00	0.0000E+00	0.0000E+00	1.8709E+09
4.0141E+08	1.4172E+03	2.1654E+00	0.0000E+00	0.0000E+00	1.8496E+09
5.0371E+08	1.3838E+03	2.2154E+00	0.0000E+00	0.0000E+00	1.7971E+09
7.1288E+08	1.2638E+03	2.1420E+00	0.0000E+00	0.0000E+00	1.6504E+09
1.1457E+09	1.0095E+03	1.8212E+00	0.0000E+00	0.0000E+00	1.3296E+09
1.4751E+09	8.2242E+02	1.5806E+00	0.0000E+00	0.0000E+00	1.1173E+09
1.5775E+09	7.5688E+02	1.5586E+00	0.0000E+00	0.0000E+00	1.1294E+09
1.6585E+09	6.9378E+02	1.5473E+00	0.0000E+00	0.0000E+00	1.2105E+09
1.8763E+09	6.5526E+02	1.5936E+00	0.0000E+00	0.0000E+00	1.2479E+09
2.1468E+09	6.3483E+02	1.6477E+00	0.0000E+00	0.0000E+00	1.2372E+09
2.4494E+09	6.1166E+02	1.6780E+00	0.0000E+00	0.0000E+00	1.2146E+09
2.7975E+09	5.8327E+02	1.6825E+00	0.0000E+00	0.0000E+00	1.1849E+09
3.2061E+09	5.4897E+02	1.6584E+00	0.0000E+00	0.0000E+00	1.1480E+09
3.6958E+09	5.0835E+02	1.6029E+00	0.0000E+00	0.0000E+00	1.1026E+09
4.2995E+09	4.6074E+02	1.5120E+00	0.0000E+00	0.0000E+00	1.0468E+09
5.0775E+09	4.0556E+02	1.3824E+00	0.0000E+00	0.0000E+00	9.7851E+08
6.1573E+09	3.4255E+02	1.2121E+00	0.0000E+00	0.0000E+00	8.9494E+08
7.8583E+09	2.7185E+02	1.0012E+00	0.0000E+00	0.0000E+00	7.9240E+08
1.0599E+10	2.0198E+02	7.7437E-01	0.0000E+00	0.0000E+00	6.7759E+08
1.4323E+10	1.4625E+02	5.7856E-01	0.0000E+00	0.0000E+00	5.7091E+08
1.9498E+10	1.0688E+02	4.3314E-01	0.0000E+00	0.0000E+00	4.8349E+08
2.7121E+10	7.9500E+01	3.2828E-01	0.0000E+00	0.0000E+00	4.1369E+08
3.8614E+10	5.7960E+01	2.4277E-01	0.0000E+00	0.0000E+00	3.4960E+08
5.6121E+10	4.1980E+01	1.7770E-01	0.0000E+00	0.0000E+00	2.9297E+08
8.3161E+10	3.1926E+01	1.3621E-01	0.0000E+00	0.0000E+00	2.4973E+08
1.2546E+11	2.7042E+01	1.1609E-01	0.0000E+00	0.0000E+00	2.2328E+08
1.9194E+11	2.6080E+01	1.1256E-01	0.0000E+00	0.0000E+00	2.1193E+08
2.9637E+11	2.7290E+01	1.1835E-01	0.0000E+00	0.0000E+00	2.0789E+08
4.6047E+11	2.9736E+01	1.2951E-01	0.0000E+00	0.0000E+00	2.0574E+08
7.2030E+11	3.0535E+01	1.3343E-01	0.0000E+00	0.0000E+00	1.9304E+08
1.1315E+12	2.4570E+01	1.0748E-01	0.0000E+00	0.0000E+00	1.4983E+08
1.7907E+12	1.2979E+01	5.6745E-02	0.0000E+00	0.0000E+00	7.7798E+07
2.8676E+12	4.1658E+00	1.8204E-02	0.0000E+00	0.0000E+00	2.2381E+07
4.6836E+12	9.3416E-01	4.0827E-03	0.0000E+00	0.0000E+00	3.4660E+06
7.8835E+12	1.4895E-01	6.5112E-04	0.0000E+00	0.0000E+00	2.8076E+05
1.3541E+13	2.2053E-02	9.6408E-05	0.0000E+00	0.0000E+00	1.9781E+04
2.3246E+13	5.4033E-03	2.3626E-05	0.0000E+00	0.0000E+00	3.3064E+03
3.8226E+13	3.3743E-03	1.4757E-05	0.0000E+00	0.0000E+00	1.4626E+03
6.4112E+13	4.9803E-03	2.1432E-06	0.0000E+00	0.0000E+00	1.5686E+03
1.0040E+14	1.1607E-02	5.0767E-05	0.0000E+00	0.0000E+00	2.7834E+03
1.5084E+14	2.7593E-02	1.2068E-04	0.0000E+00	0.0000E+00	5.0986E+03
2.2119E+14	5.7512E-02	2.5151E-04	0.0000E+00	0.0000E+00	8.3471E+03
3.0782E+14	1.1696E-01	5.1141E-04	0.0000E+00	0.0000E+00	1.3784E+04
4.0677E+14	2.4569E-01	1.0741E-03	0.0000E+00	0.0000E+00	2.4288E+04
5.2181E+14	5.0318E-01	2.1996E-03	0.0000E+00	0.0000E+00	4.2554E+04
6.6019E+14	9.0172E-01	3.9410E-03	0.0000E+00	0.0000E+00	6.5934E+04
8.2987E+14	1.4730E+00	6.4372E-03	0.0000E+00	0.0000E+00	9.3611E+04
1.0393E+15	2.3131E+00	1.0109E-02	0.0000E+00	0.0000E+00	1.2815E+05
1.2979E+15	3.5919E+00	1.5706E-02	0.0000E+00	0.0000E+00	1.7389E+05
1.6175E+15	5.5410E+00	2.4267E-02	0.0000E+00	0.0000E+00	2.3492E+05
2.0135E+15	8.4155E+00	3.6980E-02	0.0000E+00	0.0000E+00	3.1303E+05
2.5055E+15	1.2589E+01	5.5669E-02	0.0000E+00	0.0000E+00	4.1155E+05
3.1165E+15	1.8757E+01	8.3901E-02	0.0000E+00	0.0000E+00	5.4030E+05
3.8734E+15	2.8143E+01	1.2819E-01	0.0000E+00	0.0000E+00	7.1683E+05

Model 5: Chromospheric Model

MASS SCALE
1.6700001
80

-3.677000E+00	6.206114E+04	2.205369E+08	0.000000E+00	5.039727E+01
-3.674369E+00	2.161072E+04	4.744645E+08	0.000000E+00	3.702782E+01
-3.673487E+00	1.912950E+04	5.439698E+08	0.000000E+00	3.457998E+01
-3.672979E+00	1.784400E+04	5.850192E+08	0.000000E+00	3.333845E+01
-3.672480E+00	1.675024E+04	6.247315E+08	0.000000E+00	3.225459E+01
-3.671961E+00	1.590096E+04	6.598292E+08	0.000000E+00	3.137415E+01
-3.671378E+00	1.522526E+04	6.917288E+08	0.000000E+00	3.062419E+01
-3.670699E+00	1.465906E+04	7.225258E+08	0.000000E+00	2.993645E+01
-3.669905E+00	1.401674E+04	7.605501E+08	0.000000E+00	2.913795E+01
-3.668995E+00	1.328837E+04	8.080973E+08	0.000000E+00	2.820664E+01
-3.667969E+00	1.246999E+04	8.690915E+08	0.000000E+00	2.709835E+01
-3.666811E+00	1.157841E+04	9.469899E+08	0.000000E+00	2.580107E+01
-3.665484E+00	1.060733E+04	1.042985E+09	0.000000E+00	2.433214E+01
-3.663939E+00	9.865317E+03	1.108940E+09	0.000000E+00	2.316312E+01
-3.662220E+00	9.257094E+03	1.143544E+09	0.000000E+00	2.218864E+01
-3.660588E+00	8.785756E+03	1.189248E+09	0.000000E+00	2.142280E+01
-3.659390E+00	8.468941E+03	1.230967E+09	0.000000E+00	2.090643E+01
-3.658595E+00	8.258741E+03	1.261288E+09	0.000000E+00	2.056383E+01
-3.657996E+00	8.100303E+03	1.285040E+09	0.000000E+00	2.030559E+01
-3.657491E+00	7.966769E+03	1.305516E+09	0.000000E+00	2.008794E+01
-3.656985E+00	7.918129E+03	1.312396E+09	0.000000E+00	2.000616E+01
-3.656464E+00	7.871839E+03	1.318783E+09	0.000000E+00	1.992801E+01
-3.655940E+00	7.825273E+03	1.325094E+09	0.000000E+00	1.984940E+01
-3.655410E+00	7.778178E+03	1.331329E+09	0.000000E+00	1.976990E+01
-3.654866E+00	7.729833E+03	1.337544E+09	0.000000E+00	1.968829E+01
-3.654300E+00	7.679538E+03	1.343774E+09	0.000000E+00	1.960338E+01
-3.653677E+00	7.624180E+03	1.350311E+09	0.000000E+00	1.950993E+01
-3.652671E+00	7.594592E+03	1.350151E+09	0.000000E+00	1.945476E+01
-3.650504E+00	7.554652E+03	1.342420E+09	0.000000E+00	1.937400E+01
-3.647273E+00	7.515056E+03	1.316518E+09	0.000000E+00	1.928553E+01
-3.642658E+00	7.500458E+03	1.239648E+09	0.000000E+00	1.922634E+01
-3.635984E+00	7.478616E+03	1.041247E+09	0.000000E+00	1.913688E+01
-3.626341E+00	7.446568E+03	8.482888E+08	0.000000E+00	1.900492E+01
-3.612396E+00	7.398132E+03	8.503466E+08	0.000000E+00	1.880281E+01
-3.592561E+00	7.327681E+03	9.047389E+08	0.000000E+00	1.850727E+01
-3.569164E+00	7.243903E+03	9.152842E+08	0.000000E+00	1.815533E+01
-3.547536E+00	7.166411E+03	9.055087E+08	0.000000E+00	1.782976E+01
-3.525878E+00	7.088811E+03	8.884665E+08	0.000000E+00	1.750363E+01
-3.503190E+00	7.007526E+03	8.658142E+08	0.000000E+00	1.716199E+01
-3.478936E+00	6.920625E+03	8.372277E+08	0.000000E+00	1.679677E+01
-3.452481E+00	6.825850E+03	8.017243E+08	0.000000E+00	1.639848E+01
-3.422694E+00	6.719285E+03	7.574673E+08	0.000000E+00	1.595078E+01
-3.387025E+00	6.595009E+03	7.027388E+08	0.000000E+00	1.543224E+01
-3.339205E+00	6.444083E+03	6.365288E+08	0.000000E+00	1.482226E+01
-3.266997E+00	6.259751E+03	5.612291E+08	0.000000E+00	1.417014E+01
-3.175016E+00	6.063175E+03	4.844727E+08	0.000000E+00	1.363769E+01
-3.069609E+00	5.875833E+03	4.187549E+08	0.000000E+00	1.324306E+01
-2.951475E+00	5.696967E+03	3.645612E+08	0.000000E+00	1.289368E+01
-2.822256E+00	5.521418E+03	3.173582E+08	0.000000E+00	1.253142E+01
-2.683768E+00	5.346278E+03	2.740749E+08	0.000000E+00	1.214473E+01
-2.537085E+00	5.176421E+03	2.380545E+08	0.000000E+00	1.173505E+01
-2.382815E+00	5.036898E+03	2.220396E+08	0.000000E+00	1.130410E+01
-2.222183E+00	4.928297E+03	2.251747E+08	0.000000E+00	1.085538E+01
-2.057186E+00	4.837999E+03	2.431636E+08	0.000000E+00	1.039445E+01
-1.889563E+00	4.759353E+03	2.756938E+08	0.000000E+00	9.926175E+00
-1.720346E+00	4.682263E+03	3.205154E+08	0.000000E+00	9.454582E+00
-1.550488E+00	4.590317E+03	3.688632E+08	0.000000E+00	8.984976E+00
-1.380630E+00	4.440585E+03	3.929622E+08	0.000000E+00	8.525773E+00
-1.210772E+00	4.228877E+03	4.259418E+08	0.000000E+00	8.054957E+00
-1.040914E+00	3.989526E+03	5.864255E+08	0.000000E+00	7.526549E+00
-8.710550E-01	3.726176E+03	9.162314E+08	0.000000E+00	6.891743E+00
-7.011970E-01	3.461963E+03	1.232725E+09	0.000000E+00	6.128578E+00
-5.313390E-01	3.237714E+03	1.260386E+09	0.000000E+00	5.300004E+00
-3.614800E-01	3.105290E+03	1.199588E+09	0.000000E+00	4.457499E+00
-1.916220E-01	3.072035E+03	1.464475E+09	0.000000E+00	3.622242E+00
-2.176299E-02	3.088841E+03	2.096684E+09	0.000000E+00	2.907324E+00
1.480950E-01	3.123972E+03	3.131188E+09	0.000000E+00	2.400768E+00
3.179530E-01	3.158539E+03	4.568678E+09	0.000000E+00	2.121160E+00
4.806030E-01	3.186917E+03	6.369798E+09	0.000000E+00	2.020749E+00
6.177850E-01	3.219345E+03	8.628181E+09	0.000000E+00	2.003424E+00
7.403340E-01	3.264073E+03	1.188348E+10	0.000000E+00	2.000191E+00
8.535041E-01	3.302408E+03	1.576392E+10	0.000000E+00	2.000000E+00
9.613841E-01	3.331060E+03	2.008127E+10	0.000000E+00	2.000000E+00
1.066612E+00	3.354272E+03	2.502205E+10	0.000000E+00	2.000000E+00
1.170416E+00	3.375607E+03	3.090595E+10	0.000000E+00	2.000000E+00
1.273278E+00	3.396590E+03	3.804910E+10	0.000000E+00	2.000000E+00
1.375438E+00	3.417201E+03	4.670604E+10	0.000000E+00	2.000000E+00
1.477139E+00	3.436732E+03	5.706784E+10	0.000000E+00	2.000000E+00
1.578632E+00	3.454878E+03	6.937662E+10	0.000000E+00	2.000000E+00
1.679999E+00	3.473302E+03	8.434252E+10	0.000000E+00	2.000000E+00

Model 5: Hydrogen Populations

8.7909E+02	1.0688E+01	1.4879E-02	0.0000E+00	0.0000E+00	2.0022E+08
2.0916E+05	1.0061E+02	1.1767E-01	0.0000E+00	0.0000E+00	4.3073E+08
5.5053E+05	1.4223E+02	1.6185E-01	0.0000E+00	0.0000E+00	4.9380E+08
9.4248E+05	1.7004E+02	1.9101E-01	0.0000E+00	0.0000E+00	5.3103E+08
1.5529E+06	1.9869E+02	2.2095E-01	0.0000E+00	0.0000E+00	5.6703E+08
2.3536E+06	2.2481E+02	2.4849E-01	0.0000E+00	0.0000E+00	5.9882E+08
3.3359E+06	2.4873E+02	2.7428E-01	0.0000E+00	0.0000E+00	6.2769E+08
4.5252E+06	2.7176E+02	2.9994E-01	0.0000E+00	0.0000E+00	6.5554E+08
6.4499E+06	2.9979E+02	3.3141E-01	0.0000E+00	0.0000E+00	6.8988E+08
9.7017E+06	3.3360E+02	3.6953E-01	0.0000E+00	0.0000E+00	7.3275E+08
1.5370E+07	3.7524E+02	4.1646E-01	0.0000E+00	0.0000E+00	7.8764E+08
2.5216E+07	4.2776E+02	4.7580E-01	0.0000E+00	0.0000E+00	8.5772E+08
4.2321E+07	4.9852E+02	5.5657E-01	0.0000E+00	0.0000E+00	9.4703E+08
6.2648E+07	5.6233E+02	6.3600E-01	0.0000E+00	0.0000E+00	1.0305E+09
8.5139E+07	6.3799E+02	7.3572E-01	0.0000E+00	0.0000E+00	1.1133E+09
1.0869E+08	7.1319E+02	8.3997E-01	0.0000E+00	0.0000E+00	1.1809E+09
1.2852E+08	7.7911E+02	9.3297E-01	0.0000E+00	0.0000E+00	1.2271E+09
1.4357E+08	8.2742E+02	1.0022E+00	0.0000E+00	0.0000E+00	1.2586E+09
1.5606E+08	8.6647E+02	1.0587E+00	0.0000E+00	0.0000E+00	1.2828E+09
1.6746E+08	9.0123E+02	1.1096E+00	0.0000E+00	0.0000E+00	1.3035E+09
1.7419E+08	9.1377E+02	1.1353E+00	0.0000E+00	0.0000E+00	1.3104E+09
1.8118E+08	9.2576E+02	1.1610E+00	0.0000E+00	0.0000E+00	1.3168E+09
1.8853E+08	9.3791E+02	1.1873E+00	0.0000E+00	0.0000E+00	1.3231E+09
1.9633E+08	9.5025E+02	1.2143E+00	0.0000E+00	0.0000E+00	1.3294E+09
2.0477E+08	9.6297E+02	1.2425E+00	0.0000E+00	0.0000E+00	1.3356E+09
2.1406E+08	9.7623E+02	1.2721E+00	0.0000E+00	0.0000E+00	1.3419E+09
2.2492E+08	9.9082E+02	1.3052E+00	0.0000E+00	0.0000E+00	1.3484E+09
2.3871E+08	9.9491E+02	1.3344E+00	0.0000E+00	0.0000E+00	1.3482E+09
2.7074E+08	9.9365E+02	1.3836E+00	0.0000E+00	0.0000E+00	1.3405E+09
3.3033E+08	9.7628E+02	1.4312E+00	0.0000E+00	0.0000E+00	1.3145E+09
4.5110E+08	9.1305E+02	1.4275E+00	0.0000E+00	0.0000E+00	1.2376E+09
7.3106E+08	7.5495E+02	1.2689E+00	0.0000E+00	0.0000E+00	1.0391E+09
1.0273E+09	5.8785E+02	1.0629E+00	0.0000E+00	0.0000E+00	8.4604E+08
1.1281E+09	5.1943E+02	1.0135E+00	0.0000E+00	0.0000E+00	8.4799E+08
1.2216E+09	4.7700E+02	1.0136E+00	0.0000E+00	0.0000E+00	9.0222E+08
1.4131E+09	4.5924E+02	1.0588E+00	0.0000E+00	0.0000E+00	9.1254E+08
1.6313E+09	4.4462E+02	1.0928E+00	0.0000E+00	0.0000E+00	9.0253E+08
1.8774E+09	4.2693E+02	1.1091E+00	0.0000E+00	0.0000E+00	8.8523E+08
2.1633E+09	4.0513E+02	1.1067E+00	0.0000E+00	0.0000E+00	8.6228E+08
2.5022E+09	3.7885E+02	1.0838E+00	0.0000E+00	0.0000E+00	8.3334E+08
2.9136E+09	3.4772E+02	1.0382E+00	0.0000E+00	0.0000E+00	7.9740E+08
3.4332E+09	3.1107E+02	9.6669E-01	0.0000E+00	0.0000E+00	7.5261E+08
4.1308E+09	2.6842E+02	8.6698E-01	0.0000E+00	0.0000E+00	6.9716E+08
5.1650E+09	2.2033E+02	7.4045E-01	0.0000E+00	0.0000E+00	6.2987E+08
6.8635E+09	1.7040E+02	5.9785E-01	0.0000E+00	0.0000E+00	5.5285E+08
9.3565E+09	1.2585E+02	4.5846E-01	0.0000E+00	0.0000E+00	4.7374E+08
1.2835E+10	9.2738E+01	3.4789E-01	0.0000E+00	0.0000E+00	4.0523E+08
1.7918E+10	6.8935E+01	2.6459E-01	0.0000E+00	0.0000E+00	3.4803E+08
2.5589E+10	5.1085E+01	1.9959E-01	0.0000E+00	0.0000E+00	2.9809E+08
3.7352E+10	3.7272E+01	1.4758E-01	0.0000E+00	0.0000E+00	2.5240E+08
5.5638E+10	2.7287E+01	1.0913E-01	0.0000E+00	0.0000E+00	2.1289E+08
8.4378E+10	2.2491E+01	9.0651E-02	0.0000E+00	0.0000E+00	1.8963E+08
1.2994E+11	2.1245E+01	8.6207E-02	0.0000E+00	0.0000E+00	1.7976E+08
2.0238E+11	2.1865E+01	8.9281E-02	0.0000E+00	0.0000E+00	1.7678E+08
3.1750E+11	2.3749E+01	9.7554E-02	0.0000E+00	0.0000E+00	1.7725E+08
5.0074E+11	2.5803E+01	1.0658E-01	0.0000E+00	0.0000E+00	1.7531E+08
7.9282E+11	2.5459E+01	1.0562E-01	0.0000E+00	0.0000E+00	1.6011E+08
1.2627E+12	1.7290E+01	7.1899E-02	0.0000E+00	0.0000E+00	1.0923E+08
2.0323E+12	6.8420E+00	2.8476E-02	0.0000E+00	0.0000E+00	4.1260E+07
3.3205E+12	1.8626E+00	7.7571E-03	0.0000E+00	0.0000E+00	8.6503E+06
5.5563E+12	3.5935E-01	1.4978E-03	0.0000E+00	0.0000E+00	1.1142E+06
9.5534E+12	5.4250E-02	2.2618E-04	0.0000E+00	0.0000E+00	6.8104E+04
1.6636E+13	8.8285E-03	3.6822E-05	0.0000E+00	0.0000E+00	6.4667E+03
2.8697E+13	3.2042E-03	1.3370E-05	0.0000E+00	0.0000E+00	1.6726E+03
4.8249E+13	3.5691E-03	1.4896E-05	0.0000E+00	0.0000E+00	1.3671E+03
7.7980E+13	7.1188E-03	2.9715E-05	0.0000E+00	0.0000E+00	2.0353E+03
1.2097E+14	1.7000E-02	7.0966E-05	0.0000E+00	0.0000E+00	3.7053E+03
1.8215E+14	3.8767E-02	1.6183E-04	0.0000E+00	0.0000E+00	6.5775E+03
2.6522E+14	7.8825E-02	3.2902E-04	0.0000E+00	0.0000E+00	1.0663E+04
3.6096E+14	1.5598E-01	6.5103E-04	0.0000E+00	0.0000E+00	1.7529E+04
4.7278E+14	3.3816E-01	1.4114E-03	0.0000E+00	0.0000E+00	3.2316E+04
6.0703E+14	6.6150E-01	2.7609E-03	0.0000E+00	0.0000E+00	5.4504E+04
7.7208E+14	1.1452E+00	4.7804E-03	0.0000E+00	0.0000E+00	8.1925E+04
9.7754E+14	1.8543E+00	7.7432E-03	0.0000E+00	0.0000E+00	1.1558E+05
1.2343E+15	2.9266E+00	1.2232E-02	0.0000E+00	0.0000E+00	1.5931E+05
1.5553E+15	4.5798E+00	1.9181E-02	0.0000E+00	0.0000E+00	2.1819E+05
1.9569E+15	7.1104E+00	2.9901E-02	0.0000E+00	0.0000E+00	2.9709E+05
2.4604E+15	1.0885E+01	4.6113E-02	0.0000E+00	0.0000E+00	3.9968E+05
3.0932E+15	1.6398E+01	7.0355E-02	0.0000E+00	0.0000E+00	5.3041E+05
3.8873E+15	2.4716E+01	1.0820E-01	0.0000E+00	0.0000E+00	7.0670E+05

APPENDIX E

The basic equations for the constant damping length Alfvén wave-driven wind are given below. The formulation given by HEA includes the effects of the wave dissipation on the heating of the gas. Following HEA, the momentum equation in spherical symmetry, for a radial steady flow, radial magnetic field ($B_0 r_0^2 = B^2 r^2$) and assuming that the Alfvén waves are the only MHD wave mode present, is

$$v\frac{dv}{dr} = -\frac{1}{\rho}\frac{d}{dr}\left(P_{gas} + \frac{< \delta B^2 >}{8\pi}\right) - \frac{GM}{r^2}. \qquad (E.1)$$

v, ρ and P_{gas} are the gas velocity, density and pressure, respectively; δB is the magnetic field amplitude in the Alfvén wave and $\frac{GM}{r^2}$ is the gravitational acceleration. In this formulation, the driving force for the wind is the magnetic turbulent pressure. Note that if the Alfvén waves are sinusoidal, then the mean square magnetic field in the wave $< \delta B^2 >= \frac{1}{2}\delta B^2$, where δB is the wave magnetic field amplitude.

Neglecting thermal conduction (which is justified on the basis that even the hydrostatic models in Chapter 4 showed that the conductive flux is negligible) and assuming a perfect gas, the energy equation can be written,

$$\rho v\frac{d}{dr}\left(\frac{v^2}{2} + \frac{5}{2}a^2\right) + \frac{v}{2}\frac{d\epsilon}{dr} + \rho v g = Q - P_{Rad}, \qquad (E.2)$$

where Q is the heating rate due to the wind doing work on the gas and dissipating energy. P_{Rad} is the rate of energy loss by radiation. It is possible to find a relation for the magnetic pressure gradient by considering the wave action density, S (Jacques, 1977). If the wavelength of the Alfvén waves is short compared to the scale over which the physical properties of the wind change, then S is defined as,

$$S = \frac{\epsilon}{\omega}\frac{v + V_{Alf}}{V_{Alf}}, \qquad (E.3)$$

where the dispersion relation for the frequency, ω, is given by $\omega = k(v + V_{Alf})$. If the wave damping can be represented by a characteristic length, L, then the conservation of wave action is replaced by,

$$\frac{d}{dr}(v_g S) = -\frac{v_g S}{L}, \qquad (E.4)$$

where $v_g = v + V_{Alf}$ is the group velocity of the wave. From the conservation of mass flux and equation (E.3), equation (E.4) can be rewritten as follows,

$$\frac{d}{dr}\left[\epsilon M_A (1 + M_A)^2\right] = -\frac{1}{L}\epsilon M_A (1 + M_A)^2. \qquad (E.5)$$

$M_A = v/V_A$ is the Alfvénic Mach number. Integrating equation (E.5) gives,

$$\epsilon = \epsilon_0 \frac{M_{A0}}{M_A} B \left(\frac{1 + M_{A0}}{1 + M_A}\right)^2 exp\left[-\left(\frac{r - r_0}{L}\right)\right], \qquad (E.6)$$

where the subscript 0 refers to the values of parameters at a reference level which is chosen to be the base of the wind.

The heating rate Q can be written, following Hollweg (1973), as

$$Q = -\frac{1}{r^2}\frac{d}{dr}r^2\left[\epsilon\left(\frac{3}{2}v + V_A\right)\right] + \frac{v}{2}\frac{d\epsilon}{dr}. \qquad (E.7)$$

Adopting a constant damping length, L, equation (E.7) reduces to

$$Q = \frac{\epsilon (v + V_A)}{L}. \qquad (E.8)$$

Equation (E.8) and (E.6) can be combined to give the heating rate in terms of initial conditions and r and v,

$$Q = \frac{\epsilon_0 V_{A0} r_0^2}{L r^2}\frac{(1 + M_{A0})^2}{(1 + M_A)} exp\left[-\frac{(r - r_0)}{L}\right]. \qquad (E.9)$$

Computational Methods

When solving a set of equations numerically it is convenient to write them in terms of dimensionless variables. Equation (E.1) and (E.5) can be combined to give the dimensionless momentum equation,

$$\left[u^2 - \frac{a^2}{a_0^2} - \frac{\epsilon}{4\rho a_0^2}\frac{(3M_A+1)}{(M_A+1)}\right]\frac{du}{dz}$$
$$= \frac{2u}{z}\left[\frac{a^2}{a_0^2}\left(1 - \frac{1}{2}\frac{dLn(T)}{dLn(z)}\right) - \frac{\xi}{z} + \frac{\epsilon}{4\pi a_0^2}\left(\frac{(3M_A+1)}{(M_A+1)} + \frac{z}{\lambda}\right)\right], \tag{E.10}$$

where a is the local sound speed, a_0 is the initial sound speed, T is the gas temperature, $\xi = GM/(2R_0 a_0^2)$, the normalised velocity $u = v/a_0$, the normalised damping length $\lambda = L/R_*$ and $z = r/R_*$.

The Inner Wind Region

In Chapter 4 it was shown for the hydrostatic models that the energy balance is dominated by heating as radiative cooling of the gas. In this case $P_{Rad} = Q$. The radiative losses can be written in terms of the power loss function, Λ,

$$P_{Rad} = N_e N_H \Lambda(T) = \frac{\rho^2}{(\mu M_H)^2 F(T)}\Lambda(T) = Q, \tag{E.11}$$

where $F(T) = N_T^2/N_e N_H$ (N_T is the total number of particles per unit volume). F can be written in terms of the ionisation fraction defined as $f_{ion}(T) = N_e/N_H$. Assuming that $N_{He} = 0.1N_H$ then,

$$F(T) = \frac{(1.1 + f_{ion}(T))^2}{f_{ion}(T)}. \tag{E.12}$$

Equations (E.9) and (E.11) can be combined and written as a nondimensional energy equation using the relation $(M_A/M_{A0}) = (\rho_0/\rho)^{1/2}$,

$$\Lambda(T) = \frac{\epsilon_0 V_{A0}}{Lz^2}\frac{F(\mu M_H)^2}{\rho_0^2}\left(\frac{M_A}{M_{A0}}\right)^4\frac{(1+M_{A0})^2}{(1+M_A)}exp\left[-\frac{(z-1)}{\lambda}\right]. \tag{E.13}$$

Equation (E.13) can then be differentiated to give,

$$\eta\frac{dLn(T)}{dLnz} = \frac{(2+M_A)}{(1+M_A)} - \frac{z}{\lambda} + \frac{1}{2}\frac{(4+3M_A)}{(1+M_A)}\frac{dLn(u)}{dLn(z)}, \tag{E.14}$$

where $\eta = \frac{dLn(\Lambda(T))}{dLn(T)}$.

Equation (E.14) can then be substituted into equation (E.10) to give the momentum equation for the inner wind region,

$$\begin{aligned}\left\{u^2 - \frac{a^2}{a_0^2}\left[1 - \frac{1}{2\eta}\frac{(4+3M_A)}{(1+M_A)}\right] - \frac{\epsilon}{4\rho a_0^2}\frac{(3M_A+1)}{(M_A+1)}\right\}\frac{du}{dz} \\ = \frac{2u}{z}\left[\frac{a^2}{a_0^2}\left\{1 - \frac{1}{2\eta}\left[\frac{(2+M_A)}{(1+M_A)} - \frac{z}{\lambda}\right]\right\}\right. \\ \left. - \frac{\xi}{z} + \frac{\epsilon}{4\rho a_0^2}\left[\frac{(3M_A+1)}{(M_A+1)} + \frac{z}{\lambda}\right]\right]\end{aligned} \quad . \qquad (E.15)$$

The momentum equation (E.15) can then be integrated with equation (E.13) as the auxiliary equation. The text describes the solutions to these equations.

The Outer Wind Region

The approximation in the energy equation assumes that near the surface the wave heating term and the radiative cooling term dominate over the wind expansion terms. Further from the stellar surface this is no longer true and it is necessary to solve the full energy equation. Equations (E.2) and (E.10) can be combined to eliminate the terms in g and $\frac{d\epsilon}{dr}$, giving,

$$\frac{dLn(T)}{dLn(z)} = \frac{2}{3}\left[\frac{r(Q-P_{Rad})}{\rho a_0^3 u}\left(\frac{T_0}{T}\right) - \left(2 + \frac{dLn(u)}{dLn(z)}\right)\right] . \qquad (E.16)$$

Substituting equation (E.16) into (E.10) gives the momentum equation in the outer wind region,

$$\begin{aligned}\left[u^2 - \frac{5}{3}\frac{a^2}{a_0^2} - \frac{\epsilon}{4\rho a_0^2}\frac{(3M_A+1)}{(M_A+1)}\right]\frac{du}{dz} \\ = \frac{2u}{z}\left\{\frac{5}{3}\frac{a^2}{a_0^2} - \frac{zr_0(Q-P_{Rad})}{3\rho a_0^3 u} - \frac{\xi}{z} + \frac{\epsilon}{4\rho a_0^2}\left[\frac{(3M_A+1)}{(M_A+1)} + \frac{z}{\lambda}\right]\right\} .\end{aligned} \qquad (E.17)$$

These equations are solved when the dimensionless energy parameter,

$$\zeta = \frac{\rho a_0^3 u}{r_0 z P_{Rad}} \left(\frac{T}{T_0}\right) \left(2 + \frac{dln(u)}{dln(z)}\right). \qquad (E.18)$$

When this parameter exceeds 1% the wind solution passes from the inner wind equations to the outer wind equations.